NUMERICAL INVESTIGATION OF RESIDUAL STRESSES, DISTORTION AND MICROSTRUCTURE EVOLUTION IN MULTI-PASS WELDED STEEL COMPONENTS

A THESIS SUBMITTED TO
THE GRADUATE SCHOOL OF NATURAL AND APPLIED SCIENCES
OF
MIDDLE EAST TECHNICAL UNIVERSITY

BY
NURIYA GARIPOVA

IN PARTIAL FULFILLMENT OF THE REQUIREMENTS
FOR
THE DEGREE OF DOCTOR OF PHILOSOPHY
IN
METALLURGICAL AND MATERIALS ENGINEERING

SEPTEMBER 2016

Approval of the thesis:

NUMERICAL INVESTIGATION OF RESIDUAL STRESSES, DISTORTION AND MICROSTRUCTURE EVOLUTION IN MULTI-PASS WELDED STEEL COMPONENTS

submitted by **NURIYA GARIPOVA** in partial fulfillment of the requirements for the degree of **Doctor of Philosophy in Metallurgical and Materials Engineering Department, Middle East Technical University** by,

Prof. Dr. Gülbin Dural Ünver
Dean, Graduate School of **Natural and Applied Sciences**

Prof. Dr. C. Hakan Gür
Head of Department, **Metallurgical and Materials Engineering**

Prof. Dr. C. Hakan Gür
Supervisor, **Metallurgical and Materials Eng. Dept., METU**

Dr. Caner Batıgün
Co-Supervisor, **Weld. Tech. and NDT Res./App. Center, METU**

Examining Committee Members:

Prof. Dr. Rıza Gürbüz
Metallurgical and Materials Eng. Dept., METU

Prof. Dr. C. Hakan Gür
Metallurgical and Materials Eng. Dept., METU

Prof. Dr. A. Tamer Özdemir
Metallurgical and Materials Eng. Dept., Gazi University

Assist. Prof. Dr. Caner Şimşir
Dept. of Manufacturing Eng., Atılım University

Assist. Prof. Dr. Mert Efe
Metallurgical and Materials Eng. Dept., METU

Date:

21.09.2016

I hereby declare that all information in this document has been obtained and presented in accordance with academic rules and ethical conduct. I also declare that, as required by these rules and conduct, I have fully cited and referenced all material and results that are not original to this work.

Name, Last name : Nuriya Garipova

Signature :

ABSTRACT

NUMERICAL INVESTIGATION OF RESIDUAL STRESSES, DISTORTION AND MICROSTRUCTURE EVOLUTION IN MULTI-PASS WELDED STEEL COMPONENTS

Garipova, Nuriya

Ph.D., Department of Metallurgical and Materials Engineering
Supervisor: Prof. Dr. C. Hakan Gür
Co-Supervisor: Dr. Caner Batıgün

September 2016, 161 pages

Formation of residual stresses, distortion and microstructure evolution in multi-pass welding and surfacing welding on pipeline HSLA steels were numerically investigated. A procedure for three-dimensional finite element analysis of temperature field, stress-strain state and phase changes in weldments was developed by using ESI SYSWELD & VISUAL WELD software. Numerical results were verified by comparisons with the results of various tests and measurements, such as molten pool profile calibration, microstructure investigation, hardness measurement, residual stress measurement by XRD. Influences of the subsequent weld passes, the interpass temperature, and the unclamping temperature on the residual stress state were investigated. Subsequent weld passes accomplish partial PWHT on the previous weld passes. Higher interpass temperature decreases residual stresses, but shows greater effect on distortion. Besides, the effects of weld pass sequence and welding direction in surfacing welding were studied for three different cases. It was observed that the most uneven weld deposition mode results in more uniform residual stress field and deformation.

Keywords: Multi-pass Welding, Surfacing Welding, Residual Stress, Distortion, Finite Element Method

ÖZ

ÇOKLU PASO YAPILARAK KAYNAKLANMIŞ ÇELİK PARÇALARIN KALINTI GERİLMELERİN, EĞRİLİĞİN VE MİKROYAPI GELİŞMESİNİN NÜMERİK ARAŞTIRMASI

Garipova, Nuriya

Doktora, Metalurji ve Malzeme Mühendisliği Bölümü
Tez yöneticisi: Prof. Dr. C. Hakan Gür
Ortak tez yöneticisi: Dr. Caner Batıgün

Eylül 2016, 161 sayfa

Boru hatlarında kullanılan yüksek mukavemetli düşük alaşımlı çeliklerde ve yüzeysel çok pasolu kaynaklarda ve yüzey kaynak işlemlerinde kalıntı gerilmenin ve çarpılmanın oluşumu ve içyapı değişimi sayısal olarak incelenmiştir. Sıcaklık dağılımının, gerilme-şekil değiştirme durumunun ve faz değişimlerinin analizi için ESI SYSWELD & VISUAL WELD yazılımları kullanılarak üç boyutlu bir sonlu eleman prosedürü geliştirilmiştir. Simulasyonlardan elde edilen sonuçlar, erimiş havuz profili kalibrasyonu, içyapı inceleme, sertlik ölçümleri, X-ışını kırınımı ile kalıntı gerilme ölçümleri gibi çeşitli deneylerin ve ölçümlerin sonuçlarıyla karşılaştırılarak doğrulanmıştır. Ardışık kaynak pasolarının, pasolar arası sıcaklığın ve parça sabitlemenin sona erdirilmesi sıcaklığının kalıntı gerilme ve çarpılmaya etkileri incelenmiştir. Ardışık pasoların önceki pasolara ısıl işlem etkisi gösterdiği ve pasolar arası sıcaklığın artması ile kalıntı gerilme değerinin düştüğü ancak şekil bozulmasının önemli derecede arttığı tespit edilmiştir. İlave olarak, yüzey kaplama kaynağı işleminde yanyana yapılan kaynak pasosu yönünün ve sıralamasının etkisi üç farklı durum için araştırılmıştır. En düzensiz kaynaklamanın daha homojen kalıntı gerilme alanına ve deformasyona sebep olduğu anlaşılmıştır.

Anahtar Kelimeler: Çok pasolu kaynak, Yüzey kaynağı, Kalıntı gerilme, Çarpılma, Sonlu Eleman Yöntemi

ACKNOWLEDGEMENTS

First of all I would like to acknowledge my supervisor, Prof. Dr. C. Hakan Gür, for his continuous scientific guidance and support throughout my Ph.D studies. His academic, professional and personal qualities played a key role.

I express my gratitude to my co-supervisor Dr. Caner Batıgün for constructive discussions and helpful advices throughout the completion of this investigation and for sharing enthusiasm as well.

I would like to thank to my committee members Prof. Dr. Rıza Gürbüz, Prof. Dr. Tamer Özdemir and especially Asst. Prof. Dr. Caner Şimşir for their valuable criticism, comments and suggestions.

I am also grateful to all the members of METU Welding Technology and Non-Destructive Testing Research and Application Center.

This study was financially supported by The Scientific and Technological Research Council of Turkey (TÜBİTAK-BİDEB) with the fellowship from «2215 - PhD Fellowship Programme for Foreign Citizens» during 2009-2012 years.

TABLE OF CONTENTS

CHAPTERS:

LIST OF TABLES

LIST OF FIGURES

LIST OF ABBREVIATIONS

AISI	American Iron and Steel Institute
API	American Petroleum Institute
BCC	Body Centered Cubic (lattice structure)
BCT	Body Centered Tetragonal (lattice structure)
BFGS	Broyden-Fletcher-Goldfarb-Shanno (algorithm)
BM	Base Metal
CAD	Computer-Aided Design
CAE	Computer-Aided Engineering
CCT	Continuous Cooling Transformation (diagram)
CPU	Central Processing Unit
CWM	Computational Welding Mechanics
FCC	Face Centered Cubic (lattice structure)
FDM	Finite Difference Method
FE, FEM	Finite Element, Finite Element Method
FVM	Finite Volume Method
HAZ	Heat Affected Zone
HSLA	High-Strength Low-Alloy (steel)
IPS	Invariant-Plane Strain
ISO	International Organization for Standardization
MAG	Metal Active Gas (welding)
MBN	Magnetic Barkhausen Noise (technique)
PDE	Partial Differential Equation
PWHT	Post Weld Heat Treatment
RT	Room Temperature
TRIP	Transformation Induced Plasticity
WM	Weld Metal
WPM	Welding Process Modelling
XRD	X-Ray Diffraction

CHAPTER 1

INTRODUCTION

Residual stresses remain to be one of the most actual problems in industrial applications, particularly for the welded constructions. Residual stresses in welded structures may promote failure mechanisms such as progressive fatigue, brittle fracture, stress corrosion cracking, etc.

Due to large temperature gradients, phase transformation effects, strongly pronounced mechanical irregularity consisting in different mechanical properties of weld metal, of heat affected zone (HAZ) and of the base metal (BM) is inherent in the welded joints. This causes complex stress state in the welded joint and complicates residual stress assessment by standard means. In addition to non-uniform distribution of the residual stress field the magnitude of residual stresses can reach the magnitude of yield strength of the metal. Moreover, in weld and HAZ regions, stresses are unfortunately tensile. Together with the high probability of stress concentrators due to inevitable defects localization in weld joints it leads to structural failures especially at the welds. In this way, most of the crack initiation points are related with the highly tensile stressed regions on welds.

As it stands, knowledge of the distribution of residual stresses is essential for the quality management during production and also for further life management.

Currently, there are various methods in use to decrease the level of residual stresses in the welded construction during or after welding process. However, the phenomena of residual stresses is still a challenging problem that has to be solved.

Modern age is characterized by formation of global information-oriented society, one of the aspects of which is information industry. Thereupon, information technologies of obtaining, cumulation and utilization of knowledge get rapid development nowadays. Methodology of mathematical modelling and numerical experiment is referred to such kind of information technologies [1].

1.1 Relevance of the research issue

Numerical experiment is the method for investigation of structure or physical processes through the instrumentality of mathematical modelling (Fig.1.1). It assumes that followed by the construction of the mathematical model numerical study allows to «playback» the action of the object under study in different conditions or in variety of modifications. Numerical investigation of the model makes possible to determine various characteristics of the processes, to optimize constructions or modes of operations of the designed devices. Moreover, it happens that numerical analysis helps to detect new processes or properties of the object under study.

Numerical investigation takes intermediate position among the natural experiment and analytical research. Natural, or physical, experiment under the proper arrangement produces comprehensive and reliable results, but sometimes it is impossible to recreate certain critical modes, extreme conditions or it is unrealizable to take any measurements, observations or apply other methods of empirical research [1]. Also, it is known that natural measurements of residual stresses are often subject to significant scatter or variability. This scatter may be due to systematic factors such as variability in measurement location or material properties, or to experimental error in measured data, or improperly calibrated devices etc. Besides, it is impossible to obtain the data about stress development in time by means of available measurement techniques if the material goes through melting and solidification stages. Therefore, mathematical modelling may be practically the only feasible way of investigation.

In analytical approach, the mathematical model is formulated likewise in numerical experiment. But this model is studied solely by analytical calculations without involvement of any numerical methods. This approach leads to rigorous exact solution. However, analytical techniques can be applied only to plain, oversimplified models of real objects; and obtained analytical solution due to initial model roughening appears to be far from reality [1]. Given the very large number of variables involved in welding (torch properties, liquid metal behaviour, solidification, material softening, thermal contact to jig, jigging constraint, etc.) it is not currently possible to predict the stresses caused by welding *a priori* [2]. Instead the process physics is usually simplified (e.g. neglecting the behaviour of the melt, simplifying the heat input, etc.) [3]. On the contrary, numerical techniques used in computational experiment enable to study more complex models, sufficiently and completely reflecting processes under investigation [1].

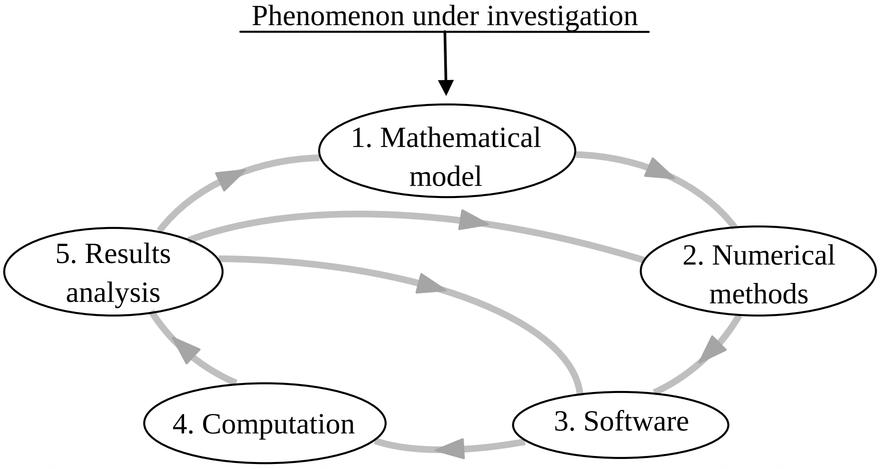

Figure 1.1 Stages of numerical experiment [1]

The accuracy of the computed results in a numerical experiment is defined by the validity of the model underlying the experiment, correctness of the algorithms and programs and preliminary testing experiments. During the numerical experiment, calculations are performed repeatedly with different input parameter values [1]. Residual stress predictions tend to follow the same trend as experimental measurements. The advantage of a reliable modelling tool is that once it has been validated it is possible to obtain results for a wide range of welding conditions with relatively little effort [4].

Thus, certain advantages of numerical experiment compared with that of natural should be noted:

1. Numerical experiment is usually cheaper than the natural.
2. It is possible to easy and safely intervene in the experiment.
3. It can be repeated again if necessary and terminated at any moment.
4. Conditions that cannot be created in laboratory can be modelled during the numerical experiment.

These capabilities of numerical simulations open opportunity to investigate even complex cases of welding, such as multi-pass welding, when it is does not seem feasible to measure or register origination, evolution and complicated interference of volumetric stress-strain states and phase transformations of entire joint coming from every weld pass. The metallurgical and thermo-mechanical aspects of each melting and solidification cycle and interaction between them is not yet well understood and has to be extensively explored. That is especially important for remote oil and natural gas resources transportation systems via long-distance pipelines the production of which includes multi-pass weldings. For that reason, the research issue of this study is oriented on numerical investigation of residual stress distribution, distortion and microstructure evolution in multi-pass welded steel components.

1.2 Aim and research objectives

Residual stress is a persistent problem caused by the welding of most kind of steels. The aim of this research is to investigate both transient and residual stresses, weld induced distortions and microstructure evolution in multi-pass weldings of pipeline steels, and characterize the influence of technological parameters on the final stress-strain state of the steel component with multi-pass welding through numerical simulations.

In the framework of this research the following objectives are stated:

1. To develop a procedure for three-dimensional numerical analysis of heat input and transfer, stress state, deformation and microstructure evolution of steel component with multi-pass arc welding, and to validate models by the experimental results.
2. To characterize stress-strain state, distortion and microstructure evolution for single-pass and multiple-pass cases during arc welding on V-groove and surfacing welding.
3. To investigate the influence of unclamping temperature on final residual stress distribution in steel components upon multi-pass welding.
4. To investigate the effect of interpass temperature on residual stress field evolution and metallurgical changes in steel components upon multi-pass welding.
5. To investigate the effect of sequencing of passes on residual stress state resulting from multi-pass surfacing welding.

Computational approach will aid to give clearer insight into the welding residual stress phenomenon, to characterize, to predict it and to determine its governing capacities. The main motivation to present research is to increase the general understanding of residual stress reduction mechanisms using optimal technological conditions during multi-pass welding of steels.

CHAPTER 2

RESIDUAL STRESSES AND DISTORTION IN MULTI-PASS WELDINGS

Residual stresses can be classified according to the manner in which they arise, the scale over which they equilibrate, or their effect on behaviour. The misfits that cause residual stresses can be introduced in many ways. Perhaps the most common origins are non-uniform plastic flow, steep thermal gradients and phase transformations. Thermal misfit stresses arise due to temperature gradients within a body. Whenever a material is exposed to severe thermal gradients there is an opportunity for non-uniform plastic deformation: this situation is characteristic of welding [3].

Because of their self-equilibrating character, the presence of residual stresses may not be readily apparent and so they may be overlooked or ignored during engineering design. However, they are stresses and must be considered in the same way as stresses due to external loading [5].

In this Chapter, origins, development and distribution of residual stresses are given. Also, reasons and mechanisms are briefly described, peculiarities concerning multi-pass weldments are touched upon. Besides, residual stress control and measurement methods are mentioned. Welding distortions and mitigation techniques are outlined. And, history and basis of mathematical modelling of welding are introduced.

2.1 Formation and distribution of welding residual stresses

Factors that significantly affect welding residual stresses and distortion can be categorized into three types, namely, material properties, design related variables and fabrication related parameters. Material related characteristics mainly include temperature dependent thermal-metallurgical and mechanical properties, work hardening coefficient, thermodynamics and kinetics of phase transformation, and transformation plasticity. Relevant design related variables consist of the joint geometry, component thickness, location of welded joint in a structure etc. Important fabrication related parameters involve chosen welding method, shape and size of groove, heat input, preheating and/or interpass temperatures, restraint conditions, tack weld, seam deposition sequence, positioning and so on.

Basic processes responsible for the appearance of welding residual stresses are the process of local intense heating to the melting and the subsequent cooling of the material in short period of time. To compare, residual stresses caused by the heat treatment processes are due to thermal stresses at nonuniform temperature field throughout the volume and much more extensive structural transformations (Fig.2.1). All these factors are mainly related to the cooling rate during the technological process.

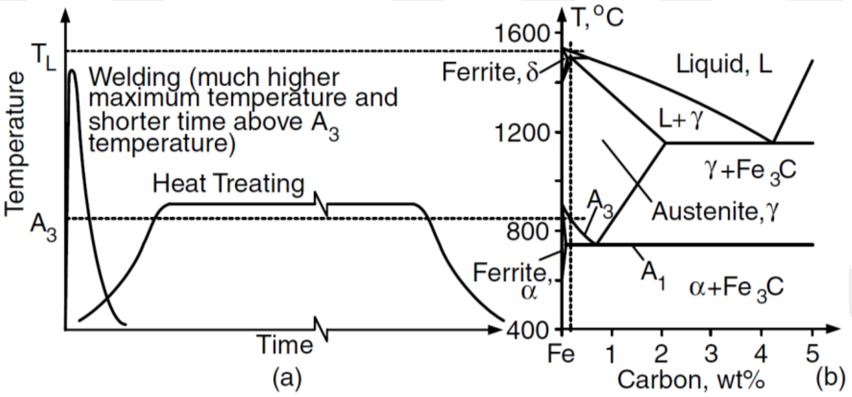

Figure 2.1 Comparison between welding and heat treating of steel: a) thermal processes, b) Fe-C phase diagram [6]

As a result of high peak temperatures during welding, grain growth can take place near the fusion boundary. The slower the heating rate, the longer the retention time above Ac_3 is and hence the more severe grain growth becomes. In the heat treating, however, the maximum temperature employed is only about 900°C in order to avoid grain growth [6].

In the case of welding thick products (bead-on-plate welds), the dissipation of heat occurs primarily radially compared to the source (Fig.2.2), in some extent resembling the heat treatment conditions. In the case of welding thin products, the heat dissipation is negligible in depth. The isotherms are thus perpendicular to the surface of the parts [7]. The heat flow is two-dimensional for the thin plate and three-dimensional for the thick plate. Heat losses through the surface are then assumed to be negligible. Consequently, thickness parameter of the component greatly influences on thermodynamics and kinetics of the welding process, defining final geometry of the structure and properties of the weld joint.

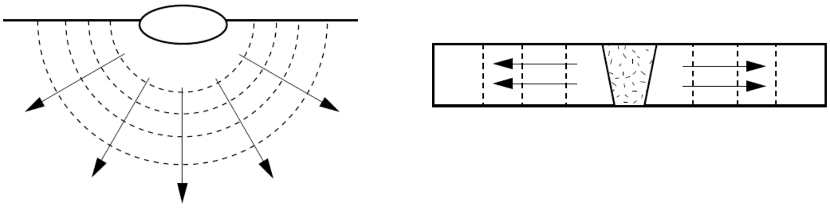

Figure 2.2 Heat flow in welding of thick and thin plates

If the kinetic of rapid heating during welding on phase transformations is neglected, welding joint of carbon steel can be associated to Fe-C diagram (Fig.2.3).

The HAZ can be conveniently divided into sub-zones. Solid-liquid transition zone is directly adjacent to the area of the weld metal; it is usually 0.1-0.4 mm of base metal heated to partial melting temperature. Grain growth zone is the part of base metal heated up to 1100-1450°C, and in this connection its metal is distinguished by coarse-grained structure and reduced mechanical properties. In most cases, a Widmanstätten structure is obtained in this region. The metal of this zone is the most brittle, though this does not significantly influence in the strength of the entire weld joint. Normalization zone covers an area heated up to 900-1100°C. Metal of this part is characterized by high mechanical properties since during cooling a fine-grained structure is formed. The area of incomplete recrystallization is heated to the temperature range of 725-900°C. Due to insufficient time and heating temperature, the metal structure consists of a mixture of the small recrystallized grains and coarse grains that do not have time to recrystallize. Properties of it are lower than that of metal from previous area. High-temperature tempered zone is observed in area heated up to 500-900°C, at that high strength and ductility as well as the maximum viscosity of a metal remain. Medium-temperature tempered zone (350-500°C) and low-temperature tempered zone (250-350°C) are characterized by decreased plasticity and viscosity of metal. By structure this area does not differ from that of the BM and is transitional from HAZ to BM. The best strength and ductility combination of the weld joint metal is obtained in the normalization zone. Thus, the weld appears to be inhomogeneous by structure and properties. The width of HAZ depends on type of welding, its parameters, thickness and of the geometry of the joined sections.

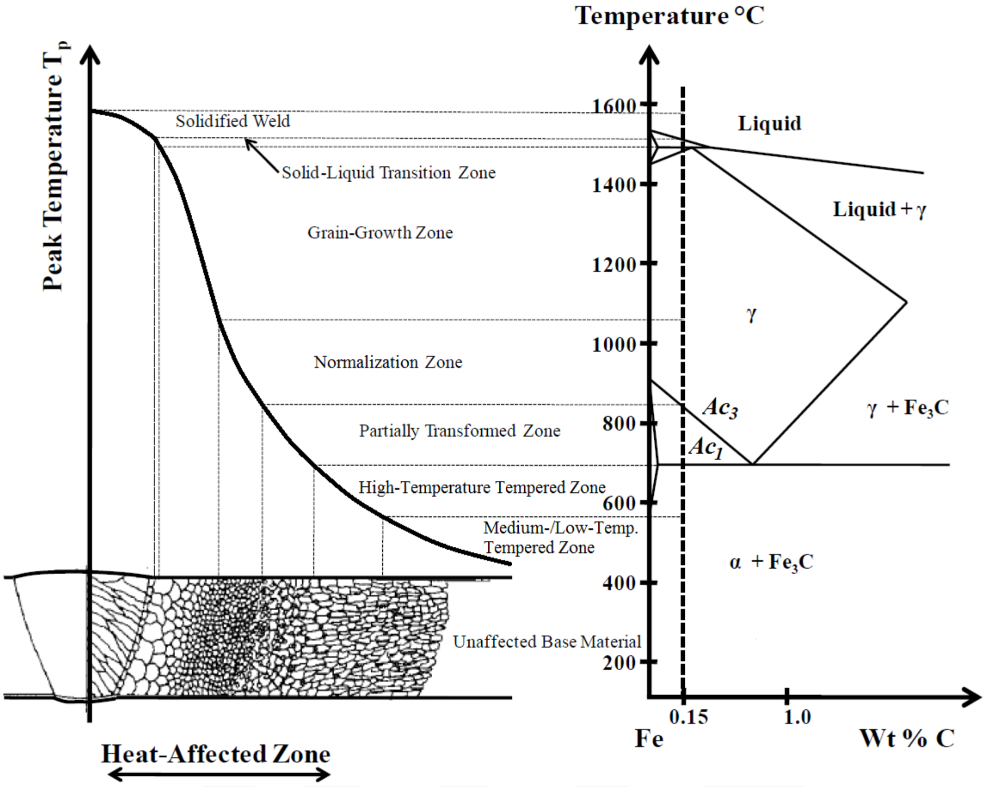

Figure 2.3 Heat-affected zone microstructure [8, 9]

The local thermal excursion usually causes plastic strain in the weld metal and base-metal regions near the weld. These give rise to residual stresses as well as to local shrinkage and distortion [3]. Fig.2.4 displays the distribution and redistribution of longitudinal stresses during welding. In front of the welding, Section A-A, thermal gradient and consequent thermal stresses tend to zero. With approaching of welding arc and melting the metal, Section B-B, stresses are zero since molten metal does not resist to a load. In the vicinity to the molten weld pool, temperature gradient abruptly increases and material experiences compressive stresses due to impeding the thermal volumetric expansion from passing weld pool. To equilibrate these compressive stresses, tensile stresses arise in direction away from the weld centerline. At cooling stage, Section C-C, thermal gradients decrease and the metal of weld bead solidifies and volumetric shrinkage occurs inducing tensile stresses. In response, adjacent regions are compressively stressed. After complete cooling down, Section D-D, temperature gradient is vanished and high tensile stresses are formed along the weld region and balancing compressive stresses grow away it. The hatched area, M'-M', indicates the area where plastic deformation forms during welding. The metal outside it remains elastic during the process.

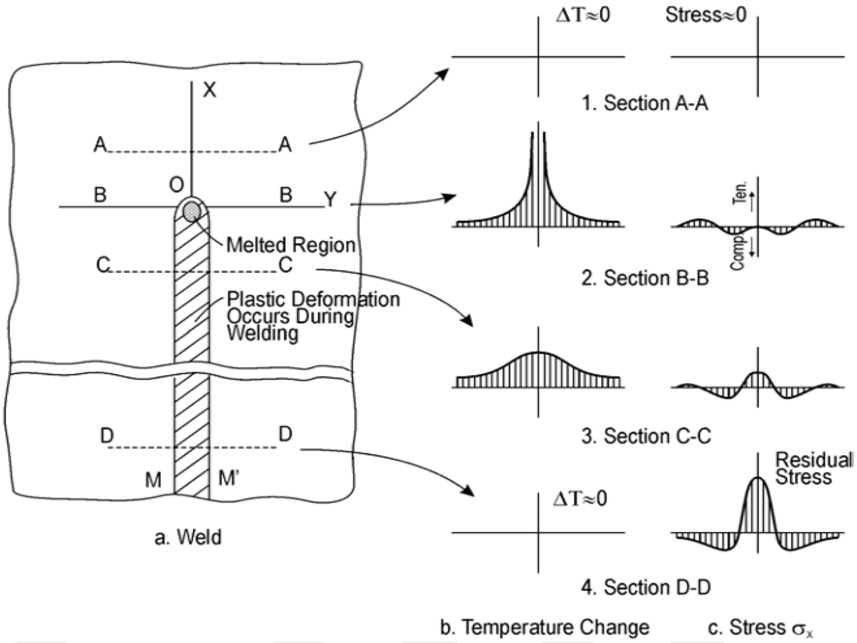

Figure 2.4 Representative graph of longitudinal thermal residual stresses and temperature variations during welding procedure [10]

A very important origin of welding residual stresses is impeded shrinkage processes, which occur when heated and cooled regions are neighbored. The basic principle is that heated volumes shrink during the cooling-down process according to their coefficient of thermal expansion and the existing temperature difference. It is assumed that melted volumes do not exert forces on surrounding volumes. Consequently, weld seams and surrounding volumes that have not been melted during the welding process exhibit different thermal and, thus, residual stresses (Fig.2.5). In the weld seam, starting from the stress-free state of the melting pool, tensile thermal stresses build up during the cooling process, which reach the temperature dependent yield strength of the material. Consequently, at the end of the cooling process, tensile residual stresses exist in the weld seam [11].

Materials volumes that are at a certain distance from the weld seam and are not melted during the welding process undergo impeded thermal strains during the heating period as well. It follows that compressive thermal stresses build up, yielding compressive plastic strains when the compressive temperature dependent yield stress is reached. These volume shrinkages build up tensile stresses when thermal contraction during cooling is impeded. The amount of tensile residual stresses is directly related to compressive strains during the heating process. For equilibrium reasons, longitudinal residual stresses change sign over the width of the plate

(Fig.2.6) and result in an inhomogeneous distribution of longitudinal residual stresses. Because inhomogeneous shrinkage means impeding of shrinkage, residual stresses build up also in the transverse direction. However, magnitude of the residual stress in the transverse direction reaches only about one-third of the values in the longitudinal direction [11].

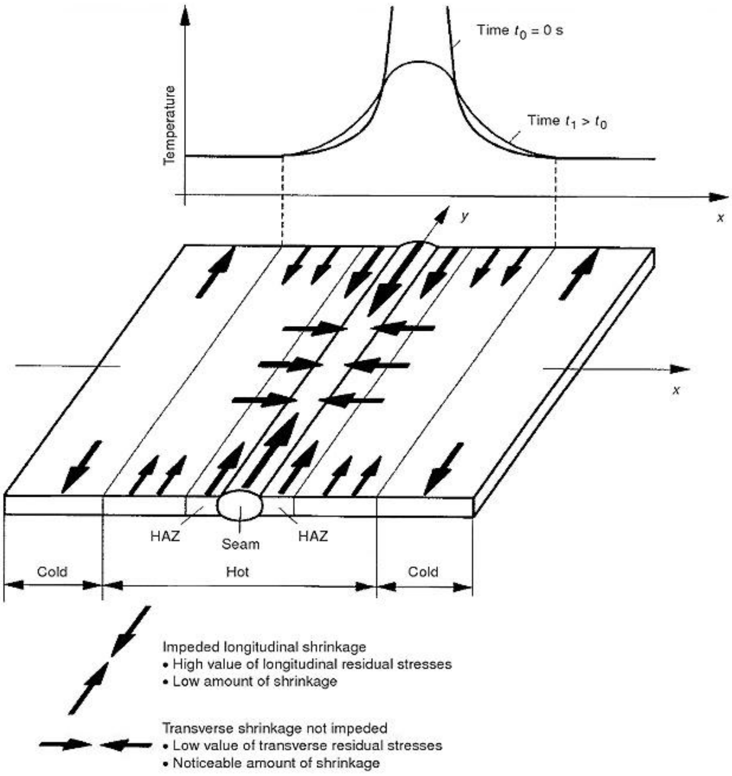

Figure 2.5 Shrinkage and impeded shrinkage as a consequence of inhomogeneous temperature distribution [12]

Particularly in the case of thicker plates, considerable temperature differences build up between the near surface and the core layers of the plate during the cooling process. The resulting thermal residual stresses may exceed the yield strength of the material, resulting in inhomogeneous plastic deformations that lead to residual stresses after cooling. If no other processes were active, compressive residual stresses in near surface layers and tensile residual stresses in the core would be expected. However, by far, quenching residual stresses develop together with residual stresses due to shrinkage processes and residual stresses due to phase transformations [11].

Within the fusion zone, the heat-affected zone (HAZ) and the adjacent parent material where the thermal softening and thermal strains caused by the heat flow from the weld are sufficient to cause yielding during welding, the residual stress field will be dominated by the weld-induced residual stresses. At greater distances from the weld, the residual stresses after welding will be a function of the superimposition of the weld-induced residual stresses and any pre-existing residual stresses in the parts being joined. The possibility of pre-existing residual stresses should always be considered when the residual stresses in welded structures are being evaluated [13].

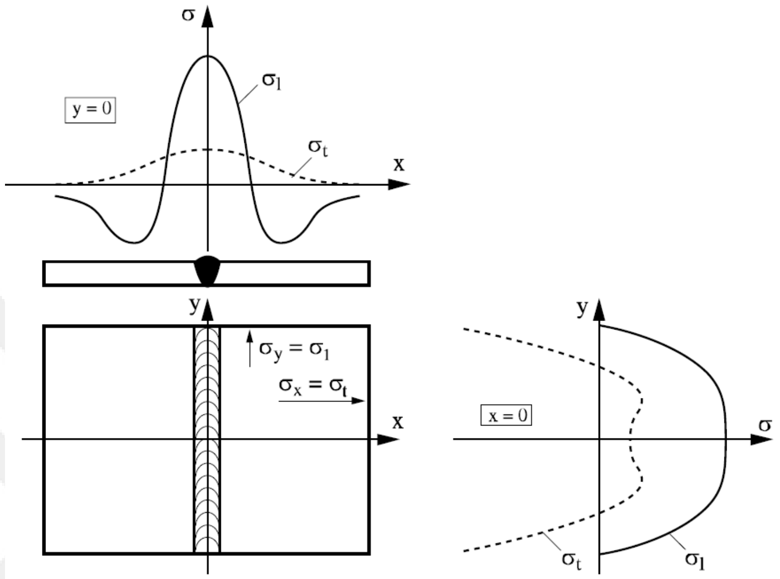

Figure 2.6 Typical example of longitudinal and
transverse residual stresses distributions within a welded joint [14]

Conceptual illustrative example of stress evolution is graphically presented further. During material heating (between two absolutely rigid fixed planes), compressive thermal stresses (curve $OA_1A_2A_3A_4$) arise in it (Fig.2.7).

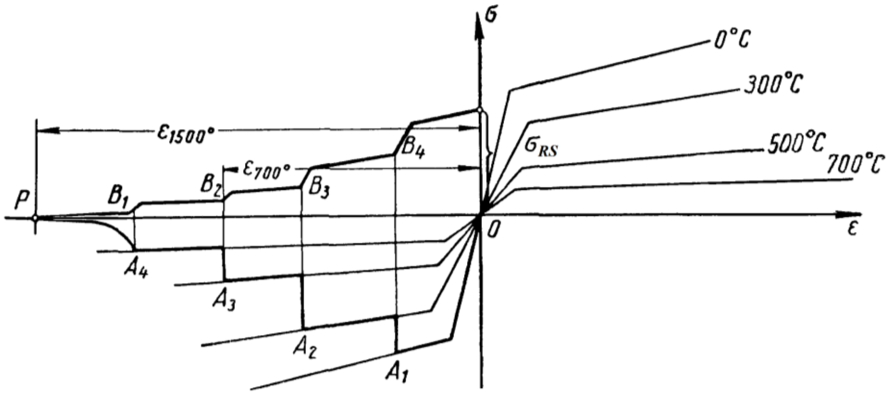

Figure 2.7 Residual stress formation during welding
(at complete constraint of deformations) [15]

With increasing temperature above 300°C, thermal stresses are reduced due to the decrease of the material's resistance to plastic deformations. Heating from 700°C to the melting temperature of steels (~1500°C) occurs at very low thermal stresses. While cooling, stress growth in the material begins at temperatures lower than 700°C (curve $B_1B_2B_3B_4$). Stresses become tensile and rise as the yield stress and elastic modulus increase. After cooling down, when thermal deformation disappears residual stresses remain in the structure. As it is seen from Fig.2.7, residual stresses are tensile and can achieve yielding strength of material [15].

When heated to ~250° (for carbon steels) mechanical properties remain almost constant and relative change in linear dimensions occurs basically only due to thermal expansion. During heating at higher temperatures, phase, structural and other processes related to the temperature are added to the reasons.

Inhomogeneity of transformation processes may be attributed to different reasons, as different peak temperatures during the welding process, different cooling velocities, or local changes of chemical composition. In practice, shrinkage and transformation processes overlap, and the amount as well as the sign of the resulting residual stresses strongly depend on the temperature range in which transformation takes place. The consequences are schematically outlined in Fig.2.8 (R_e is yield strength) [11].

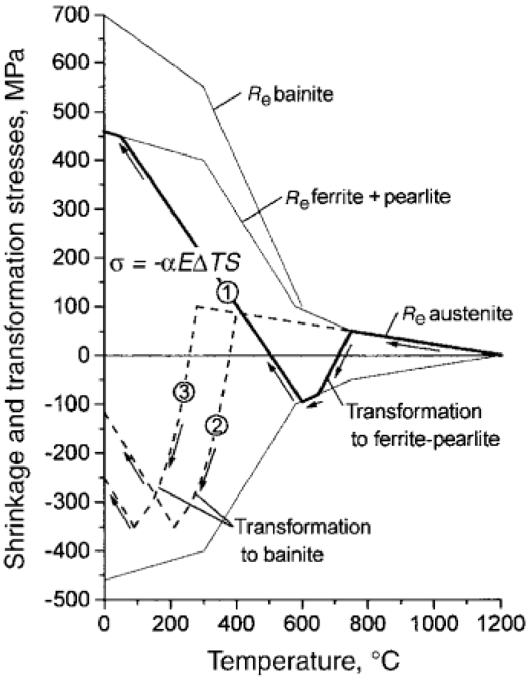

Figure 2.8 Interaction of impeded shrinkage and transformation for different cooling rates. Example 1, low velocity; Examples 2 and 3, high velocity [12]

It shows, as a function of temperature, the tensile or compressive yield strength of a ferritic-pearlitic or a bainitic microstructure. Starting at high temperatures, tensile stresses build up due to shrinkage processes and according to the temperature dependent yield strength of austenite. If phase transformations occur as a consequence of volume increase, tensile stresses rapidly decrease and change to compression. If, in the transformed volume, a ferritic-pearlitic microstructure develops, maximum compressive stresses are limited by the respective compressive yield strength of the phases created (Example 1 in Fig.2.11). If a martensitic transformation takes place, because of the high yield strength, the highest compressive stresses can develop. At the end of the transformation process, compressive residual stresses decrease because of continuous temperature decrease along with accompanying shrinkage (Examples 2 and 3 in Fig.2.8). Depending on Young's modulus, E, the stiffness, S, of the component, the coefficient of thermal expansion, α, and the remaining temperature difference, ΔT, up to RT, compressive or even tensile residual stresses result. Highest tensile residual stresses are expected if the transformation process is finished at relatively high temperatures. In that case, the tensile yield strength of the ferritic-pearlitic microstructure may be reached by the residual stresses [11].

Multi-pass welding has some features: since each layer has time for complete cooling before next weld layer is laid, a softened thermal effect of subsequent layers may alter the structure of WM and HAZ (Fig.2.9). In welding, large strains usually occur only in very hot areas.

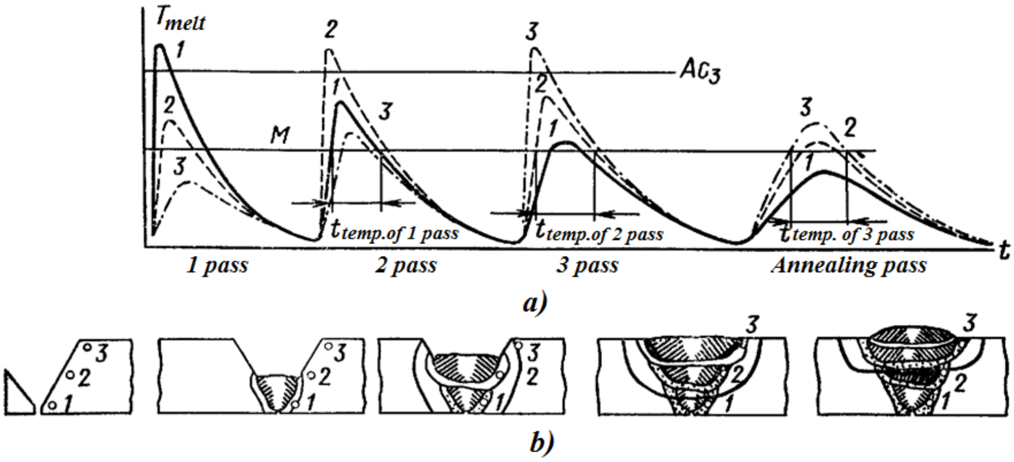

Figure 2.9 Thermal cycle (a) and scheme of structural changes(b)
for multiple pass welding of long sections [8]

The various regions of a HAZ of multi-pass weld in pipeline steel API X70 are defined in Fig.2.10. The complicated metallurgy is a direct result of the overlapping thermal profiles. Metallographic analyses reveals that a CGHAZ can be roughly categorized into four characteristic zones according to the peak temperature of subsequent thermal cycles in a multipass welding procedure: (i) unaltered CGHAZ (UA CGHAZ), the region reheated above specific temperature of grain growth or not reheated at all, (ii) supercritically reheated CGHAZ (SCR CGHAZ), the region reheated above A_{C3}, (iii) intercritically reheated CGHAZ (IR CGHAZ), the region reheated between A_{C1} and A_{C3}, and (iv) subcritically reheated CGHAZ (SR CGHAZ), the region reheated below A_{C1} [16].

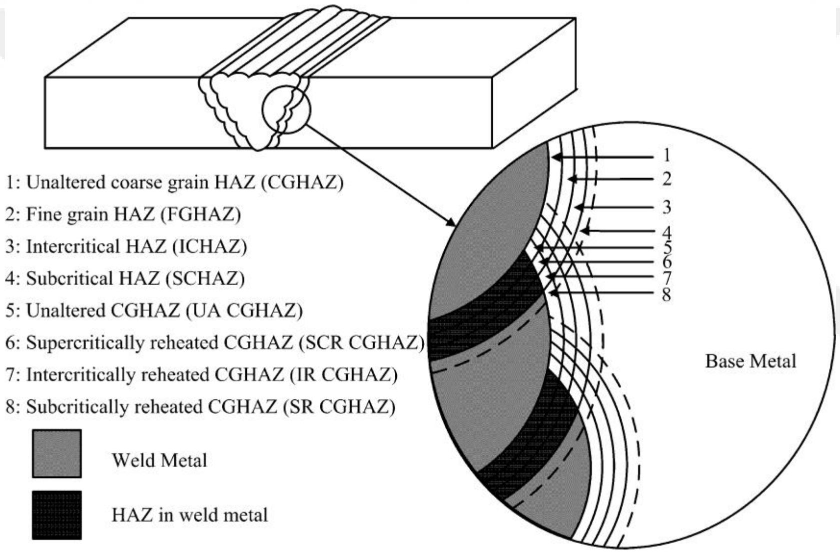

Figure 2.10 Schematic representation of various HAZ regions in a multi-pass weld [16]

Corresponding these regions thermal cycles and schematic microstructure is presented in Fig.2.11

The residual stresses may have been affected by operations other than welding occurring during material manufacture, fabrication or service life. The residual stresses may be sensitive to small changes in the joint geometry, welding conditions, inter-pass time, ambient environment, bead lay-up, material composition and mechanical properties, within the permitted ranges for these parameters [13].

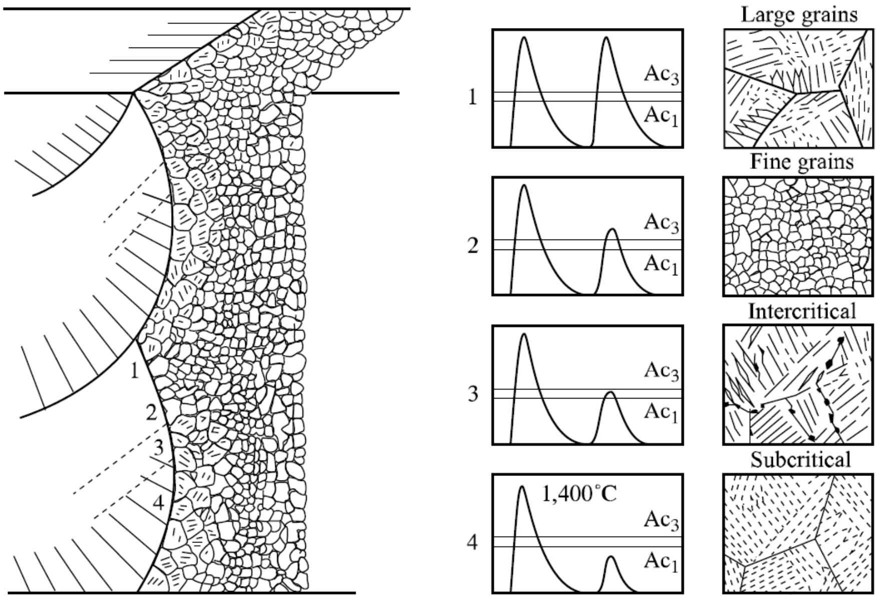

Figure 2.11 Diagrammatic illustration of the thermal cycles and the microstructures encountered in multi-pass welding [7]

2.2 Review of residual stress control methods

With development of manufacturing and facing with first problems caused by residual stresses, a lot of work have been done on implementation of measure techniques in order to reveal, control the distribution, depth and magnitude of residual stresses. Nowadays, there is a wide variety of different methods which are applied in accordance with technological feasibility, required accuracy, economic expediency.

The characteristically nonuniform, high stress gradient nature of residual stresses require that either the induced stress field is well understood and predictable, or many residual stress measurements must be performed on one or more components in order to reveal the nature of the stress fields. Often, scientists attempt to gain an understanding of a residual stress field by making a few measurements on one or two components, and from this often arise erroneous conclusions regarding the nature of the stress field. Therewith, stress is never the quantity measured because stress is a quantity that is applied to a metal and can only be measured in the process of its application [17].

Further, classification of stress measurement techniques and description of the magnetic Barkhausen noise and X-ray diffraction methods will be given in detail.

2.2.1 Classification of measurement approaches

During the past years many different methods for measuring the residual stresses in different types of components have been developed. Techniques to measure macro residual stresses may be classified as either destructive or semi destructive or non-destructive. The destructive and semi destructive techniques, called also mechanical method, are dependent on inferring the original stress from the displacement incurred by completely or partially relieving the stress by removing material. These methods rely on the measurement of deformations due to the release of residual stresses upon removal of material from the specimen. Sectioning, contour, hole-drilling, ring-core and deep-hole are the principals destructive and semi destructive techniques used to measure residual stresses in structural members. Non-destructive methods include X-ray or neutron diffraction, ultrasonic methods and magnetic methods. These techniques usually measure some parameter that is related to the stress. For inspection in the field or on large constructions, small, mobile and easy to handle devices are essential. Additionally, cost minimizing requires short measuring times without time-consuming preparation of the part prior to the test [18].

Once the decision is made to measure the residual stresses destructively, the following steps are usually applied in a typical stress-relief technique for residual stress measurement:

1) *stress field conditions*: failures of the component in service, distortion of a product in storage or during manufacturing, the shape of the component, the processes by which residual stresses were introduced, the justification for simplifying assumptions regarding the condition of the residual stresses field must be analyzed;

2) *strain measurement technique*: with the stress-reconstruction approach established, the method of strain measurement and the number and spatial frequency of measurements can be determined;

3) *preparation for strain measurement*: the measurement location must be established and the component and/or element prepared for the measurement. A prestress-relief reading must be made before stress relaxation and isolation of the element is initiated;

4) *isolation of gaged element*: material removal to isolate the gaged volume must be performed escaping introducing surface residual stresses that can be as great as the yield strength;

5) *post-stress relaxation measurement*: strain measurements are repeated, the final reading is subtracted from the initial to obtain the strain change resultant from the residual stresses relaxation, and the original stress state of the component is obtained through residual stresses reconstruction equations [17].

Comparative diagram of various residual stresses measuring techniques is presented on Fig.2.12 The destructive and semi destructive methods are coloured grey.

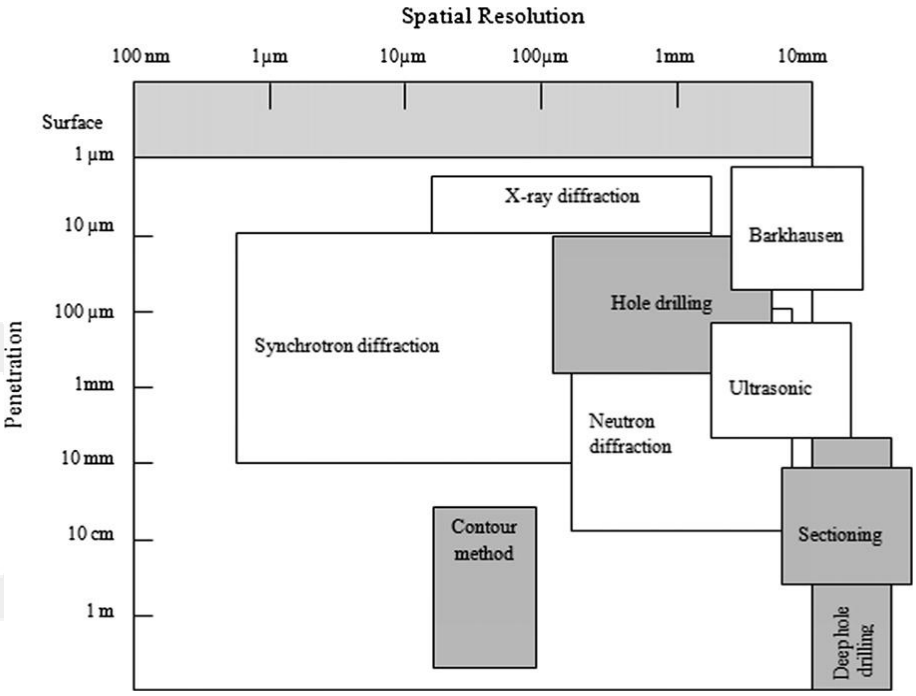

Figure 2.12 Penetration and spatial resolution of the residual stresses measuring techniques [18]

The neutron diffraction, in particular, is capable of evaluating residual stress in three orthogonal directions deep inside a welded structure with a spatial resolution of 1 mm or smaller. In contrast, the synchrotron X-ray can measure residual stress in two dimensions while the high-energy shorter wavelength radiation allows a fast measurement sufficiently deep in the weld. The laboratory X-ray based measurements, however, has remained an effective tool to measure surface and sub-surface residual stress. The synchrotron X-ray and neutron diffraction methods are usually preferred as they are non-destructive and free from near surface defects that inhibit the use of other techniques, and also facilitate mapping of stresses over a large area. Comparison between the neutron and X-ray based diffraction techniques has shown that the former is capable of monitoring bulk residual strain while the later can be used to characterize small-scale residual strain variation such as the strains in crystallographic structure. Both synchrotron X-ray and neutron diffraction are also used to trace the *in situ* evolution of residual strain [19].

Summarizing, the following remarks should be considered when choosing the residual stress measurement techniques [18]:

- X-ray diffraction method can be used for ductile materials to obtain both macro and micro residual stresses, but it is generally a lab based method and can be used for small components.
- Hole and deep hole drilling methods are easy and fast. They can be used for wide range of materials, but they are semi destructive method and it has limited strain sensitivity and resolution.
- Neutron diffraction has an optimal resolution but it needs an expensive and specialist facilities.
- Barkhausen noise and Ultrasonic both are fast, easy and low cost methods but they have limited resolution.
- Sectioning method is fast and can be used for a wide range of materials but it is a destructive method and has a low strain resolution.
- Contour method has a high resolution and can be used to high range of materials and for large components, but it is a destructive method.
- Synchrotron method is fast method for both macro and micro residual stresses, but it needs a very special equipment.

2.2.2 Barkhausen noise technique

The magnetic Barkhausen noise (MBN) method is applicable to ferromagnetic materials, which are composed of small order magnetic regions called magnetic domains. Each domain is spontaneously magnetized along the easy axes of the crystallographic magnetization direction. However, magnetization vectors inside the domains oriented in such a way that the total magnetization of the material is zero except or the natural magnets. Domains are separated each other by domain walls also called Bloch walls. There are two types of Bloch walls in a ferromagnetic material. 180° Bloch walls have greater mobility than 90° walls so their contribution to MBN is bigger. If an external D.C. magnetic field is applied to a ferromagnetic substance, the magnetization of the sample changes due to the domain wall movements. Domains with alignments parallel or nearly parallel to the applied field vector expand and others annihilate during magnetization. When all of the magnetization vectors inside the domains align themselves in the direction of the applied field by domain wall movements the saturation occurs. Grain boundaries, lattice dislocations, second phase materials (e.g., carbides in iron) and impurities in the ferromagnetic material act as an obstacle for the movement of domain walls. By the application of higher magnetization force values, force on the domain wall exceed the restraining force due to pinning sites, so there is an increase in the magnetization in small jumps, which also give rise to hysteresis. This increase can be determined by placing an inductive coil near to the specimen being magnetized. Because of this magnetization change an electrical pulse is induced on the coil [18]. Pulses are random in amplitude, duration and temporal separation [17]. When all electrical pulses produced by all domain movements added together a noise like signal called as Barkhausen Noise is generated. Fig.2.13 schematically shows the design of a micromagnetic sensor. A U-shaped yoke is excited by a coil connected to a bipolar power-supply unit. By the orientation of the poles, the direction of the resulting alternating magnetic field is defined and thus the corresponding stress component can be measured. The Barkhausen noise is detected by a small air coil whereas the tangential field strength is measured by a Hall probe. Both signals are amplified, filtered and evaluated in the micromagnetic testing system [18].

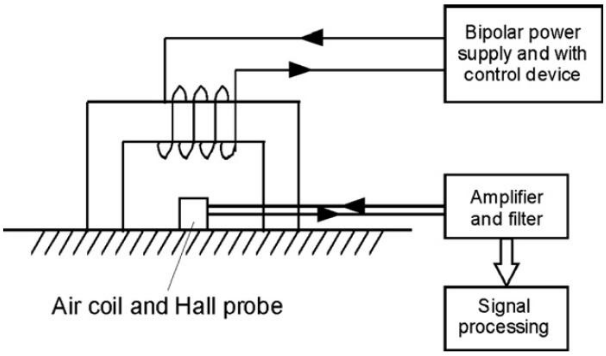

Figure 2.13 Scheme of the MBN measurement system

MBN method has the advantages of being rapid, suitable for the circular geometry like rings, and requiring no direct contact. The measurement depth depends mainly on the permeability of the material and it is typically up to 0.2 mm for surface hardened components. Since this depth is 100 times more than that of X-ray diffraction, the MBN method is also capable of quantifying subsurface stress without need of removing the surface layer [18].

2.2.3 XRD method

The X-ray diffraction method is a non-destructive technique for the measurement of residual stresses on the surface of materials. XRD technique is valid only for materials which are elastic, homogeneous and isotropic. XRD techniques exploit the fact that when a metal is under stress, applied or residual stress, the resulting elastic strains cause the atomic planes in the metallic crystal structure to change their spacings [18]. XRD can directly measure this inter-planar atomic spacing; from this quantity, the total stress on the metal can then be obtained [17]. When the material is in tension the distance between crystallographic planes increases and when the material is in compression, this distance decreases. The presence of residual stresses in the specimen produces a shift in the XRD peak angular position that is directly measured by the detector.

The changes in the positions of the diffraction peaks can then be used to calculate the strain and/or stress tensor components of interest in the diffracting regions by using the appropriate formulations of solid mechanics [5].

One of the major disadvantages in using XRD measurements is the limitation imposed on the test component size and geometry which has to provide X-ray hitting the measurement area and possibility to be diffracted to the detector without meeting any obstacles. Irregular geometry can cause getting unclear diffraction results.

The X-ray based measurement is difficult due to the preferred orientation of the unidirectional solidification and grain growth in the heat-affected zone [19].

Need to note, portable diffractometers that can be taken out into field for measurements of structures such as pipelines, weld, and bridges are now available.

2.3 Welding distortions and mitigation methods

In practical welding, welding deformations have often been the main concern. The deformations may be so large that they are visible and cause construction misfit problems, and their correction can be costly. Welding distortion is inevitable consequence and has been widely investigated along with welding residual stresses phenomenon. General classification of distortion types is given in Fig.2.14. Need to note, that combinations of distortion types are often observed in practice, and sometimes it is hard to distinguish an exact mode.

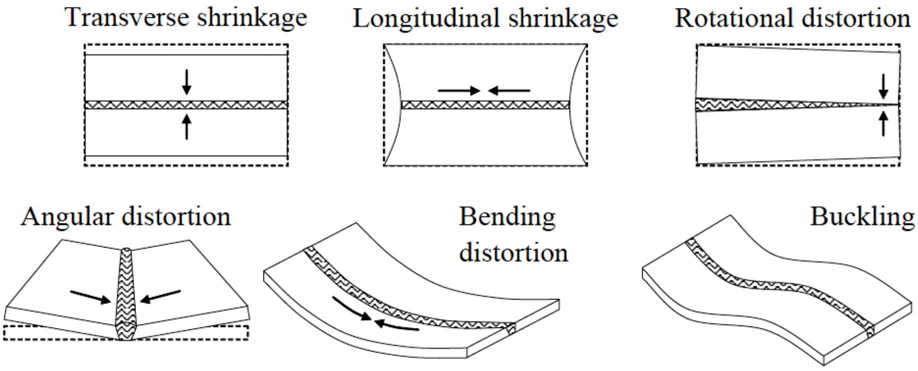

Figure 2.14 Types of welding induced distortions [10]

For thin-walled components, attention is largely focused on distortion. For stiffer thick-walled components, distortion is comparatively low, but residual stresses are relatively high due to the fact that the structure is more resistant to distortion.

In general, the main factors affecting weld distortions may be designated as [20, 21]:

1) Welding parameters and sequencing: the higher the heat input, the larger the welding residual stresses and distortion.

2) Restraint: opposing the shrinkage of the weld, it minimizes distortions. But, extra-restraint causes stress and strain in the component to build-up resulting in cold cracking of the joint or fatigue problems in-situ.

3) Preheating and reheating the weld: these parameters can increase or decrease welding distortion.

4) Weld and joint design: the more uniform the joint size across and through the weld (symmetry), the lower the risk of distortion. The bigger the weld volume, the larger the welding residual stresses and distortion. The thinner a welded plate is in comparison with size of the weld, the larger the deformations become.

5) Inherent stress state: if there is an initial stress inside a component before welding (preceding cold metalworking, thermal cutting processes), the residual stresses and distortion of the plate after welding will be rearranged − increased or decreased.

6) Thermo-mechanical properties of the parent metal: both thermal and mechanical properties influence the magnitude and distribution of the residual stresses and distortions in the welded joint.

Application of balanced placing of weld passes, appropriate use of restraints including tack welds, minimizing heat input, etc., are the attempts to reduce these deformations. A classification of mitigation methods is based on when they are applied during the manufacturing stage [21, 22]: prewelding methods, postwelding methods and in-situ welding techniques.

Prewelding methods cover reasonable weld joint design, preshaping, preheating etc.

During preshaping, the design of a structure is altered in a way to compensate angular shrinkage after welding distortion. Fig.2.15 shows two common methods used in design modification named presetting and prebending. Preheating can reduce as welding residual stresses, so distortion due to decreasing the high temperature gradient in welding.

Postwelding methods work by stress relieving and include post weld heat treatment (PWHT), vibration technique etc. PWHT consists in annealing of the workpiece.

Vibrating the material on a small amplitude frequency leads to reduction of residual stresses as a result of global and local plastic deformation. The last technique has such advantages as short time and low energy and avoids thermal distortion [22].

In-situ mitigation methods include rolling, mechanical tensioning, thermal tensioning and so on.

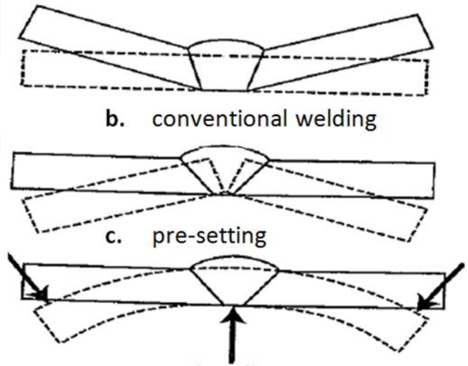

Figure 2.15 Preshaping method, the dashed line is initial state [23]

In case of direct rolling, the operation is applied during welding on the top of the weld. Whereas at roller tensioning technique, rolling is employed alongside of the weld. Mechanical tensioning technique consists on the uniform application of a load to the plates before fixing them prior to welding. This tensioning load continues the influence during welding and is removed together with unfixing after welding. In thermal tensioning, local heating and/or cooling is applied during welding. In case of static thermal tensioning when operation is performed with stationary heating and/or cooling sources, there is a preset temperature distribution in the component. Whereas at dynamic/transient thermal tensioning when heating source is moving, no preset temperature can be employed. As heating sources may act gas flames, high energy density beams, electric arcs; and as cooling medium − solid CO_2-snow, water or liquid nitrogen.

In literature, Nikolaev et al. [21] have given thorough review of distortions and mitigation techniques. Akbari Pazooki [24] has extensively investigated distortions of large plates after welding with additional side heating sources. Hansen [25] presented numerical analysis of the butt weld joint with special attention to the influence of the initial stress state before welding, that is, the residual stress state after preparation of the plates by flame cutting. Birk-Sørensen [26] simulated welding distortions of ship sections in order to obtain values for in-plane shrinkage and out-of-plane distortion. Finding appropriate ways to alleviate distortion and residual stress in welding has remained an important priority [19].

2.4 Approaches for mathematical modelling of welding

Methods of mathematical modelling of welding processes have been intensively developed after 1930s when the first works on the calculations of the temperature fields generated by a moving concentrated and distributed heat sources in the bodies of various shapes and sizes. Further, the theory of thermal processes in welding has been expanded by Rykalin, improved and brought to wide practical application in a large number of applied research. At 1960, Boley and Weiner introduced their comprehensive work on general theory of thermal stresses described as non-linear phenomena. Some of the first publications in weld modelling were by Hibbit and Marcal, Argyris et al. and Papazoglou and Masubuchi [27]. In early 1980s, two-dimensional numerical models transverse to the welding direction using either plane-strain or generalized plane strain conditions with lots of assumptions have been employed to study the welding. However, these models were not capable of predicting angular distortion and longitudinal buckling and bowing. In the mid 1980s, with increasing computing power the first three-dimensional transient heat transfer analyses were presented. Significant research in the 1980s includes the development of the 'double-ellipsoid' heat input model by Goldak et al. and the modelling of phase transformations [28-30]. After several years, the ideas of coupling thermal and mechanical fields began to find the ways of implementation. Karlsson [31], Radaj [22], Goldak [32] and Lindgren [33] and other authors have discussed different interactions that should be considered while welding simulations. Since thermal field is governed by parabolic partial differential equations (PDE) and mechanical field is governed by elliptic PDE and due to the consequent fact that thermal stresses generated by the welding process travel over the complete structure while the thermal-microstructure analysis only involve material in a short distance from the weld path and therefore a smaller geometrical model have to be analyzed, the thermal stress analysis of welds is a much more challenging problem than thermal-microstructure analysis. From the 1990s, transient and residual stresses caused by most standard joints as butt welds, pipe girth welds, T-joints have been numerically investigated. There appear commercial software packages for numerical simulation of general welding applications, one of the most comprehensive of which is SYSWELD from ESI Group.

In order to build a bridge between theoretical mathematics and practical computations in science and technology, several numerical approaches have been developed. Numerical methods provide adequate approximations to the solutions of non-linear transient problems running in complex body shapes. Among elaborated ones are the Finite Difference Method (FDM), the Finite Volume Method (FVM), the Finite Element Method (FEM), the Boundary Element Method (BEM) and the Boundary Domain Integral Method (BDIM).

In general, the time integration of governing differential equation can be carried out by either implicit or explicit integration schemes. Each type of integration has its own advantages and disadvantages. Implicit methods require a much larger computational effort per time step when compared with explicit methods. However, implicit methods can be designed to have unconditional stability, in linear analysis, so that the time step size can be selected solely based on the characteristics of the problem to be solved. On the other hand, explicit methods when using a diagonal mass matrix may require only vector calculations. Hence, the computational cost per time step is much lower. However, an explicit method can only be conditionally stable. Therefore, explicit methods may be effective when the time step size required by the stability limit is about the same as the time step size needed to describe the physical problem [34].

The distinguishing feature of above-listed numerical methods is how the discretization of governing PDEs is handled.

The FDM is the oldest and is based upon the application of a local Taylor expansion to approximate the PDEs to be solved. Each derivative is replaced with approximate finite difference equation. Computation domain is divided into cells and the solution is obtained at each node. The discretization gives a system of equations of the variables at nodes. The FDM is typically defined on a regular grid, and therefore not usually used for irregular CAD geometries, but more preferred for simpler block-shaped models. Upon finding solution, discrete representation of solution is obtained. The FDM is more difficult to use for simulation of material discontinuities. In addition, it is not possible to implement local grid refinement or technique like "adaptive mesh refinement". At early times, FDM has been utilized for heat and flow calculations and some cases of stress-strain states until the development of the more flexible methods. Today, it is used in weather calculations, astrophysics, seismology, in computer graphics etc.

The FVM first divides the spatial domain of the CAD model into very small but finite-sized volumes of geometrically simple shapes. The nodal points are placed in the centers of the discrete volumes of control. Since many physical laws are conservation laws, the FVM states the idea that inflow into one volume of control from one side should outflow the same volume from another side. Volume integrals in a PDE that contain a divergence term are converted to surface integrals, using the divergence theorem. The derivatives that remain on surfaces are approximated through interpolation functions. Finally, one obtain an algebraic system of equations to solve. The finite volume discretization can be in the form of regular or irregular mesh but regular mesh is preferred choice in most cases. Main shortcoming of the FVM is that the functions approximating the solution cannot be easily made of higher order as it is in FDM and FEM. In history, this method has been very successful in solving fluid flow problems. In present, an application in heat transfer and chemical engineering is developed as well.

The FEM was first proposed in works by A. Hrennikoff [35] at 1941 and by R. Courant at 1943, and then intensely developed in 1950-1960s. The FEM subdivides the domain of interest of a CAD model into very-small but finite-sized elements of geometrically simple shapes. The collection of all these shapes forms the finite element mesh where elements connect to each other by nodes. Then, a physical problem represented by PDEs is formulated as a set of approximating equations formulated for each element. The field within each element is expressed as a simple function, it may be linear or higher-order polynomial, with a finite number of degrees of freedom. This introduces local description of the physics by system of simple linear or nonlinear equations. After that, the contributions from all elements are combined and a large matrix equation system is obtained. Usually, the finite element is irregular because using regular mesh gives no special benefit. Main advantages of the FEM for increasing the solution accuracy are the possibility to use higher-order polynomials, local refining of the mesh close to irregular complex CAD geometry, "adaptive mesh refinement", mixed formulations allowing to combine different kinds of functions. For a thorough description of FEM a work by Zienkiewicz [36] is recommended further. The FEM finds an application in all kinds of structural analysis, heat transfer, electromagnetics, chemical engineering, multi-physics etc.

Nowadays, all of briefly presented methods found implementation in commercial software products.

CHAPTER 3

COMPUTATIONAL APPROACH IN MODELLING OF WELDING PROCESS

Computer simulation is indispensable for research, development and design in industry. Popularization of general-purpose programs based on the FEM enables engineers to execute highly reliable analysis and design [37].

Material science and constitutive modelling are essential ingredients in the modelling of welding processes due to the severe thermal cycle(s) during welding. The centrepiece in welding simulations is the heat generation process. Weld process modelling (WPM) focuses on modelling the physics of heat generation. CWM models, on the other hand, start with a given heat input that replaces the details of the heat generation process and focus on larger scales. The use of computational models does not replace experimental methods but does mean their role is redesigned. Fewer experiments (tests), are needed to evaluate different design concepts when the power of computer models is applied. Furthermore, the more established simulations become in a given field, the less validation testing is needed. However, more demands are placed on determination of material properties and boundary conditions needed for the computational model [38]. Welding simulation is a combination of heat conduction analysis and elastic-plastic stress analysis.

The earliest numerical predictions of residual stresses were probably those of Tall in 1961 [39]. He performed a one-dimensional analysis of thermal stresses during bead welding. In 1960s, Vinokurov [40] applied computer modelling of welding process to determine stress-strain state. The other earliest two-dimensional computational analysis was published in the early 1970s, Ueda and Yamakawa [41] first proposed a thermo-elastic-plastic FEM to predict welding residual stresses and deformation in a bead-on plate joint in 1971. Around the same time, Iwaki and Masubuchi [42], Fujita et al. [43], Hibbitt and Marcal [44], Friedman [45], Karlsson [31], Goldak et al. [46], Radaj [47] have developed numerical models to simulate the thermo-mechanical behaviors during welding process. In 1990s, Näsström et al. have firstly used a combination of solid and shell elements [48, 49]. Bhadeshia [50] emphasized on the essence of the modelling approach for steel welds. Recently, with the development of computer hardware, advances in multi-core CPU technology and improvement of software, three-dimensional models have been increasingly used to predict welding residual stresses and distortion. A comprehensive survey about the development of the computational approach in WPM has been given by Lindgren [33].

Today, a number of commercial software packages such as ESI SYSWELD®, WELDSIM®, Simufact.welding®, ANSYS®, ABAQUS®, MSC MARC®, ADINA®, COMSOL® etc. based on FEM theory are available to carry out the welding process simulations.

In this Chapter, a brief introduction to ESI SYSWELD software is provided; governing equations identifying the fields of heat conduction and transfer, stress/deformation and phase transformations are stated, and effects of model dimensionality is discussed.

3.1 Methodology and structure of ESI SYSWELD simulation package

In order to perform numerical experiments in a specific area of engineering, a large software systems are created. It consists of associated applications and system software including those providing the user controlling the calculations, post-processing and presentation of the results. Such a program complex is called a problem-oriented application package [1].

Algorithm of the ESI SYSWELD software code is based on the thermo-elastic-plastic FEM. The code is built of three software engines:

- The meshing engine (geometry / mesh pre-processor);
- The solver engine (analysis pre-processor and solver);
- The post-processor engine.

Visual-Environment^{TM} provides one single environment which covers interfacing to CAD formats, CAD cleanup, meshing, assembling the model, model set-up, post-processing using one single data model. Visual-Mesh is a complete meshing tool which supports CAD import, 2D and 3D meshing and editing for linear and quadratic meshes. Visual-Viewer^{TM} is a post-processing tool with plotting utilities. It caters to the requirements of the CAE community. Visual-WELD is a software package enabling setting up of welding work-flows through a guided interface [51].

The significance of virtual simulation method is the capability to isolate essential parameters of the complex welding process to study the effects of respective parameters on the formation of welding-induced stresses and deformation [27].

The software makes it possible to simulate welding while taking thermal, metallurgical and mechanical aspects into account and working by sequential analysis. Starting from the welding parameters, thermo-metallurgical calculation makes it possible to obtain the temperatures and phases formed at any point according to time. This stage takes into account the variations of thermal conductivity, specific heat and volumic mass according to the temperature [7].

CWM extends the capability to analyze the evolution of temperature, stress and strain in welded structures together with the evolution of microstructure. Distortion caused by volumetric strains due to thermal expansion and phase transformations are a dominate load in the stress analysis. The microstructure evolution influences the constitutive equations. In particular, as the temperature changes from above the melting point to room temperature, the stress-strain relationship changes from linear viscous, to visco-plastic to rate independent plasticity [52]. Though, SYSWELD does not take the last into account. The coupling between material behaviour and temperature and deformation fields is shown in Fig.3.1 and explained in Tabl.1.

Specific material law formulations take into consideration the removal of mechanical history when melting and activation of mechanical history during solidification, handling of weld material which is yet to be deposited (activation and deactivation of elements), thermal-elastic-plastic material behaviour and hardening including phase transformations, visco-plastic material behaviour including phase transformations, transformation plasticity, individual properties of phases, nonlinear mixture rules of properties of phases and restoring of strain hardening during phase transformation. In more detail, this interactions will be partly presented later in Section 3.3.

A fundamental work by Gür [53] gives keen insight into the physical origins of various aspects of material behaviour during thermal process modelling of steels.

The computational approach consists of two steps. The first step is thermal analysis, when temperature histories of all nodes contained in finite element model are calculated in relation with welding and thermal boundary conditions.

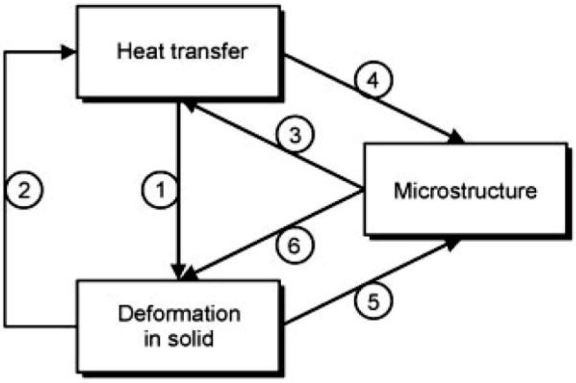

Figure 3.1 Couplings in thermomechanical models [38]

Table 1.1Thermomechanical couplings in Fig.3.1

Coupling	Description
1	Temperature changes drive the deformation via thermal expansion and volume changes due to phase changes
2	a) Deformation generated heat b) Deformation affects thermal boundary conditions
3	Thermal properties depend on microstructure and phase changes are associated with latent heats
4	Thermal driven phase changes
5	Deformation driven phase changes
6	The mechanical material behaviour depends on the microstructure and temperature

The second step is mechanical analysis, when thermal information of all nodes from previous step is taken as thermal load. Concurrent, external mechanical boundaries are taken into account.

Software SYSWELD fully couples thermal and phase transformation calculations. At each time step, temperature at a node and the corresponding phase proportions are calculated; that, in turn, in accord with mixture laws defines thermal-physical properties of the material (conductivity, specific heat etc.) at each given moment. In order to provide the highest efficiency of computation time, the mechanical computation is by default de-coupled from the thermo-metallurgical computation.

Calculated load results from thermal and microstructural part of simulation (temperature fields, thermal strains and phases) are stored according to the time steps, time increments are used to compute and record results from the mechanical part. Therefore, thermal, microstructural and mechanical results can be compared in process and analyzed in an objective manner [51].

3.2 Welding process representation model

In order to achieve appropriate representation of the welding process, the inherent fundamental physical phenomena should be mathematically incorporated into the model. The physical phenomena driving the weld pool formation and the directions of their actions on the heat and mass transport are presented in Fig.3.2.

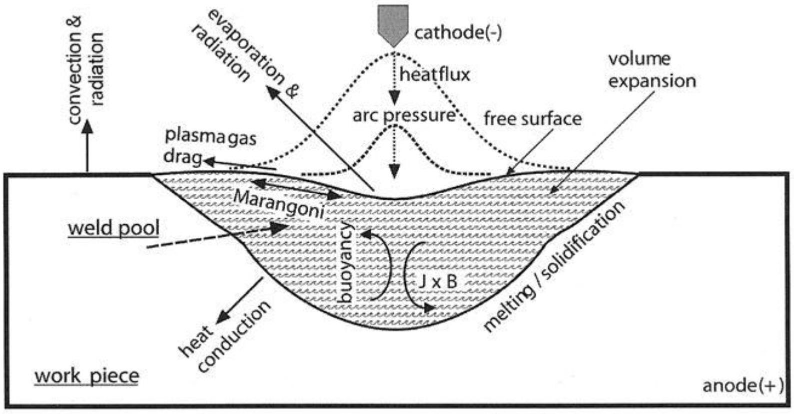

Figure 3.2 Physical phenomena driving the heat and fluid flow in the weld pool [54]

Simulation of welding process of practical components by means of FEM initially requires the model meshed with finite elements. This model is constructed on the basis of the work piece geometry that is previously generated in a CAD system.

The thermal, microstructural and mechanical FE modelling of the welding process is explained subsequently.

3.2.1 Heat source

The welding process is divided into the following three stages with respect to temperature changing with time: 1) heating of metal by given heat, 2) melting of metal, and 3) cooling of metal and solidification [55].

Simulation of welding stresses and distortion requires that the thermal energy supplied in practice is effectively introduced into the component. This can be carried out by means of a moving solidus area in the component (Fig.3.3a), or by means of an analytically specified heat source (Fig.3.3b). If a solidus area data is not available for transfer into the thermomechanical simulation, then an analytically specified volumetric heat source is used. The parameters of the heat sources are adjusted in a way that the result is approximately the shape of the molten zone [51].

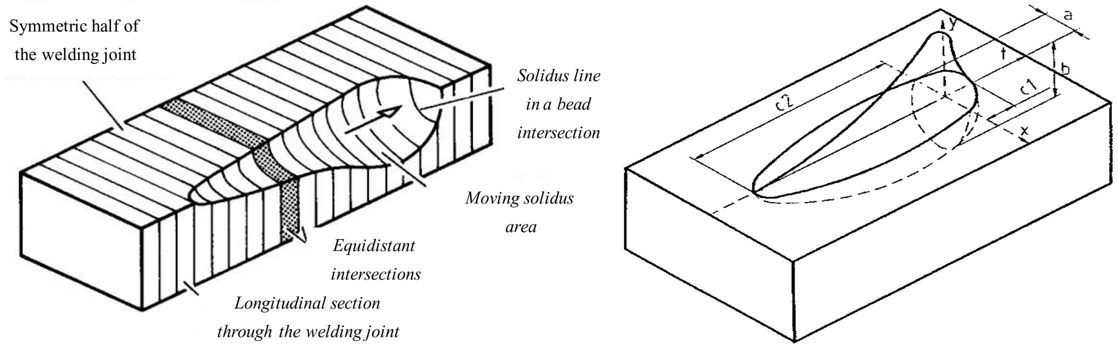

a) b)

Figure 3.3 Heat source shape: a) solidus area of the moving molten pool [56]; b) Goldak double ellipsoid heat source model

For each welding process a specific type of heat source is most effective. A heat source in the shape of a double ellipsoid presented by Goldak and Akhlaghi [52] is appropriate for the simulation of MIG welding processes by FEM. SYSWELD enables the definition of heat sources as function of space coordinates and time (Fig.3.3b). The power density distribution q inside the front and rear quadrants of the heat source, which are denoted by the subscript 1 and 2, respectively, is defined as:

$$q_{1,2}(x,y,z,t) = \frac{6\cdot\sqrt{3}\cdot f_{1,2}\cdot Q}{a\cdot b\cdot c_{1,2}\cdot\pi\cdot\sqrt{\pi}}\cdot e^{\frac{-3x^2}{a^2}}\cdot e^{\frac{-3y^2}{b^2}}\cdot e^{\frac{-3(z-v(\tau-t))^2}{c_{1,2}^2}} \tag{3.1}$$

where a is the width of heat source; b is the depth of heat source; $c_{1,2}$ are the semi-major axis of the front half and the rear half of heat source, respectively; Q is the heat input from the welding source, v is the welding speed and t is the welding time.

Each double ellipsoid heat source model is a combination of two ellipsoidal sources. The front half of the source is the quadrant of one ellipsoidal source, and the rear half is the quadrant of another ellipsoid. The coefficients f_1 and f_2 denote the fraction of the heat deposited in the front and rear quadrants, respectively, and $f_1 + f_2 = 2$. The power density distribution inside the front quadrant is higher than that in the rear quadrant. Therefore, the factor f_1 is larger than f_2. In SYSWELD, from FE point of view, a heat source is modelled by a volume density of energy (W/mm^3) applied to elements along the welding trajectory.

In arc welding processes, arc power and heat input are both measures of how much energy has been supplied to the workpiece to form a weld. Heat generated by arc is dictated by the power of the arc which is measured in watts. Effective heat power of the welding arc is calculated as:

$$Q = 0.8 \cdot U \cdot I \tag{3.2}$$

where 0.8 is efficiency coefficient; U is the arc voltage and I is the welding current.

Heat input of the weld pass is the ratio of effective heat power of the welding arc consumed for metal heating to the arc travel speed, and defines the amount of heat introduced by the arc into 1 mm of one-pass weld or bead:

$$H = \frac{60 \cdot Q}{v} \tag{3.3}$$

where v is linear welding speed in mm/min.

It should be pointed out that heat input limitations are applicable to each weld pass and are not considered cumulatively. They are applicable only to single-arc welding processes. It comes from the nature of the parameter since it influences the cooling rate which is the primary factor that determines the final metallurgical structure of the weld and HAZ and by association, the mechanical properties. In turn, travel speed affects heat input, weld cooling rates, and weld metallurgy, which are important for the HAZ and for fracture toughness control.

The heat input is known to influence the cooling rate (Fig.3.4).

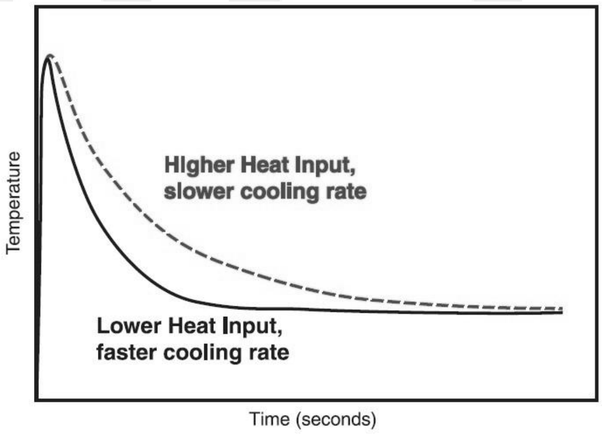

Figure 3.4 Heat input influences cooling rate [57]

The effect of welding parameters on the HAZ strength is explained in Fig.3.5. Both the size of the HAZ and the retention time above the effective recrystallization temperature T_x increase with increasing heat input per unit length of the weld. Consequently, the loss of strength in the HAZ becomes more severe as the heat input per unit length of the weld is increased [6].

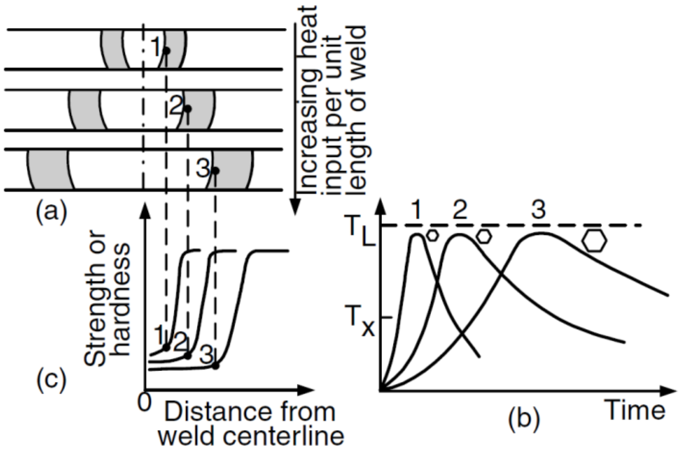

Figure 3.5 Effect of heat input per unit length of weld on: a) width of HAZ (shaded), b) thermal cycles near fusion boundary, and c) strength or hardness profiles [6]

3.2.2 Heat conduction and heat losses

In heat conduction, the flow of heat is proportional to the thermal conductivity λ, which is an index showing how well the heat flows in the material with the temperature gradient. This relation is known as Fourier law. The amount of heat flow becomes large when the cross-sectional area and the time are large [55].

The classical heat conduction equation comes from enthalpy-based formulation of energy conservation law and is taken into consideration via an equation:

$$\rho \frac{dH}{dt} = Q + div(\lambda \cdot \mathrm{grad}T) \tag{3.4}$$

where $\rho(T)$ is the density; $C_p(T) = dH/dt$ is the specific heat; $\lambda(T)$ is the thermal conductivity; Q is the internal heat source. Here, the product $\rho C_p(T)$ reflects the capacity of the material to store energy.

The heat conduction equation, together with initial and boundary conditions, defines the problem to be solved. Modelling of non-linear thermal boundary conditions such as convection, radiation is important stage for simulation.

Heat transfer is the phenomenon in which heat flows out or across the surface of the material. In heat transfer, two forms of heat flow are involved. The first form is the heat that moves from the metal surface to the surrounding fluid, such as the air, and is carried away by convection of the fluid. The second form is the radiation where the heat is emitted in the form of light [55].

Newton's law is applied to the convection. The heat flow from the metal surface to the atmosphere is proportional to the product of difference between the temperature of the atmosphere and that of the metal surface $(T - T_\infty)$ and the heat transfer coefficient α, which is a material characteristic that shows how easily the heat moves across the metal surface [55].

The heat flow from the metal surface to the atmosphere by radiation is given by Stefan-Boltzmann's law, and the amount of heat going out from the metal surface is proportional to the difference between the fourth power of the temperature on the surface and that of the atmosphere [55].

In heat transfer in welding, both convection and radiation occur simultaneously, and the heat loss by heat transfer becomes the sum [55]. Convective and radiation heat losses are more complex boundary conditions for the outward flux. Then the flux depend on the temperature of the body and the surrounding and is written as:

$$q_n = \alpha(T - T_\infty) + \epsilon\sigma_{SB}(T^4 - T_\infty^4) \tag{3.5}$$

where q_n is the heat flux in the outward normal direction, T is the surface temperature of the plate, T_∞ is the ambient temperature, the first term is convective heat loss and α is the heat transfer coefficient. The second term is the heat loss due to radiation and σ_{SB} is Stefan-Boltzmann's constant and ϵ is the emissivity of the material. The latter term is a nonlinear boundary condition.

Worth to note, that in low-temperature range, the convection is dominant while the radiation becomes dominant when the temperature is high [55]. In a welding process, the cooling of the part due to radiation and convection does not play a dominating role in comparison to the cooling due to the heat conductivity of the material.

Apart from the classical phenomena of non-linear thermal conduction, additional phenomena also have to be taken into consideration during welding. Thermal properties of materials depend not only on the temperature, but also on the constituent phases (austenite, ferrite/pearlite, bainite and martensite). As it is reflected in Fig.3.1, the metallurgical transformations depend on the thermal history of the process. And, thermal properties depend on the proportions of phases p_i:

$$\lambda(p_i, T) = \sum_{phases} p_i \lambda_i(T) \tag{3.6}$$

$$\rho(p_i, T) = \sum_{phases} p_i \rho_i(T) \tag{3.7}$$

$$H(p_i, T) = \sum_{phases} p_i H_i(T) \tag{3.8}$$

In case of the microstructure transformations and melting/solidification cycles, latent heat should be taken into consideration since it influences the formation of the transient temperature field. Latent heat $\dot{p_2}(H_2 - H_1)$ due to metallurgical transformation is taken into account as:

$$\rho\left(p_1\frac{dH_1}{dT}+p_2\frac{dH_2}{dT}\right)\dot{T}-div(\lambda\cdot\text{grad}T)-Q+\rho\dot{p_2}(H_2-H_1)=0 \tag{3.9}$$

$$H(p_1,p_2,T)=p_1H_1(T)+p_2H_2(T) \tag{3.10}$$

$$p_1+p_2=1 \tag{3.11}$$

Thermal conductivity of FCC (γ phase) and BCC iron lattice (α phase) and enthalpy shift during transformation between FCC (γ phase) and BCC iron lattices (α phase) are schematically presented in Fig.3.6.

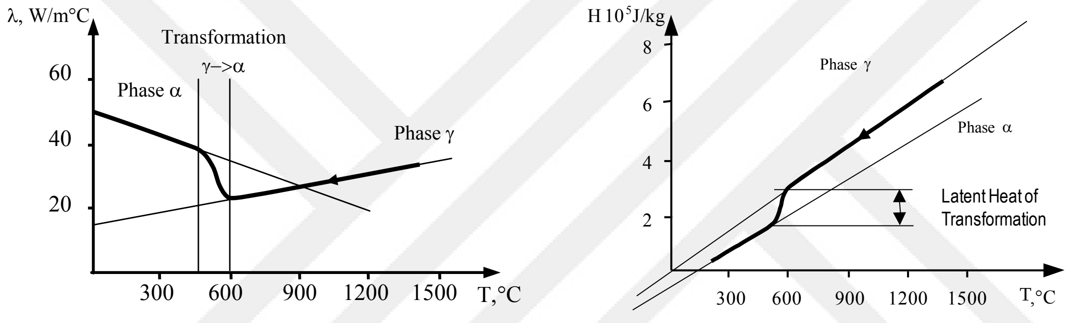

Figure 3.6 Effect of transformation on thermal conductivity and enthalpy

For the transient heat transfer analysis, FEM involves the solution of the system of differential equations as follows:

$$[C]\frac{\partial}{\partial t}\{T\}+[K]\{T\}=\{Q\} \tag{3.12}$$

where $\{T\}$ is a vector of the nodal temperatures; $[C]$ is a specific heat matrix; $[K]$ is a conductivity matrix, and $\{Q\}$ is a vector of nodal heat loads equivalent to internal heat sources and boundary conditions. The equation is integrated into the SYSWELD software code by a direct integration algorithm (generalized trapeze method). Upon numerical solution of the system of differential equations, results at discrete points are obtained.

3.2.3 Material description

Material data from ESI Group is known to be optimized from the numerical point of view and this allows time steps at the physical limit. No artificial calibration of material properties is needed [51].

Besides manganese (up to about 1.5%) and silicon (up to about 0.7%), as in carbon steels, HSLA steels often contain very small amounts of niobium (up to about 0.05%), vanadium (up to about 0.1%), and titanium (up to about 0.07%) to ensure both grain refinement and precipitation hardening. As such, they are also called microalloyed steels [6].

Nb, V and Ti are strong carbide and nitride formers. Fine carbide or nitride particles of these metals tend to hinder the movement of grain boundaries, thus reducing the grain size by making grain growth more difficult. The reduction in grain size in HSLA steels increases their strength and toughness at the same time. This is interesting because normally the toughness of steels decreases as their strength increases. Among the carbides and nitrides of Nb, V and Ti, titanium nitride (TiN) is most stable; that is, it has the smallest tendency to decompose and dissolve at high temperatures. This makes it most effective in limiting the extent of grain growth in welding. The higher the heat input during welding, the more likely the carbide and nitride particles will dissolve and lose their effectiveness as grain growth inhibitors. The low toughness of the coarse-grain regions of the HAZ is undesirable. The HSLA steels are usually welded in the as-roller of normalized condition [6].

The required combination of strength, plastic and viscous properties in X65 steel plates (σ_{UTS} = 530-628 N/mm^2) is achieved due to ferrite grain refining typical for controlled rolling, and in X70 (σ_{UTS} = 590-710 N/mm^2) also due to formation of required amount of bainite [58]. Spivakov et al. [58] noted that steel of X65 type also can contain Mo as steel of X70 type, therefore after analysis of 345 industrial batches of rolled metal an average chemical composition of X70 (X65) with respect to content of major (C, Mn, Si) and alloying elements was used for construction of CCT diagram (Fig.3.7). Enlarging the bainite area is caused by the presence of Mn, Ni, Nb, V and especially Mo (up to 0.228%) in steel. Also, weak capacity for hardening of steels X70 (X65) is mentioned. Mainly ferrite-perlite structure across the plate section is characteristic for controlled rolling (V_{cool} = 1-3 °C/s). The area of austenite → perlite transformation is restricted by a narrow temperature range. At the cooling rates $V_{cool} \geq$ 10 °C/s austenite decomposition of steel X70 (X65) leads to formation of ferrite and bainite structures in the absence of perlite. At cooling rates exceeding 15-20 °C/s, there is a probability of martensite formation instead of bainite structure and, as a result, decrease of plastic and viscous properties of plate products.

The chemical composition of API 5L X70 steel according to its standardization is known to have a wide tolerable chemical composition range. The continuous cooling transformation diagram for the average chemical composition (Tabl.3.1) taken from [58] is given in Fig.3.7. In SYSWELD database, the practical part of CCT diagram is implemented (Fig.4.7). The real diagram is presented in Fig.3.8.

Table 3.1 Chemical composition (wt. %) of API 5L X70 [59]

C	Si	Mn	P	S	Cr	Ni	Cu	Nb	Ti	V	Al
0.065	0.258	1.66	0.009	0.003	0.151	0.037	0.049	0.051	0.010	0.0525	0.017

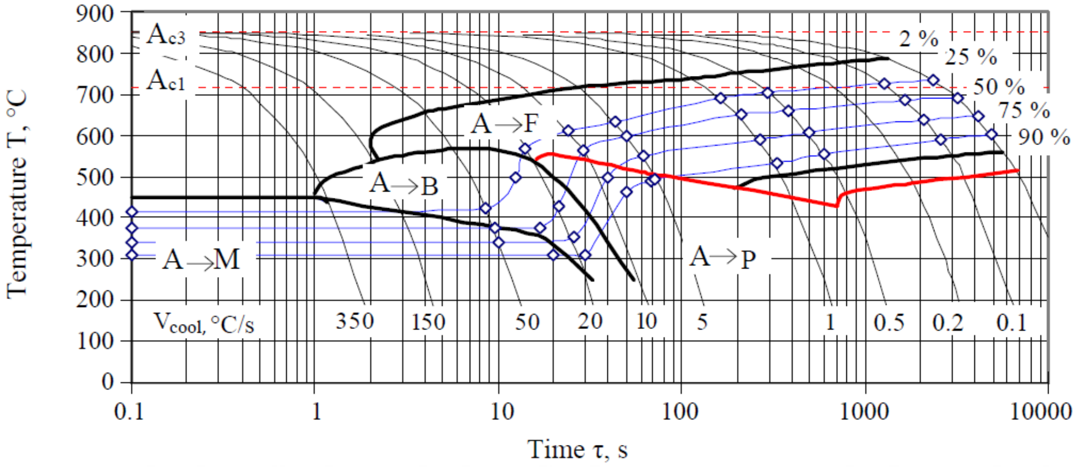

Figure 3.7 CCT diagram of steel X70 (X65) for the average chemical composition [58]

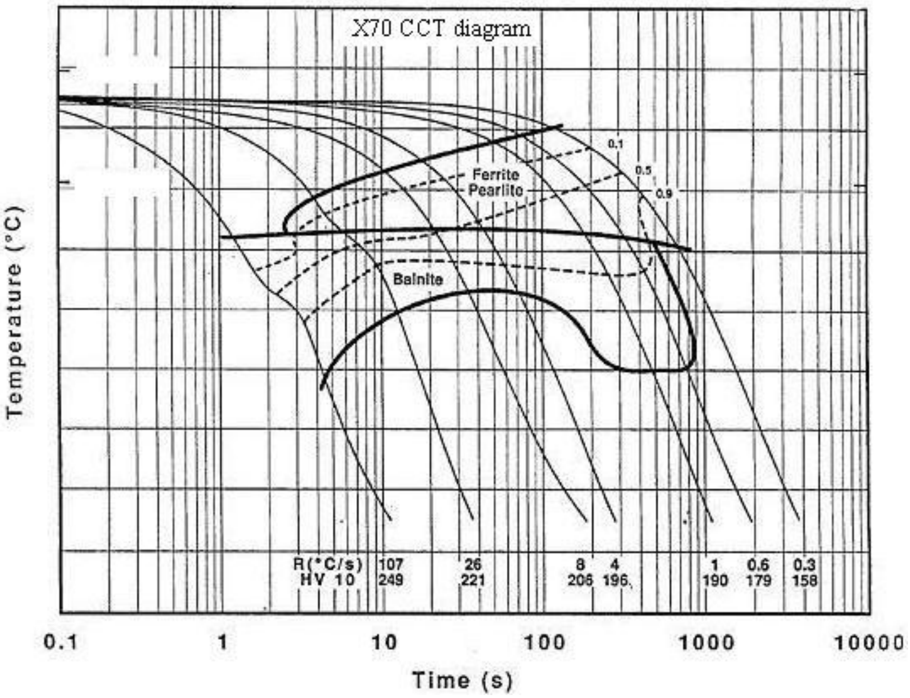

Figure 3.8 CCT diagram for X70 steel [60]

3.2.4 Microstructure transformations

As it was mentioned above, computation of the microstructure transformations is directly coupled with the thermal analysis. Except for austenitic steels, microstructural changes typically occur during welding processes, and they decisively influence the formation of post-weld stresses and distortion. The main reason of microstructural changes in steel welding processes is heating and cooling cycle. When the temperature exceeds A_{C3} during heating, a phase transition into the austenite starts in the metal. The lattice system changes from BCC into FCC configuration, the specific volume becomes smaller and carbon from dissolved carbides dissolves in the austenite structure (Fig.3.9). The transformation start temperature and the degree of austenitization depends on the heating rate, the maximum temperatures reached and the residence time above the austenitization temperature. During steel welding, austenite develops in the HAZ and in the melting zone before weld pool when heating. Deng and Murakawa [61] reported of significant effects of volumetric change and yield strength change due to solid-state phase transformation on welding residual stresses.

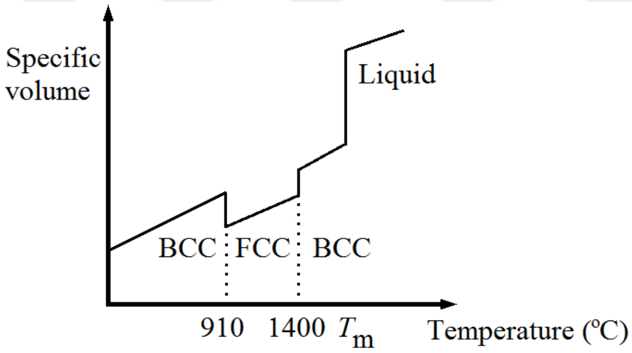

Figure 3.9 Specific volume of iron as function of temperature and crystal form

During the cooling process, depending on alloy composition and rate of cooling, when the temperature passes below the austenitization temperature, the FCC structure of austenite begins transformation to a BCC or BCT lattice. If the cooling rate is swift, the dissolved carbon is not able to diffuse and appears to be caught in the metallic matrix, almost no carbon atoms can diffuse out of the ferrous cell, which experiences a large lattice distortion known as martensitic transformation and the BCT structure formed undergoes a maximum “inner stress”. Martensite is known to be a very hard microstructure with a high yield stress, a high yield strength, a low strain at break and low notch impact reaction. Since reaction is diffusionless, martensite inherits the composition of the parent austenite. In case of a slower cooling speed, intermediate stages, also referred to as bainite or ferrite, can develop by means of more or less carbon diffusion, that causes the formation of carbides. Transformation of carbon-supersaturated ferrite with the subsequent diffusion of carbon and the precipitation of carbides forms bainite phase. Bainite has a mean yield stress, a mean yield strength and a mean strain at break. Ferrite and pearlite are comparatively softer microstructures with a low yield stress, a low yield strength, a high strain at break and high notch impact reaction. During welding, different microstructures are formed depending on the carbon content and added alloy elements based on different austenitizing stages and cooling rates. The cooling rate determines the relative proportions of phases, and, thus, determines the mechanical properties of the resulting weld joint, such as hardness and tensile strength. As can be seen, the microstructure changes substantially effect on the welded structures, and consequently have to be taken into consideration in weldment evaluations.

All the transformations cause changes in shape which for reconstructive transformations simply reflects the change in density (Fig.3.10). For displacive transformations, the shape change is an invariant-plane strain (IPS), that is, a combination of a shear on the invariant plane and a dilatation normal to that plane [62]. Displacive transformations are characterized by a rapid distortion of the crystal lattice from one structure to another, thereby generating a misfit between the transformed and untransformed regions which may give rise to residual stresses as well as a sudden macroscopic shape change. The most well known example of a displacive transformation is provided by the martensitic transformation in steel [3].

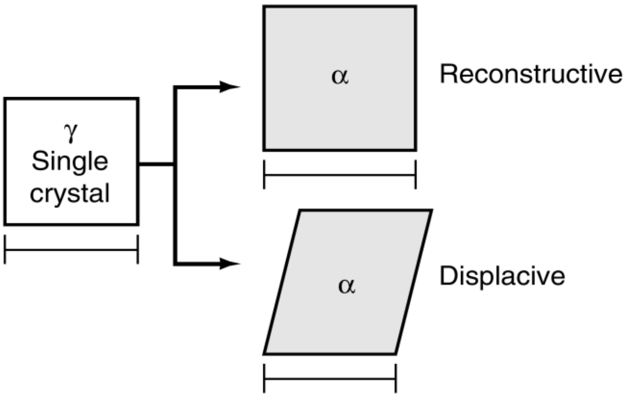

Figure 3.10 The two kinds of crystal shape changes as a function of the mechanism of transformation [62]

The interaction of an applied elastic stress with a phase change can occur in two ways:

1. The stress can alter the driving force for the transformation.
2. The stress can change the appearance of the microstructure by favoring the formation of those variants which best comply with the applied stress.

For reconstructive transformations, only the hydrostatic component of stress can interact with the volume change. The corresponding interaction with displacive transformations is much larger because of the shear component of the IPS.

Since the shear stress remains positive irrespective of whether the sample is pulled in tension or uniaxially compressed, and since the shear component of the shape change is large, a uniaxial stress will always cause a temperature increase for displacive transformations in steels. Hydrostatic stress, on the other hand, has no deviatoric components and consequently interacts only with the dilatational component of the shape change. Thus, hydrostatic compression is expected and found to lead to a decrease in the transformation temperature (Fig.3.11) [62].

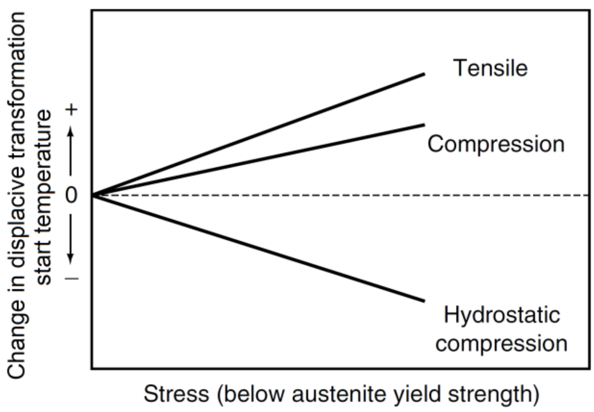

Figure 3.11 Indication of displacive transformation start temperature variation as a function of the nature and magnitude of an applied stress whose magnitude is less than that of the yield stress [62]

At temperatures close to that at which the equilibrium transformation occurs, an applied stress can assist reaction when the chemical driving force is insufficient to achieve the change on its own. There must exist a point, however, when the applied stress simply cannot provide enough mechanical driving force to complement the chemical term to give a driving force large enough to induce transformation. After all, the magnitude of the stress that can be applied is limited by the yield point of the parent phase. Thus, there are limits to what can be achieved by the application of stress as a stimulus to transformation (Fig.3.12). The mechanical driving force is estimated for an applied stress that is equal to the yield stress of austenite. Since this yield stress becomes small at high temperatures, the contribution of the mechanical driving force also decreases. Therefore, transformation becomes impossible as the temperature exceeds about 700°C [62].

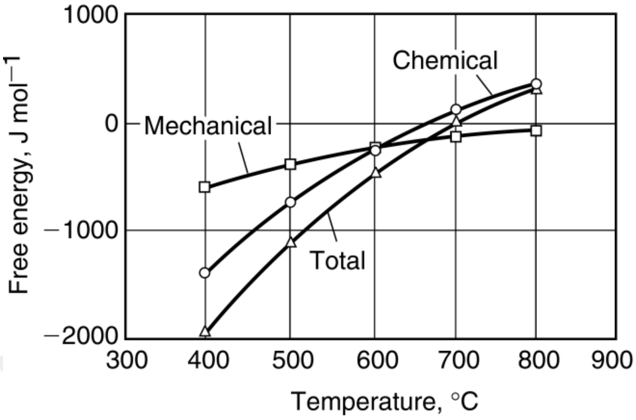

Figure 3.12 Typical magnitudes of the chemical and mechanical driving forces for stress-affected transformation [62]

Metallurgical changes during welding simulation are described by several models:

- Johnson-Mehl-Avrami and Leblond model − for diffusion transformations (austenite, ferrite, pearlite and bainite transformations) $f(T, \dot{T}, p)$;
- Koistinen-Marburger model − for displacive transformation (martensite transformation) $f(T, p)$.

Leblond model based on phenomenological approach and on equations of the kinetic-chemical type is generally presented as follows:

$$\frac{dp}{dt} = f(\dot{T}) \cdot \frac{p_{eqm}(T) - p}{\tau(T)} \tag{3.13}$$

where p is metallurgical phase proportion; $p_{eqm}(T)$ is metallurgical phase proportion at equilibrium; T is temperature; $\tau(T)$ is equivalent to a "time delay" and $\dot{T}$ is heating/cooling rate.

Koistinen-Marburger law for martensitic transformations:

$$p_M(T) = p_A\left[1 - \exp\left(-b(M_s - T)\right)\right] \tag{3.14}$$

where b is experimental material parameter; M_s is martensite transformation start temperature.

A thorough analysis of weld metal microstructure evolution, related mechanical properties and modelling aspects can be find in paper by Bhadeshia [50].

3.2.5 Stress and strain fields

The mechanical behaviour of structures and machine parts can be described by the following three variables: the displacement u, the strain ε and the stress σ. These variables should satisfy the following conditions: strain-displacement relation, stress-strain relation and equilibrium equation (Fig.3.13). The conditions required on the surface are called boundary conditions, and there are two types, namely displacement boundary condition and stress boundary condition [55].

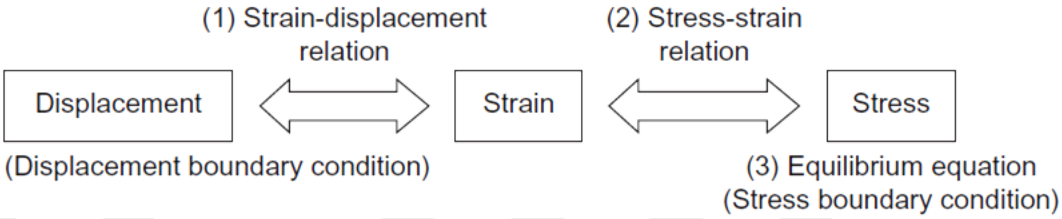

Figure 3.13 Variables and relating equations in stress analysis [55]

The equivalent differential equations to be solved in displacement analysis are presented in the form of common system of equilibrium equations throughout the entire FE model of a deformable body that is composed as:

$$[m]\frac{d^2}{dt^2}\{u\} + [K]\{u\} = \{P\} \tag{3.15}$$

where $\{u\}$ is a vector of the nodal displacements, $[m]$ is a mass matrix dependent on the material density, $[K]$ is a stiffness matrix, and $\{P\}$ is a vector of given external nodal forces. The former part is neglected in static and quasi-static analysis.

In welding, the strain is produced through different mechanisms, namely:

1) Elastic strain produced by stress that is reversible.

2) Thermal strain produced by temperature gradients.

3) Plastic strain produced by movement of dislocations that is irreversible.

4) Strain due to transformation plasticity phenomena.

The most important assumption is that the total strain ε can be decomposed into the sum of the elastic strain, the plastic strain, the strain caused by transformation plasticity, the thermal strain and strain induced by phase transformations, that is

$$\varepsilon = \varepsilon_e + \varepsilon_p + \varepsilon_{tp} + \varepsilon_{th} + \varepsilon_{pt} \tag{3.16}$$

Since welding is a thermoplastic process, in SYSWELD the total strain rate contains the following parts:

$$\dot{\varepsilon} = \dot{\varepsilon}_e + \dot{\varepsilon}_p + \dot{\varepsilon}_{tp} + \dot{\varepsilon}_{th} + \dot{\varepsilon}_{pt} \tag{3.17}$$

where $\dot{\varepsilon}_e$ is elastic strain rate; $\dot{\varepsilon}_p$ is plastic or viscoplastic strain rate; $\dot{\varepsilon}_{tp}$ is rate of strain caused by transformation plasticity; $\dot{\varepsilon}_{th}$ is thermal and $\dot{\varepsilon}_{pt}$ is metallurgical strain rates.

Thermal expansion and shrinkage during welding causes development of thermal stresses. Apart from the classical thermal phenomena, the mechanical analysis of steel materials is basically influenced by two microstructure phenomena (Fig.3.1): 1) volume changes, which accompany microstructure transformations of steels, and 2) specific material behaviour dependent on existing phase combinations. The volume changes (Fig.3.9) have a decisive influence on the component distortion and on the development of the stresses due to the fact that they cause additional transformation stresses, which in optional time intervals interfere with the thermal stresses that are time dependent. A combination of both phenomena results in a complicated, multiaxial stress and strain state of the component.

Thermal expansion of the metal consist of the classical thermal expansions of the respective constituent phases. And, thermo-metallurgical strain is involved to simulation as volume changes during metallurgical transformations:

$$\varepsilon^{th}(T) = \sum_{phases} p_k \cdot \varepsilon_k^{th}(T) \tag{3.18}$$

$$\varepsilon_k^{th}(T) = \alpha_k(T) \cdot [T - T_{ini}] \tag{3.19}$$

where ε_k^{th} is thermal strain of metallurgical phase *k*; α_k is dilatation coefficient of the phase *k* and p_k is proportion of the phase *k*.

The thermal strain of each phase differs not only by its gradient (dilatation coefficients of the phases depend on the temperature), representing the coefficient of expansion, but also by the position of its origin, reflecting change of volume during phase transformation. The temperature dependant yield stress is a function of the phases as well.

3.2.6 Strain hardening

The elasticity domain is known to evolve in presence of a plastic strain. This phenomenon is referred to as the strain hardening of the material. The transformation from austenite to ferrous phases during cooling is a continuous process, and there are moments when parts of the steel already have transferred into ferrous phases, whereas the rest is still in austenitic state. Austenite has usually a much lower yield stress as the ferrous phases (Fig.4.9) and a lower specific volume (higher density) as the ferrous phases (Fig.3.9). The increase in specific volume accompanying the formation of ferrous phases causes plastic deformation in austenite. Accordingly, the density of dislocations in the austenite, which is responsible for the strain hardening, increases. Consequently, a more or less high amount of strain hardening occurs in the austenite during the cooling process. If the austenite transfers into martensite, there is no time to eliminate the dislocations by diffusion, and thus the martensite keeps the strain hardening of the austenite. In case of diffusion controlled transformations, the dislocations disappear more or less due to diffusion and the strain hardening is thus partially lost. In most cases, modelling of strain hardening is necessary, especially in the case of processes involving a quick heating phase.

The strain-hardening parameter is identified depending on the loading history, and the evolution is expressed by equivalent plastic strain:

$$\dot{k} = \dot{\varepsilon}^{p}_{eqv} = \sqrt{\frac{2}{3}\dot{\varepsilon}^{p}_{ij}\dot{\varepsilon}^{p}_{ij}} \tag{3.20}$$

How the subsequent yield surface develops during the course of successive plastic loading is called the hardening rule. Experiments determining the surface show that the yield surface expands its diameter accompanying the shift of center position in stress space [37].

Generally, in CWM four types of strain hardening is employed:

- ideal plastic (no strain hardening);
- isotropic hardening;
- kinematic hardening;
- mixed isotropic/kinematic hardening.

According to isotropic hardening rule (Fig.3.14a), the yield surface is assumed to expand in the stress space isotropically in size, keeping the center constant. This expansion is governed by an internal scalar variable ε^{p}_{eqv} − cumulative equivalent plastic strain:

$$\varepsilon^{p}_{eqv} = \int_{0}^{t} \dot{\varepsilon}^{p}_{eqv} dt \tag{3.21}$$

Kinematic hardening model (Fig.3.14b) assumes that due to plastic deformation the yield surface with unchanging shape undergoes translation in the nine-dimensional stress space. This model considers the material as a non-isotropic continuum and can be used to represent the Bauschinger effect.

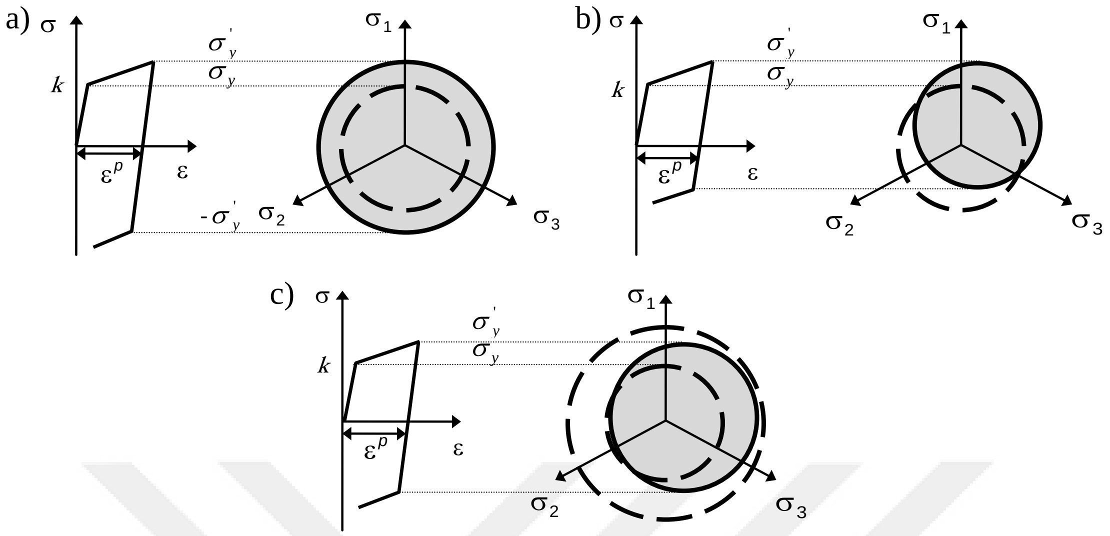

Figure 3.14 Strain hardening models: a) isotropic; b) kinematic; c) combined

In reality, the behaviour of steels is rarely purely isotropic or kinematic. Generally, combined or mixed (combined) isotropic/kinematic strain hardening model veraciously represents an "expansion" and a "translation" of the elastic domain (Fig.3.14c).

The material behavior during the transformation of phases is assumed to be elastic-plastic. Visco-plastic phenomena (dependent on temperature) is especially important for the simulation of thermal effects on stress relief.

Material hardening model has great influence on the residual stress calculations. For example, Xu et al. [63] notes that the isotropic hardening model only can give a tensile part of tension-compression simulation. But when the specimen is reloaded in simple compression beyond the yield point, the stress decreases continuously and the yield point of compression is equal to the last tensile stress. Therefore, the isotropic hardening model cannot properly describe the Bauschinger effect during the reverse loading and results in overestimating the residual stresses. The linear kinematic hardening model assumes that the total stress range is equal to the twice the yield stress, which considers the Bauschinger effect. The mixed hardening model combines the isotropic and kinematic hardening models. This model is the most appropriate to describe the expansion and translation of the yield stress surface during plastic deformation. Combined type of hardening is suggested as optimal for welding process simulations and mixing in proportion of 30% isotropic and 70% kinematic models is declared as most appropriate for welding simulations, since both Bauschinger effect and cyclic hardening with plastic shakedown can be predicted.

Muránsky et al. [64] published that mixed isotropic-kinematic formalism predicts a highly accurate post-weld residual stress field. In contrast, the isotropic hardening model over-predicts the stresses developed, while the kinematic hardening model under-predicts these stresses. Authors strongly recommended for multi-pass welds application of mixed hardening formalism and noted that isotropic hardening formalism may be valid for single-pass austenitic steel weld studies. Also, it was pointed that under-prediction of the accumulated plastic strain occurs when using the isotropic hardening model, as this results in non-conservative predictions of some failure characteristics of the weldment. A series of works [65-68] was devoted to this issue and similar conclusions were obtained.

3.2.7 Transformation plasticity

Solid-phase transformations that occur during the thermal cycle produced by welding lead to irreversible plastic deformation known as transformation plasticity. This phenomenon is driven by the volume change during solid-state phase transformations [27]. Large inelastic deformation is induced under relatively low stress applied during phase transformation [37]. In the 1970s, investigations of this effect was published by Satoh [69] and Jones and Alberry [70].

The permanent strain caused by any transformation is called transformation plasticity. A phase change in a stress-free material is usually triggered by heat treatment, when the parent phase passes through an equilibrium transformation temperature. Alternatively, the application of a stress in isothermal conditions can trigger transformation in circumstances where it would not otherwise occur. Unusual effects can occur when stress and temperature work together. The transformation may occur at remarkably low stresses or at very small deviations from the equilibrium temperature. This is why even minute stresses can greatly influence the development of microstructure, and vice versa. It is not surprising that transformation plasticity can be obtained at stresses that are much smaller than the conventional yield stress of the parent phase [62].

Transformation induced plasticity (TRIP) phenomenon is an anomalous plastic strain which can be observed, even far below the yield stress of the phases, when metallurgical transformations from austenite to ferritic phases occur under mechanical loading (stresses, external loading). Transformation plasticity can be explained by Greenwood-Johnson or Magee mechanisms (Fig.3.15). First one states that transformation plasticity arises from micro plasticity in the weaker austenitic phase induced by the difference of specific volume between the phases. This plastic flow is oriented by the external load. When a phase change is accompanied by a change in volume, the tensile strain expected when transformation occurs under the influence of a tensile stress. The role of shear strains associated with transformation has been emphasized in work by Magee [62]. Second one explains transformation plasticity by orientation of the newly formed martensite plates by the external load.

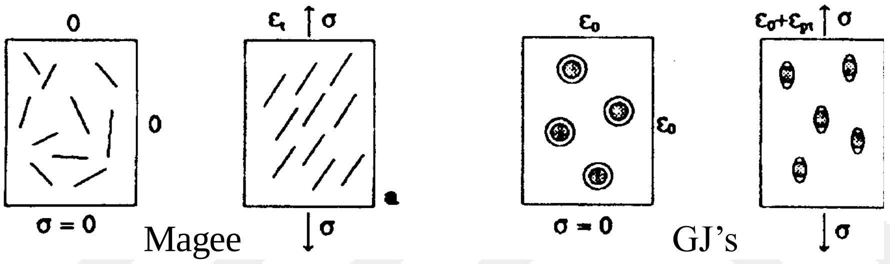

Figure 3.15 Illustration of Magee and Greenwood-Johnson mechanisms

A discussion of the welding induced stresses and microstructure relationship was given by Bhadeshia [71]. Wolff et al. [72] pointed that generally the two phenomena (plasticity and TRIP) are present at the same time, and they are coupled. The effect of TRIP in welds was first analyzed by Dubois et al. [73] and later by Leblond et al. [74] using plane-strain conditioned two-dimensional FE models. The first three-dimensional thermal stress analysis accounting TRIP was performed by Oddy [75].

Not only does transformation affect stress, but the latter modifies the development of microstructure. The microstructure tends to be more organized when transformation occurs in a stress's parent phase, because the stress favors the formation of certain orientations relative to others [62].

Using bainitic, martensitic, and stable austenitic steels, Jones and Alberry [70] demonstrated that transformation plasticity during the cooling of a uniaxially constrained sample from the austenite phase field acts to relieve the buildup of thermal stress as the sample cools. By contrast, the nontransforming austenitic steel exhibited a continuous increase in residual stress with decreasing temperature, as might be expected from the thermal contraction of a constrained sample.

When the steels were transformed to bainite or martensite, the transformation strain compensated for any thermal contraction strains that arose during cooling. Significant residual stresses were therefore found to build up only after transformation was completed and the specimens approached ambient temperature (Fig.3.16) [62].

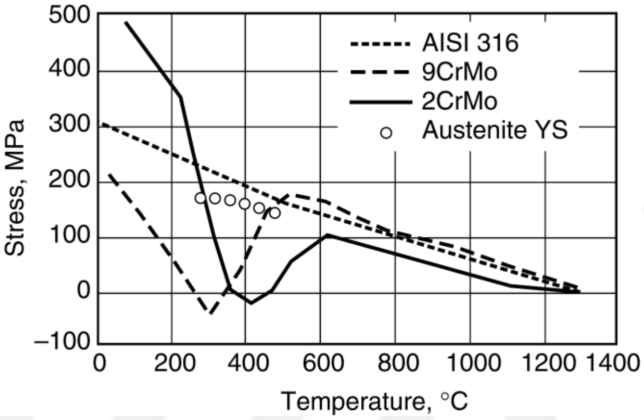

Figure 3.16 Plot of residual stress versus temperature for a martensitic (9CrMo), bainitic (2CrMo) and austenitic steel (AISI 3160) [70]

The residual stress at ambient temperature is larger when the austenite finishes transformation at a high temperature. This is because thermal contraction strains can no longer be compensated by transformation plasticity once the austenite has decomposed. Low transformation temperatures help minimize residual stresses. Bhadeshia [62] showed that the distortion depends on the temperature at which the majority of the transformation is completed. The distortion appears to be clearly larger for the case where the transformation is exhausted at the higher temperature.

Transformations in steel play a major role in the development of residual stresses. For reconstructive transformations, it is the difference in density between the parent and product phases that contributes to transformation plasticity. The plasticity can be much larger for displacive transformations (Widmanstätten ferrite, martensite) because of the large shear component of the shape deformation when these transformation products form. These are quite sophisticated effects which, with few exceptions, are not incorporated in most residual stress analyses [62].

Transformation plasticity can be measured and characterized by an influence factor. SYSWELD computes automatically this influencing factor for the transformation plasticity from the properties of the phases. The model of transformation plasticity implemented in SYSWELD rests on a micromechanical approach. The macroscopic constitutive laws derive from homogenization mathematical development [51].

The mechanical and physical properties of the material are assumed to be expressed by the mixture law as a linear or non-linear combination of the properties of the constituents [37]. Leblond model considers a mixture of austenite (phase γ) with volume fraction $(1 - p_2)$ and ferrite, bainite or martensite (phase α) with volume fraction p_2, and assumption that phase γ is being transformed into phase α. The nonlinear function law is employed for an austenite-ferrite mixture and linear mixture law to mixture of hard ferrite phases (Fig.3.17).

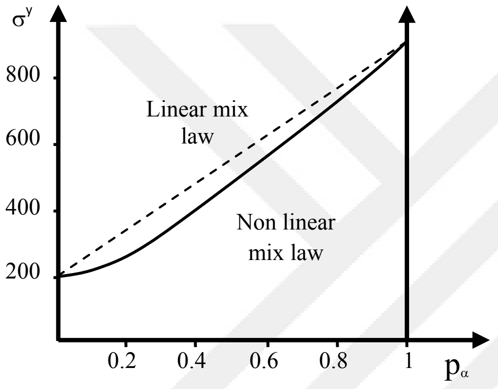

Figure 3.17 Phase mixture laws

Non-linear law:

$$\sigma_y = [1 - f(z)] \cdot \sigma_y^\gamma(E_{eff}^\gamma) + \\ + f(z) \cdot \sigma_y^\alpha(E_{eff}^\alpha) \qquad (3.22)$$

Linear law:

$$\sigma_y^\alpha(\theta) = \sum_{\substack{Ferritic \\ phases\ \alpha}} p_i \sigma_y^i(\theta) \qquad (3.23)$$

When the temperature exceeds a certain value, the material history is fully automatically removed.

In SYSWELD, the plastic behaviour model of steel during transformation presented above was extended to take into account the viscoplastic phenomena. These phenomena are introduced by having the yield stress of the phases dependent on the rate of plastic deformation. The numerical implementation has been achieved in such a way that elastic-plastic and elastic-viscoplastic behaviours can be combined. The resultant model proposes an isotropic strain-hardening both in the additive and multiplicative form [51].

3.3 Solver parameters

Since all the components of stress-strain relation are nonlinear problems and material properties change with temperature, the overall welding problem is a highly nonlinear problem and it is solved incrementally. In the incremental solution process, the time or the change of temperature is divided into small increments. The change of deformation and stress is computed in small increments and this process is repeated successively with the progress of time [55].

Computation is started from time $t = 0$ and proceeds step by step with the time increment Δt. In each step increments, increments of temperature, displacement, strain and stress (ΔT, Δu, $\Delta \varepsilon$, $\Delta \sigma$ respectively) are computed. The values at time $t + \Delta t$ can be estimated by adding these increments to those at time t according to the following equations:

$$T(t + \Delta t) = T(t) + \Delta T \tag{3.24}$$

$$u(t + \Delta t) = u(t) + \Delta u \tag{3.25}$$

$$\varepsilon(t + \Delta t) = \varepsilon(t) + \Delta \varepsilon \tag{3.26}$$

$$\sigma(t + \Delta t) = \sigma(t) + \Delta \sigma \tag{3.27}$$

First, the temperature field is computed from the start of welding until the structure cools down to room temperature. The temperature at each time step is stored in a file in the computer. In stress analysis, the temperature is imported from the file to compute the deformation and stress at each time step. This process is continued from the start of the welding until the complete cool down [55]. Thus, a multi-pass welding is represented as a transient nonlinear dynamic thermo-metallurgical and mechanical problem.

To carefully apply the loads in order to integrate the load path in a correct manner, a time-stepping in pseudo-time is implemented in SYSWELD software. This time-stepping is applied in the form of consecutive pseudo-time step by pseudo-time step. The time range that is utilized for the pseudo-time stepping is the process time.

From physical positions, in simulations of transient welding processes, SYSWELD software applies the maximum possible time steps without convergence problems: a time required to cross the half of the length of the molten zone in thermo-metallurgical computations, and a time required to cross the length of the molten zone in mechanical computations.

Automatic time stepping was used in further investigations. Parameter named "Correction factor if no convergence" was kept at least 0.7, nominally 1.0 for successive iteration and limitation factor was maximum 1.1 within the welding process, 0.5 during arc initiation at weld start and 1.5 for postweld cooling stage. Since, as it was noted earlier, time step is directly related to the crossing the length of the molten zone, consequently, it is related to the given welding speed. For welding with 400 mm/min, time step was in the range of 0.0001...0.374983 s; for welding with 600 mm/min, time step was in the range of 0.0001...0.25 s; and for welding with 800 mm/min, time step was in the range of 0.0001...0.187508 s.

If the thermal storage step is chosen too coarse, the integration of the mechanical material laws leads to wrong results, no matter how fine the mechanical time step is.

A too small time step regarding element size and material properties leads to a numerical oscillation of the computed temperature [51].

Also, welding process is characterized by extremely high heating and cooling rates which consequently cause extremely high gradients of thermal, microstructural and mechanical properties. These gradients have to be numerically controlled by the program through reasonable time expenditure. Apart from the robust solvers and dedicated numerical algorithms, special element formulations have been developed in SYSWELD for simulation of welding processes.

To solve the linear systems of equations, solver defined by "method" command is utilized. In this investigation a symmetrical optimized method has been employed. Optimized BFGS algorithm with implicit time integration scheme is well suited for welding simulation. Solver is direct symmetric with double precision where precision is settled absolute for thermal problem and relative for mechanical problem.

In case of use BFGS, for each iteration additional memory is needed to store the vectors that modify the tangent matrix for the iteration. BFGS is not that efficient any more above 15 iterations, it is not useful to ask for more than 30 BFGS iterations. In the *.par files, the number of BFGS iterations is set to 30 for the thermo-metallurgical simulation and 25 for the mechanical simulation. A combination of BFGS and a re-computation of the tangent matrix after a certain number of iterations allows the largest time steps without divergence in combination with the iterative solver [51].

3.4 Three-dimensional computer simulation

Before the mid-1990s, the general trend in welding simulation was based on the two-dimensional axisymmetric models. This assumption was mainly due to limited computer capacities. Depradeux and Jullien [68] noted that two-dimensional simulations considering a cross-section, orthogonal to the welding direction, assuming a plane strain [76, 77], or a generalized plane strain hypothesis, were typically for common use for the simulation of multi-pass welding. Plane strain conditions means that the weld is divided into thin slices perpendicular to the motion of the source and these slices are assumed not to interact with each other. The use of plane strain conditions entails certain subtle consequences. Longitudinal heat flow and longitudinal displacements are assumed to be zero [33]. Consequently, the plane strain hypothesis is not satisfactory as it usually leads to an invalid representation of distortion, and to an overestimation of the longitudinal residual stress, parallel to the direction of welding. The agreement between a plane strain model and a three-dimensional model can be quite good in the case of beam-like structures [33, 78].

There have also been two-dimensional simulations assuming a plane stress hypothesis, usually used when modelling the welding of a thin plate. Then the stress in the thickness direction is ignored and the deformation is assumed to be in the plane of the plate. These models follow the heat source that moves in the plane of the mesh, which requires a large number of elements for a long weld. Therefore, the size of the smallest element is usually larger in these models than in the previously mentioned two-dimensional models of the weld cross-section [33]. But plane stress model cannot reproduce transient displacements and final shape of the plate.

In reality, the distortion around the molten zone of weld pool during welding is blocked by colder material before and behind the molten zone. This natural block cannot be represented in two-dimensional simulations.

In general, the required time for simulation increases as the dimension increases. Effort has been exerted to decrease computation time by idealizing three-dimensional problems into two-dimensional problems, such as plane stress, plane strain, plane deformation, or axis-symmetric problems. Although, one-dimensional models are useful for understanding the basic phenomena in welding, they cannot be applied to quantitative prediction of distortion and residual stresses in actual welded structure [55]. If problem is not axis-symmetric, it must be treated as a three-dimensional. If the structures are assembled by thin plates and have a three-dimensional complex geometry, they can be modelled using shell elements [79]. In such cases, the analysis may be simplified using a shell model in which the stress is two-dimensional (plane stress), while the deformation is three-dimensional [55]. Perhaps, the first such three-dimensional residual stress simulations of full welds of thin-walled pipes was performed by Lindgren and Karlsson [80]. Another early three-dimensional computation of a 2.5 cm short weld were presented by Goldak et al. [81]. Using shell elements, Troive [79] performed three-dimensional numerical investigation of deformations and stresses in butt-welding of thin-walled pipes.

Regardless of if the problem is one-, two- or three-dimensional problem, the variables and the equations to be solved are the same. The only difference is the number of coordinate axes and the component of the variables, such as the displacement, the strain and the stress [55].

Theoretically, it is difficult to use two-dimensional model to investigate the influences of variables acting in spatial domain, such as deposition and/or welding sequence on the final residual stresses distribution and distortion. As an example, Michaleris et al. [82] compared two-dimensional and three-dimensional models of a multi-pass butt-welded plate. They simulated the first pass with both models. The two-dimensional model had a larger fusion zone, despite a reduced heat input, and a larger zone with high tensile longitudinal stresses than the three-dimensional model [33]. Sakkiettibutra and Vollertsen [83] presented a comparative calculation using two- and three-dimensional modelling, and the former model predicted neither the distortion nor the residual stresses correctly. Duranton et al. [84] reported that 3D model has also the advantage to provide more information concerning the effect of pass overlapping and ovalization as it considers proper boundary conditions.

Summarizing, neglecting computational considerations, full three-dimensional models are preferred for welding simulation as they allow for consideration of all stress and strain components [85].

CHAPTER 4

ANALYSIS OF MULTI-PASS WELDING ON V-GROOVE

One of the widely-used joint geometries in welding is V-groove type, and lots of research work have been conducted to understand the residual stress and distortion related to it. Deng and Murakawa [61] considered a multi-pass welding on V-groove during pipes joining. Näsström [49] presented the simulations of butt-welding of a pipe using V-groove of 60°. Sattari-Far and Farahani [86] reported the study on weld groove shape effects.

In this Chapter, experimental and numerical procedures are defined. Three-dimensional model, mesh characteristics, thermo-metallurgical and mechanical properties of material are described. Then, verification by test studies is given, namely, calibration of molten pool profile, microstructure evaluation, hardness calculations, surface residual stress distributions, XRD measurements are presented. Also, adjustment of clamping parameters, plate size are discussed. Further, detailed characterization of single-pass and multi-pass weldments are given. Withal, effects of unclamping and interpass temperatures are demonstrated and discussed.

4.1 Experimental setup

In order to provide full-scale investigation for verification of simulation, a series of real experiments on multi-pass welding on API 5L X70 grade HSLA steel plates with V-groove has been carried out by altering the number of weld passes and welding process parameters. The experimental work was done by the group of Dr. Gür and partially presented also in study by Erian [87].

As a result of controlled rolling in the production route of API 5L X70, directionality is introduced to grains of the sample. This directionality in the grain orientation results in differences during residual stress measurement. Due to the formed texture residual stress statue is different for rolling (longitudinal) and transverse direction.

The difference between the rolling and transverse direction is nearly doubled at the as received state of the material. Therefore, a heat treatment procedure was decided to be applied to all sample plates in order to reduce the magnetoelastic parameter difference between rolling and transverse direction. At first, stress relief treatment was applied at 620°C for 2 hours. Unstable data still obtained and directionality was yet not fixed. Additionally, annealing procedure at 960°C for 1.5 hour was decided to be done to minimize directional response.

Initial thickness of API 5L X70 steel plates was 19.6 mm. Each specimen was cut and machined to dimensions of 280x150x18 mm. Prior to machining operations, heat treatment was applied to minimize the directionality of the measurements. During heat treatment because of the equipment used, decarburization of the samples was inevitable. To get rid of decarburized layer on the surface samples were grinded. To avoid differences in dimension, all six specimen were set at the same time on the stoning bench. To avoid grinding burn oil-water cooling is applied at the stoning bench and finally to avoid changing residual stress state during grinding all samples were ground same amount from front and back sides [87].

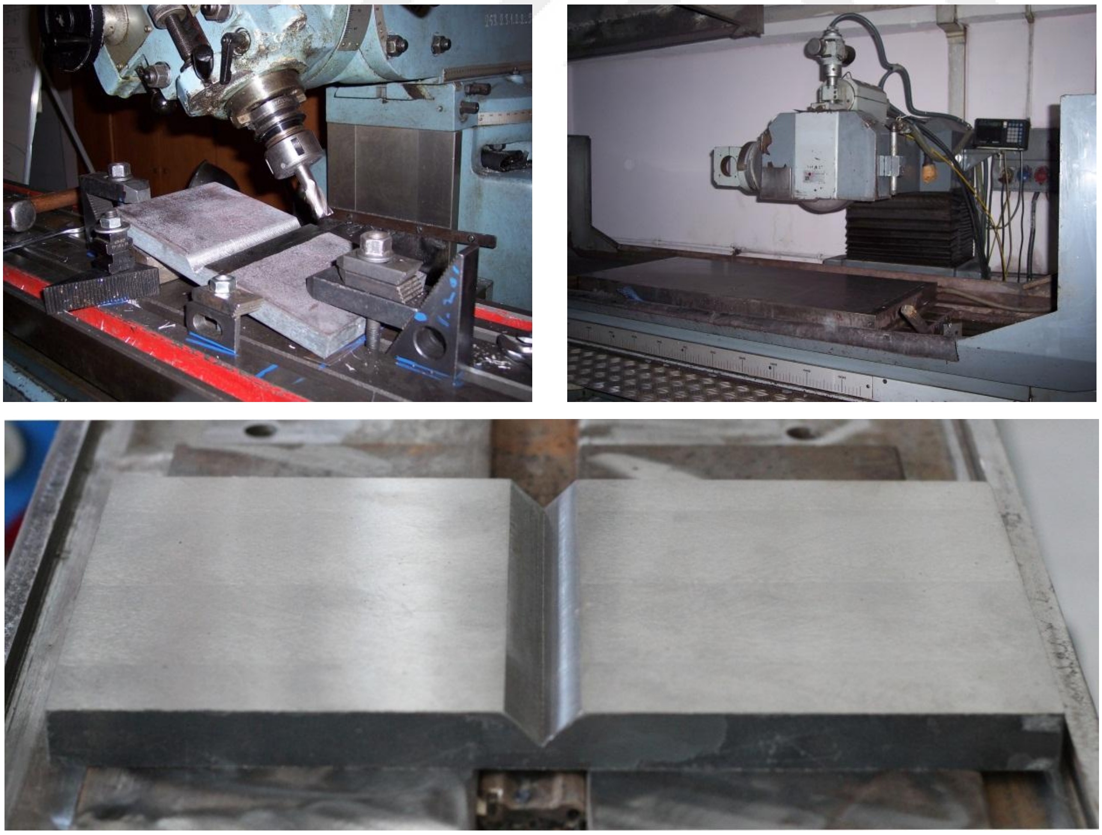

Figure 4.1 Machining of V-grooved plates

Upon grinding operation, at the middle of each plate the grooves of the V-shape (90° included angle) were prepared with sizes of 18 mm in width and of 9 mm in height. Fig.4.1 demonstrates the processing steps of the components, and the ending dimensions of the plates are given in Fig.4.2. Three nominally identical components were manufactured.

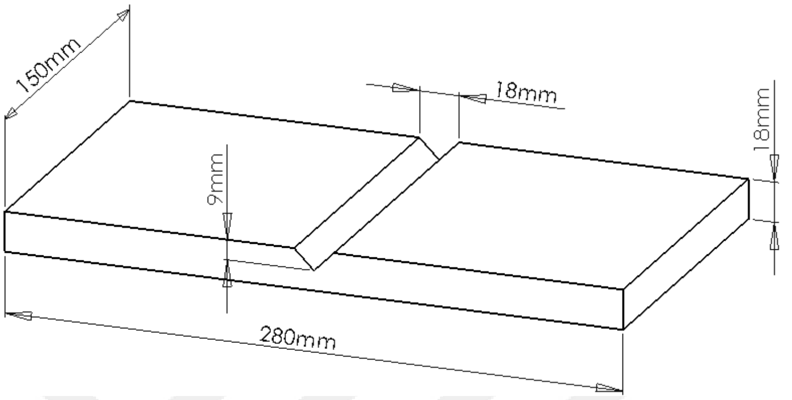

Figure 4.2 Final dimensions of the API 5L X70 steel components

Three cases of multi-pass welding were planned with parameters of the process presented in the Tabl.4.1. Metal Active Gas (MAG) welding was employed since the technique is commonly used in construction applications.

Table 4.1 Parameters of welding processes

№ of passes	Length of weld pass, mm	Wire feed speed, m/min	Arc voltage, V	Welding current, A	Effective heat power of the welding arc, kW	Linear welding speed, mm/min	Pass heat input, kJ/mm
1	150	11.5	29	290	6.728	400	1.008
2	75						
1	150	9.0	26	282	5.866	600	0.587
2	100						
4	50						
3	150	6.5	21	266	4.468	800	0.335
5	100						
8	50						

In all cases, in order to prevent deflection during welding plates were restrained with four clamps from each corner. In welding operations ISO 14341-A G 42 3m G3Si1 electrodes with diameter of 1.2mm were used. The welding was performed at an ambient temperature of 20°C. In process weldments are presented in Fig.4.3.

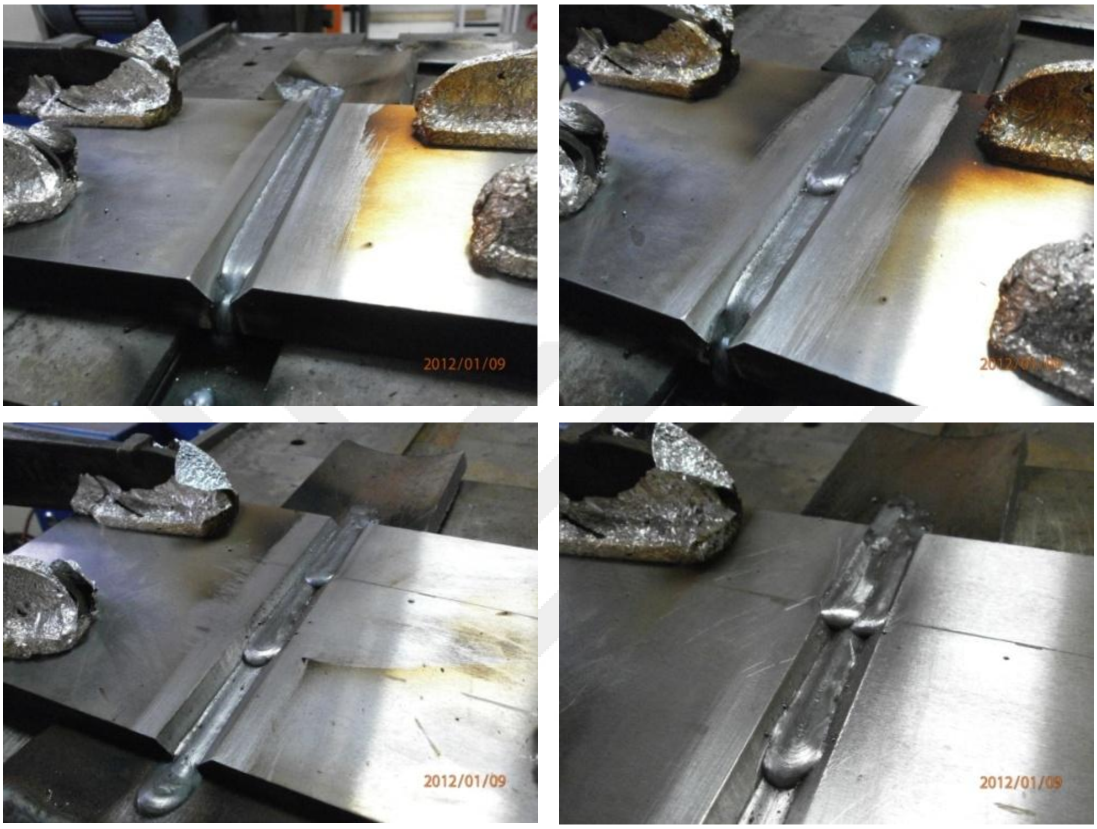

Figure 4.3 Welding of 2-pass and 4-pass configurations

During welding process, a shielding gas have been used in a mixture of 20% CO_2 and 80% Ar. According to recommendations to avoid cold cracking on the metal of the weld zone and HAZ, interpass temperature was maintained to maximum 200°C.

Residual stress measurements were carried out by MBN technique (roll-scan method) with the use of Rollscan/µscan 500-2 instrument with code 4316 probe (Fig.4.4). In order to provide stable and continuous measurements, the probe was connected to motor controlled platform. Calibration procedure was done to transform the MBN data into stress values in MPa unit. The plates, set on the motor controlled platform, move under the probe with velocity of 0.2 cm/sec in the horizontal direction [87].

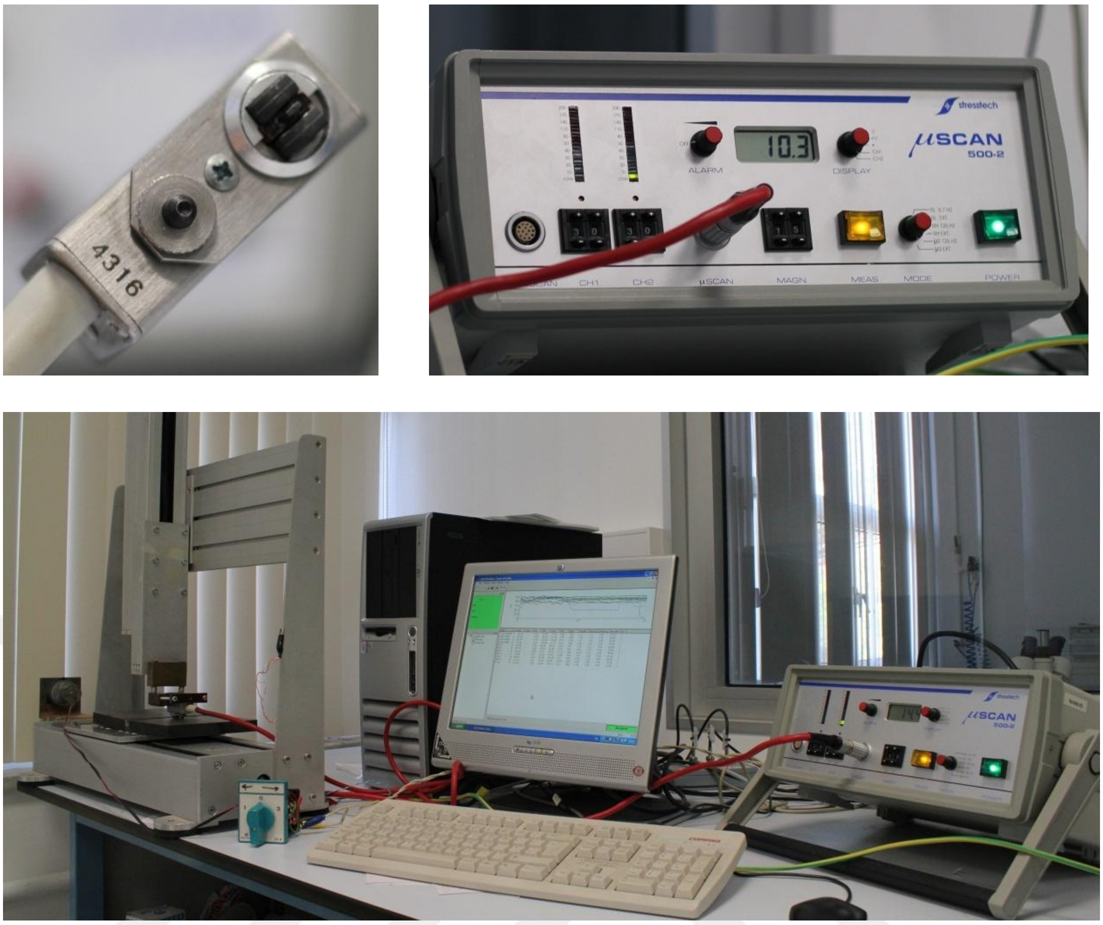

Figure 4.4 The instrument set-up and 4316 roll-scan/micro-scan probe [87]

The measurements were taken from the surfaces of the plates in the middle of the pass sections along the dash lines as shown in the Fig.4.5. Measuring was made in roll-scan mode on the distances of 100 mm from both sides of the specimens, except for the weld bead zone on the upper side.

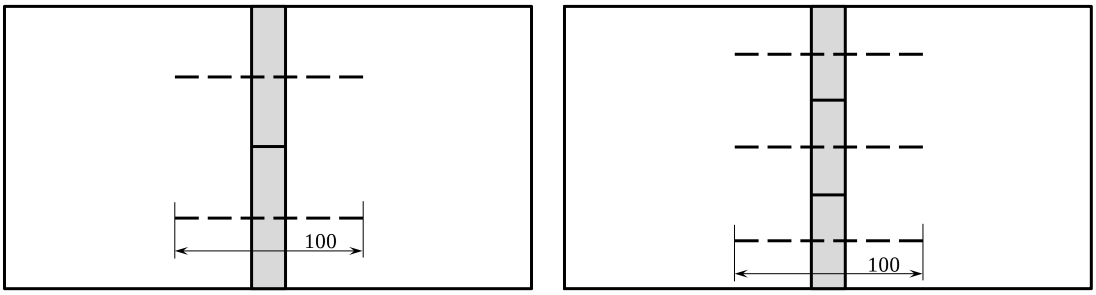

Figure 4.5 Layout of residual stress measurements

4.2 Definition of 3D numerical model of the welding procedure

Construction of three-dimensional numerical model of the welded component began from basic 2D surface creation that represents the cross-section of future weld joint.

All dimensions and weld pass proportions were kept in accordance with the real specimens. Then, meshing of 2D surfaces were performed using finer elements in the weld regions and HAZ, and coarser elements far away from the areas of high gradients (Fig.4.6). Triangular and quadrilateral type of elements of linear order were employed. After that, extrusion from 2D elements were performed into 3D elements in the form of pentahedrons (triangular prismatic) and hexahedrons. Elements lying in the regions of future WM and HAZ were defined as elements with thermal loads. This influences on the correct modelling of weld pool and heat transfer that sooner become apparent in the molten weld pool profiles (Fig.4.14-16). Further, clamping conditions were set in accordance with positions and sizes of the real restraints (Subsection 4.3.5). Free and coincident nodes of the model, coincident elements and elements quality by min Jacobian parameter were controlled. Also, for excluding possible cracks, bad connections, intersections and overlaps, all element boundaries were carefully checked. After all, weld trajectories and reference lines were assigned, and heat transfer skin generated through extraction of 2D elements from the opened faces of 3D elements. Then, material was set for component and weld wires, welding process parameters were specified (Tabl.4.1), cooling conditions were predefined, timing of clamping conditions was assigned. Finally, solver was started. A nonlinear thermal analysis was followed by nonlinear mechanical analysis. The temperature history was input information for mechanical calculations for each time step increment. The initial temperature of the of the component was assumed to be at 20°C. The size of the heat source was assumed to be the same as that of the weld region. The entire weld was assumed to be formed at the same time. And, the filler material was assumed to be the base material. Handling of the weld material which is in status "yet to be deposited" was taken into consideration through activation and deactivation (dummy low values of material properties) of elements; mechanical history was automatically activated during solidification. Comparing with the "element birth technique", for example Shan et al. [4] obtained similar transient thermal profiles for both approaches. No energy ramps of weld arc at the beginning and termination of weld have been applied since technological laths had been used for weld start and finish. After all, post-processing of FE model data was performed in order to process the output files.

4.2.1 Mesh characteristics

Along with numerically and physically well-adjusted material properties, process parameters and numerical options that fit to the problem, the mesh characteristics show the great influence on results accuracy as well. If mesh does not meet the certain conditions, it may become the source of problems. Welding as a transient process involve high gradients in local sites, and this appears to be one of the challenging tasks for numerical system.

A too coarse simplified mesh can lead to incorrect results; whereas a too fine mesh necessitates prolongated computation time. In order to reflect the gradients in the model, the mesh should always be refined in direction of increasing gradients. HAZ indispensably should have the same mesh density as that in the molten zone.

In current FE model, both size (area) and shape of cross-section of each bead were determined according to the macrographs of the real weldments (Fig.4.13-4.16). The areas of separate weld passes in cross-sections were selected as equal among each other. Table 4.2 presents quantitative information concerning the FE model used in numerical studies. Dimensions of the plates are 280x300x18 mm. The choice of these parameters will be discussed in Section 4.4.

Table 4.2 FE mesh information for welding on V-groove

Pass №	Number of elements in the weld lines	Number of elements				Number of nodes
		Beam	Shell	Solid	Total	
2 of 2	3600	480	8 220	33 600	42 300	36 461
1 of 4	1 440	240	9 496	43 200	52 936	46 684
4 of 4	7 800	960	9 602	49 560	60 122	52 129
1 of 8	1 440	240	10 104	50 880	61 224	54 549
3 of 8	3 840	720	10 144	53 280	64 144	56 485
5 of 8	7 200	1 200	10 200	56 640	68 040	59 389
8 of 8	11 640	1 920	10 274	61 080	73 274	63 140

Beam elements are one-dimensional objects that represent the weld trajectory curve and the reference line, which provides data to calculate the local frame at the center of the weld heat source. Shell elements are two-dimensional objects that act as a solid-air heat exchange interface during the cooling stage. Solid elements are three-dimensional objects that construct the body of the component and the weld joint.

Side and top views of 2-pass weld FE model are presented in Fig.4.21c and j in the Subsection 4.3.4 that concerns the FE mesh calibration subject which was performed first of all, before construction FE meshes for 4- and 8-pass models. Fig.4.6 displays partial views of the 4- and 8-pass welding models.

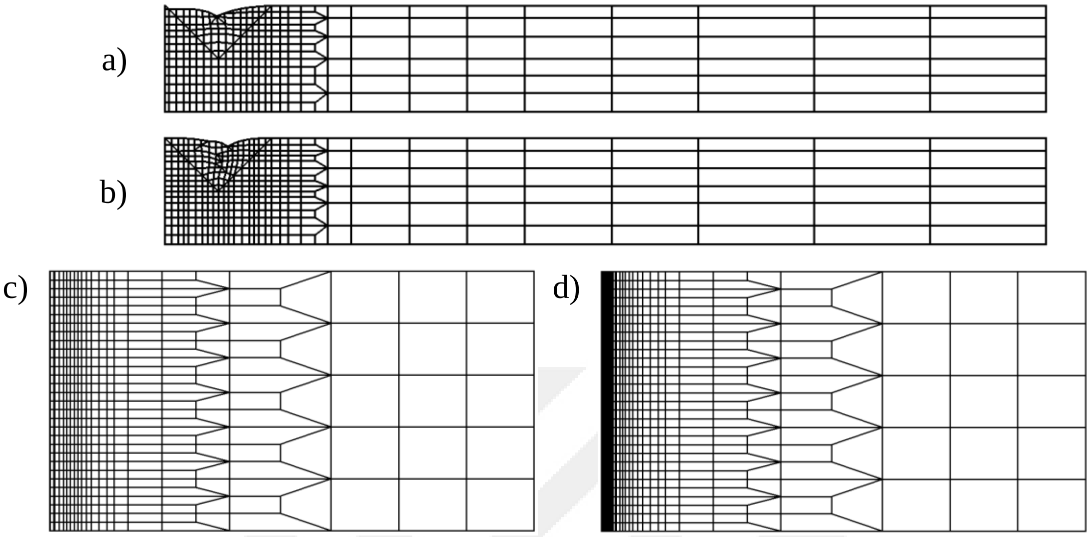

Figure 4.6 Side partial views (a-b) and top one-eight-views (c-d) of the FE meshes for 4- and 8-pass weldings on V-groove

Step size in the weld line for all cases was set as 2.5 mm. As can be seen, meshes have fine elements at the WM and HAZ and coarse elements far away from the zones with high gradients. These meshes are verified in Subsection 4.3.6 with experimental measurements as well.

4.2.2 Thermo-metallurgical properties

As it was mentioned earlier, thermo-metallurgical description of the material is one of the base points in numerical experiment. The accuracy of information defines the results of the computations. In this work, API X65 steel information is employed. CCT diagram (Fig.4.7) is taken from the ESI Group database. Comparison with those presented in Fig.3.7 and 3.8 shows its good agreement.

At the temperatures where material is melting or close to melting, the material history is removed from elements. Usually the solidus temperature is taken as limit, but a temperature below the solidus temperature can be taken. The lower the indicated temperature, the more stable is the numerical solution process. However, it should be higher than the temperature where the yield stress is still 5% of the yield stress at RT. For X65 steel, such a limit is pointed at 1300°C.

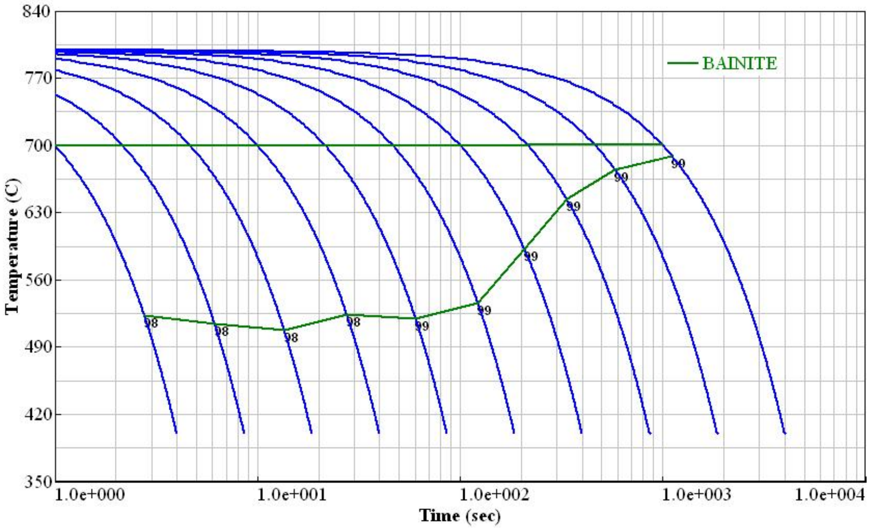

Figure 4.7 CCT diagram for X65 steel from ESI SYSWELD database

The thermal material properties, including heat conductivity and specific heat, change with temperature. Among these, the specific heat becomes large at around 800°C due to the latent heat associated with the phase transformation [55]. Fig.4.8 displays thermal conductivity and specific heat graphs of X65 steel used in current calculations.

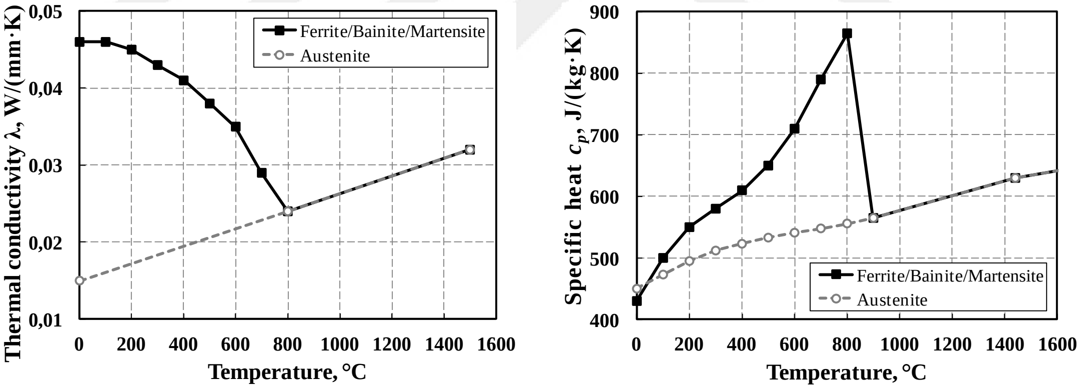

Figure 4.8 Thermal properties of X65 steel from ESI SYSWELD database

For welding, the melting and solidification should be modelled with specific heat rather than with enthalpy. From the numerical point of view, the approach with specific heat is much more efficient.

4.2.3 Mechanical properties

The mechanical material properties, including density, Young's modulus, yield stress and thermal strains, change with temperature. The yield stress becomes very small at high temperatures over 600−700°C. Yield stress close to zero means that the material loses its resistance to deformation or behaves like fluid. For this reason, this temperature is called the mechanical melting temperature [55].

Austenite is the soft phase with low Young's modulus and yield stress, while martensite is the hard phase (Fig.4.9). Austenite is a stable phase when the temperature is high, and ferrite is stable when the temperature is low. When austenite is cooled at a high cooling rate, martensite forms. Because martensite is hard and brittle, it may cause welding cracking and low toughness. The relation between the cooling rate and the resulting phase can be predicted using the CCT diagram (Fig.3.7, 3.8, 4.7).

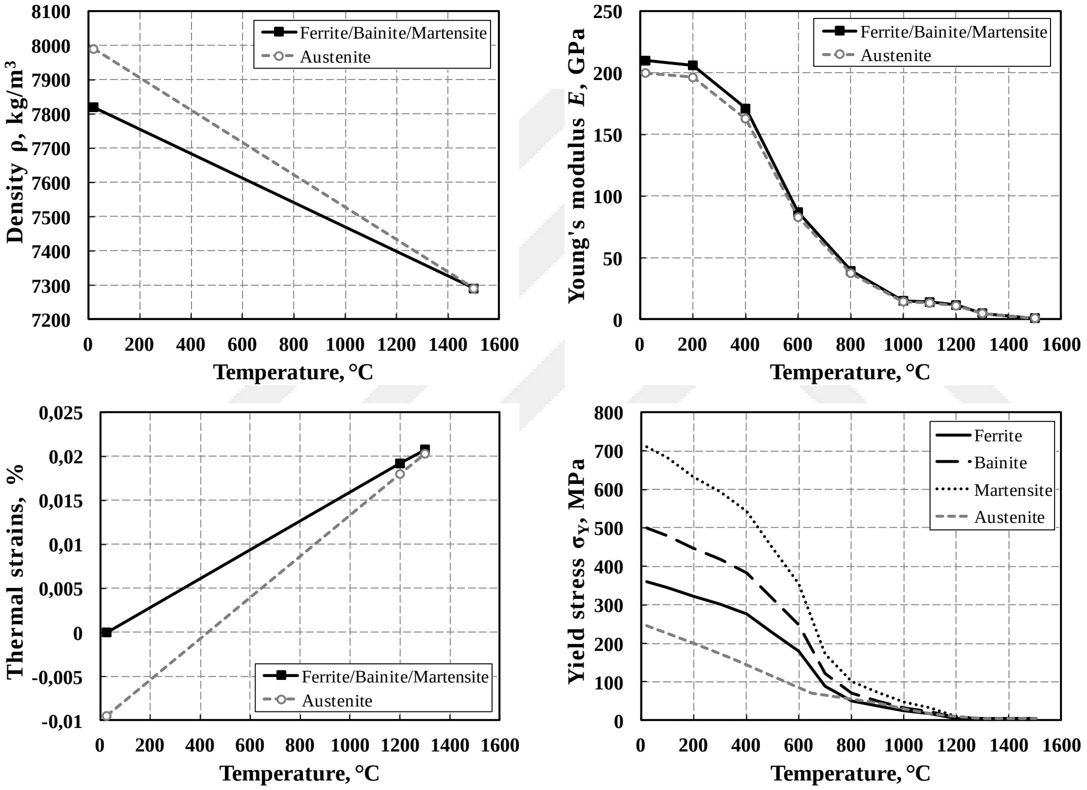

Figure 4.9 Mechanical properties of X65 steel from ESI SYSWELD database

When the temperature is higher than the mechanical melting temperature, the deformation of the metal becomes plastic deformation dominant. Since the welding residual stresses and the distortion are produced by an irreversible strain component such as plastic strain, the area heated above the mechanical melting temperature is very important. Specifically, the transverse shrinkage and the transverse bending (angular distortion) are mostly produced in this temperature range. In contrast, the longitudinal shrinkage and the residual stresses are produced at a relatively low temperature above the yield temperature (which is determined as relation of the yield stress to the thermal expansion ratio and the Young's modulus) that is the temperature at which the material fully restraint in one direction reaches the yield stress by thermal expansion. The reason of these comes from the large restraint in the welding direction and small restraint in the transverse direction [55]. For example, for mild steel yield temperature is in range of 100-200°C.

In SYSWELD, the transformation plasticity is computed as a function of the yield stress of austenite and the thermal strains. Additionally, a nonlinear factor is applied, which is a function of the yield stress of the ferritic phases [51].

Poisson's ratio was accepted as stable value at 0.3 for all temperature range, since in temperature dependent case the convergence speed of calculations slows down.

4.2.4 Stress-strain curves

Stress-strain dependencies of ferrite, bainite, martensite and austenite phases of X65 steel are displayed in Fig.4.10.

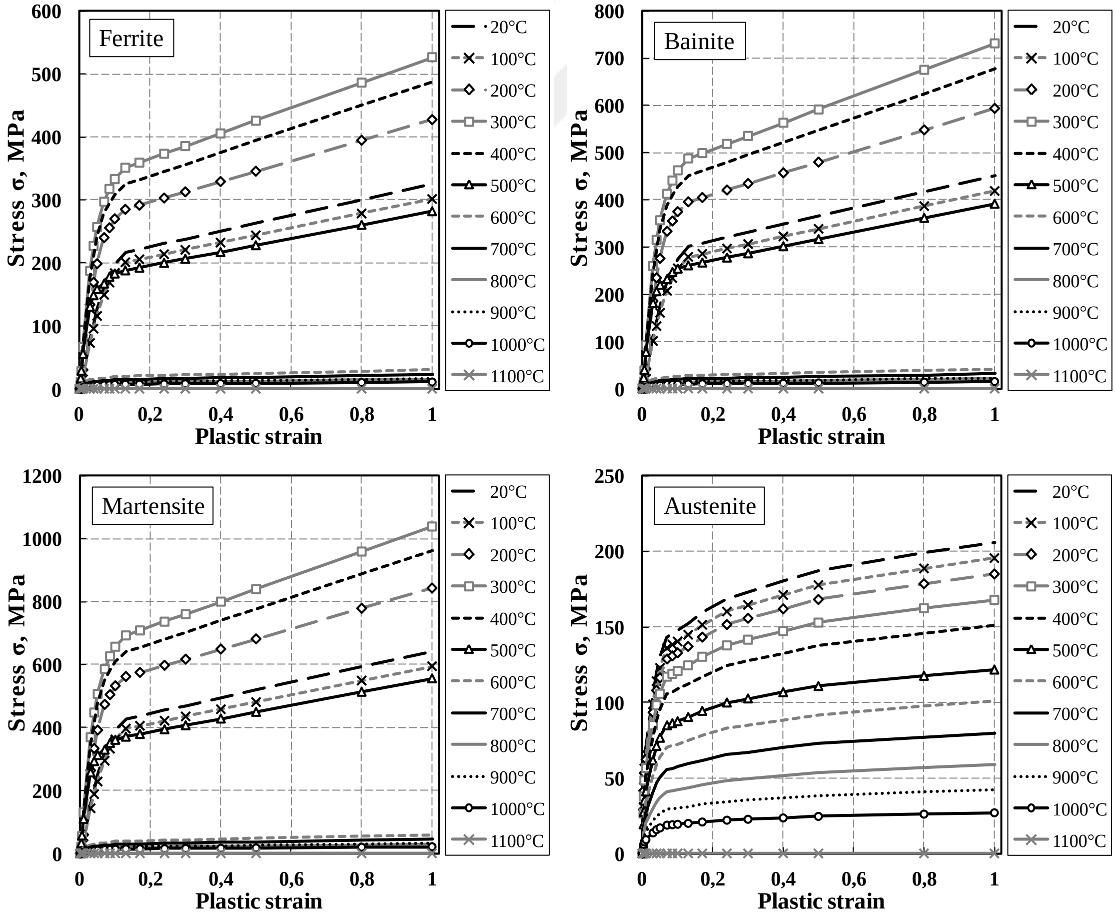

Figure 4.10 Temperature-dependent stress-strain curves
for main phases of X65 steel from ESI SYSWELD database

As it can be seen for ferrite, bainite and martensite phases, the peak strength corresponds to 300°C, then less strength is observed at 400°C, then at 200°C, 20°C and 100°C. Similar characteristic of resembling S355 steel was reported in work by Schenk [65] which employed experimental results of S355 by Peil et al. [88]. It was noted that this phenomenon is related to dynamic strain aging and is typical for temperature range of 100°C...400°C.

4.3 Verification by test studies

In order to verify the prediction accuracy of the developed computational approach, the few computational test calculations have been carried out. A transient thermal analysis was performed. Calibration of molten weld pool profiles have been done to verify the heat input from heat source, comparison of calculated and natural microstructure was performed, hardness profiles from measurements and FEM were compared, the longitudinal residual stresses distribution on the middle cross-sections measured by MBN and XRD techniques and simulated by FEM were compared. Clamping system model adjustment is presented as well.

4.3.1 Calibration of molten pool profile

Cooling rate profiles of three different welding regimes are presented in Fig.4.11. Information about pass heat input is presented in Table 3.

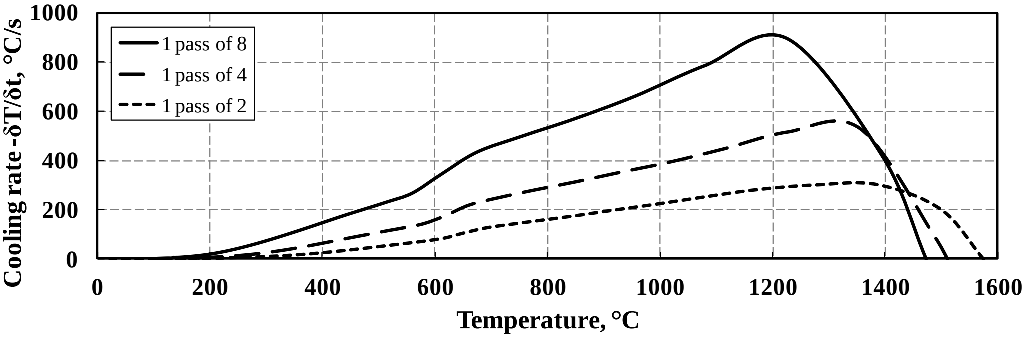

Figure 4.11 Cooling rates taken from the roots of first passes

As can be seen, cooling rate of 8-pass welding is approximately twice higher than that of 4-pass welding, and about four times higher than that of 2-pass welding.

Corresponding temperature history profiles for the nodes in the middle section of the plates are given in Fig.4.12.

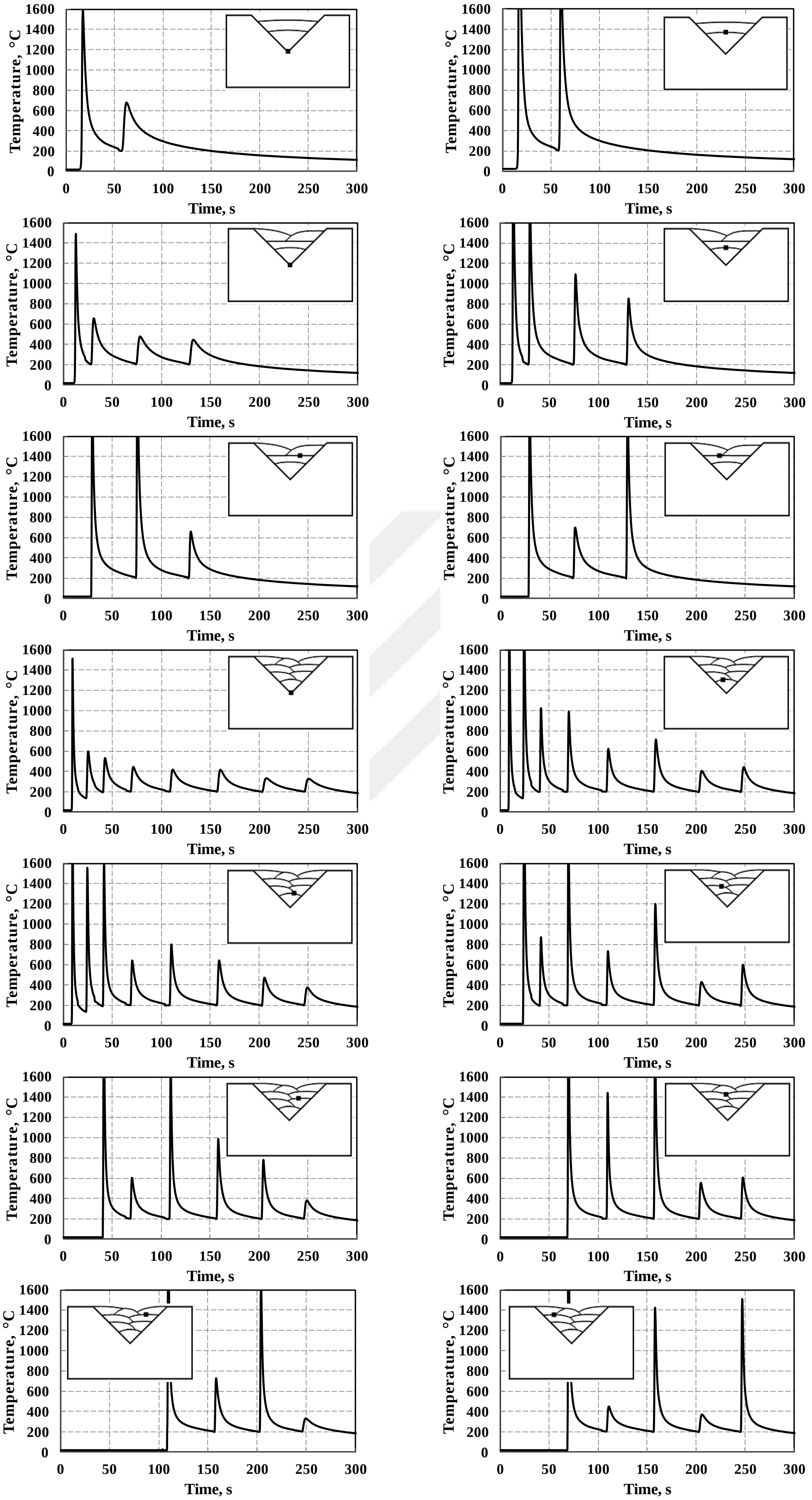

Figure 4.12 Temperature history profiles for 2-pass, 4-pass and 8-pass weldments

The cross-sectional area of a weld is generally proportional to the amount of heat input. As more energy is supplied to the arc, more filler metal and base metal will be melted per unit length, resulting in a larger weld bead. As the heat input increases, the rate of cooling decreases for a given base metal thickness. Slow cooling rate, resulting from high heat inputs, can soften the material adjacent to the weld, reducing the load-carrying capacity of the connection [57].

As can be seen from Fig.4.12, at low temperatures range, a uniform distribution of temperature field in WM and HAZ is observed. This means that interpass temperature can be controlled at any point of WM or HAZ in the weld cross-section.

The material heated above the metallurgical melting temperature can be regarded as the molten metal in the weld pool. By comparing the computed penetration shape and the measured shape, one can judge whether the heat input distribution and the net heat input per unit length of weld are correctly given in the simulation [55].

Calibration of fusion boundary profile has been done, as well. Lindgren [38] resumed that the measured cross-section of weld metal and/or HAZ can be used to calibrate the heat input model. The cross-section dimensions are important as the heat flow in the transverse direction dominates in welding. If the weld pool boundary is correct, then the temperature field outside this region will also be correct [38].

SYSWELD [51] specifies that sizes of the WM and the HAZ have to be obtained near experimental data, whereas thermal cycle and hardness are optional for verification parameters. Presented calculated results show good conformity with the real phenomenon signifying correct heat input model used.

Lewis et al. [89] reported that the shape and form of the heat source had some influence on the form of the residual stress predictions very close to the weld, but this influence was small compared to the influence of the material hardening model.

Fig.4.13 shows transverse fusion boundaries from the cross-sections prepared from real specimens, Fig.4.14-16 show those predicted by FE simulation. All planes are located at mid-lengths of the welds.

From these figures, the predicted transverse fusion profiles are close to the measured ones, all weld pass elements are encompassed by melting temperature region, adequate HAZ is observed outside the fusion zone. In addition, penetration capabilities of the heat source are approved.

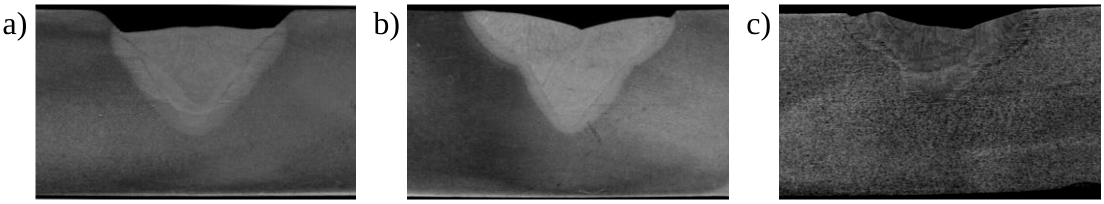

Figure 4.13 Macro-sections: a) 2-pass weld; b) 4-pass weld; c) 8-pass weld

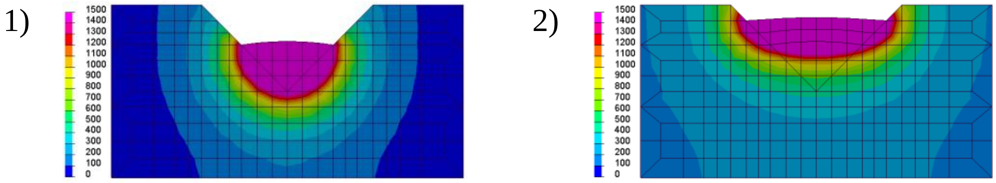

Figure 4.14 Molten weld pool profiles for 2-pass weld

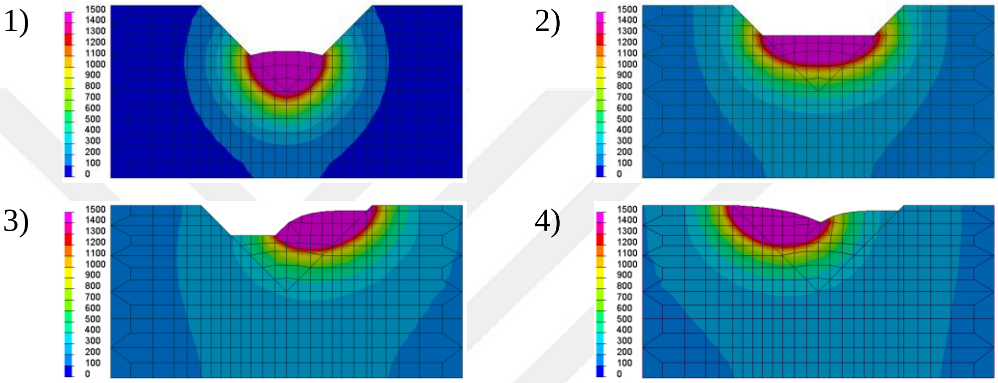

Figure 4.15 Molten weld pool profiles for 4-pass weld

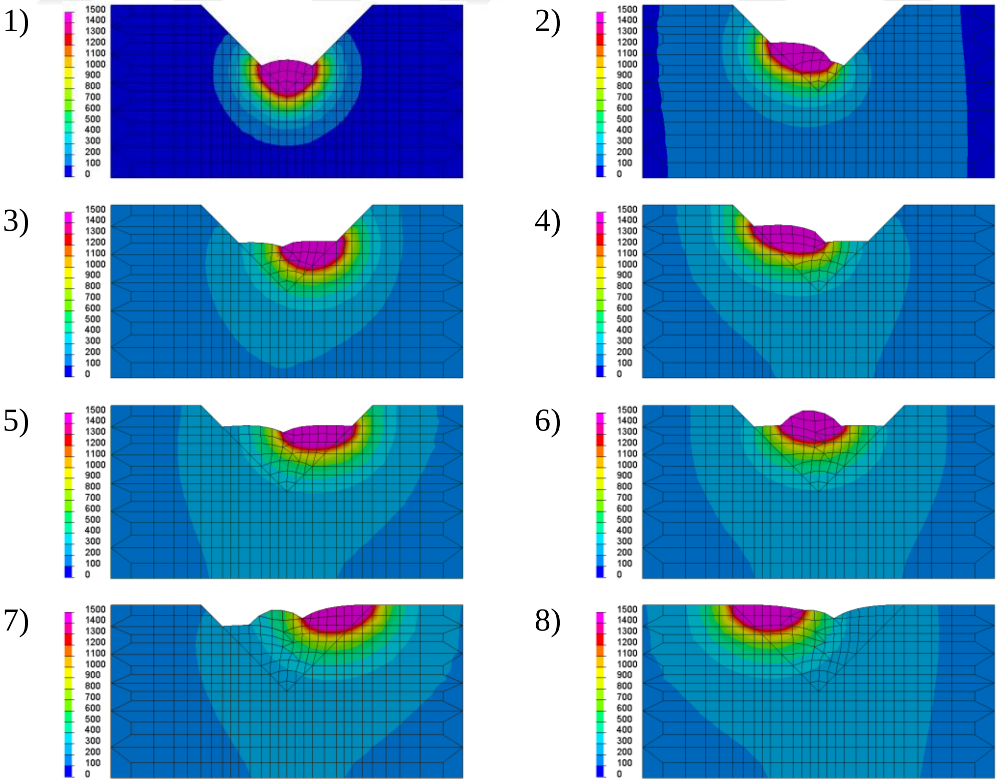

Figure 4.16 Molten weld pool profiles for 8-pass weld

4.3.2 Microstructure evaluation

Microstructures from WM, HAZ and BM regions are presented on Fig.4.17, 4.18 and 4.19 for two-pass, four-pass and eight-pass weldments, respectively. WM is characterized mainly by bainite and Widmanstätten ferrite, whereas BM remain in ferrite-pearlite phases. HAZ is a mixed region containing ferritic-perlitic microstructure with increasing amount of bainite in direction to WM.

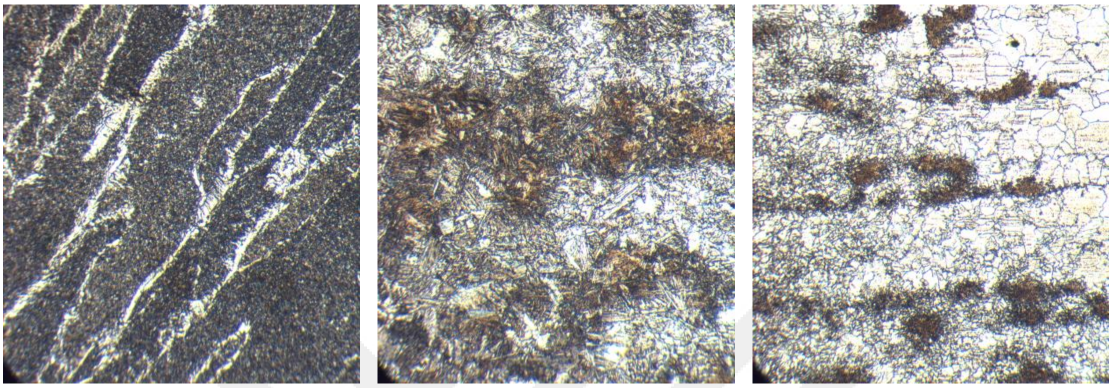

Weld Weld to HAZ HAZ to BM

Figure 4.17 The microstructure of two-pass weldment in different zones

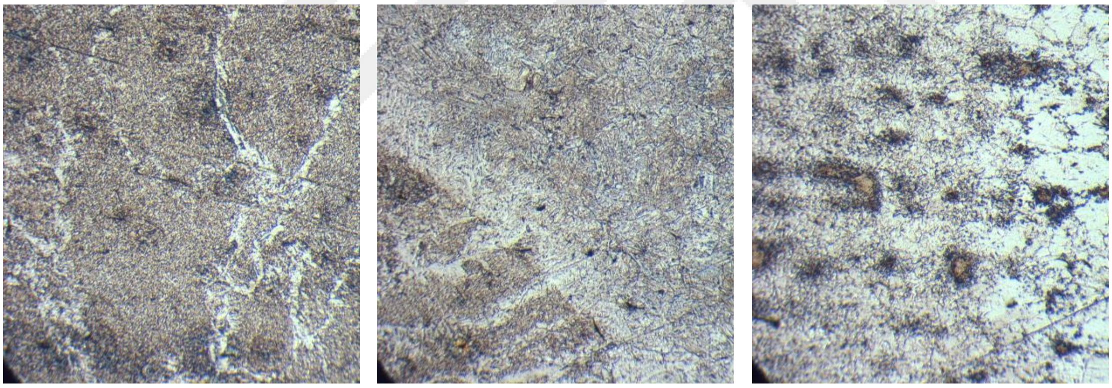

Weld Weld to HAZ HAZ to BM

Figure 4.18 The microstructure of four-pass weldment in different zones

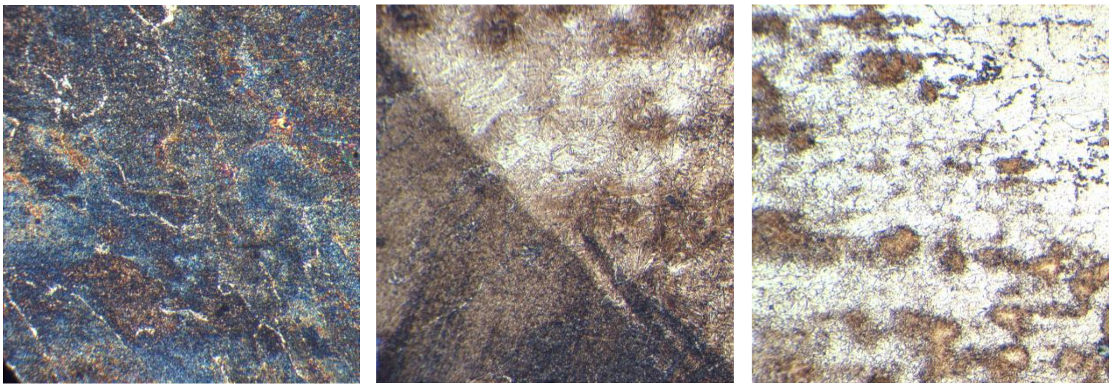

Weld Weld to HAZ HAZ to BM

Figure 4.19 The microstructure of eight-pass weldment in different zones

4.3.3 Hardness calculations

Hardness profiles are given in Fig.4.20 for the measured and computed cases.

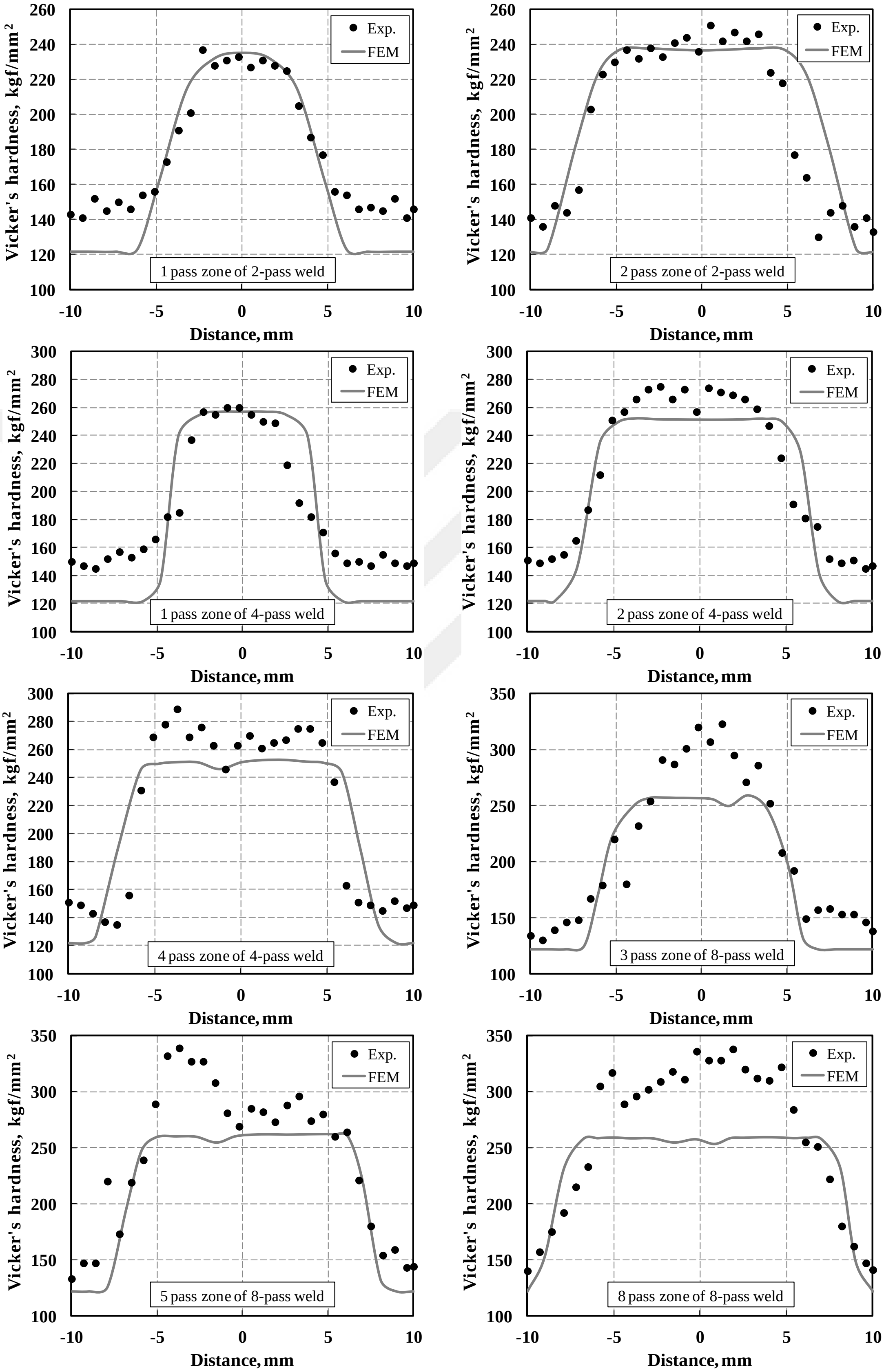

Figure 4.20 Vicker's hardness profiles: measurements and numerical results

Coincidence of results for 2-pass welding looks sufficiently good as for width of the weld pool, so for measured values. For 4-pass welding, with increasing the pass quantity light discrepancies come out in magnitudes, though concerning the width of melted zone there is also good agreement. Whereas, for 8-pass welding mismatch in values of hardness in weld zone is more evident.

There may be few reasons of this, one of which is that with increasing the number of weld passes (and overall duration of welding, respectively) influence of other processes, namely chemical reactions in WM, elements evaporation of the WM etc., is increased as well. And computation of such processes is not yet incorporated to the simulation software. Also, hardness is known to be closely related to the cooling rate. In addition with the fact that material of welding wire in computer simulation was taken as that of the base metal, and in conditions of raised welding speeds it may show some deviations. To remind, the welding speed in 4-pass case is one and a half times and in 8-pass case is two times higher than that in 2-pass welding. And yet, in computer simulation the widths of weld pools in 8-pass weld specimen show good agreement with measured results as well.

4.3.4 Mesh size calibration and surface residual stresses examination

In order to attain the best accuracy and determine the optimal step size in the weld line, mesh calibration has been performed with four different models for 1-2-pass weldings. Welding parameters are given in Tabl.3. Experimental results are obtained through the measurements by MBN technique. Considered FE meshes with different step sizes, number of elements and nodes (Tabl.4.3) are presented in Fig.4.21.

Table 4.3 FE mesh information of the models to optimize the mesh size

Mesh №	Step size in the weld line, mm	Number of elements in the weld lines	Number of elements				Number of nodes
			Beam	Shell	Solid	Total	
1	5	270	90	3 468	3 870	7 428	4 581
2	3.125	768	144	6 024	9 408	15 576	10 554
3	2.5	1 260	180	8 804	16 260	25 244	17 921
4	1.5625	4 128	288	7 628	39 072	46 988	41 593

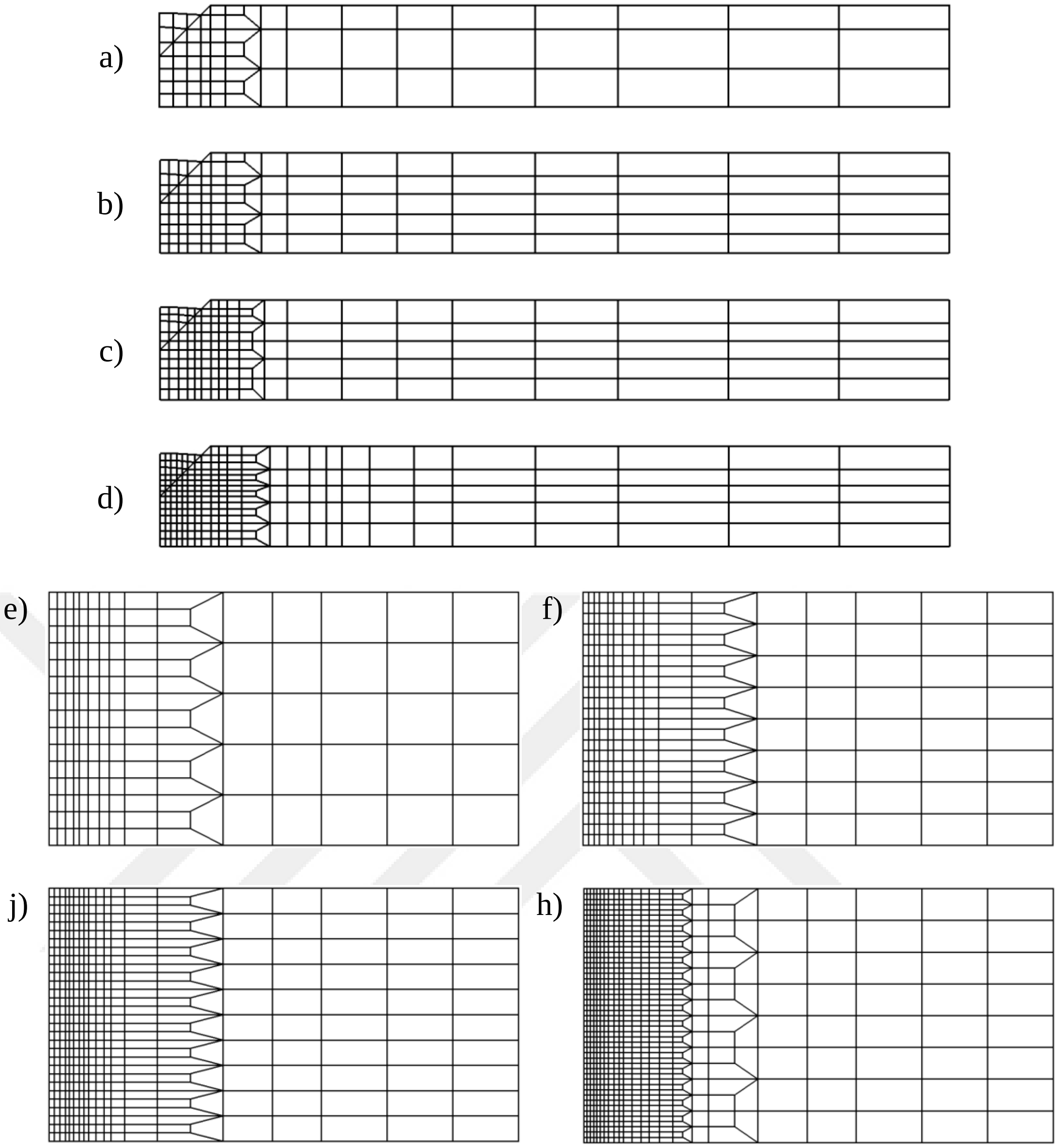

Figure 4.21 Top quarter-views and side half-views
of FE meshes for 2-pass welding on V-groove

A finer grid was designed in and near the weld zone, while the mesh size was gradually increased with distance from the weld zone.

Meshes №3 and №4 showed good coincidence with residual stresses measured by Barkhausen noise technique (Fig.4.22). Therefore, for further calculations a choice in favour of lighter mesh by number №3 that provides reasonable calculation time has been made. Step size in the weld line in the range of 1.5...2.5 mm is acceptable for getting good reproduction of residual stress state.

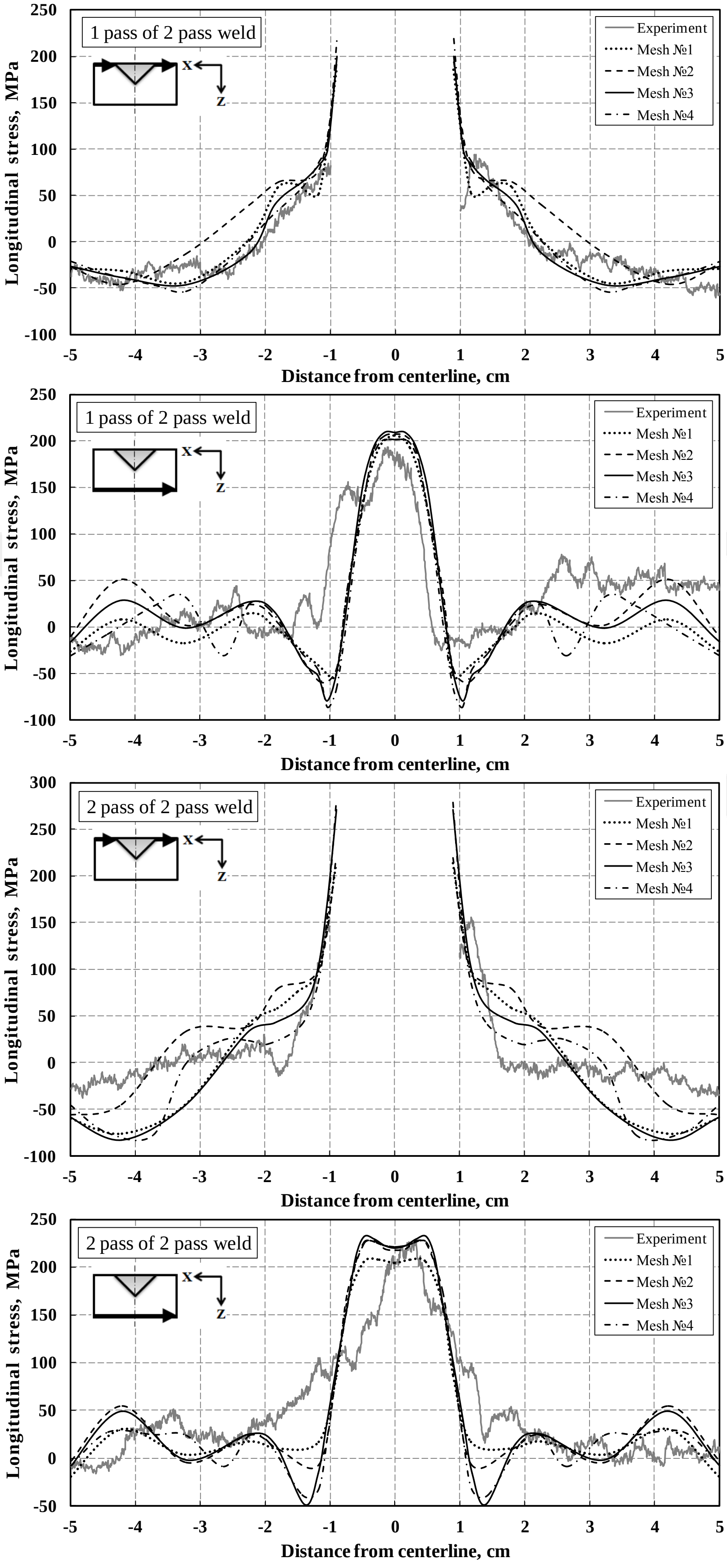

Figure 4.22 Comparison of four FE meshes on the base of 2-pass weldment

4.3.5 Adjustment of the clamping model

Clamping conditions are known to play a critical role in welding technology, so are their models in welding computer simulations. Javadi [90] studied clamping effect on the Monel 400 plate of 6 mm thickness and reported 10% increase in longitudinal residual stress and decrease in angular shrinkage of a quarter comparatively to the unclamped case. Leggatt [13] explored the effect of bending restraints in combination with pass sequencing in multi-pass butt weld of the 50 mm thick type 316L stainless steel plate, and the effect of in-plane restraints of low, high and very high resistance for similar plate. Expectedly, for very high restraint the tensile stresses generated by transverse shrinkage appeared to be also increased.

The restraint at a welded joint may be described as the resistance to the free thermal expansion and contraction of the heated material. It sounds like a simple concept, but in fact is complex: it varies with direction and position in the weld and it changes continuously during the fabrication of a welded component or structure. It is affected by a wide range of factors, including the geometry of the parts being joined, the use of fabrication aids such as tacks, cleats and jigs, the pass sequence for multi-pass welds and the welding sequence for structures with more than one weld [13].

Influence of clamp model types on residual stress has been studied. Firstly, point-type clamps (Fig.4.23), plate like clamps rigid in Z-direction and clamps rigid in XYZ-directions have been considered (Fig.4.24). The gap on bottom clamps was kept 45 mm for considered study. The convention used in this thesis for describing the directions relative to a straight weld in a plate is given in Fig.4.23.

In the first case, the only clamped node that didn't change its position during welding was the rigid in XYZ-directions; node rigid in XZ-directions shifted on 0.002 mm and other two clamped nodes rigid only in Z-direction moved on 0.069 and 0.150 mm. All clamp nodes was at maximum 20°C. Besides, angular distortion of cold regions far away from operation zone reached during welding 0.2 mm (at 20°C) and 0.4 mm (at 115°C), and these did not correspond to the reality.

In the second case, when clamps were rigid in Z-direction, plate showed unsteadiness in XY-plane − clamped node extended away for about 0.3 mm (at 21°C) by that also showing incompatibility with actuality.

Such insubstantial node drifts at low temperatures were excluded when rigidity in XYZ-directions was taken into account in third case of clamp model.

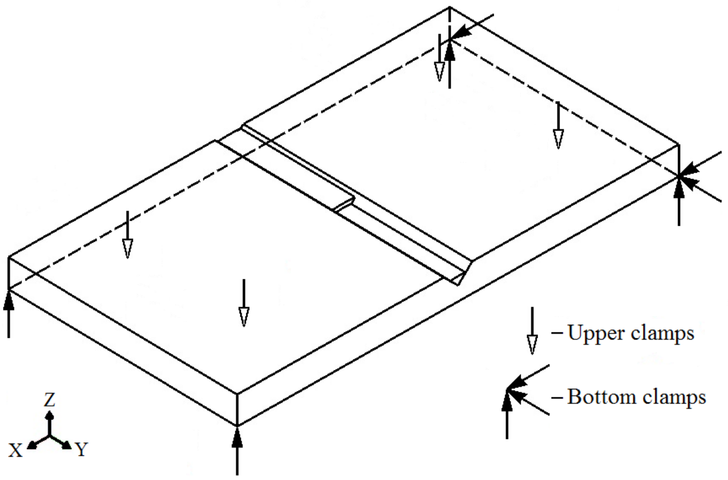

Figure 4.23 Point type clamps model

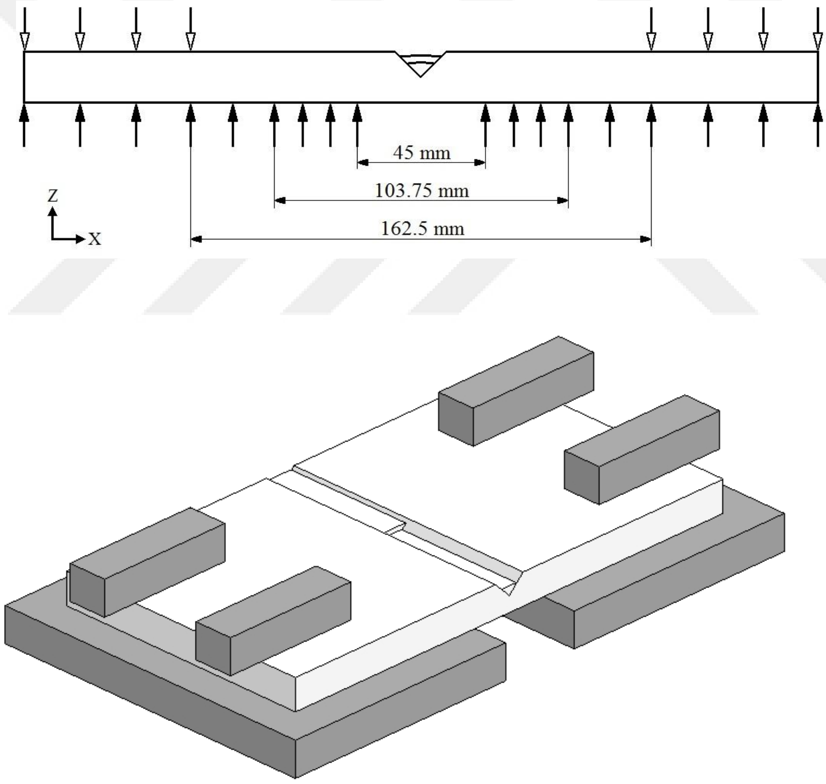

Figure 4.24 Plate type clamps model: side and general views

Fig.4.25 displays comparison of the longitudinal residual stress distributions in the middle cross section of the one-pass welded plate from top and bottom sides. On both surfaces, the best coincidence with experimental measurements is obtained for XYZ-rigid case only.

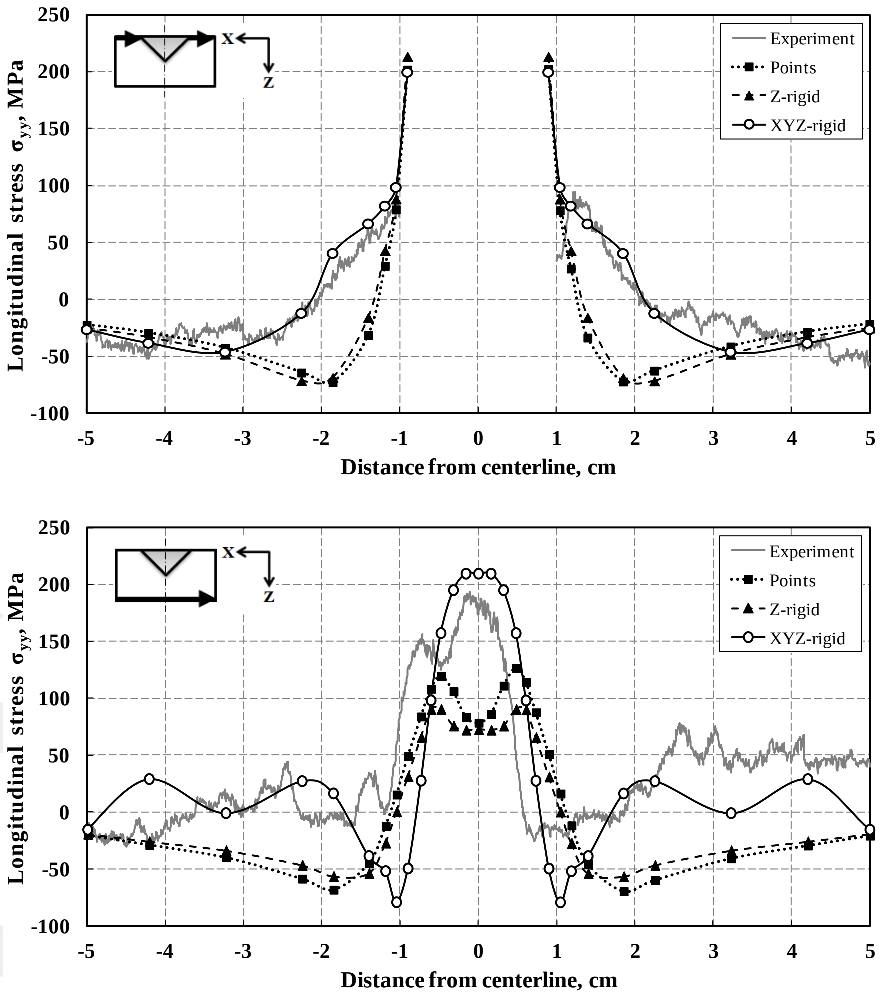

Figure 4.25 Clamp models. Residual stress for the 2-pass weldment (1 pass zone)

Same analysis for two-pass weldment is presented in Fig.4.26. Again, on both sides the best coincidence with experimental measurements is obtained for XYZ-rigid case. Noticeable that point-type model and plate-type model rigid in Z-direction produce almost similar results. And plate-type model rigid in XYZ-directions demonstrates the importance of restraints of free movements during welding in longitudinal and transverse directions that in fact implement the function of friction process between welded plate and clamp plate. Contact problem currently cannot be considered in combination with clamping conditions in SYSWELD. Therefore, such assumption as XYZ-rigidity was accepted for clamping parameter in order to approach to real circumstances. According to the residual stress profiles (Fig.4.25 and 4.26), the effect of such approach can be significant. Deshpande et al. [91] using point-type clamps obtained angle of distortion twice different from experiment.

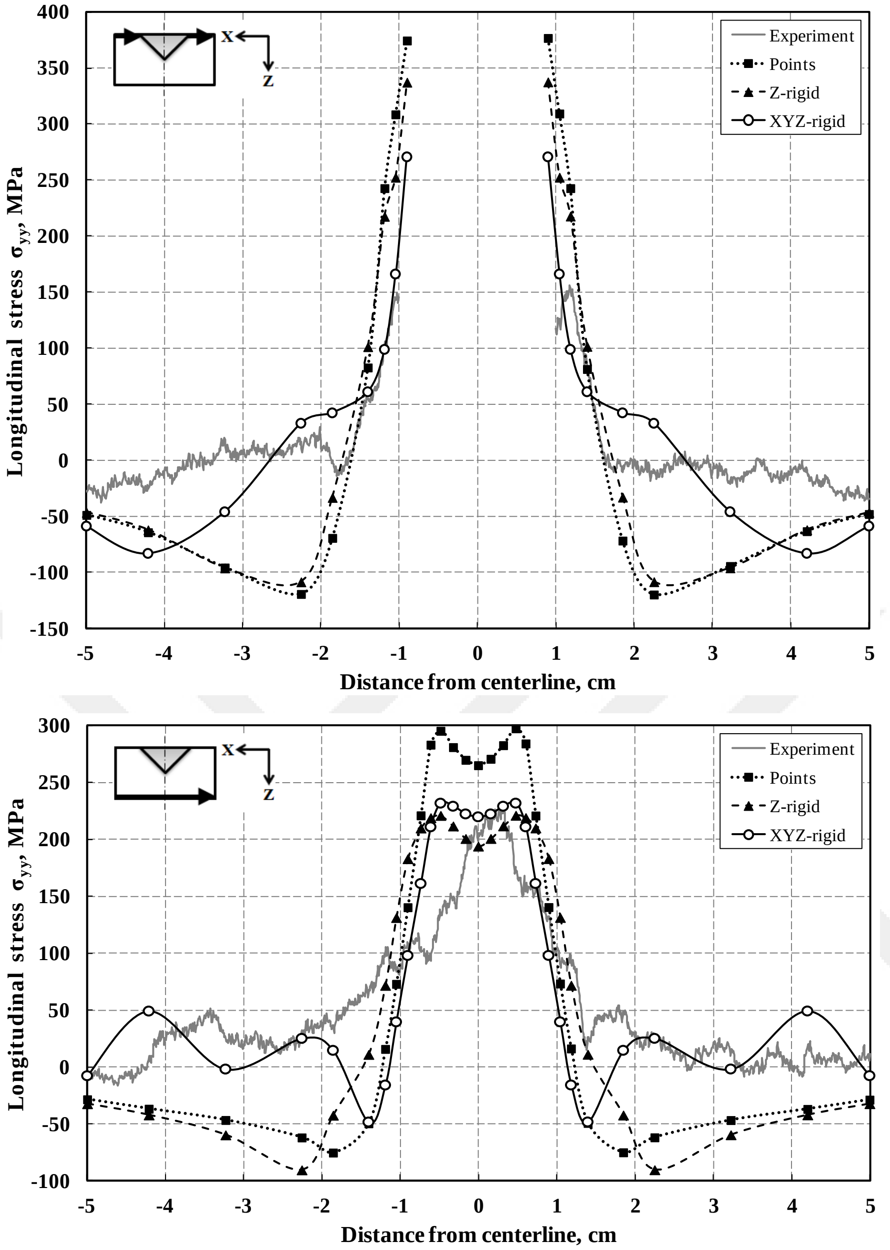

Figure 4.26 Clamp models. Residual stress for the 2-pass weldment (2 pass zone)

Dimensions of the bottom plate-type clamps have been varied and its effect on residual stresses field has been investigated (Fig.4.24). Gap under the plate where welding torch is passing has been altered as 162.5, 103.75 and compared with initial 45 mm. As in the case of point-type restraints there was an appreciable sagging in Z direction during the welding, and it obviously depends on the dimensions of the bottom clamp.
From Fig.4.27, it is seen for one-pass weld region that as less the restrained area, so more relieved the plate from bottom side. And if the boundary conditions in numerical model are not reproduced in accord with the real circumstances, obtained residual stress results may be under- or overestimated.

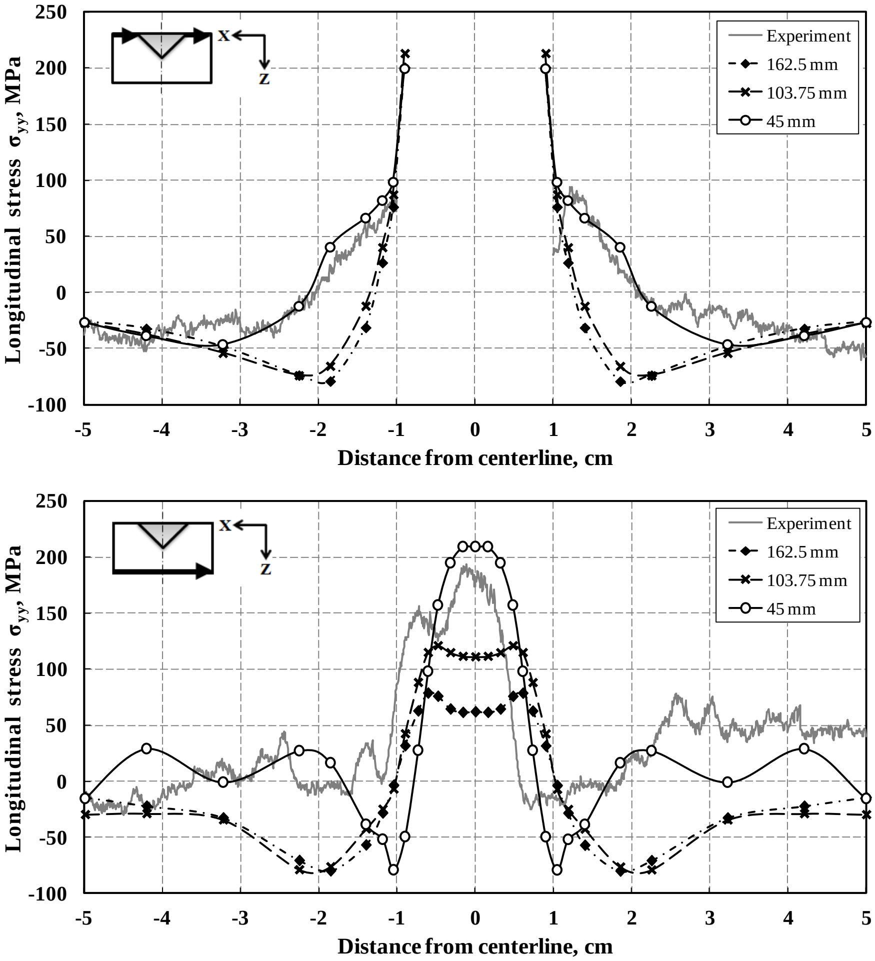

Figure 4.27 Clamp sizes. Residual stress for the 2-pass weldment (1 pass zone)

Fig.4.28 demonstrates same analysis for zone with two weld passes. Here, the situation is complicated, since with increased restraint same behaviour is registered for 162.5 and 103.75 mm, but for 45 mm in spite of that the stresses are decreased on bottom side. Taking into consideration the influence of heat from previous weld pass, the explanation should be in the phenomenon of stress relaxation which is directly related to constantly deformed body conditions. Relaxation will be discussed in more detail later in Subsection 4.4.3. Here, need to note that stresses under second weld pass in conditions of raised temperature and constant tight constraints relax, and, thus, show decrease at final state. Summarizing, longitudinal residual stresses distribution for two-pass welded region with 45 mm gap shows the best agreement with experimental measurements, and provides required behaviour of the numerical model through the entire process. In literature, Schenk [65] also reported that closer clamping to the weld seam reduces both residual distortion and residual stresses after unclamping.

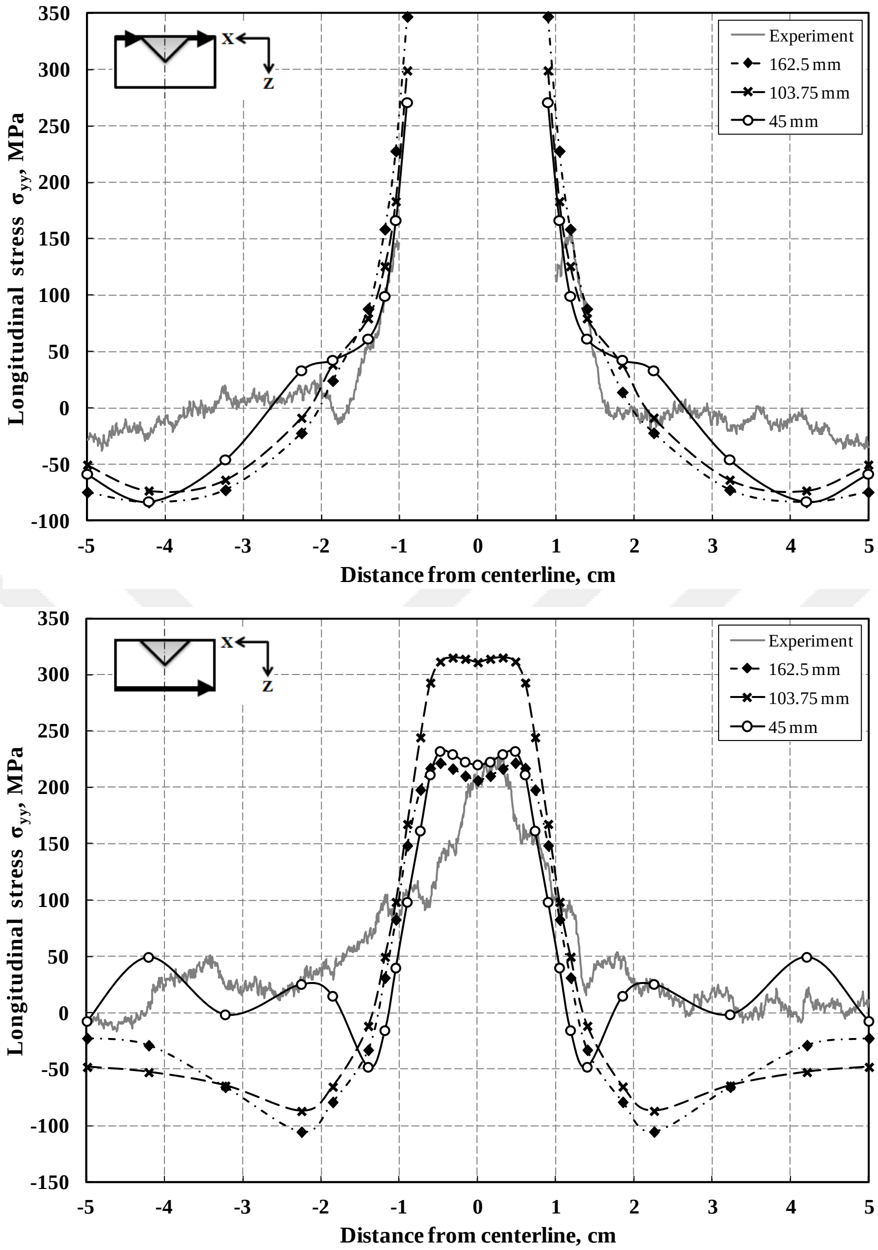

Figure 4.28 Clamp sizes. Residual stress for the 2-pass weldment (2 pass zone)

Obtained results allow to conclude that modelling of restraints is one of the critical aspects in welding simulation. And if nodal clamps can meet the requirements of accuracy in thin plate welding simulations, then in modelling of welding of intermediate thickness plates such simplifications may lead to inadequate results. Also, thick plates may demonstrate rigidity due to thickness, and this decreases the requirements to the models of restraints. For example, Brickstad and Josefson [76] classified small thicknesses as $t \leq 9$ mm, intermediate thicknesses as $9 < t \leq 25$ mm, and large thicknesses as $t > 25$ mm.

4.3.6 Test models computation

Test calculation for 1-2-4-pass and 3-5-8-pass weldings have been performed as well, and acceptable correctness of arranged conditions of computer modelling has been proven. Calculated stress states on the face and back sides of the component generally fit with the real measurements by MBN method. Arrangements of weld passes and measurement lines are displayed in Tabl.4.1 and Fig.4.5. Residual stresses on the top surface are plotted in Fig.4.29, and on the bottom surface in Fig.4.30.

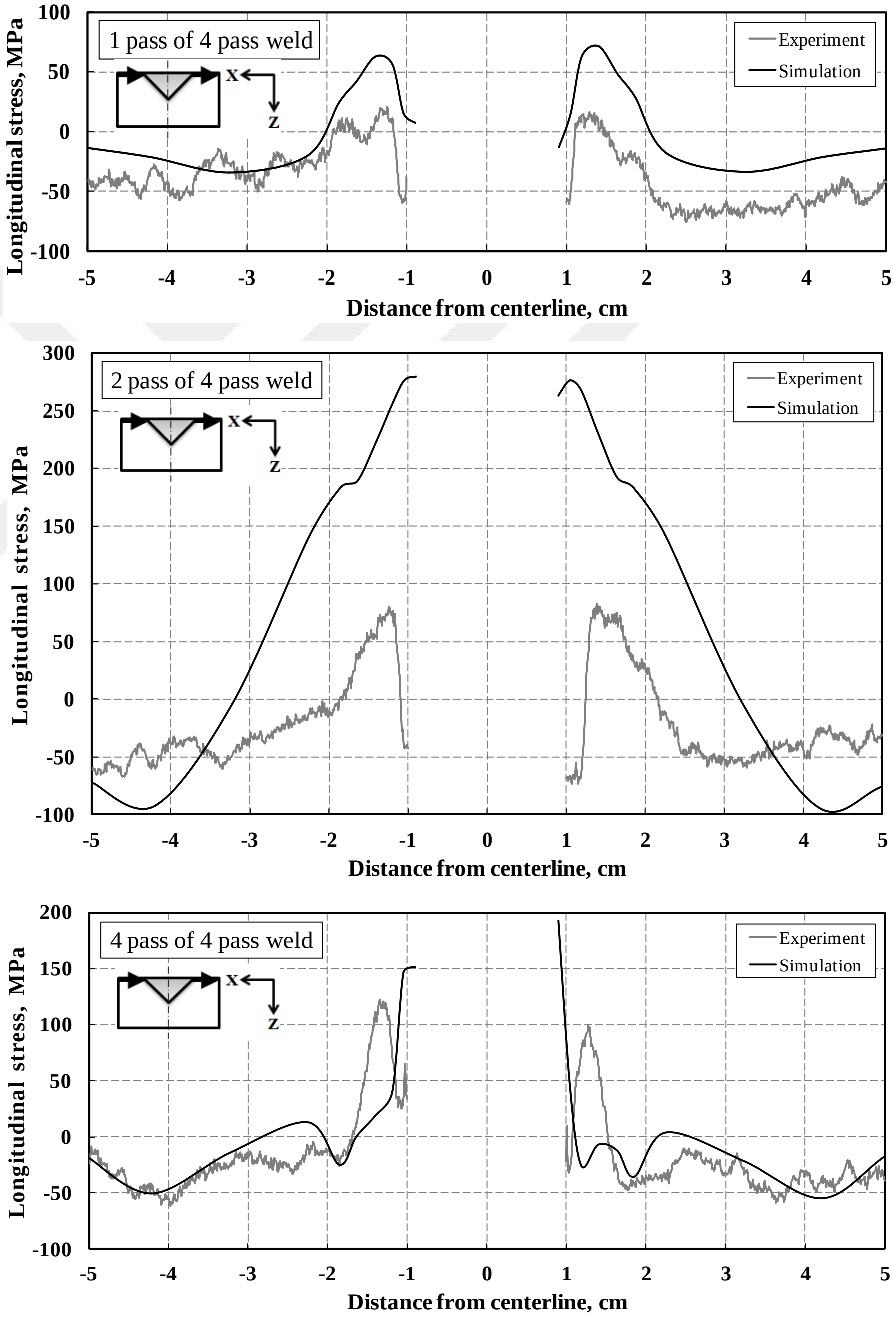

Figure 4.29 Residual stress profiles for the 4-pass weldment from top surface

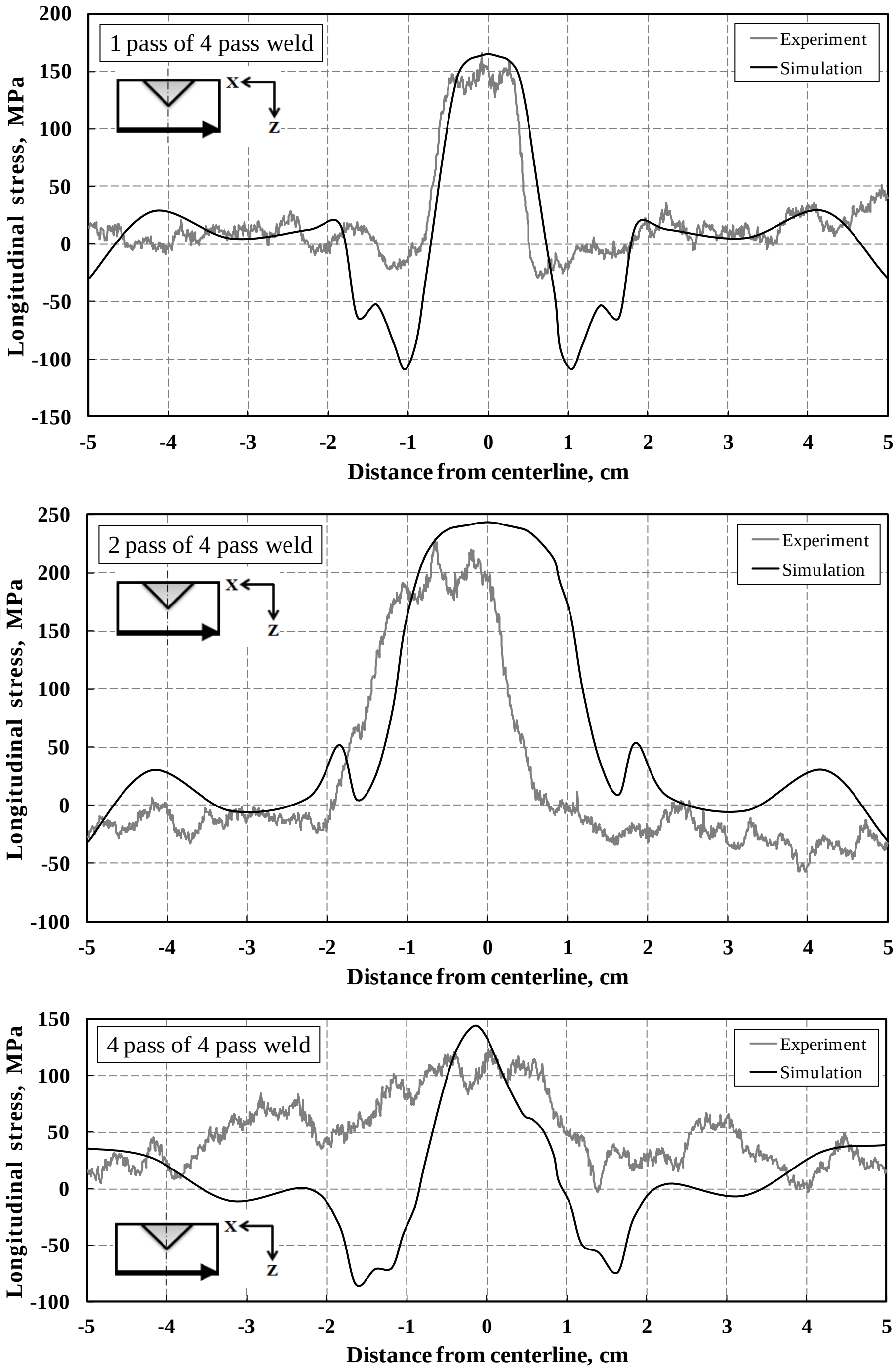

Figure 4.30 Residual stress profiles for the 4-pass weldment from back surface

Some discrepancy can be observed for top surface near locations of the V-groove edge that is actually stress concentrator. For 4-passes zone, the edges are melted during welding. For 1-pass zone, the groove fullness is about 25% and the edges are comparatively far from weld zone. Whereas for 2-passes zone, the groove fullness is about 50%, the edges are closer to weld zone and contribute as stress concentrators. Verification on eight-pass weldment is presented in Fig.4.31 and 4.32.

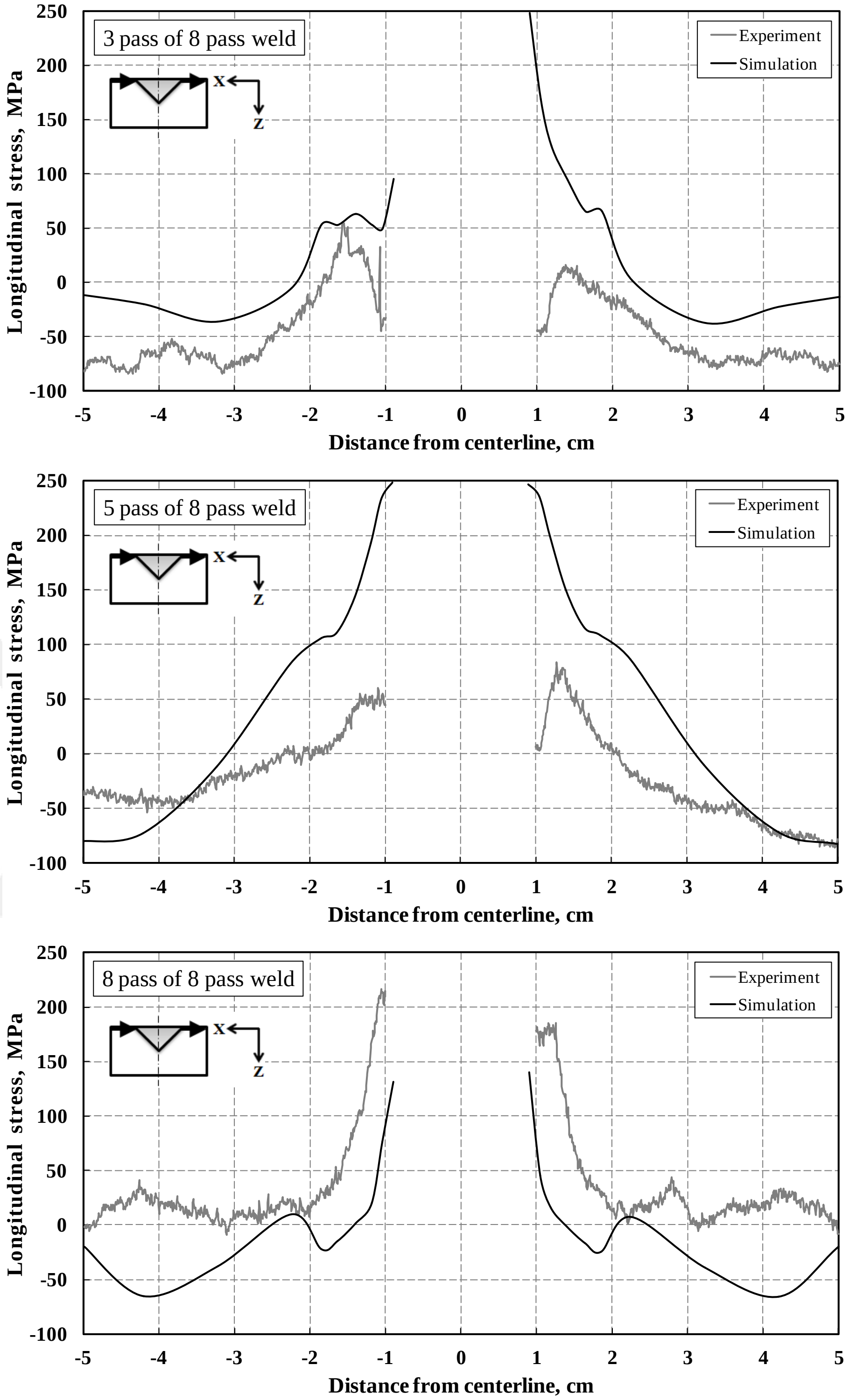

Figure 4.31 Residual stress profiles for the 8-pass weldment from top surface

Resembling picture is for 5-passes zone where the groove fullness is about 63%. Obtaining the perfect coincidence in such locations is complicated due to possible light variations of technological parameters during welding.

In total, good agreement have been achieved for all considered test models.

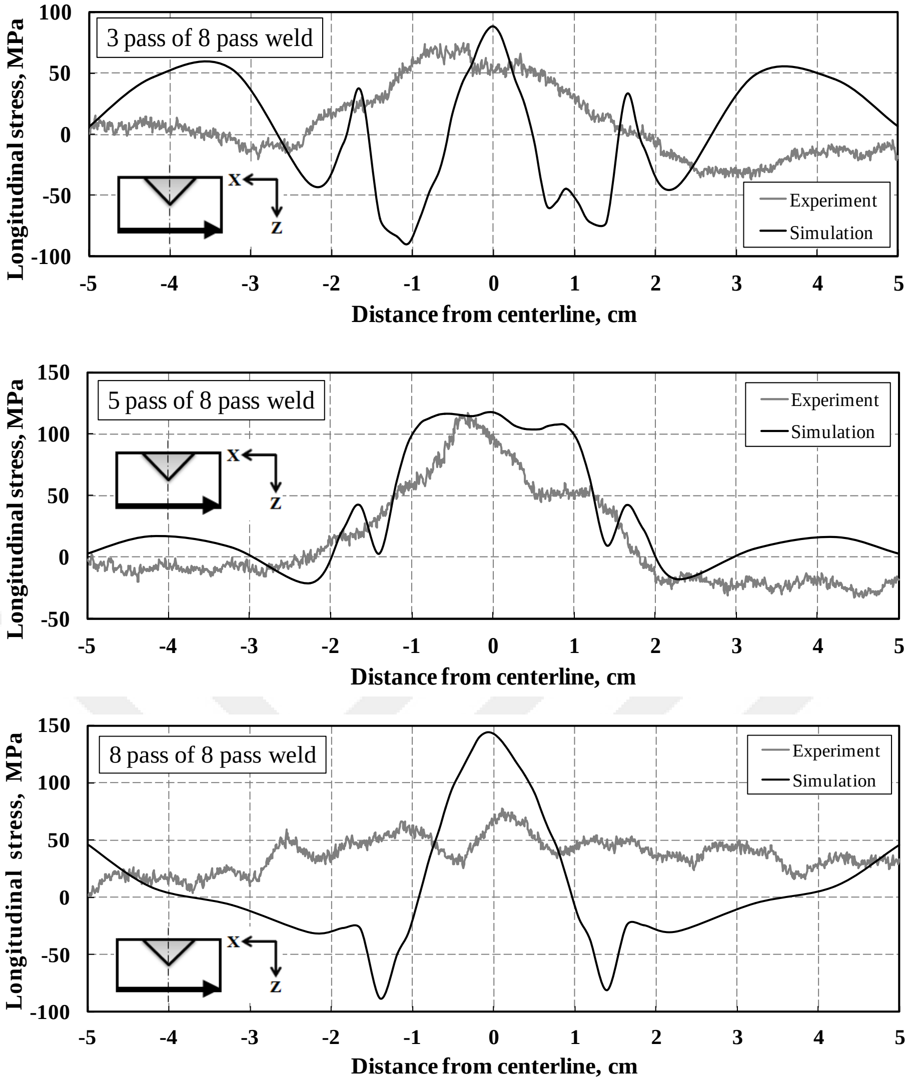

Figure 4.32 Residual stress profiles for the 8-pass weldment from back surface

4.3.7 XRD measurements

Measurements with the aid of XRD technique was taken from the bottom surface of four-pass welded specimen in the zone of 4th weld pass. Prior to X-ray measurements micro-polish was done on the specimen surface. In Fig.4.33 comparison of the obtained residual stresses distribution measured by XRD and MBN methods is given. CoG: Mean method was applied to study the state of residual stress. Cr-K_α radiation X-ray beam directed to acquire data from the (211) α-Fe diffraction line profiles. Also, it should be taken into account that each method has different penetration capacity. Depth of MBN signal is about 0.02 to 0.30 mm whereas the penetration depth of Cr radiation into steel for the (211) peak is nearly 5 microns [87].

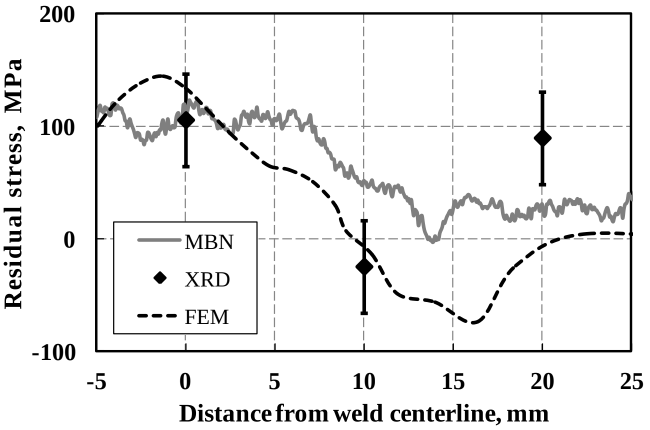

Figure 4.33 Comparison of the residual stress values obtained by MBN, XRD [87] and simulation

Results show good agreement under the weld pass zone and acceptable deviation under HAZ. The last can be explained by the fact that in the HAZ material properties change with considerable gradient, and even 1-2 mm drifting may result in noticeable difference of measured value. As Leggatt [13] also pointed residual stresses may vary rapidly with position relative to the fusion boundary, such that measurements are very sensitive to location and sampling volume.

Summarizing all the considered test studies, it is possible to conclude that although there are some discrepancies between the numerical predictions and results of measurements in local regions, however, computational approach has basically captured the features of compared parameters in both distributions and magnitudes on the whole. This allows to continue conduction of further detailed numerical investigations of multi-pass welding cases.

4.4 Results and discussion of multi-pass welding on V-groove

In this Subsection, numerical investigation of the multi-pass welding on V-groove is presented. Starting with characterization of the single-pass weldment, continuing with the study of the stress- strain state evolution as function of weld pass numbers, and finishing with analysis of unclamping and interpass temperatures.

However, there is an important issue concerning the plate dimensions. Effect of a plate size on residual stress field is shown in Fig.4.34. Computations were made based on the case of 2-pass welding on plates of different lengths − 150, 300 and 450 mm. Conditions, like plate thickness, groove geometry, welding speed, heat input, interpass and unclamping temperatures etc. were the same. Profiles obviously point at the influence of the plate size on the measured results of residual stress. Also, in all cases there is "an effect of a border" in the form of the peaks is observed. For considered cases, the length of this zone appeared to be about 60 mm from start and end borders of the welded plates. Apparently that measurements on the specimens of insufficient dimensions can lead to misunderstandings of the residual stress phenomena. Alike study have been performed by Batıgün [92] showing the effect of changing sample size on the distortion characteristics. With the decreased length of a sample, the angular deformation increased due to heat accumulation in the sample during welding and consequent local expansion and plastic deformations due to decreased flow stress values at higher temperatures.

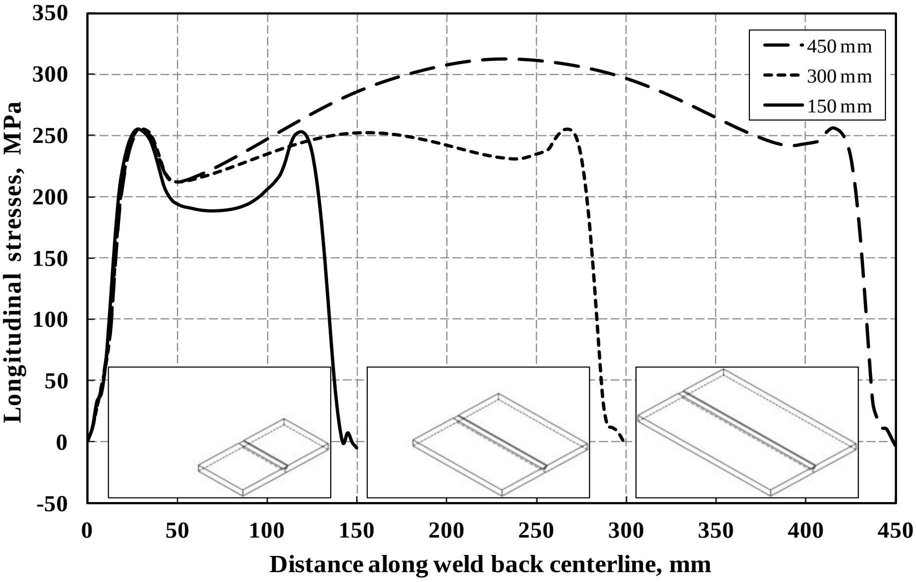

Figure 4.34 Effect of the plate size on residual stress distribution at the back surface of the workpiece along the weld centerline

Sakkiettibutra and Vollertsen [83] reported results of parametric study concerning geometric simplifications for calculations of residual stresses and distortions, and pointed the sensitivity of the distortion angle to the plate length less than 300 mm (constant width). Also, plate width less than 200 mm (constant length) gave serious variations in values of residual stresses taken in the HAZ and weld pool region.

Also, specification and qualification of welding procedures for metallic materials (ISO 15614-1: 2004) [93] states the minimum length of a test piece for butt joint as 350 mm and minimum width of every plate to be joined as 150 mm (300 mm in total). These means that short components may be used for the purpose of verification of modelling and parameters adjustment, but for phenomena investigations metal pieces should be taken not less than 300 mm in length. Further numerical investigations are performed on the components of 300 mm. And, clamping system applied to the plate of 300 mm is presented in Fig.4.35.

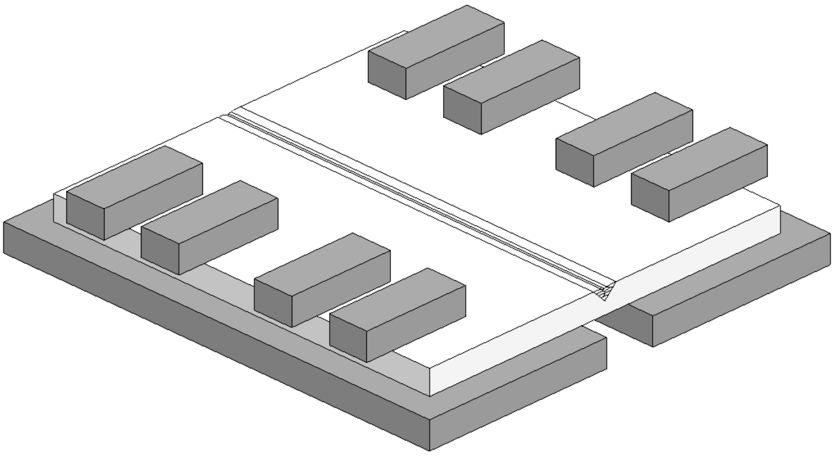

Figure 4.35 Clamping conditions for 300 mm plate (welding on V-groove)

4.4.1 Characterization of single weld pass

Fields of residual stress and plastic strains at the start, the middle-way, transverse and longitudinal cross-sections along the weld pass have been carefully inspected. Distributions of longitudinal, transverse and normal stresses of one pass welding, as well as equivalent plastic strain field, are presented in Fig.4.36 and 4.37. Evidently, that all stress components are almost uniform over the middle part of the plate, and thus the conditions are approaching steady state conditions. Along the weld length, the highest tensile longitudinal stresses σ_{yy} are observed in the plate directly under the weld seam with peaking values at the regions close to the weld start and end. Transverse stress σ_{xx} is tensile in the middle regions of the plate and in order to balance the state is highly compressive at the edges. As it is expected, the normal stress component σ_{zz} demonstrates the lowest magnitudes. Distribution of plastic strain shows two prolongated regions: the deeper one is 4.7% and formed due to tension-compression cycle caused by approaching weld pool, the upper one is 4% and is the result of the following austenite-bainite phase transformation in the material of the weld. Later, detailed stress development analysis for middle cross-section will demonstrate these two reasons: first plastically strained zone in the WM border appears just before melting between approximately 14 and 16 s, and second one forms in the WM body just after WM solidifies between 17 and 19 s.

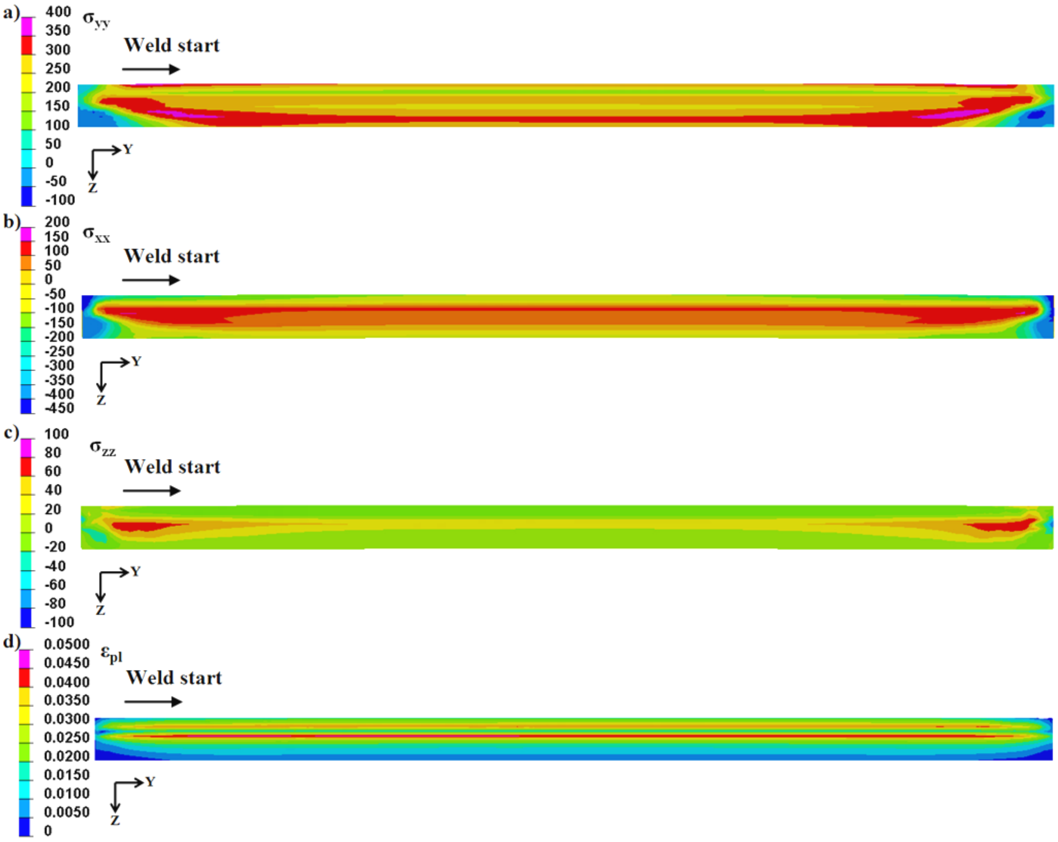

Figure 4.36 Distribution of residual stress components on the longitudinal plane: a) longitudinal, b) transverse, c) normal, and d) equivalent plastic strain field

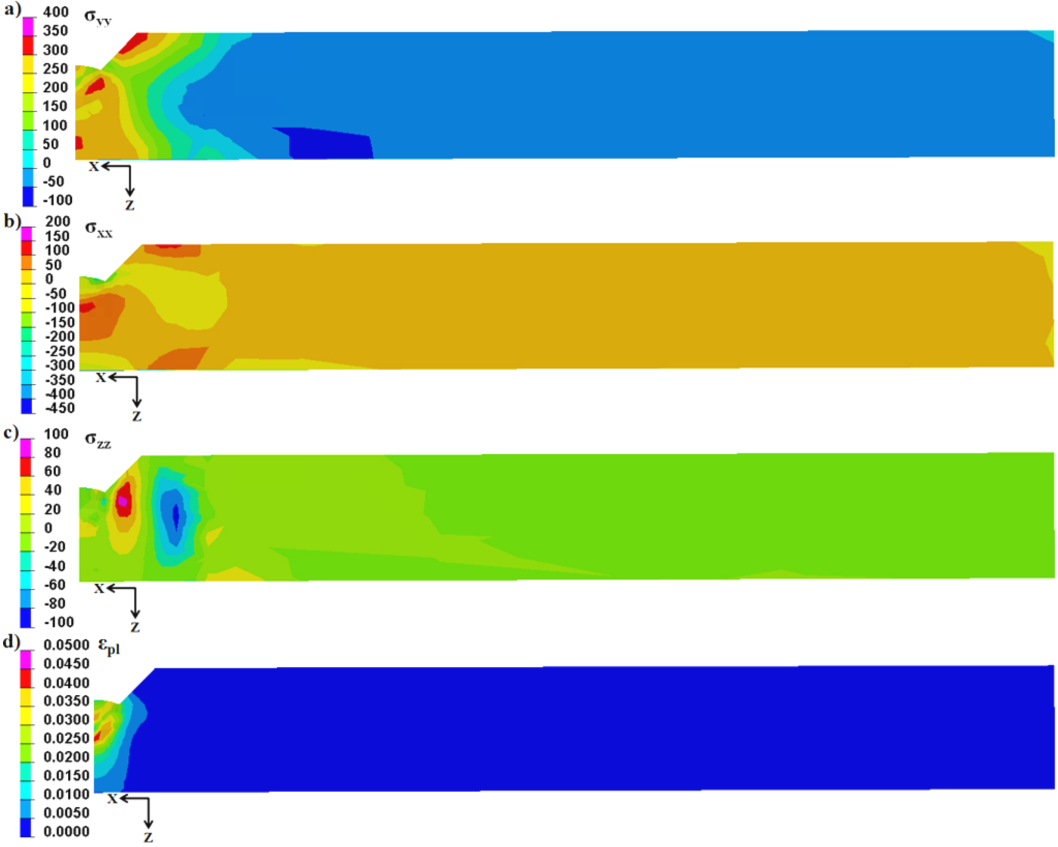

Figure 4.37 Distribution of residual stress components on the transverse plane: a) longitudinal, b) transverse, c) normal, and d) equivalent plastic strain field

In the transverse cross-section, as shown in Fig.4.37 the high tensile stresses near the fusion boundary are equilibrated by the compressive stresses in the body of the plate. Fig.4.38 displays, that the peak tensile stress is always found in the longitudinal direction (σ_{yy}) at all levels of the thickness. Excepting the edges, at the upper layers of the plate just under the weld bead, as longitudinal, so transverse stresses are tensile along the weld bead. At the bottom surface (Fig.4.38c), transverse stress σ_{xx} is completely compressive. As regards normal stress σ_{zz}, it introduces light tensile stresses in the upper regions and equals to zero at the bottom plane. Stress peaks are located near the edges of the plate, where weld pass starts and finishes. Stress components are distributed symmetrically around the weld centerline. Generally, the formed stress state in the welded component can be characterized as tri-axial.

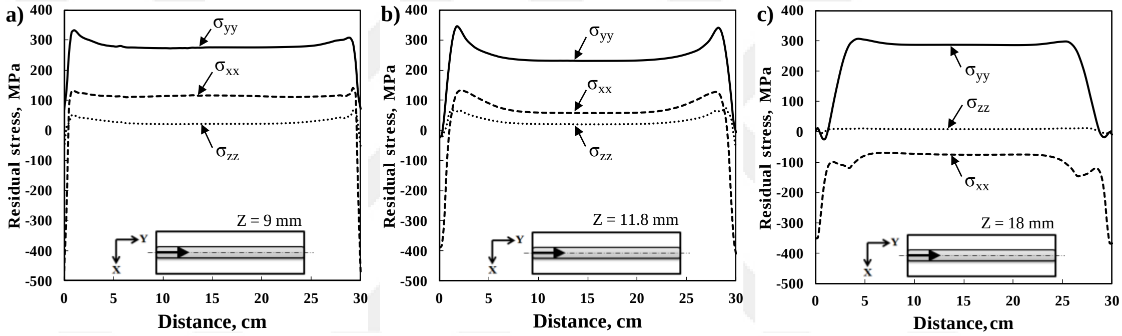

Figure 4.38 Residual stress components for one-pass weldment at different depths in the longitudinal direction of the plate

Fig.4.39 shows residual stress components profiles at the different depths of the plate under the weld bead at mid-way in the transverse direction. The maximum tensile stress σ_{yy} is located in the weld bead zone and reaches 297 MPa (Fig.4.39a), transverse stress σ_{xx} is 132 MPa and normal stress σ_{zz} is 58 MPa. Stresses are in moderate level and taking into account that yield strength of the weld metal is 507 MPa, and maximum von Mises stress is 222 MPa, the region is in safe state. In the bottom plane (Fig.4.39c), situation does not differ too much − longitudinal stress σ_{yy} is again dominant, transverse stress σ_{xx} from the positions of equilibrium shifts to compressive values.

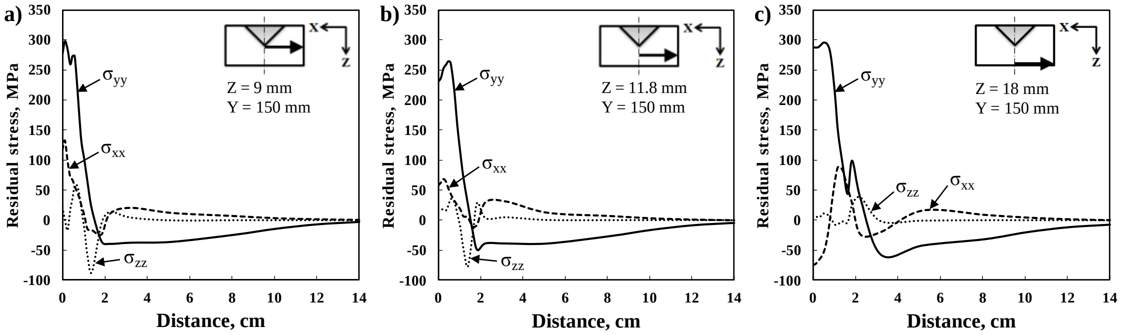

Figure 4.39 Residual stresses components for one-pass weldment at different depths in the transverse direction of the plate

Profiles of stress components as function of distance through the plate is presented in Fig.4.40. At the weld start (Fig.4.40a), the highest tensile stress is in the root of the weld bead, longitudinal stress σ_{yy} is 67 MPa. But transverse stress σ_{xx} reaches the values of -494 MPa in the weld bead, increasing the risk of damage. Resembling situation is observed at the weld end as well (Fig.4.40c), where σ_{yy} is 71 MPa, and compressive σ_{xx} is -488 MPa, respectively. In the weld pass center (Fig.4.40b), situation is different, namely, longitudinal stress approaches to the values of 302 MPa in the lower part of the plate, 275 MPa in the WM/BM boundary and 296 MPa at the top surface of the weld bead. In regard to the transverse stress, its upmost magnitude is 116 MPa. Distribution of the normal stress σ_{zz} is approximately the same for all cases, more stable in the center of the weld, the highest magnitudes lie in the range: at the end side -80 MPa and 38 MPa in the center. Summarizing, the most critical zones are at the weld start and end sides where σ_{xx} is highly compressive.

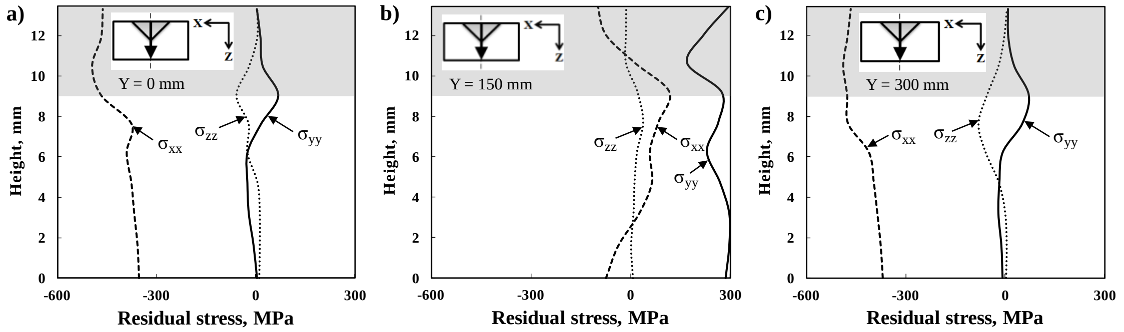

Figure 4.40 Residual stresses components for one-pass weldment at different lengths in the normal direction of the plate

Equivalent plastic strain distributions along the different paths are plotted in Fig.4.41. Profiles from perpendicular to the weld pass plane can be seen in

Fig.4.41a-c. Variations in the weld start and end sides are relatively low than that in the center of the weld. High value zones are located directly under the weld seam, and make about 1-1.3% in the plate edges and 3.9% in the plate center (Fig.4.41b). Due to V-groove geometry used, the peaks are lightly shifted from the centerline. At the bottom surface local peaks of plastic strain are also observed, and this is explained by the influence of clamping. The development of plastic strains in longitudinal direction (Fig.4.41d) indicates the levels of plastic strains as follows: about 1.6% in the root of the welding, 2.7% lower in the body of the component and 0.6% in the bottom surface. So, HAZ is expectedly the most influenced zone. Profiles in through thickness direction (Fig.4.41e) point at two peaks in the WM body (4.1%) and in the HAZ (4.5%). The reason of first one is weld pool approach and of the second one is phase transformation as it was already mentioned earlier. The start and end side profiles repeat this behaviour in less values. Maximum in the start side is 1.4%, and that in the end side is 1.9%.

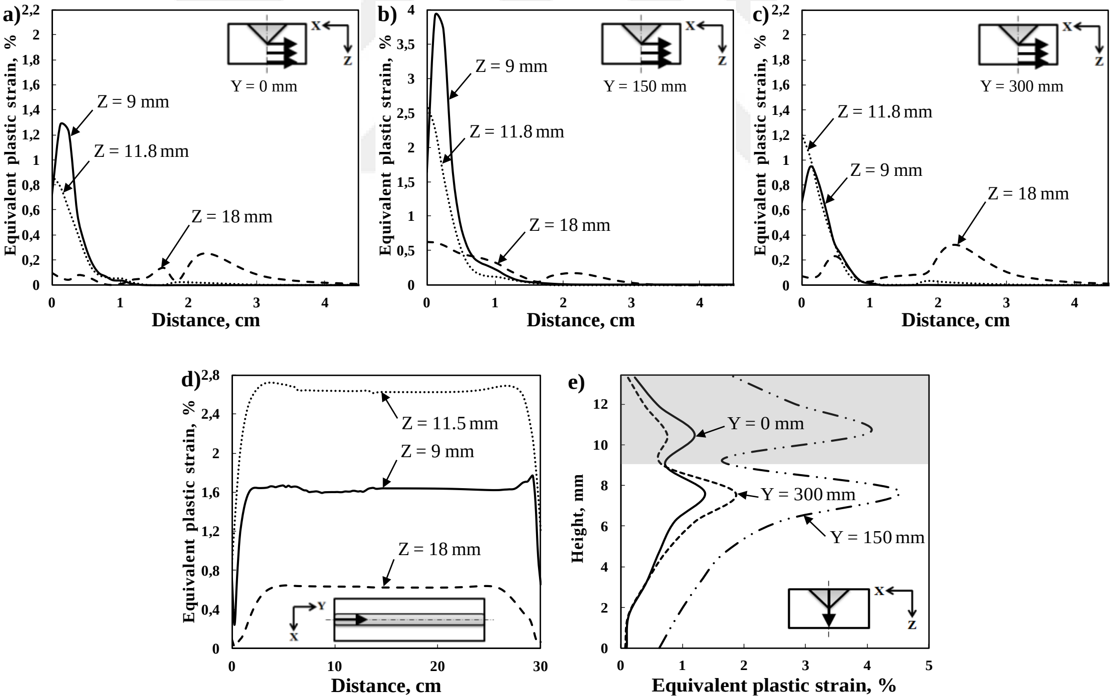

Figure 4.41 Equivalent plastic strain distribution for one-pass surfacing weldment: a) weld start; b) midway; c) weld end; d) along the weld; e) through-thickness

Development of transverse and longitudinal stresses in time at different points from cross-section area of the weldment at the weld midway are presented in Fig.4.42.

Before the parent material melts, it undergoes a loading from compressive wave coming from approaching weld bath consisting of expanded liquid metal. Melted material in the weld bath, is completely stress-free. With beginning of WM solidification, metal cools and a consequent austenite-bainite phase transformation occurs, and thus, material endures tension-contraction-tension cycle in both transverse and longitudinal directions resulting in final tensile transverse and longitudinal stress. Below the melted zone (approximately 11.8 mm below the root of V-groove), the metal of the plate passes through a heating-cooling cyclic process. Before heat source reaches the mid-length of the weld pass, the parent material undergoes light tensile stress (about 50 MPa) in the transverse direction and moderate compressive stress (about -150 MPa) in the longitudinal direction. When the welding torch comes to the mid-way of the weld, the metal is heated and becomes subjected to the large compressive stresses both in the transverse and longitudinal directions. When the welding arc leaves the mid-length of the weld, the material begins to cool and undergoes the tensile stresses in the transverse and longitudinal directions. Thus, the transverse stress σ_{xx} undergoes a tension-compression-tension cycle caused by heat transfer. Whereas, the longitudinal stress σ_{yy} undergoes compression-tension cycle only. Need to note, that the values of the transverse and the longitudinal stresses reach to the yield stress during the period of tension. And this means the risk of cracking at the root of the welding. Deeper in the plate (from 14.8 mm below the surface), the transverse stress σ_{xx} is undergoes a tension-compression-tension cycle, and the longitudinal stress σ_{yy} is subjected only to a compression-tension cycle. Finally, at the bottom plane, the transverse stress σ_{xx} undergoes a tension-compression-tension cycle, and the longitudinal stress σ_{yy} endures a compression-tension-compression-tension cycle; and tensile longitudinal stress dominates in final residual stress pattern.

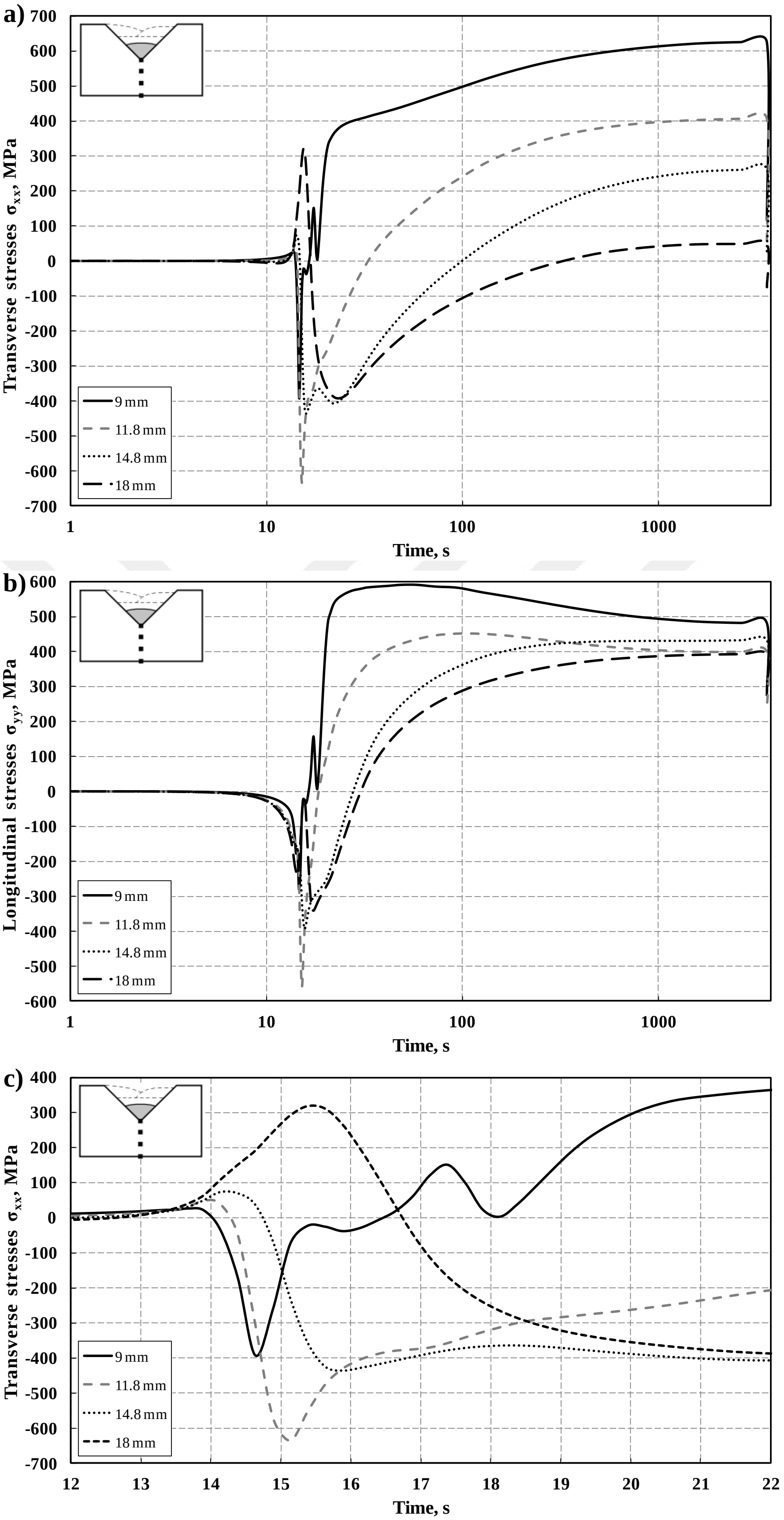

Figure 4.42 Stress development at various points in through-thickness direction

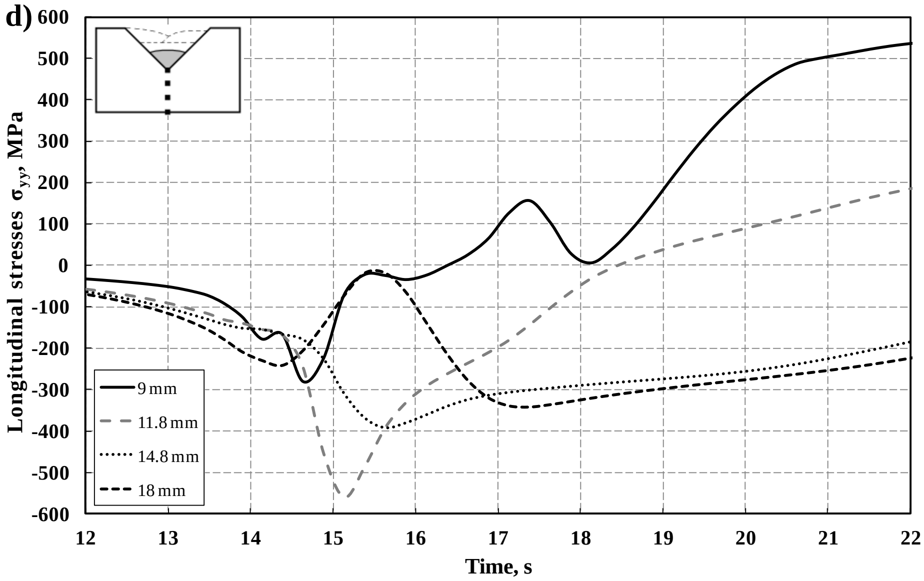

Figure 4.42 Stress development at various points in through-thickness direction (continued)

Phase transformation effect on the stress development at the WM during the welding thermal cycle which is imposed on the same plot is shown in Fig.4.43. The start of ferrite phase from 66% is explained by the mesh configuration when the node at a root of weld is shared by 4 elements of BM and by 2 elements of WM which is in status "yet not deposited" before welding (Fig.4.6(1)). Initially, the parent material of the plate consists of ferrite phase. With approaching of the heat source and increasing the temperature, a transformation from ferrite to austenite is observed just before melting. After complete solidification, austenite phase exists, and with cooling to approximately 800°C the austenite-bainite transformation starts and finishes at about 500°C.

In the lower figure, corresponding to the described phase transformations, stress peaks are displayed. First one occurs between 14 and 15 s, the second one occurs between 17-18.5 s. Simultaneous development of the all stress components at the peaks indicates to the volumetric character of the process and confirms its relation to the phase transformations.

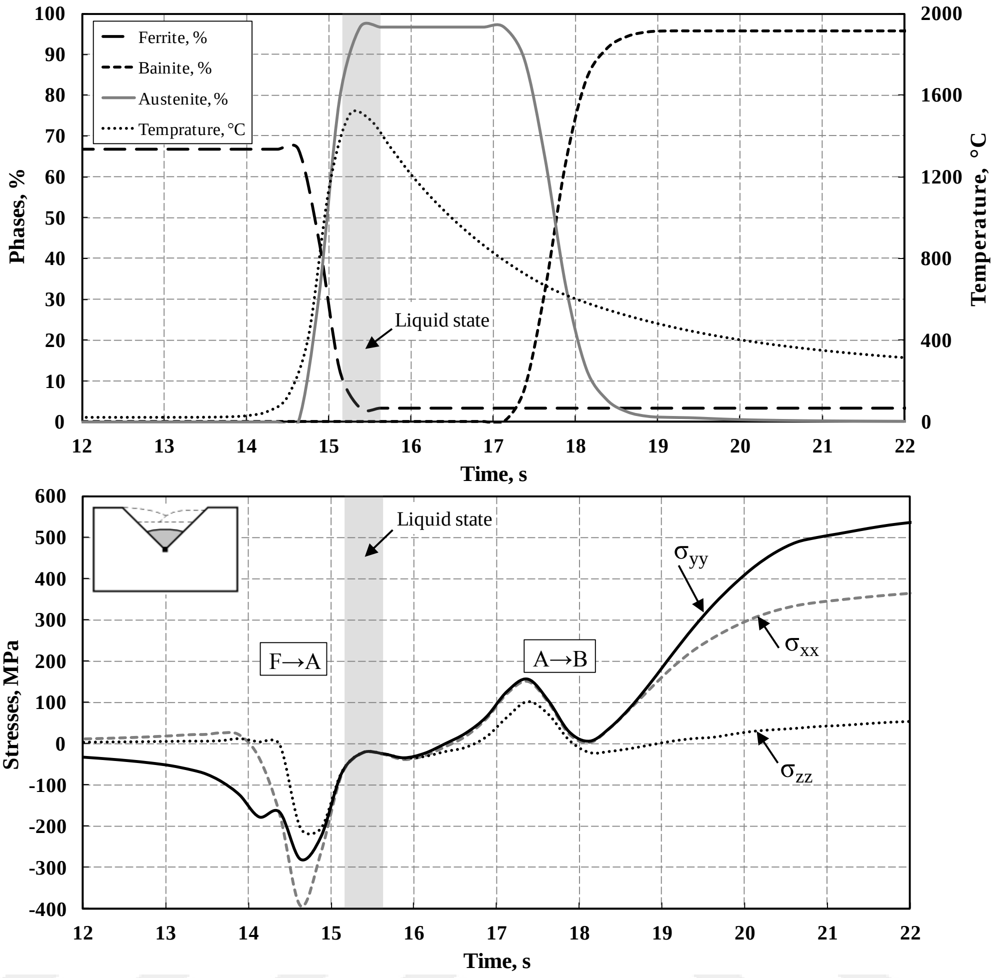

Figure 4.43 Influence of phase transformations on stress evolution

The change of sign of stress over time is the principal characteristic of transient internal stresses during the process of intense cooling when large difference of thermal and phase deformations excites plastic deformations in the material. At the beginning and at the end of the cooling process, the temperature of the components is the same, therefore the greatest difference of strain occurs at intermediate time points. If in these moments stresses are so big that plastic deformation appears, then it leads to a change of sign of the stress. In more complex cases the change of sign of stress can happen several times [15].

4.4.2 Multi-pass welding on V-groove

The influence of multi-pass welds on residual stress field has been widely investigated accounting different aspects. Yaghi et al. [94] studied the effect of the ratio of the pipe radius to its wall thickness and number of beads on the residual stresses.

Detailed analysis of the stress, strain and deformation evolution (strain, distortion) through the process of multi-pass welding by FE modelling will be given in this Subsection. The FE model and its arrangement of weld passes are shown in Fig.4.6, FE statistics of the meshes is presented in Table 5. Applied welding process parameters were identical to that employed in natural experiments and verified by test calculations in Section 4.3. Inter-pass temperature was kept 205°C and unclamping applied at complete cooling of the component to RT.

To clarify the influence of additional weld passes during multi-pass welding, four simulation cases with 1-, 3-, 5- and 8-pass weldings were performed in this study.

Fig.4.44 illustrates distribution of residual stress components obtained in each case. As can be seen, the most effect from 1-pass welding is experienced by bottom surface. Tensile longitudinal stress is reaching 298 MPa under the weld bead, and transverse stress is compressive under the weld zone and tensile under the HAZ. At the upper surface, transverse stress is tensile near the V-groove edges and exceeds longitudinal stress. For 3-pass welding, at top surface tensile longitudinal stress is prevailing over the transverse and reached 306 MPa, transverse stress is almost unaltered. As for bottom surface, longitudinal stress is evidently decreased till 263 MPa and transverse stress becomes more uniform and less in value than in 1-pass case. After 5-pass welding, on the upper surface there is no significant change, but on the bottom surface there is considerable reduction in the utmost magnitude of longitudinal stress till 154 MPa. Whereas, transverse stress show growth in the zone under the weld seam. Finally, after 8-pass welding on the top surface some increase of transverse stress is noticeable and the zone of high tensile longitudinal stress narrowed till the range of V-groove edges. As o the bottom surface, maximum tensile stresses under the weld pass are of 117 MPa in the x-direction and that in HAZ are of 125 MPa in the y-direction. Thus, transverse and longitudinal stresses appear to be almost equal in values. In all considered cases, the longitudinal stresses are compressive and transverse stresses are tensile far away from HAZ. Thereby, reduction in tensile longitudinal stress for considered cases: after 3-pass welding is 12%, after 5-pass welding 48% and after 8-pass welding 58%. Such stress relief is inherent for multiple pass weldings due to partial heat treatment from the welding of consequent beads.

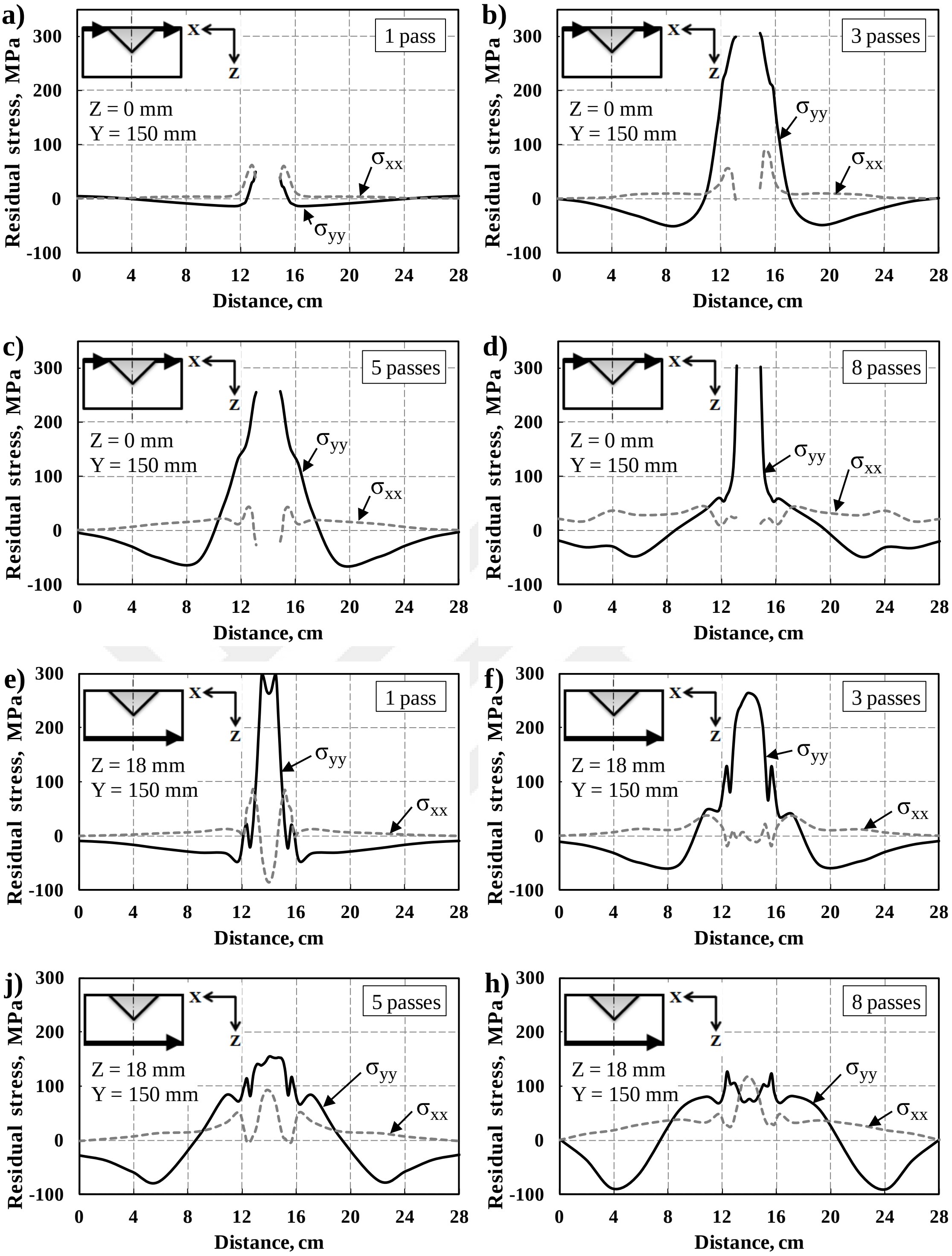

Figure 4.44 Distribution of σ_{xx} and σ_{yy} residual stress components in the transverse direction at midway section

Distribution of the same stress components at the bottom surface in longitudinal direction along the weld centerline is plotted in Fig.4.45.

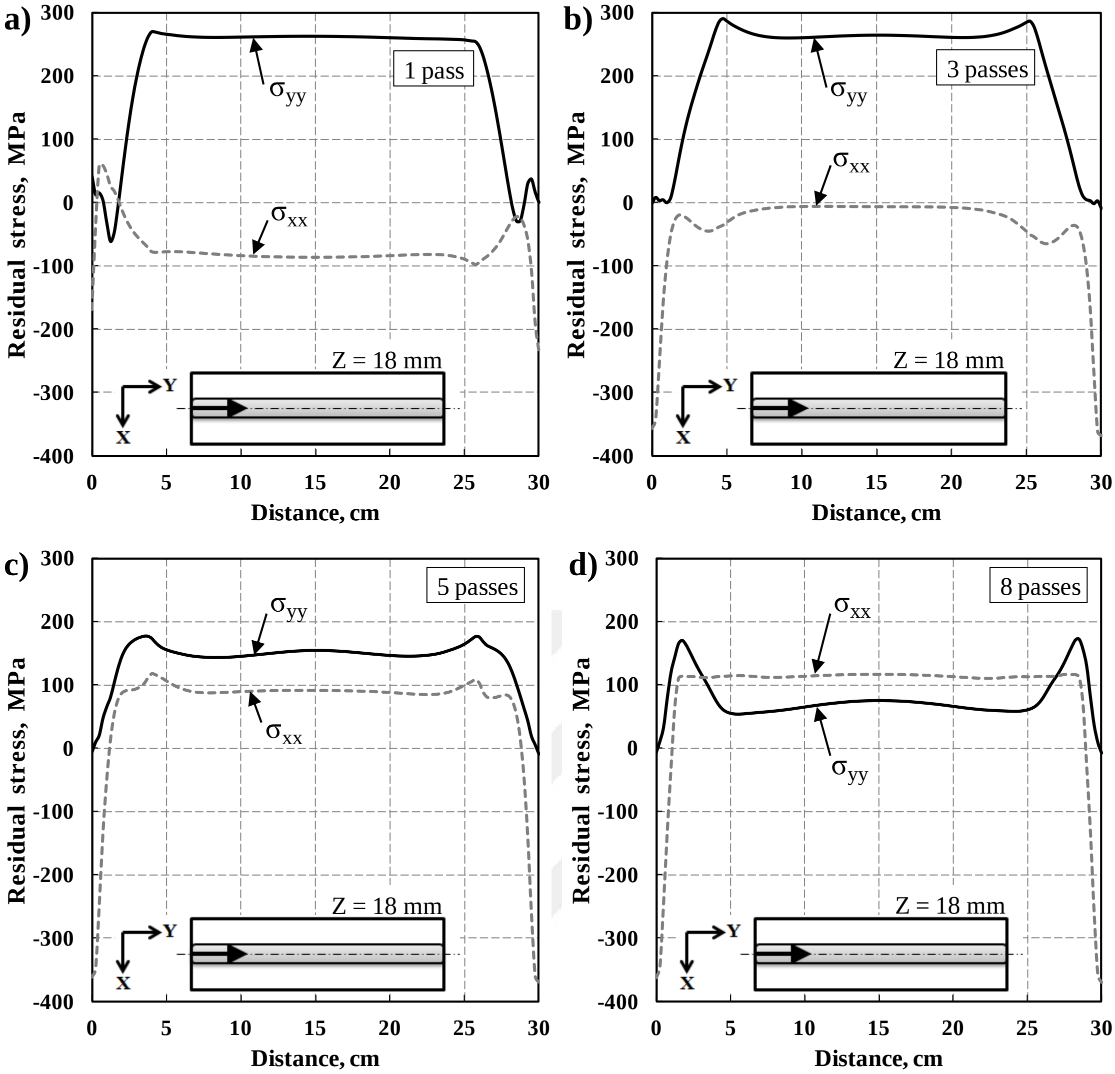

Figure 4.45 Distribution of σ_{xx} and σ_{yy} stress components in the longitudinal direction at midway section

For all cases, distribution of stresses is uniform in the middle part of the plate. Also, plate border influence is apparent of about 60 mm, as it was discussed earlier and shown in Fig.4.34. Except the 1-pass weldment, in all other cases longitudinal stress is always tensile and high compressive transverse stresses are observed at the edges of the plate, and its magnitude is almost constant at -360...-370 MPa independently of weld pass quantity. Worth to note, that transverse stress profile show peaks at the plate edges in 1-pass welding which are diminishing with addition of weld passes, and at 8-pass welding there is no peaks; whereas, longitudinal stress profile is flat at upper part and with weld pass addition it shows considerable peaks at the plate edges. Most probably, this happens from positions of maintaining of equilibrium.

Fig.4.46 demonstrates development of longitudinal stress in through-thickness direction and according to it normalized stress profiles.

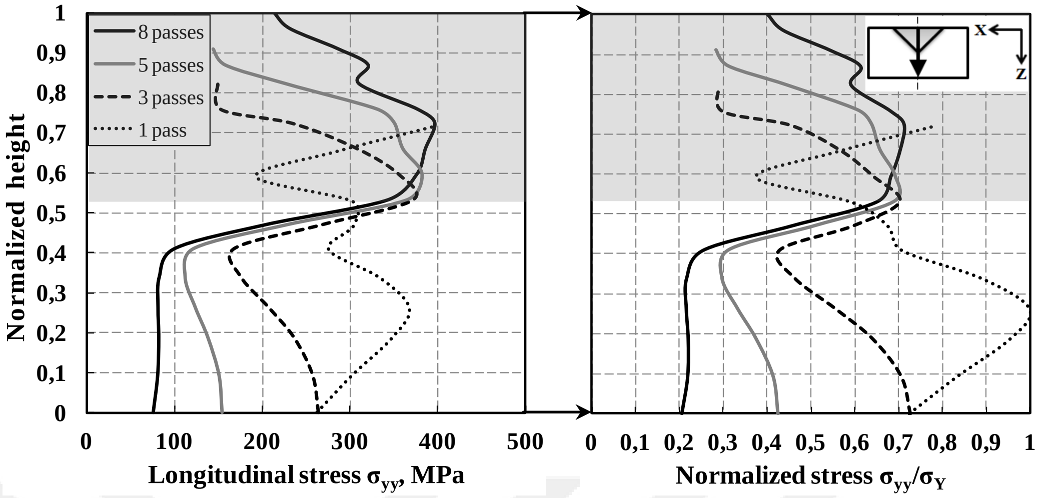

Figure 4.46 Through-thickness distribution of residual stresses
for 1-, 3-, 5- and 8-pass separate weldments with interpass temperature 205°C

The most dangerous situation is observed for 1-pass welding since under the weld bead in the body of the plate a combination of high tensile stress and low yield strength of unhardened plate material takes place. Next weld passes partially relief tensile stresses in the plate and shift it to the weld bead region where material is hardened and, thus, yielding risks reduce. Ponomareva [95] has also got a shift of residual stresses deep inside the weldment during multi-pass welding of 7.3-33.4 mm API X80 HSLA steel if number of passes is higher than 4-5 weld beads. Alipooramirabad et al. [96] reported about the decrease of residual stresses with weld depth due to tempering effects of the later weld passes onto the earlier weld runs.

Development of plastic strains as function of weld passes is displayed in Fig.4.47. At the bottom surface, with increasing the weld pass number the amount of plastic strain does not grow, but the range of the influenced zone is broaden (Fig.4.47a). Also, the geometry of V-groove slightly moves the peaks to the side when last passes are welded. At the top surface, the more the pass quantity the higher and wider the zone of plastic strains (Fig.4.47c). In the longitudinal direction at the bottom of the plate, the effect of plate edges is also noticeable and peaks are higher with bigger number of passes (Fig.4.47b). In through-thickness direction, the plastic strains unchangeably overlap in the plate with each weld pass (first peak) till about 5%, but in the weld metal due to the melting-solidification cycles amount of plastic strain decreases (second peak).

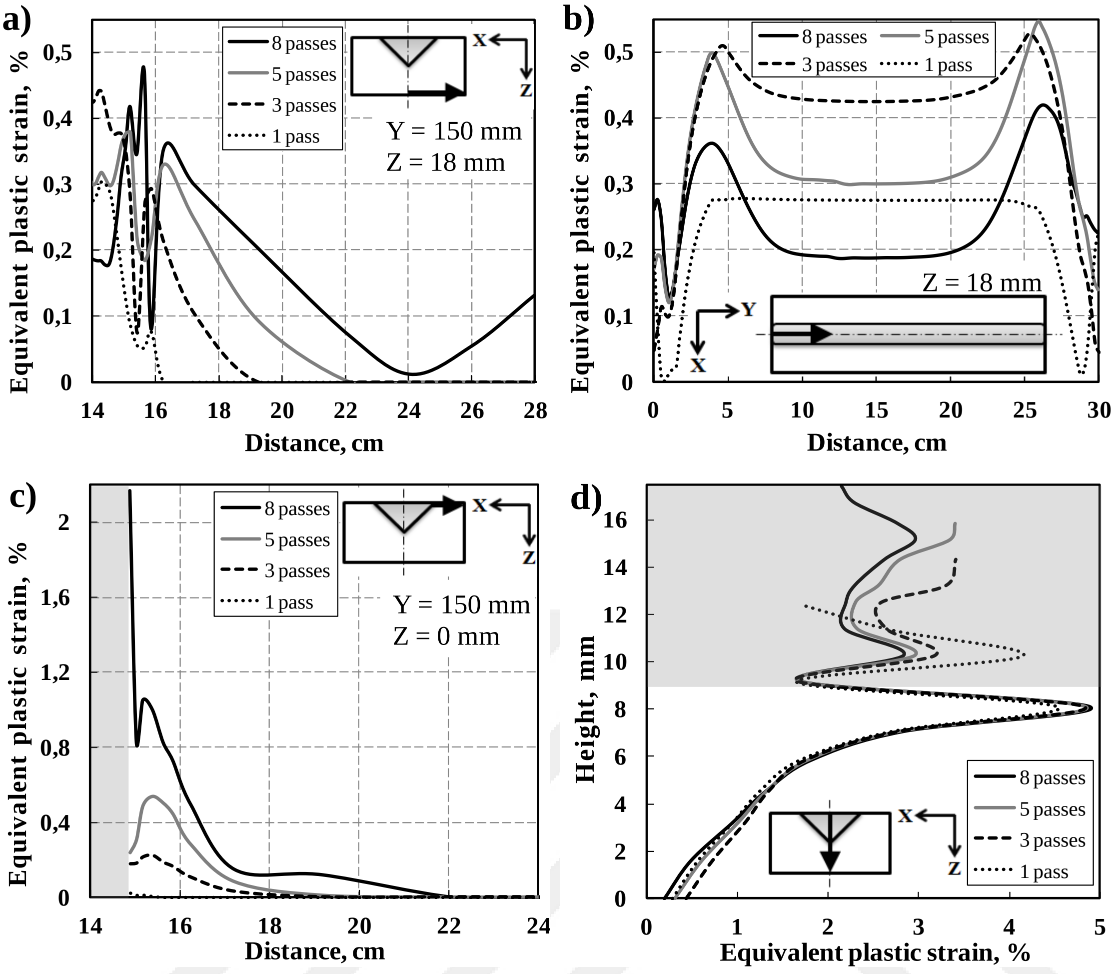

Figure 4.47 Distribution of equivalent plastic strains

Fig.4.48 shows displacement profiles in longitudinal and transverse direction. Here, further used terminology should be clarified (Tabl.4.4). Rotational distortion and buckling modes are more complicated cases, characterized by uneven profiles in space and therefore are not presented in Tabl.4.4.

Table 4.4 Distortion components and their physical meaning

u_{xx}	Transverse distortion (shrinkage/expansion)
u_{yy}	Longitudinal distortion (shrinkage/expansion)
u_{zz}	Angular distortion (in the transverse direction)
	Bending distortion (in the longitudinal direction)
u	General displacement, overall distortion $\sqrt{u_{xx}^2 + u_{yy}^2 + u_{zz}^2}$

Part distortion and change in shape is caused by plasticity due to thermal gradients, transformation plasticity and phase transformations. Increasing the pass quantity with corresponding increasing heat influence to the component raises the overall distortion of the plate. If after first weld pass which is positioned straightly along the weld centerline, distortion is symmetrical, then after consequent shifted beads laying the plate inclines more evidently. The highest displacement after 1-pass welding is explained by its relative proximity to the bottom surface where the measurements are taken from. Following weld passes are located higher to the top and their effect is smoothed, though after 8-pass welding this effect disappears and distortion again increases.

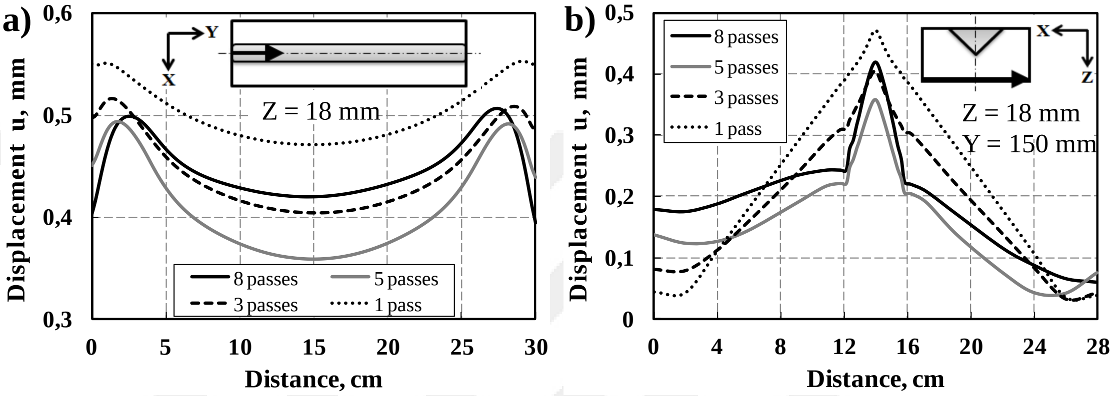

Figure 4.48 Displacement profiles in the longitudinal and transverse directions

As it is seen, for the case of one-pass welding a post-weld heat treatment is necessary, and for multi-pass weldings PWHT is performed in part by the heat from consequent weld passes. Ponomareva [95] have concluded about residual stress relief effect upon following weld passes and about the absence of necessity to apply PWHT after 16-pass welding of 33.4 mm X80 pipeline steel.

Besides, a comparative study have been performed concerning the welding of the same V-groove by three different weld modes: as 2-, 4- and 8-pass welding. Parameters of the welding procedures are the same as presented in Table 3 and verified in Section 4.3. Interpass temperature was kept in the range of 200±5°C.

Fig.4.49 demonstrates obtained profiles of longitudinal stresses on the bottom and top surfaces. For all cases as at the upper so at the lower surfaces, longitudinal stresses are tensile in the middle zone and compressive in the direction to the sides of the component. Analysis shows that there is no significant difference among considered cases since parameter of heat input per pass is relatively proportional. Namely, heat input of 2-pass welding (1.008 kJ/mm) is about twice higher than that of 4-pass welding (0.587 kJ/mm) and, accordingly, about four times higher than that of 8-pass welding (0.335 kJ/mm). Certainly, the heat dissipation and losses should be taken into account because cumulative time of welding the same V-groove also increases: 45 s x 2 passes = 90 s, 30 s x 4 passes = 120 s, 22.5 s x 8 passes = 180 s.

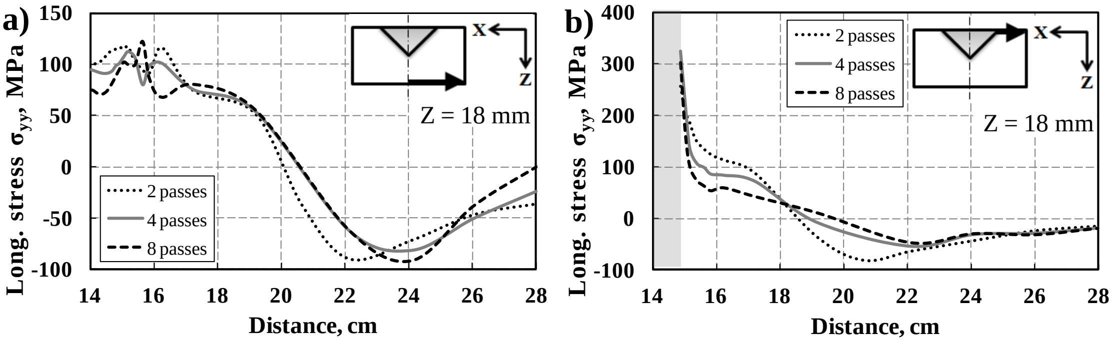

Figure 4.49 Distribution of longitudinal residual stresses on the bottom and top surfaces of the welded plates

Sattari-Far and Farahani [86] reported that the weld pass number has no significant effect on residual stress distribution in the outside surface (weld reinforcement side) of 6mm butt-welded pipes, and hoop residual stresses (along the weld bead) in the inner surface (weld root side) significantly decrease when pass number increases.

In regard to equivalent plastic strain distributions (Fig.4.50), greater values are observed under the weld zone for 2-pass welding due to higher heat input and resembling profiles for 4- and 8-pass welding. In through-thickness direction, again proportionality in accord with the heat input is evident in plastic strain fields in the body of the plate, and distributions of the plastic strain in the WM of the same range.

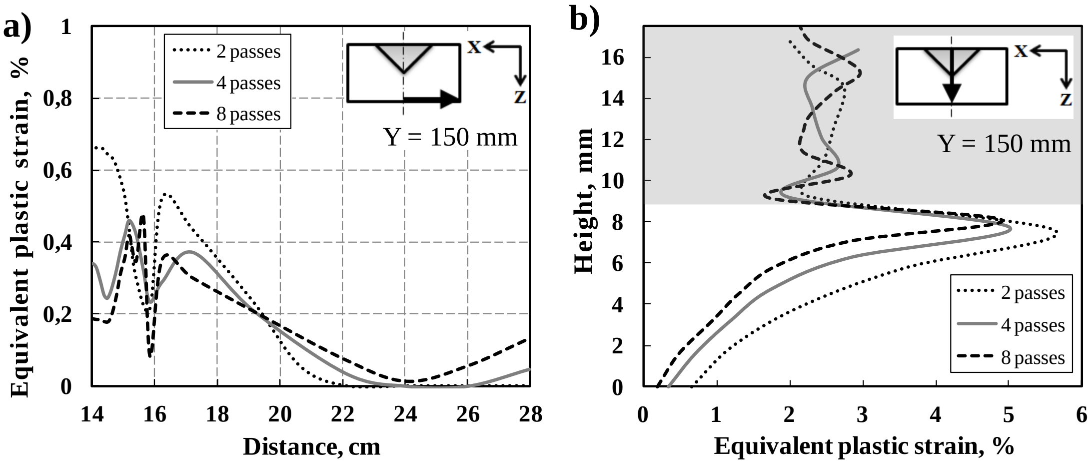

Figure 4.50 Distribution of equivalent plastic strains

Evolution of microstructure is presented in Fig.4.51. The main phases in the numerical models are ferrite in the BM and bainite formed in the WM, also very low amounts of martensite may appear in the WM. The higher heat input per pass of 2-pass welding process broadens the zone of the phase transformations deep inside to the plate (Fig.4.51a). And, relatively high cooling rate of 8-pass welding process gives reasonable rise of martensite fraction in the weld root (Fig.4.51b). Definitely, martensite development should be taken into account at comparative studies of multi-pass welding regimes when martensite formation is considerable.

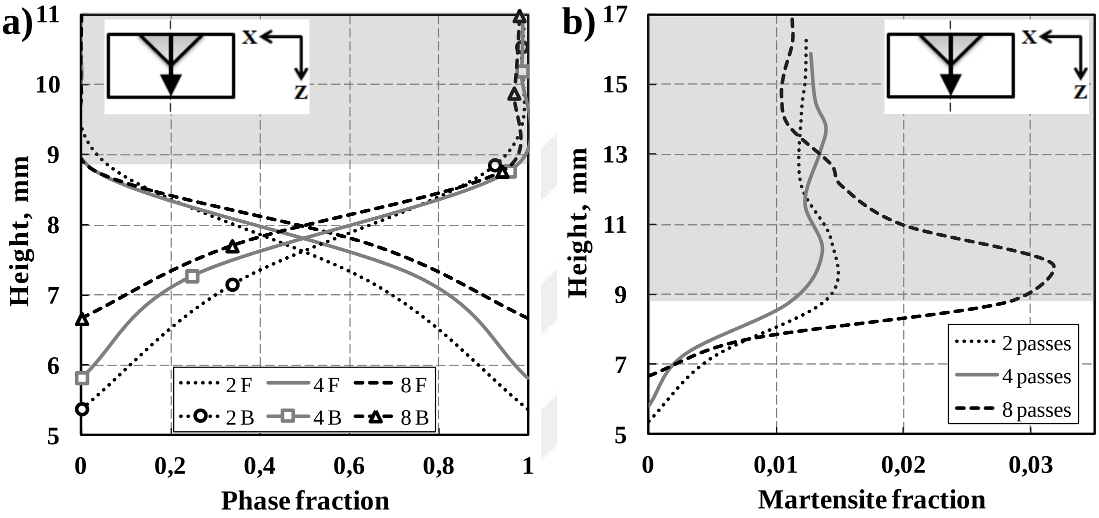

Figure 4.51 Phase fractions at midway sections of the plates

Summing up, weld pass addition in the multi-pass weldings changes the stress-strain state and distortion of the components. Along with that, in conditions of appropriate welding parameters and interpass temperature 200±5°C, there is no significant difference in the number of passes if the same geometry of weld joint is considered.

In multiple-pass welds, a portion of the previous weld pass is refined, and the toughness improved, as the heat from each pass tempers the weld metal below it. If the beads are smaller, more grain refinement occurs, resulting in better notch toughness, all other factors being even [57].

4.4.3 Effect of unclamping temperature

Effect of unclamping temperature on residual stress state has been studied on the welded plate with two passes. Interpass temperature was kept on 195°C. Cases of plate unfix at 89°C, 56°C, 33°C and 25°C temperatures have been studied (corresponding to unfix time of 10, 20, 40 and 60 minutes). According to obtained results, clamp release temperature turns out to be important factor in further functionality of the weldment; early unclamping is not recommended since leads to elevated tension residual stresses.

Fig.4.52 demonstrates the change of longitudinal residual stress profiles in the middle length of the plate in dependence of unclamping temperature. The general behaviour in all cases is similar − tensile stresses in the middle part of the component and compressive stresses far away from HAZ. At the bottom surface, near the centerline the maximum value of the tensile stress is 253 MPa for 89°C, and 117 MPa for 25°C, that means reduction in stress is 53% (Fig.4.52a). At the upper surface of the plate, resembling behaviour is observed and decrease of stress values, as well (Fig.4.52b).

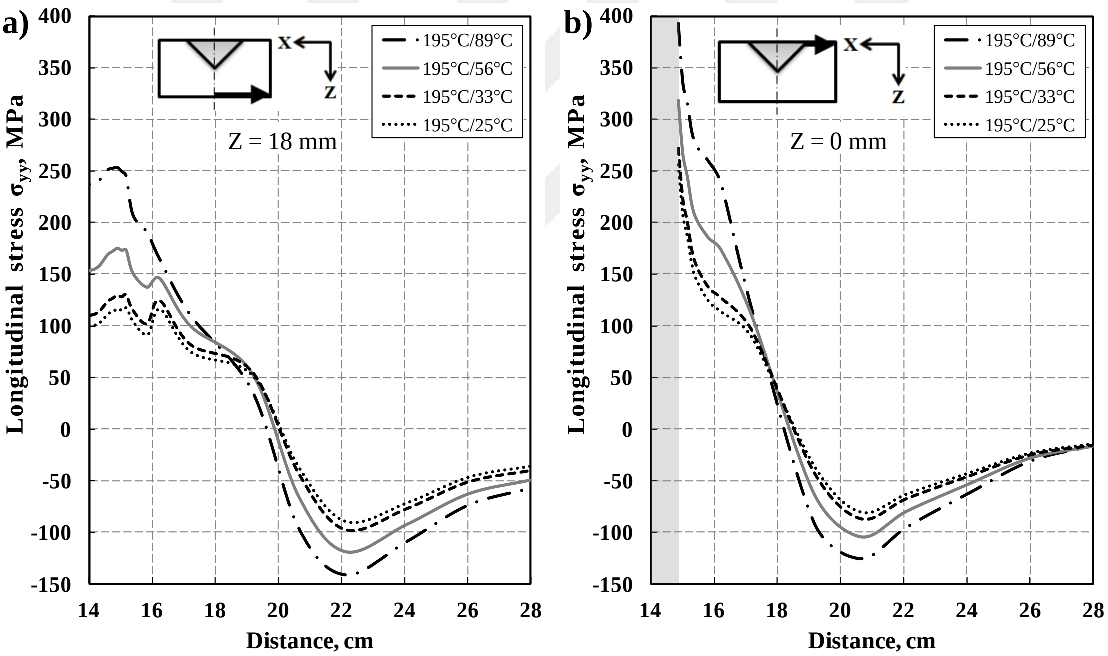

Figure 4.52 Effect of unclamping temperature on residual stress distribution in transverse direction (2-pass weldment)

Fig.4.53 displays distribution of longitudinal residual stresses in normal direction in the middle of the plate. For all cases, behaviour is again similar, but stress magnitudes are lower as lower the unclamping temperature. The highest tensile stresses are located in the welded zone with mitigation trend in direction to the weld bead surface.

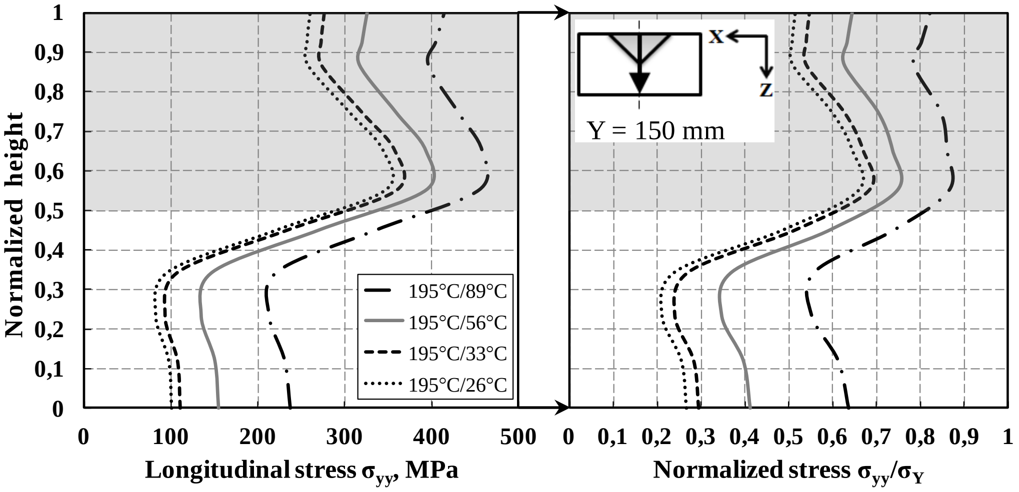

Figure 4.53 Effect of unclamping temperature on residual stress distribution in through thickness direction (2-pass weldment)

Plastic strain profiles are shown in the Fig.4.54a and the only difference is magnitudes under the weld bead zone. Early unclamping leads to increased plastic strain. Need to note, that the values for the deeper layers, more close to the weld seam, exhibit much higher levels of plastic strain. Here, the bottom surface is chosen just due to more uniform distribution of plastic strain fields.

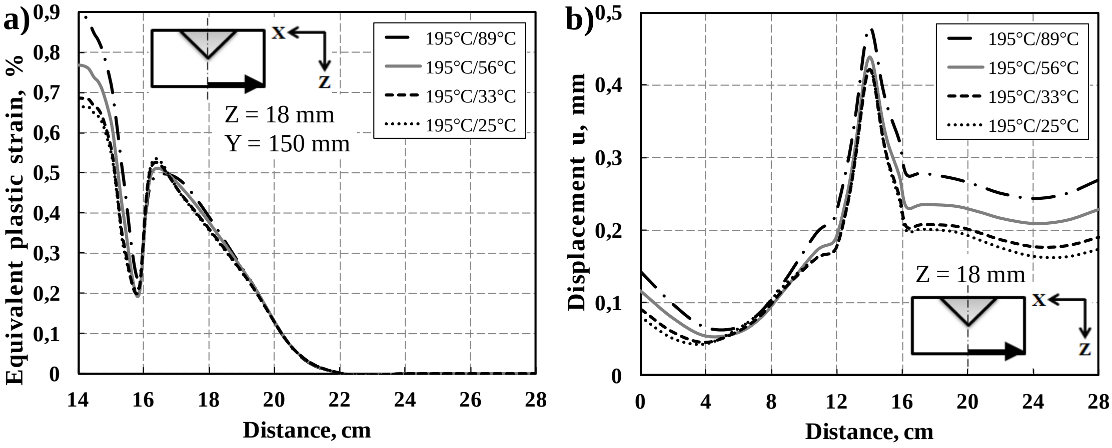

Figure 4.54 Distribution of equivalent plastic strains and distortion profiles (2-pass weldment)

In Fig.4.54b effect of unclamping temperature on the final distortion is presented. Evidently, the "hotter" unclamping causes elevated displacement of the component. For considered model, unfixing at 89°C and at 25°C leads to reduction in distortion of the plate side of about 35-40%.

In order to better understand the dynamics of the process for "hot" and "cold" unclamping, additional calculation for the first pass of 4-pass welding with unclamping at 92°C, "hot" case, have been performed to see the stress and the strain developments. Unclamping for the "cold" case has been measured as 25°C (Fig.4.56). Need to mention, that the closest node of bottom clamp group goes through upmost 109°C during the welding procedure and in this conditions clamps nodes rigidity in modelling sense plays no harmful role.

For controlling the tendency, the distributions of residual stress components are illustrated below in Fig.4.55. The most influenced is the longitudinal stress, as for transverse stress even if not much, but is influenced as well − both components diminish with "colder" release from restraints.

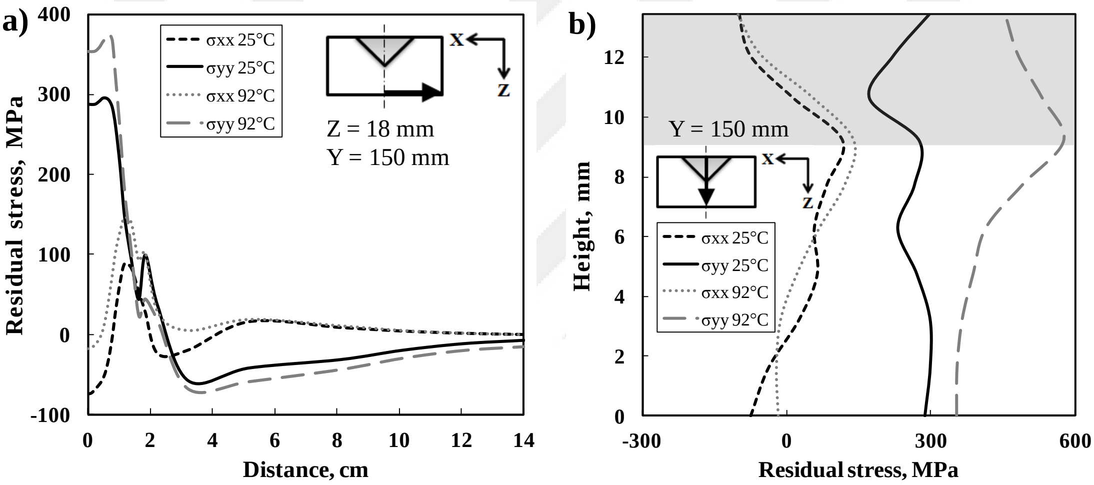

Figure 4.55 Distribution of residual stress components (4-pass weldment)

Longitudinal stress history for different points along the through-thickness direction is given in Fig.4.56. Straight lines indicate "cold" unclamp at 25°C, dashed lines related to the "hot" unclamp at 92°C (at 100 s). For the WM and HAZ, there is a slow stress reduction to about 50-150 MPa is observed in clamped position, whereas, for the material of the plate, stress continues slow increasing.

By the way of an example of the rod with the ends embedded in the absolutely rigid planes which in reality represents parts of the design that are not subjected to temperature influence, it is demonstrated that thermal stresses eventuating even at small temperature differences turn out to be quite significant. In conditions of constraints of the total deformations, thermal stress equal to the yield strength may be achieved even by heating to about 100°C. During the solidification process of the molten metal, intensive growth of residual stresses occur at lower temperature ranges when elastic modulus and yield strength increase [15].

Residual stresses are known to be self-equilibrating over the entire structure. Obviously, residual stresses in clamped component undergo relaxation process when system in non-equilibrium state returns to equilibrium through the slow decreasing of stresses with time in constantly deformed body when elastic strains partially convert to plastic strains.

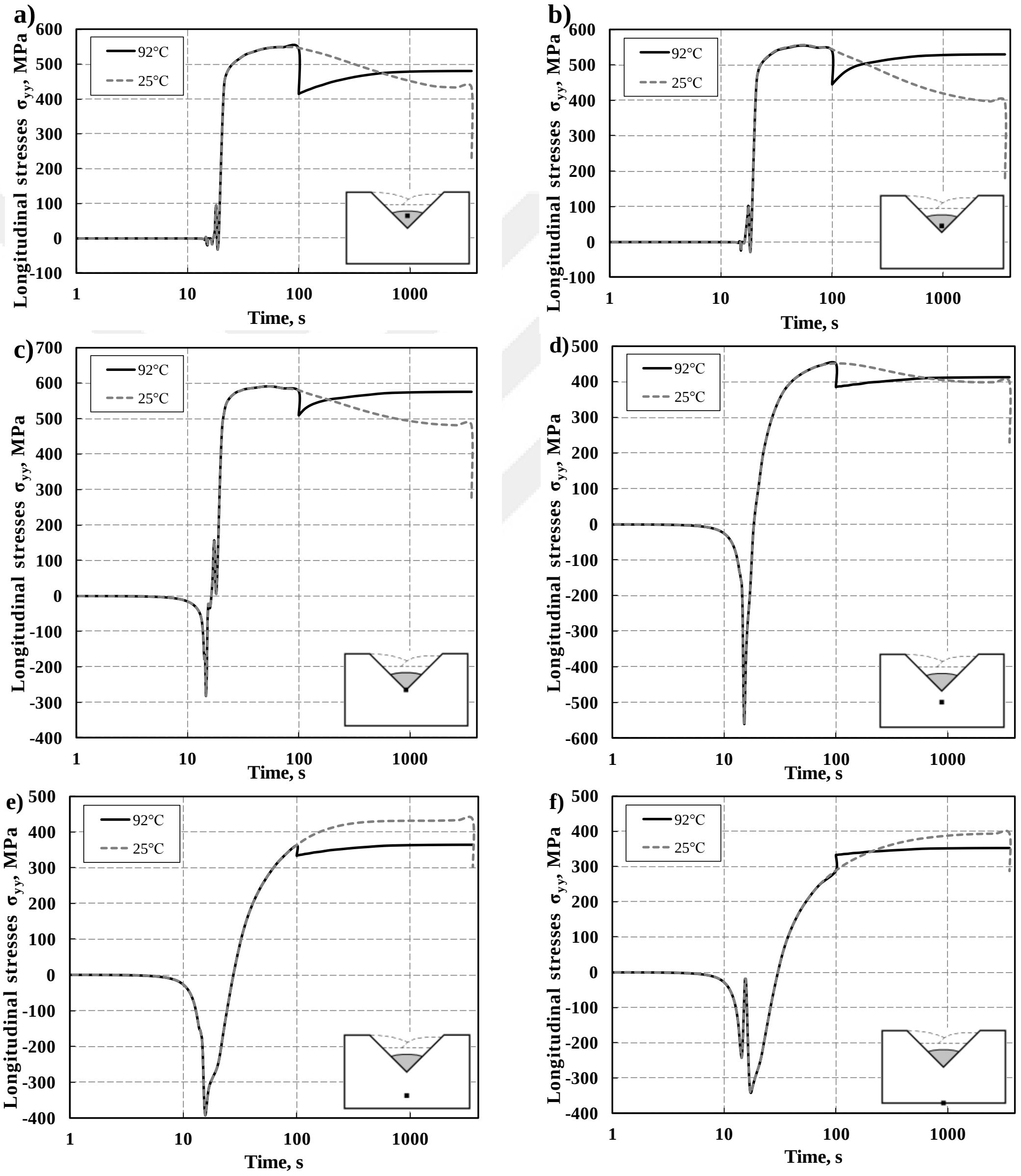

Figure 4.56 Stress development at points in through-thickness direction

For considered cases, this is completely proved in Fig.4.57 (0 mm is the bottom surface as in Fig.4.55). Black lines indicate strain development in the material of the component which did not pass melting-solidification cycle, and grey lines belong to WM and HAZ. Indicated dimensions corresponds to that in Fig.4.55b, zero is the bottom surface. Distribution for the weld bead surface is not presented due to complication of the graph, its range lies close to 9 mm values, namely, about 1.5%. The most effect is found in the center of the weld seam, in the diapason of 10-12 mm from the bottom plane.

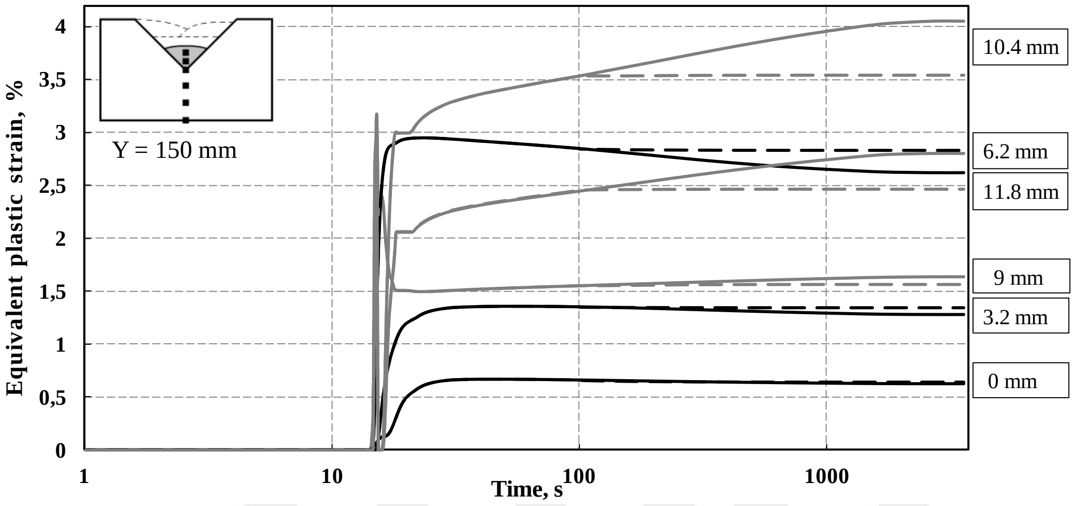

Figure 4.57 Plastic strain development at points of the mid-section

As Löhe and Vöhringer [97] note, plastic strains of several tenths of a percent maximum are produced by complete residual stresses relaxation. The onset and extent of residual stresses relaxation is influenced in a complex manner by the combined effects of heat treatment, unidirectional and cyclic stress, and multiaxial applied and/or residual stresses states.

Physically, stress relaxation is one of the types of plastic deformation, but has a number of features. Stress relaxation is characterized by two main mechanisms: 1) action of processes occurring at the grain boundaries of polycrystalline metal and representing diffusion processes and 2) action of processes running in the body of the grain and representing shear effects. More correct is to consider the stress relaxation as a result of imposition of both processes, though at high temperatures diffusion processes are dominating whereas at low temperatures shear processes are prevailing. Relaxation proceeds intensively at elevated temperatures, but happens at normal temperatures as well but at much lower speeds. Sometimes, stress relaxation leads to such unfavourable stress redistribution that under certain conditions it may cause a sudden brittle failure. Relaxation is one of the two extreme cases, the other one is creep process when plastic strain increases with time under the constant stress state (Fig.4.58). Stress relaxation phenomena should not be confused with other cases of stress relief passing in absence of constant strain.

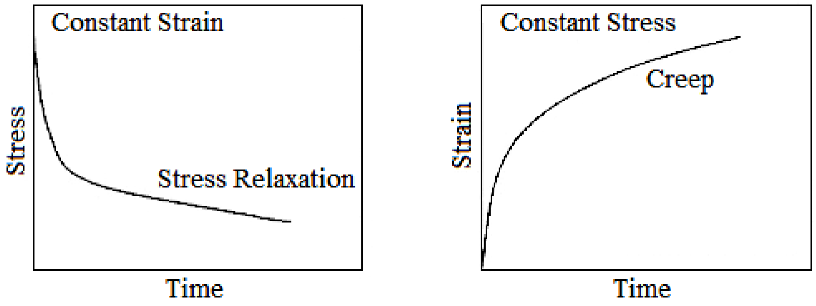

Figure 4.58 Stress relaxation and creep behaviour

Vinokurov [40] published results of the experimental and analytical investigations on post-weld stress relaxation phenomena. Holzapfel et al. [97] gave a quantitative description of the relaxation behaviour of multiaxial macro residual stresses under uniaxial deformation at 25 and 400°C for AISI 4140 with the aid of FE modelling and obtained good agreement between experimental results and FE modelling.

In the considered case, cooling from 89-92°C to steady state temperature conditions took 58 min. For the unclamping temperature of 25°C, the governing mechanism for reduction of residual stress with time is stress relaxation process that should not be ignored for multi-pass weldings.

The influence of clamping system on the material behaviour during welding was the subject under investigation in numerical study by Schenk [65], Deshpande et al. [91]. In both works, a longer clamping of the workpiece was found to reduce as residual distortion, so residual stresses after unclamping. Obtained results agree in principle with the results presented in this thesis. However, in both studies clamping release was linked to the time that can vary from sample to sample, but not to unclamping temperature, also detailed stress and strain developments were not explored and phenomena of the stress relaxation was not considered.

4.4.4 Effect of interpass temperature

A big emphasis is made on interpass temperature parameter during welding procedure development. According to Standard Welding Procedure Specification, multi-pass weld joints of HSLA steels used in pipeline systems meet the requirement of interpass temperature to be not higher than 220°C. Technology of X70, X80 steels welding employed by "Gazprom" company requires the interpass temperature to be in the range of 50...250°C and preheat of 80°C [95]. Also, Brickstad and Josefson [76] reported that the weld specifications normally specify a maximum allowed interpass temperature of 100°C or 180°C depending on the type of stainless steel.

Zondi [98] giving review on preheat and interpass temperature influences noted that both of these parameters reduce shrinkage stresses in the weld, prevent excessive hardening, slow down the cooling rate, and can therefore assist in resisting welding induced residual stresses during welding, thereby improving fatigue life of welds.

In order to clarify the effect of interpass temperature on final stress-strain state of the component, a numerical experiments were performed on the basis of 8-pass welding FE model with 80°C and 205°C interpass temperatures. Welding procedure parameters were taken from Table 3. Unclamping was done upon achieving the RT in both cases.

Temperature histories at the node from the root of the first weld bead are shown in Fig.4.59. Since plate is heated and cooled in comparatively uniform manner, temperature history of only one node is presented. As can be seen, welding procedure with 205°C interpass temperature proceeds about 5 times faster than that with 80°C.

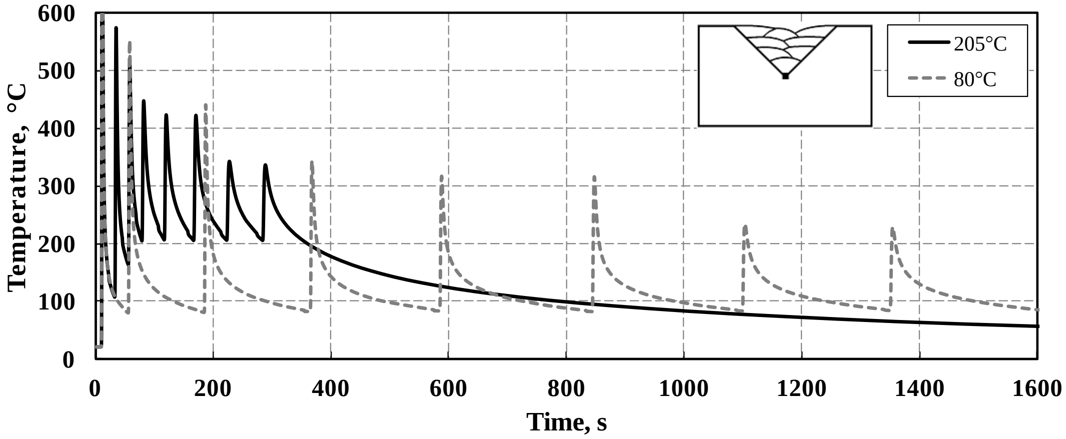

Figure 4.59 Weld thermal cycles taken at root node

Computed residual stresses are displayed in Fig.4.60. In the upper surface, after welding with 80°C interpass temperature, at the borders of V-groove transverse stress σ_x becomes compressive, whereas after welding with 205°C interpass temperature, transverse stress σ_x is always tensile.

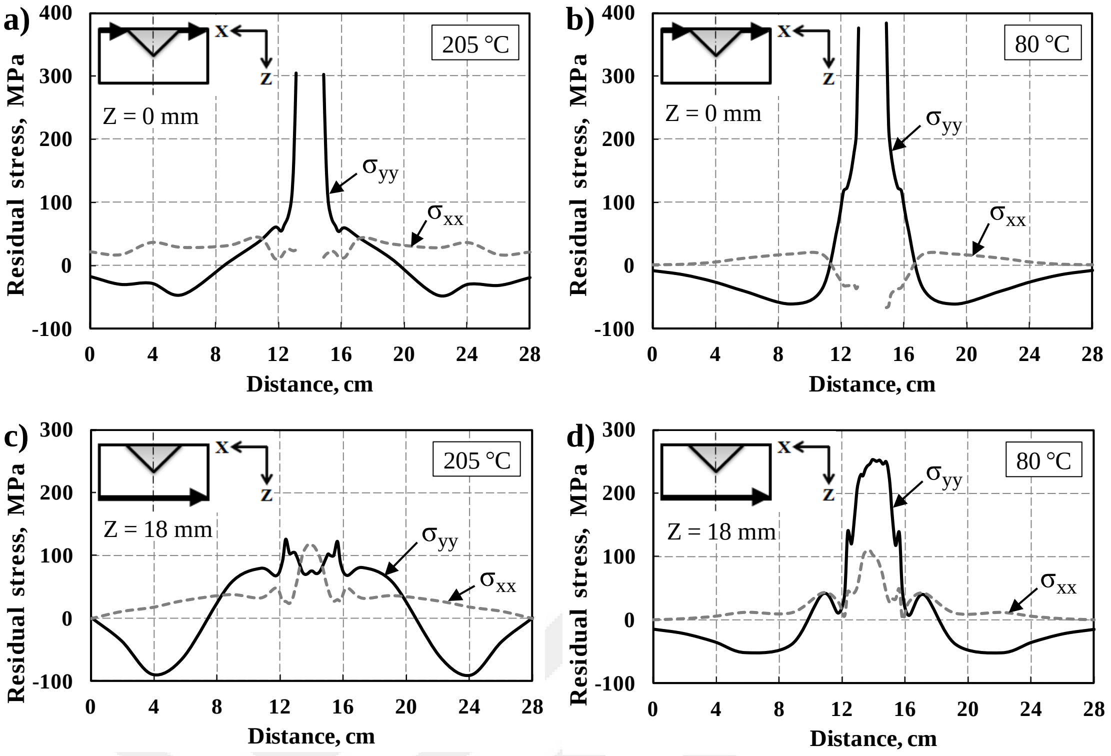

Figure 4.60 Distribution of residual stresses on the top and bottom surfaces of the welded plate in the middle section

Extension of tensile stress region of longitudinal stress σ_y directly points at the broadening of the HAZ at about 35 cm from both sides in the welding with 205°C interpass temperature. For the rest, there is no significant change in the stress distributions at the top plane. At the bottom surface, maximum value of longitudinal stress σ_y is twice raised when 80°C interpass temperature is applied instead of 205°C. Again, broadening of the HAZ is observed. Concerning transverse stress σ_x, there is almost the same profile in both cases.

Obtained results correspond to those by Lee and Kang [99] who reported that the residual stress values for specimens welded at an interpass temperature below 30°C were higher than for specimens welded with interpass temperatures of 100-120°C.

Stress distribution in normal direction at the middle section of the component is plotted in Fig.4.61. The biggest tensile stresses lie in the WM, but the effect of the interpass temperature is more pronounced deeper in the metal of the plate. Reduction in longitudinal stress is 14-22% in WM and up to 70% in the plate material.

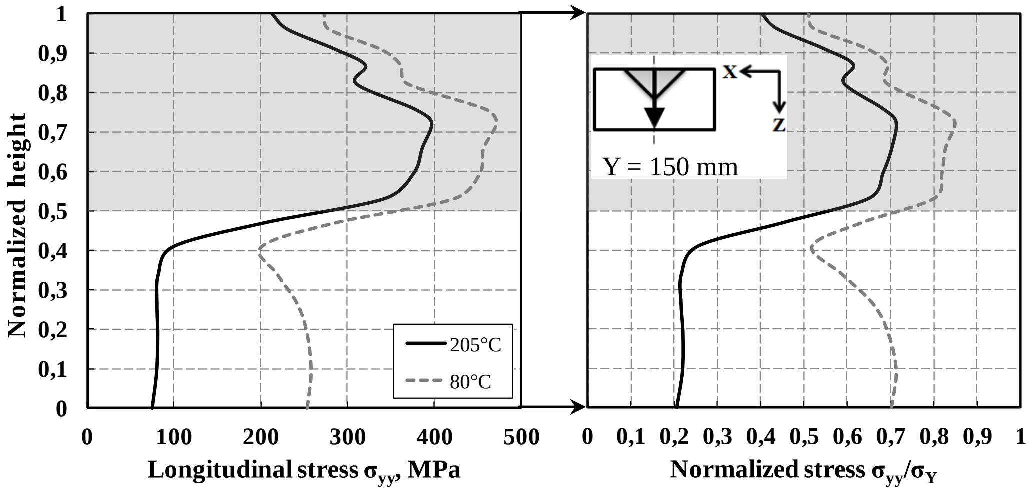

Figure 4.61 Distribution of residual stresses in through-thickness direction

To explain these results, it is necessary to consider the Bauschinger effect. During welding with 205°C interpass temperature, bottom surface of the plate is in the higher temperature range than that in 80°C (Fig.4.62). The Bauschinger effect is known to be largely removed after mild annealing, and process with 205°C satisfies this condition; whereas during the welding with the interpass temperature of 80°C strain hardening accumulates with each weld pass. Also referring to the Fig.4.56e,f, obviously that there is no stress relaxation at the bottom surface in both cases, but during welding with 80°C duration of thermal cycles are longer in restrained plate, and this contributes to the stress enhancement after every weld pass. Combined with the Bauschinger effect, these result in higher stress level at the bottom side of the section after welding with lower interpass temperature.

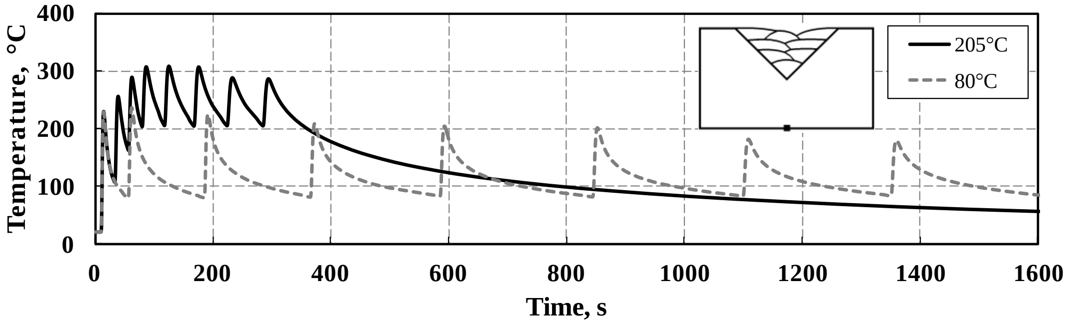

Figure 4.62 Weld thermal cycles at the bottom node

As for the WM and HAZ, need also to refer to the Fig.4.56a-d, in both cases under consideration, stress relaxation occurs. But there is a transient state − as closer the following weld pass to the considered point, so less the residual stress since it is annihilated by the high heat from following weld pass. When consequent weld pass is in process that is further from considered point, the influence of the Bauschinger effect becomes stronger and stress relaxation process is restarted with every following weld pass. For the case of 205°C interpass temperature, in the WM and HAZ, Bauschinger effect again is less than for the case of 80°C, but for the last case durations of pass operations are longer and, therefore, stress relaxation process is more pronounced. Hence, combination of two governing processes gives opposite effects and the difference of residual stresses in the WM and HAZ is less than that in the material of the plate. Eventually, welding with low interpass temperatures obviously leads to increased tensile stresses in the multi-pass welded joint, with possibility of approaching the yielding stress values.

Fig.4.63 demonstrates displacements of the upper plate edges at start and end sides.

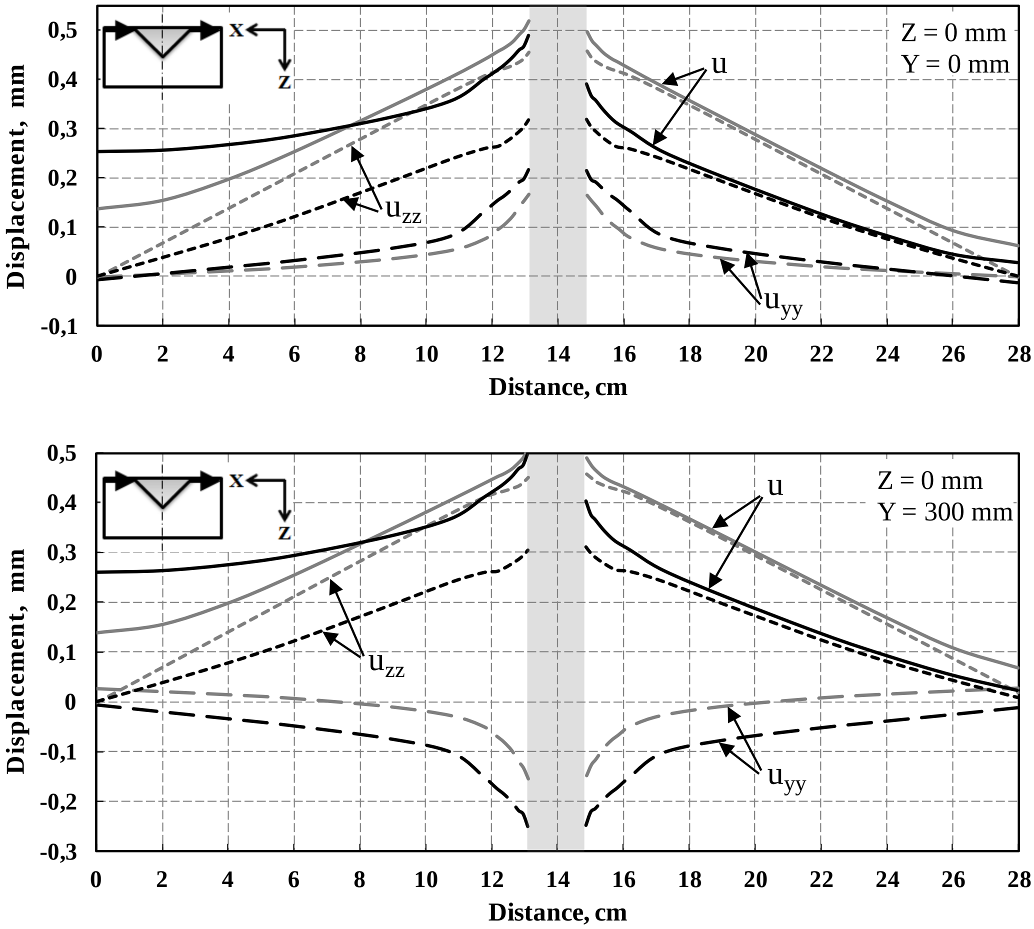

Figure 4.63 Displacement profiles at the plate edges from start and end sides for interpass temperatures of 80°C (grey lines) and 205°C (black lines)

As can be seen, overall displacement u is identical as for start side, so for end side. Longitudinal shrinkage u_{yy} in process with 205°C is expectedly higher than that in the welding with 80°C due to prolongated influence of high temperatures on the component. This difference is bigger in the end side since the heat dissipated in the plate is more to the finish of the welding process. In contrast, angular distortion u_{zz} is prevailing in the case with 80°C interpass temperature. This is the result of the interrelation with longitudinal shrinkage u_{yy}. Also, distortion asymmetry in transverse plane is more considerable for the case with 205°C.

Distortions on the bottom surface in longitudinal and transverse directions at middle sections are illustrated in Fig.4.64. For higher interpass temperatures less distortion is observed due to increased longitudinal shrinkage which pulls the weld seam and the regions around. Similarly, distortion inequality is higher for the welding with 205°C interpass temperature. Welding with higher interpass temperatures are more sensitive for the weld pass deposition sequencing.

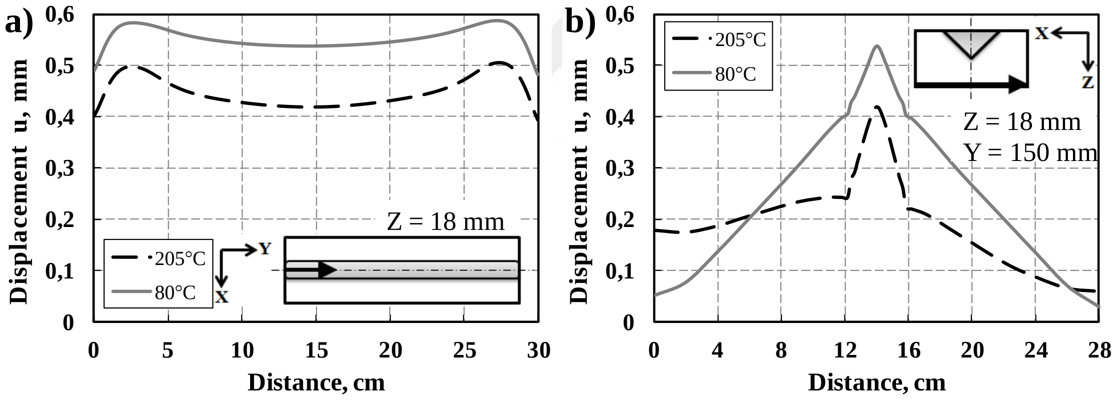

Fig.4.64 Distortion profiles for bottom surfaces of the plates
in (a) the longitudinal, (b) the transverse directions

There was revealed no significant difference in distribution of ferrite and bainite phases in cross-section, therefore only martensite phase profiles are given in Fig.4.65. First passes show matching peak at about 3.2%, then due to heated plate in case of 205°C less amount of martensite is observed than in the case of 80°C interpass temperature. Though, for the multi-pass welding of the steels with considerable amounts of martensite, interpass temperature parameter definitely appears to be vital.

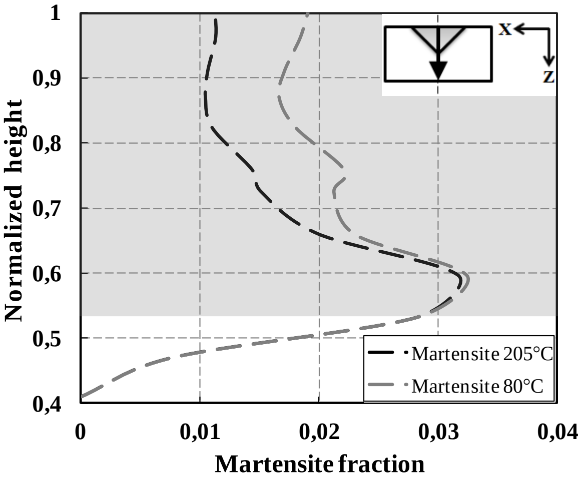

Figure 4.65 Martensite fractions for 80°C and 205°C interpass temperatures at the midway section of the plate

Kou [6] describes that at welding with preheating, the size of the HAZ increases but the maximum hardness decreases. Examination of the HAZ microstructure near the fusion boundary of the preheated weld revealed more pearlite and ferrite but less martensite. This is because the cooling rate decreases significantly with preheating. This can be related to the higher interpass temperature, as well.

CHAPTER 5

ANALYSIS OF MULTI-PASS SURFACING WELDING

One of the fundamental works on welding surfacing belongs to Morigaki [100] in collaboration with Hasui. A theory, practice, applications, materials, methods, properties and testing of surfacing weldings were described in detail. Though nowadays in literature, multi-pass surfacing welding is not widely numerically investigated process. Usually, industrial cases are modelled where the number of passes reaches order of several tens [101-104] and the complex configuration of construction surely effects on final residual stress distribution. Whereas, clear phenomena of surfacing welding is studied mainly on a single bead-on-plate welding sample.

Many researchers reported of 3D FE analysis of a benchmark problem of a single bead-on-plate welding of austenitic stainless steel [4, 63, 67, 89, 105, 106]. In all these cases the bead length was 60 mm. Whereas according to specification [93] and calculations given in Section 4.4 (Fig.4.34), it may be a scarce length for studying the phenomena, but sufficient for the purposes of validation of the FE weld simulation method. Price et al. [107-109] have investigated up to three-pass surfacing welding by neutron diffraction measurements and noted that additional beads tend to reduce the stress in previous beads and that the peak stress tends to be in the middle of the last bead − at the last point of solidification.

In this Chapter, the model of surfacing welding is formulated and presented. Characterization of single bead-on-plate and multiple pass surfacing welding is given. Effect of interpass temperature is considered and discussed, as well. And, weld deposition sequence using three cases is demonstrated and discussed.

5.1 Formulation of physical model of the surfacing process

Building of three-dimensional FE model of the plate with surfacing welding began from definition of basic 2D cross-section. Dimensions and proportions of the component were taken from that of the specimen with four pass welding on V-groove. Further, meshing of 2D surfaces were accomplished using finer elements in the regions of high temperature gradients, and coarser elements far away (Fig.5.2). Triangular and quadrilateral type of elements of linear order were utilized. After that, stretching from 2D elements were implemented into 3D elements in the form of pentahedrons (triangular prismatic) and hexahedrons. Thermal loads were applied on the 3D elements lying in the regions of future WM and HAZ. These loads result in adequate modelling of weld pool and heat transfer in the component (Fig.5.3). Clamping conditions were similar to that from welding on V-groove, bottom sizes were adjusted according to the weld pass number. Free and coincident nodes of the model, coincident elements and elements quality were controlled. Next, weld trajectories and reference lines were assigned, and heat transfer skin generated through extraction of 2D elements from the opened faces of 3D elements. Material was chosen for plate and weld wires, welding process parameters were assigned (Tabl.5.2), cooling conditions were specified, timing of clamping conditions was defined. Energy ramps of weld arc at the beginning and termination of weld have been provided because the start and finish are designed within the plate. Solver procedure was initiated. As in previous simulations, a nonlinear thermal analysis was followed by nonlinear mechanical analysis. The results of thermal calculations was input data for mechanical computations for each time step increment. After all, post-processing of FE model data was performed in order to process the output files. The same steel API X65 was used. Correspondingly, the temperature-dependent material properties were taken from that of welding modelling. Employed clamping model is displayed in Fig.5.1.

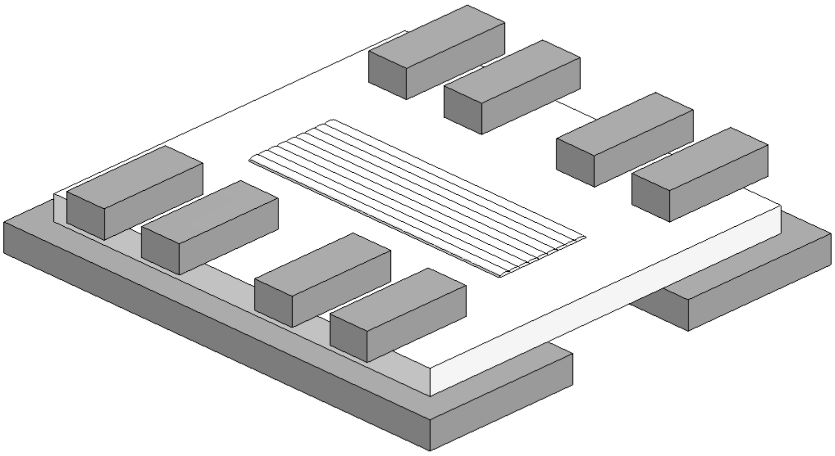

Figure 5.1 Clamping conditions for 300 mm plate (surfacing welding)

5.2 Results and discussion of multi-pass surfacing welding

In order to model the surfacing welding, average square of weld cross-section was taken into account and that of 4-pass welding was chosen to further FE mesh construction (Fig.5.2, Tabl.5.1). Plate parameters are the same, namely 280x300x18 mm (WxLxT), but the length of the weld passes is made shorter leaving 50 mm from start and end borders.

Table 5.1 FE mesh information for surfacing welding

Pass №	Number of elements in the weld lines	Number of elements				Number of nodes
		Beam	Shell	Solid	Total	
1	1 440	160	10 084	20 496	30 740	23 621
3	4 000	480	9 364	33 584	43 428	37 859
5	6 560	800	12 188	46 512	59 500	51 887
9	11 680	1 440	17 932	72 528	91 900	80 153

Step size in the weld line for all cases was set 2.5 mm. Fig.5.2 presents the side views of the FE meshes of surfacing welding models used in numerical experiments.

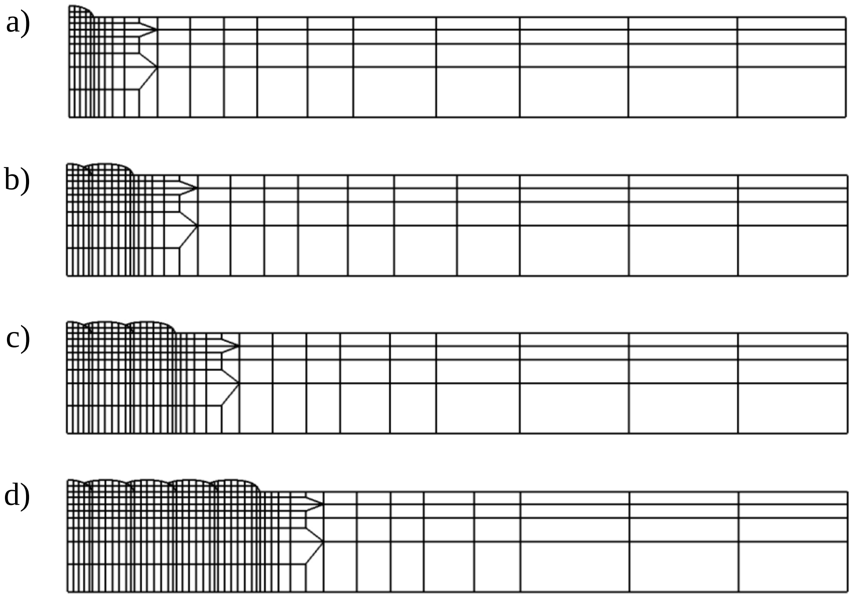

Figure 5.2 FE meshes for surfacing weldments. Side half-views: a) 1-pass, b) 3-pass, c) 5-pass and d) 9-pass; top quarter-views: e) 1-pass; f) 9-pass

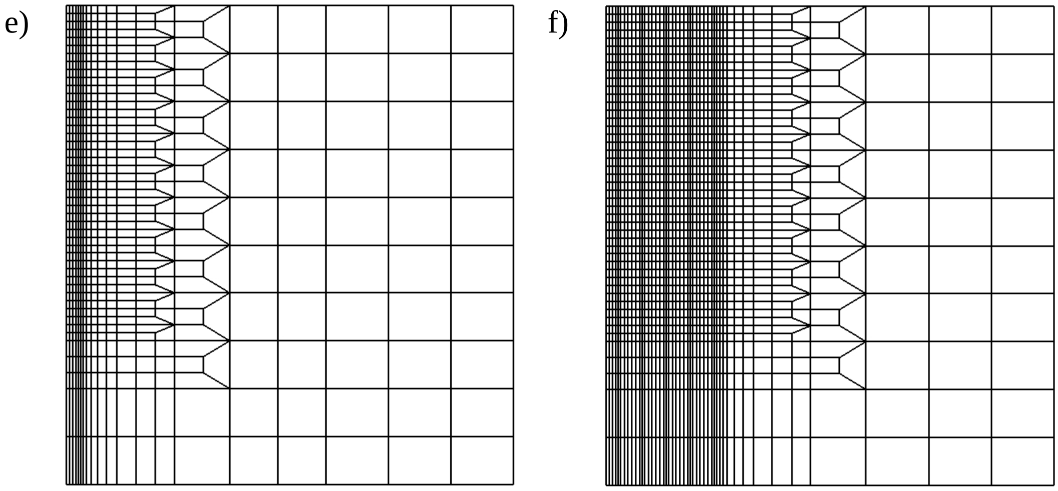

Figure 5.2 FE meshes for surfacing weldments. Side half-views: a) 1-pass, b) 3-pass, c) 5-pass and d) 9-pass; top quarter-views: e) 1-pass; f) 9-pass (continued)

Heat input is directly related to mass transfer phenomena. Accordingly, parameters of welding process of 4-pass weld model was utilized for calibration of molten pool profiles (Fig.5.3). Also, temperature profiles are plotted there, plates are cut from the sides for better view. The best appropriate results were produced by welding parameters presented in Tabl.5.2. Little correction on heat input almost did not influence on cooling rate which appeared to be similar to that of 4-pass welding on V-groove (Fig.4.11). Maximum cooling rate is 575°C/s at 1283°C for surfacing welding and 530°C/s at 1355°C for welding on V-groove (Fig.5.4).

Table 5.2 Parameters of surfacing welding process

Linear welding speed, mm/min	600
Pass heat input, kJ/mm	0.52
Efficiency coefficient	0.80
Start/End energy ramp at:	
beginning of weld	1.25
termination of weld	0.75
Weld pass length, mm	200
Ambient temperature, °C	20
Unclamping temperature, °C	20

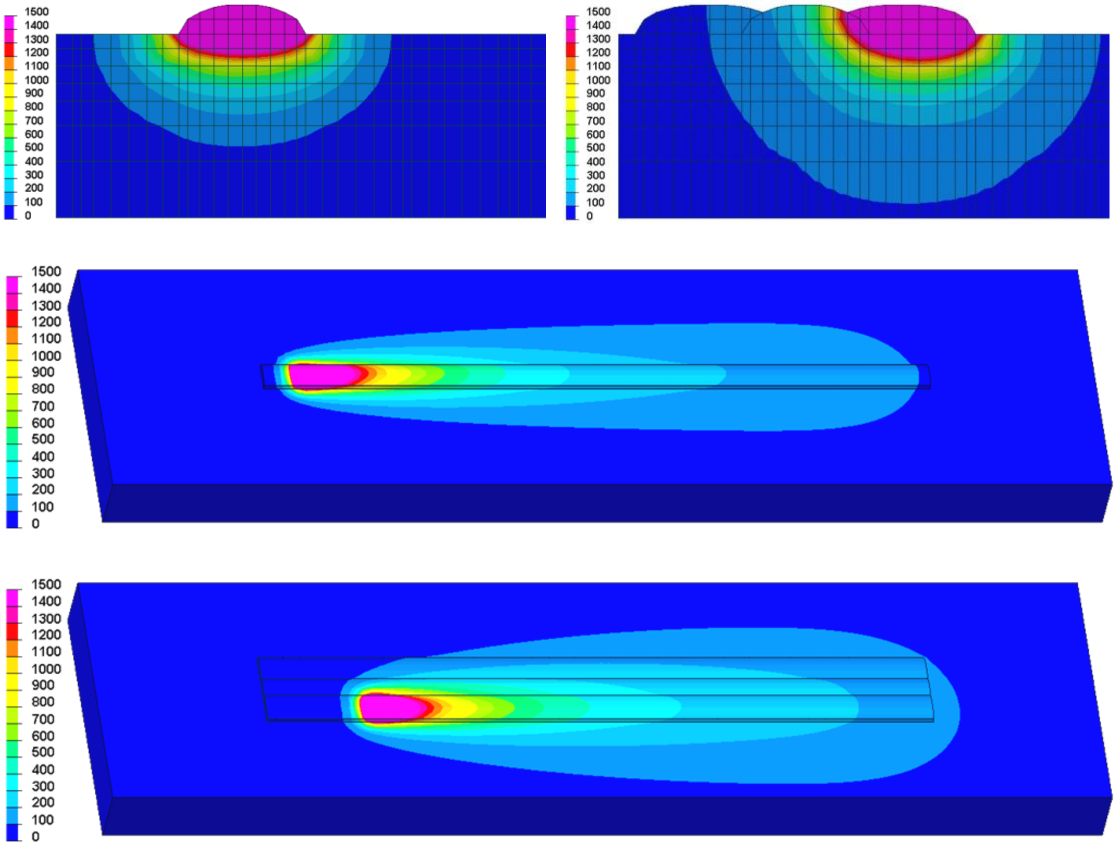

Figure 5.3 Molten pool and temperature profiles for the first and the last beads (interpass temperature 80°C)

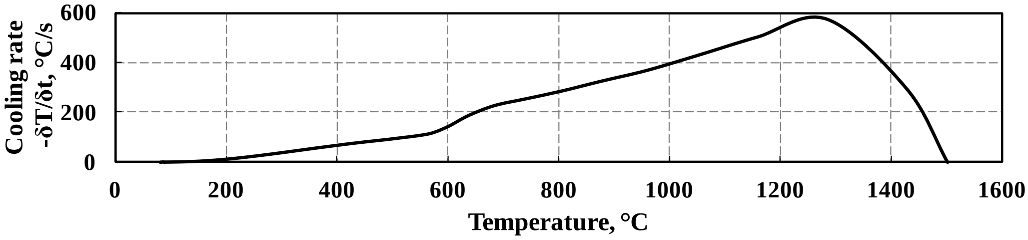

Figure 5.4 Cooling rate profile for the single-bead-on-plate

5.2.1 Characterization of single-bead-on-plate welding

The most common model is of 60 mm length on 120x180x17 mm austenitic steel plate. According to the results presented on Fig.4.35, 60 mm may be insufficient size to escape length effect. Taking into consideration this influence, the length of weld bead of 200 mm on the 280x300x18 mm plate have been chosen for current numerical investigation.

Contours of the direct residual stress and equivalent plastic strain at the start, the middle-way, the end transverse cross-sections and at the longitudinal cross-section along the weld bead have been examined. The results on the longitudinal plane are shown in Fig.5.5. Results of the transverse plane are presented in Fig.5.6.

Equilibrium considerations require that the transverse stress σ_{xx} over longitudinal plane (Fig.5.5b) should average to zero, and it is evident that the zones of high tensile stress are balanced by zones of compressive stresses. Highest tensile stresses are observed in the body of the plate directly under the bead at the welding start and end regions. It is also obvious, that the longitudinal stress σ_{yy} is tensile at the upper part of the plate and compressive at the lower part, as expected from equilibrium arguments (Fig.5.5a). Worth to note, that the σ_{yy} stresses in the region of the weld bead are reasonably independent of the longitudinal position, Y, and thus the conditions are approaching steady state conditions. Expectedly, the highest magnitudes belong to the longitudinal stress component, and the lowest values to normal stress component (Fig.5.5c). The peak plastic strains (Fig.5.5d) reach 2% and are spread at two zones: first one is formed near the fusion boundary from tension-compression cycle caused by weld pool advancing in the plate, and second one is the consequence of the austenite-bainite phase transformation in the body of the WM. Further detailed stress development analysis for middle cross-section (Fig.5.11-5.12) illustrates these two cycles in the WM border and the WM body: first one rises just before melting between approximately 9 and 11 s, second one processes just after WM solidification between 12 and 14 s. In single weld bead-on-plate analysis performed by other investigators [4, 63], austenitic stainless steel AISI Type 316L have been considered, and because of the absence of phase transformation only one plastically strained zone was observed − that at WM border.

In the transverse plane, as displayed in Fig.5.6 the high tensile stresses near the WM/BM boundary are balanced by the compressive stresses in the body of the component. The longitudinal (Fig.5.6a) and normal stresses (Fig.5.6c) appear to be discontinuous at the WM/BM interface. As it is shown in Fig.5.6d, the region of high plastic strain is situated mainly at the WM and HAZ. Plastic strain is negligible at the rest region of the detail.

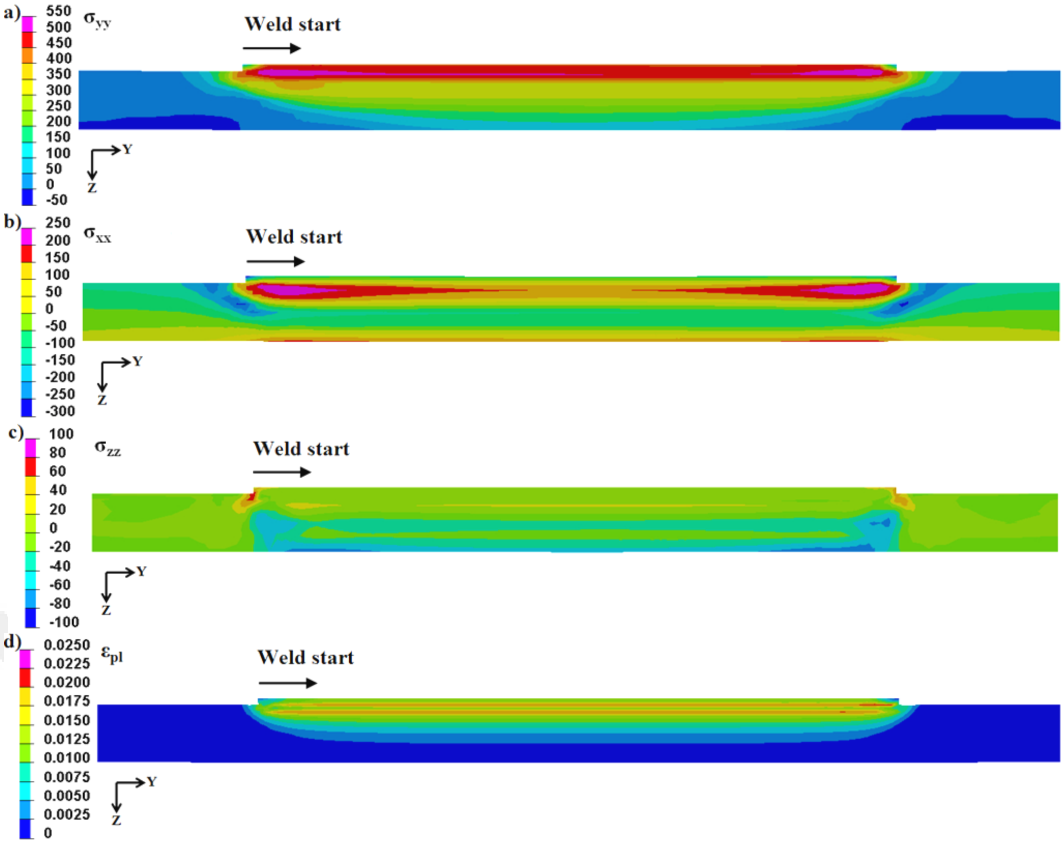

Figure 5.5 Distribution of residual stress components on the longitudinal plane: a) longitudinal, b) transverse, c) normal, and d) equivalent plastic strain field

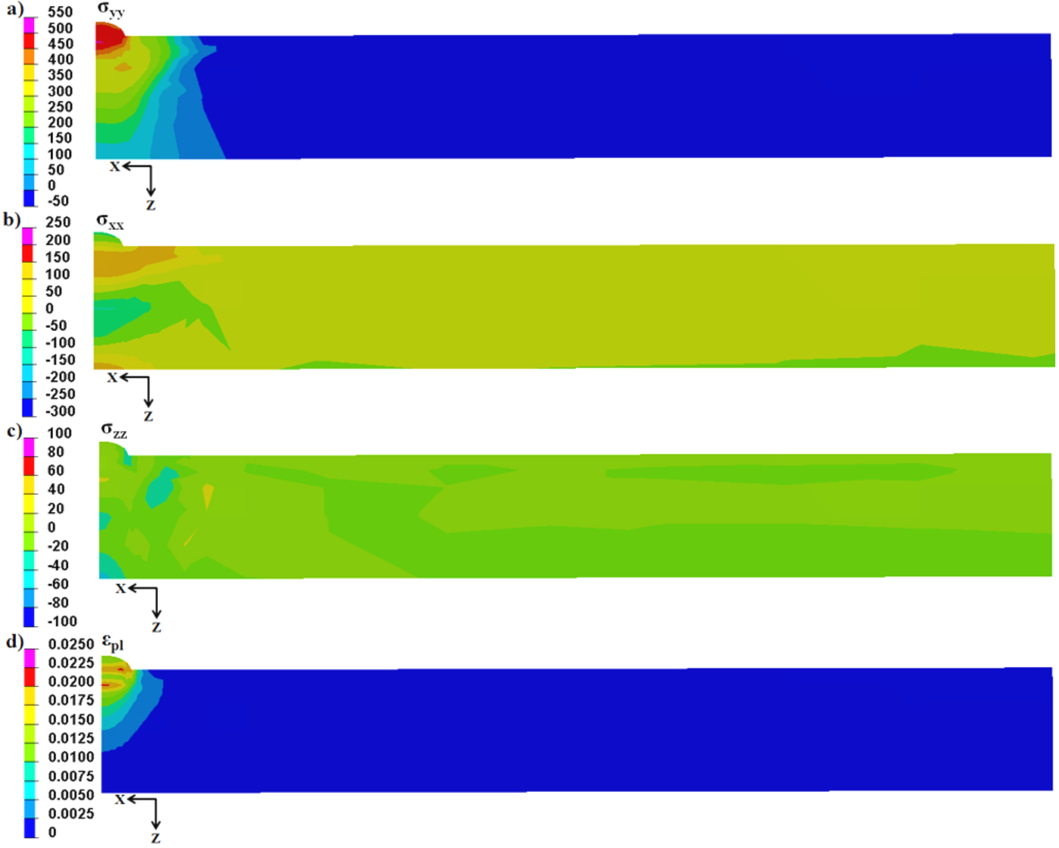

Figure 5.6 Distribution of residual stresses components on the transverse plane: a) longitudinal, b) transverse, c) normal, and d) equivalent plastic strain field

As can be seen in Fig.5.7a,b, the peak tensile stress is always found in the longitudinal direction (σ_{yy}) for upper layers of the plate, whereas at the bottom surface (Fig.5.7c) transverse stress σ_{xx} exceeds the longitudinal stress, though the magnitudes of both are sufficiently low. As longitudinal, so transverse stresses are generally tensile along the weld pass length. The normal stress σ_{zz} at the upper layers it is near zero and is compressive at the bottom plane under the weld seam. All stress components are distributed relatively symmetrical around the weld centerline. Stress peaks are located at the weld start and stop positions which correspond to the distances of 50 and 250 mm, respectively. At the regions close to the weld, plane stress state is prevailing and at remote areas tri-axial residual stress state exists.

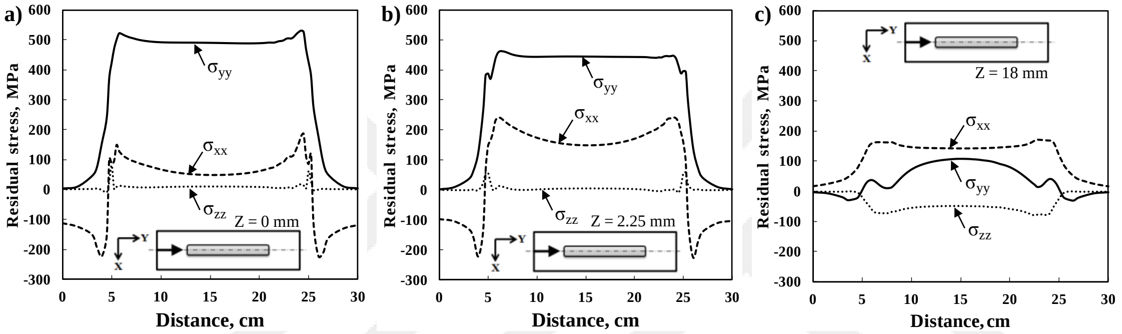

Figure 5.7 Residual stress components for one-pass surfacing weldment for different depths in the longitudinal direction

Fig.5.8 illustrates residual stress components profiles taken from the different depths of the plate at mid-way in the transverse direction. The peak tensile stress σ_{yy} is positioned in the weld zone and reaches 492 MPa, transverse stress σ_{xx} is 23-50 MPa at the weld zone and 147 MPa at the HAZ. Yield strength of weld metal is 505 MPa, and maximum von Mises stress is 463 MPa, therefore the region is appeared to be in dangerous state.

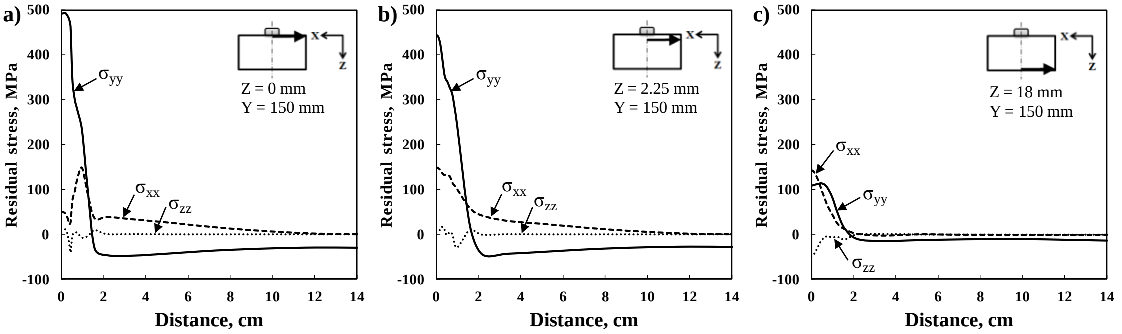

Figure 5.8 Residual stress components for one-pass surfacing weldment for different depths in the transverse direction

At lower layer (Fig.5.8b), which belongs to HAZ (max 1087°C) σ_{xx} is 148 MPa. In the bottom plane (Fig.5.8c), it is confirmed that transverse stress σ_{xx} is dominant.

Dependence of the stresses on distance through the plate is presented in Fig.5.9. At weld start (Fig.5.9a), longitudinal stress is attaining its peak value of 437 MPa in the body of the weld bead. At the top of weld seam, compressive transverse stress reaches the value of -303 MPa, the next peak is in the middle of the plate and is -255 MPa. Similar pattern is found at the weld end (Fig.5.9c), where σ_{yy} is 465 MPa, and compressive σ_{xx} are -268 and -242 MPa, respectively. In the mid-way of the bead (Fig.5.9b), situation differs, namely, longitudinal stress draws near the risky values of 502 MPa in the metal of the surfacing weld bead. Concerning transverse stress, it is more balanced than in the start and the end sides. And distribution of the normal stress σ_{zz} is approximately the same for all cases and the magnitudes lie in the range of -49...61 MPa. Thus, the most critical place is positioned in the weld bead.

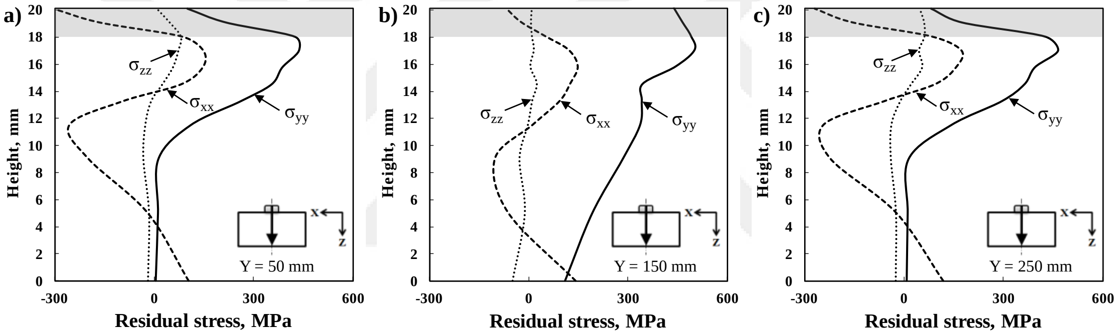

Figure 5.9 Residual stress components for one-pass surfacing weldment for different lengths in the normal direction

Fig.5.10 shows the distribution profiles of plastic strain along the different directions. The variations in equivalent plastic strain in the transverse directions (Fig.5.10a-c) show comparatively low values in the weld start and the weld end positions than in the mid-way of the weld pass, about 1.1-1.3%. The maximum of 2.0-2.1% is achieved in the WM and HAZ (Fig.5.10b) in the middle of the plate. The variation in strain in longitudinal direction (Fig.5.10d) points at the peak plastic strain values of about 2.2% at the weld stop position in the body of WM, and 1.9% along the weld pass. Though in general, region of HAZ along the weld path is the most plastically strained; magnitudes are of 2 %. The least plastically strained zone is at the bottom, the values reach to about 0.08%. Profiles in through thickness direction (Fig.5.10e) show two peaks in the WM body (1.9%) and in the HAZ (2%) as it was mentioned and explained earlier. In the start end of the weld bead only one peak is observed and it is much less in value, about 1.3%. At the end side of weld bead, two barely noticeable peaks are observed again, 1% and 0.8%.

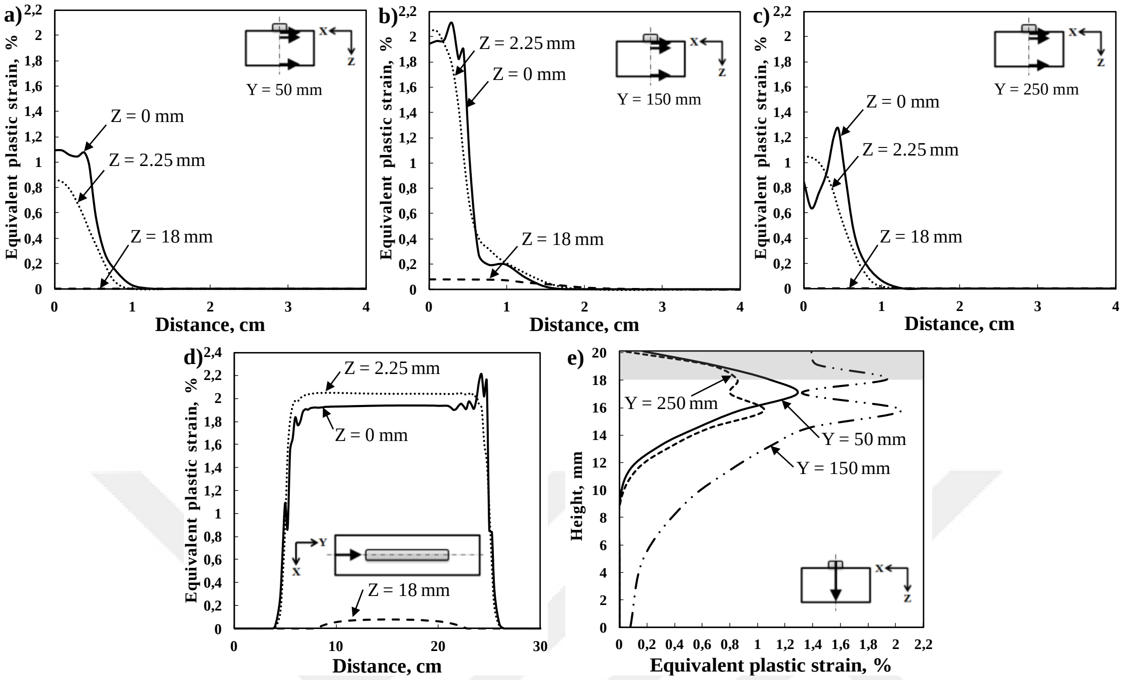

Figure 5.10 Equivalent plastic strain distribution for one-pass surfacing weldment: a) weld start; b) midway; c) weld end; d) along the weld; e) through-thickness

Development of transverse and longitudinal stress components during welding at different points located in through thickness direction are plotted in Fig.5.11-5.12. With welding torch approaching, material before weld seam is subjected to increasing compressive stresses. Upon materials melting in weld bath, all stresses are reset to zero. After solidification beginning in the melted zone, the material experiences a cooling process and then an austenite-bainite phase transformation and, therefore, creates tension-contraction-tension cycle dominated by longitudinal contraction in the welding direction, which produces tensile longitudinal stress. Beneath the melted zone (approximately 2.25 mm below surface) at a HAZ, the material of plate experiences a heating-cooling cyclic process. When the heat source does not reach the mid-length of the weld pass, the parent material undergoes moderate tensile stress in the transverse direction and similar compressive stress in the longitudinal direction. When the welding torch reaches the mid-way of the weld, the BM is heated and becomes subjected to compressive stresses both in the transverse and longitudinal directions. When the heat source leaves the mid-length of the weld, the parent material begins to cool and undergoes the tensile stresses in the transverse and longitudinal directions.

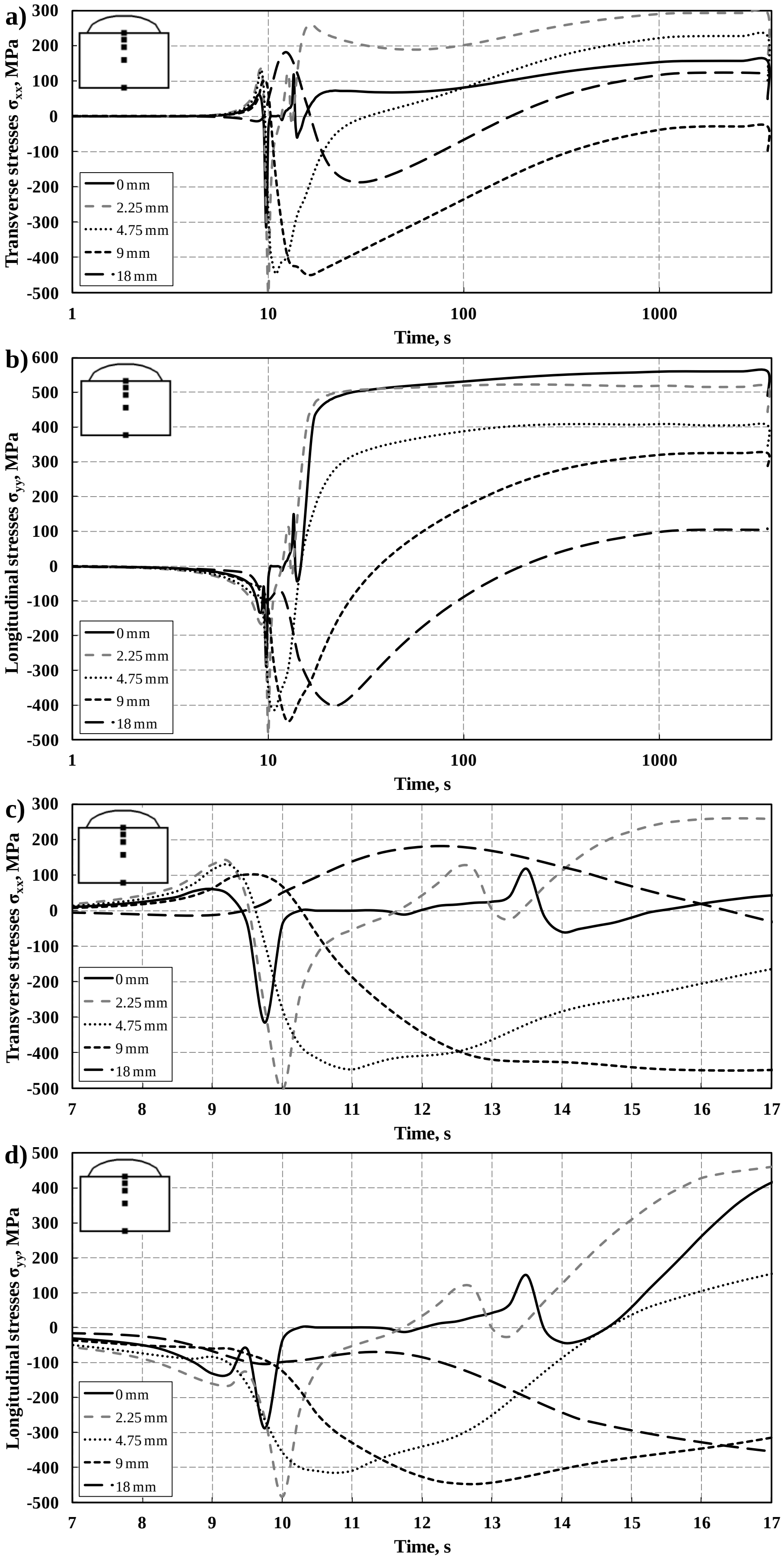

Figure 5.11 Development of the stress at points in through-thickness direction

Hence, the transverse stress σ_{xx} undergoes a tension-compression-tension cycle caused by heat transfer and additional compression-tension cycle caused by partial austenite-bainite phase transformation resulting in approximately 57% bainite + 43% ferrite structure. While, the longitudinal stress σ_{yy} undergoes compression-tension cycle due to heat transfer and additional compression-tension cycle due to the same phase transformation. Need to note, that the longitudinal stresses come up to the yield stress during the period of tension. Deeper in the plate (from 4.75 mm below the surface), the material does not influenced metallurgically, but endure a biaxial loading. The transverse stress σ_{xx} is subjected to a tension-compression-tension cycle, while the longitudinal stress σ_{yy} undergoes only a compression-tension cycle. In the middle of the plate (9 mm below the surface), the transverse stress σ_{xx} is passing through tension-compression cycle, and the longitudinal stress σ_{yy} − tension-compression-tension loading. Finally, at the bottom plane, the transverse stress σ_{xx} undergoes a tension-compression-tension cycle, and the longitudinal stress σ_{yy} endures a compression-tension-compression-tension cycle.

Fig.5.12 illustrates evolution of the phases at the WM during the welding thermal cycle which is imposed on the same plot. The start of ferrite phase from 50% is explained by the mesh configuration when the node at a root of weld is shared by 2 elements of BM and by 2 elements of WM which is in status "yet not deposited" before welding (Fig.5.2a). From the graph, it is seen that parent material consists of ferrite that is transformed to the austenite which melts, and just after the solidification, WM consists of austenite phase which at about 800°C starts transformation to bainite phase which completes at about 500°C.

In the lower plot, corresponding to the phase transformations, stress peaks are displayed. First one occurs between 9 and 10 s, the second one occurs between 13-14.5 s. Coincidence of the peak profiles in transverse, longitudinal and normal directions indicates the volumetric character of the process, and confirms its relation to the phase transformations.

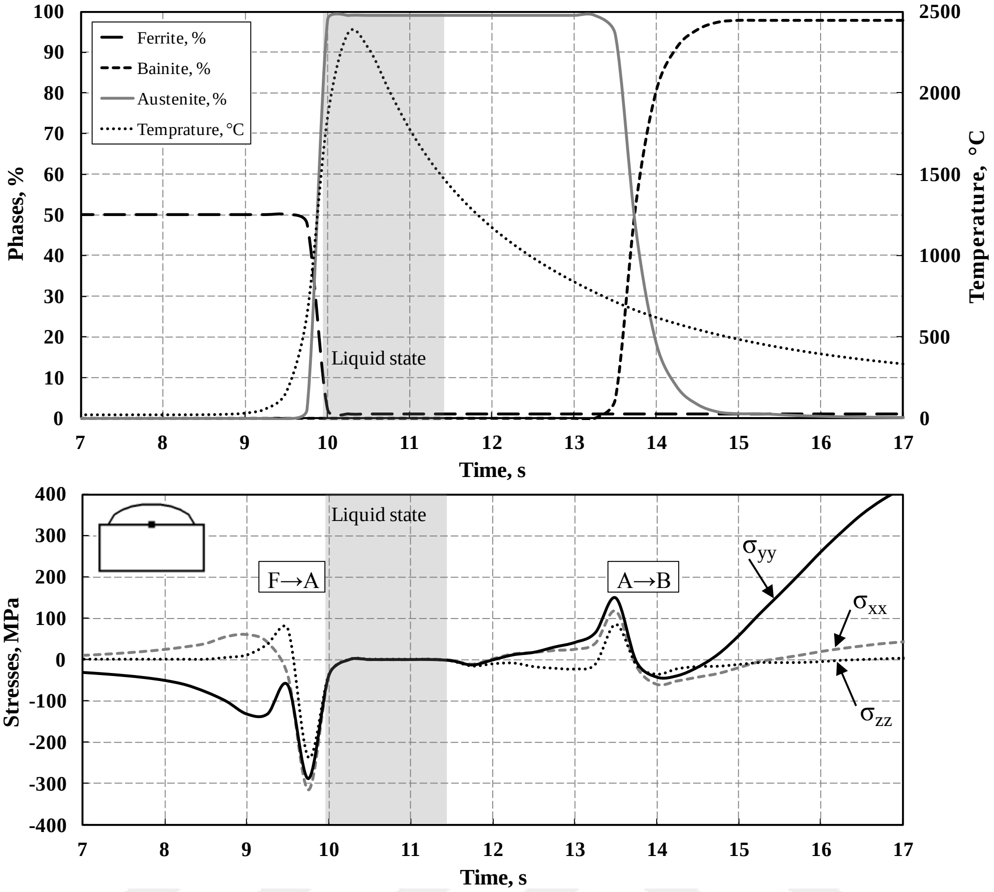

Figure 5.12 Phase transformation influence on stress evolution

5.2.2 Multi-pass surfacing welding

Three cases of surfacing welding with different weld deposition sequencing will be considered further: Case A, Case B and Case C (Fig.5.13). Geometrical dimensions are identical for all variations. The square of the surfacing welding is 200 mm in length and 70 mm in width on the plate of 280x300x18 mm. FE meshes differ only with positioning of the first weld bead which is laid straightly perpendicular to the X-axis. All consequent weld pass depositions are performed under the angle to the Z-axis in order to provide the fusion with previous weld bead.

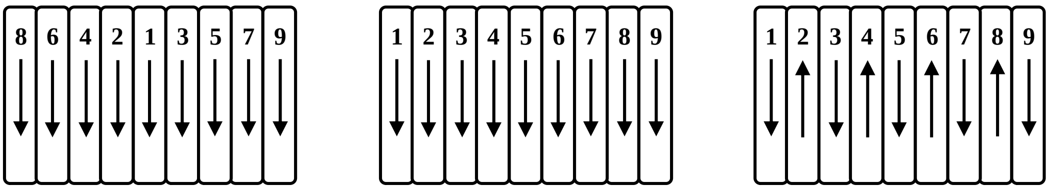

Case A

Case B

Case C

Figure 5.13 Layouts of surfacing welding

In Case A, the welding directions of separate weld passes are similar and the overall movement of surfacing is from the center of the plate to the sides. In Case B, the overall route is in one direction − from one side to another. In Case C, welding of individual passes starts from the end side of previous weld pass, and proceeding welding direction is in one way as that in Case B. In all the simulations, the interpass temperature was controlled not to exceed 80°C. For all cases, unclamping was performed after complete cooling down to the RT. In this Subsection, development of stresses, strains and displacements based on the Case A is considered. Examples of 1-, 3-, 5- and 9-pass surfacing weldings will be described and discussed. Residual stress distributions on the HAZ layer (Z = 2.25 mm) and on the bottom surface (Z = 18 mm) taken from the middle cross-sections are shown in Fig.5.14 for all four cases. Deposition of single-bead-on-plate exerts the highest, up to 444 MPa, tensile longitudinal stress σ_{yy} on the upper layers of the section (Fig.5.14a). Transverse stress σ_{xx} is achieving 148 MPa. After three weld passes (Fig.5.14b), tensile longitudinal stress is decreased by 12% up to 390 MPa under the welded zone, and compressive longitudinal stresses besides the welded region are enhanced. Also zigzag profile appears on the top, and these valleys of the curve correspond to the weld bead positions. The first pass experiences the twice heat influence from the neighbouring beads, and stress relief occur during it. These result in decrease of the stress under the weld seam. Other two passes form comparatively very small valleys due to the fact that they are final and did not endure heat treatment. Concerning transverse stress, it is in almost the same ranges, however showing increase at the near regions. After 5 weld passes (Fig.5.14c), same tendency is observed. Longitudinal stress is diminished up by 17% up to 369 MPa under welded zone, same way compressive stresses away from the HAZ are raised. The valleys on the zigzag profile now estimated as five according to the weld seams applied, and again final passes are smaller alongside with others. As regards transverse stress, its values approaches to 133 MPa, and peaks at HAZ regions appear as a result of the clamps resistance which are 60 mm in length. After nine weld passes (Fig.5.14d), the stress pattern develops in resembling way. Longitudinal stress is decreased by 21% up to 351 MPa under welded zone, compressive stresses show peaks due to restraints. Number of valleys of the curve is exactly nine, and finishing ones are the smallest. Maximum value of transverse stress is 112 MPa, its distribution under the welded zone becomes more uniform. In all cases transverse stress is tensile.

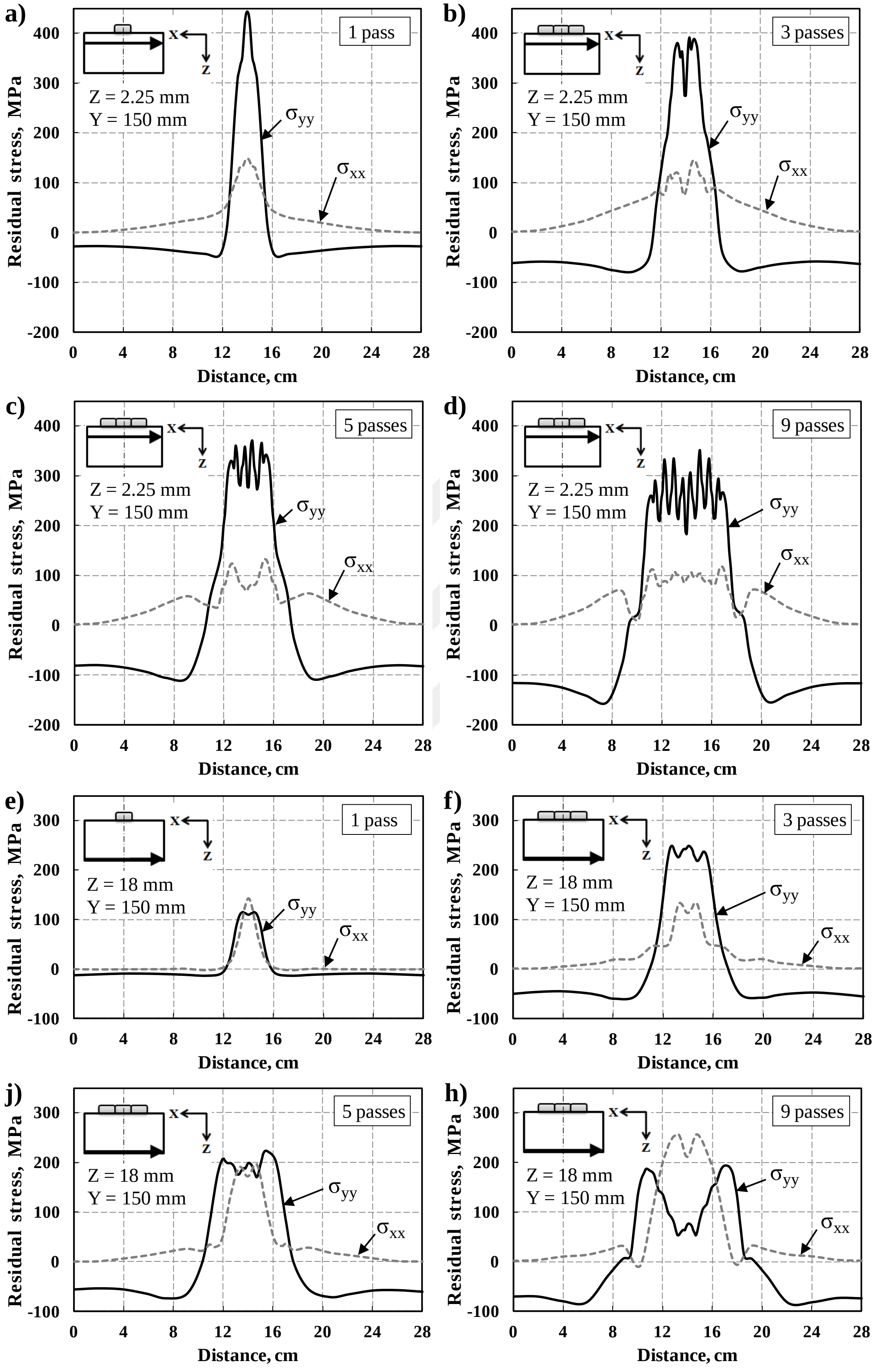

Figure 5.14 Distribution of σ_{xx} and σ_{yy} stress components
in the transverse direction at midway section (Case A)

On the bottom surface, single-bead-on-plate (Fig.5.14e) produces approximately equal peaks of moderate longitudinal (114 MPa) and transverse stresses (142 MPa). After three weld passes, longitudinal stress is increased by 18% up to 248 MPa, whereas transverse stress is of the same level, 132MPa. In longitudinal direction, stresses far away from HAZ become compressive (Fig.5.14f). After five weld passes, longitudinal stress slightly decreases to the values of 223MPa, while transverse stress continues growing to 196 MPa almost equating to the longitudinal stress (Fig.5.14j). After nine weld passes, transverse stress reaches 257 MPa and turn to be dominating over longitudinal stress (Fig.5.14h). The last takes the form of two peaks with a valley among them. This is due to the partial relieving heat treatment of the beginning weld passes from the heat of consequent weld passes. And peaks location is the consequence of the weld pass deposition fashion. Later, in Fig.5.29a longitudinal residual stress field in cross-section will be presented.

Distribution of residual stresses along the weld centerline on the bottom surface is plotted in Fig.5.15. These graphs should be evaluated in combination with previous series of plots (Fig.5.14e-h).

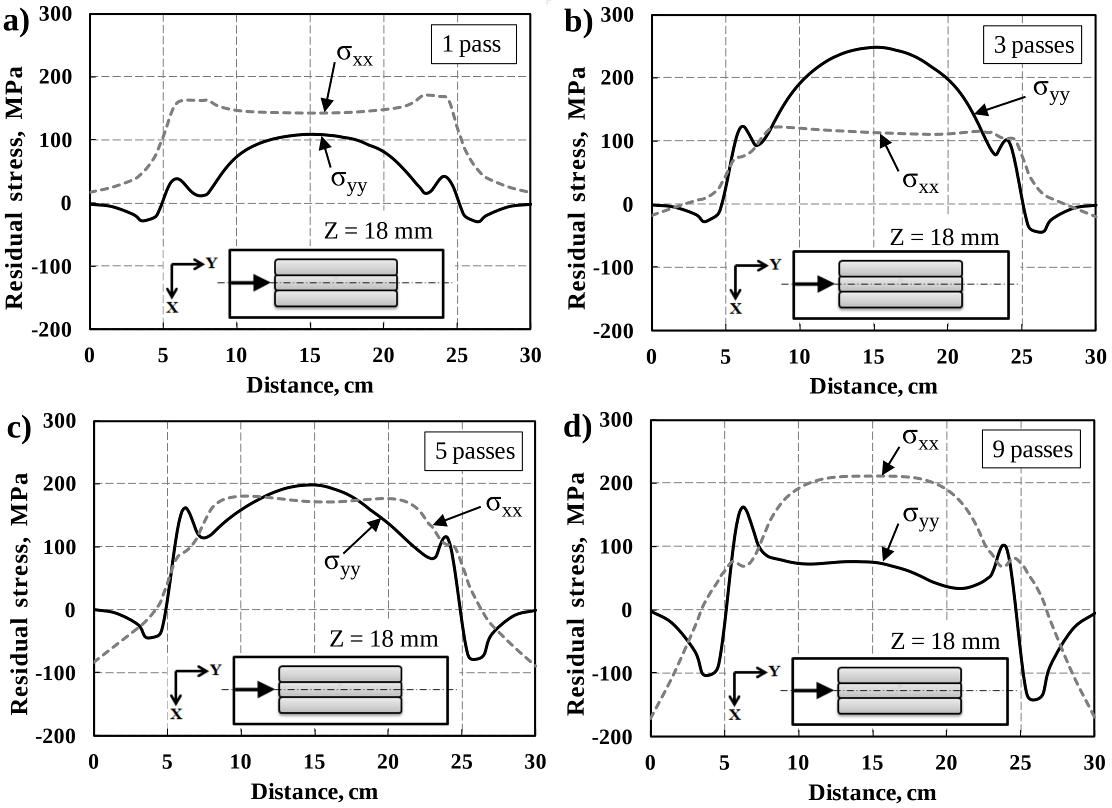

Figure 5.15 Distribution of σ_{xx} and σ_{yy} stress components in the longitudinal direction at midway section (Case A)

Stress profiles of single-bead-on-plate in longitudinal direction demonstrate more obvious prevalence of transverse stress over longitudinal stress, especially in the start and end sides of the bead. After three weld passes, values in the start and end sides of the weld seam become roughly equal, but in the middle of the surfacing welding there is an essential increase of longitudinal stress. After five weld passes, longitudinal and transverse stresses are about of the same range values. Also, both stress components, from positions of equilibrium, exhibit increase of compressive stresses at the edges of the plate. After nine weld passes, these compressive stresses at the plate edges are twice bigger. Worth to note, that only longitudinal stress component is sensitive to the welding direction of the passes. In considered case, all weld passes starts at the same side, and stress profile indicates it with higher stress peak.

Fig.5.16 shows the distribution of longitudinal stress in normal direction at the middle section of the component, means under the first pass. As can be seen, one-pass surfacing welding undergoes critical values at upper layers of the plate right under the weld seam. The heat from consequent weld passes partially mitigates previously formed residual stresses.

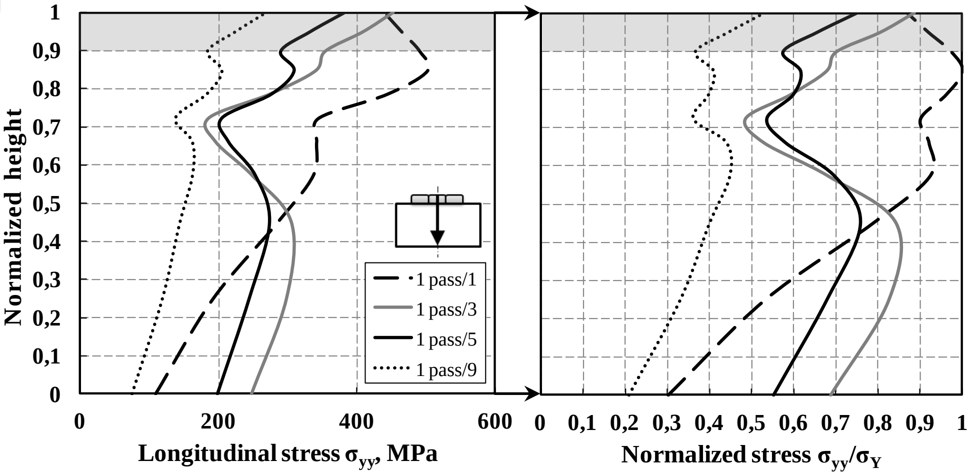

Figure 5.16 Through-thickness distribution of residual stresses at midway cross-section (Case A)

Similarly, as for multi-pass welding on V-groove a partial heat treatment of previous passes occurs in the surfacing welding. Though, due to last passes final pattern of the residual stresses is very inhomogeneous, therefore still requires a finishing stress levelling heat treatment.

Equivalent plastic strain graphs in different depths are presented in Fig.5.17. One pass surfacing welding forms the plastic strain of 0.08% on the bottom surface. Three weld passes raise three corresponding peaks of plastic strain closer to the HAZ. At the bottom plane, the order of weld pass deposition plays much less role and only two peaks remain at limits. After five weld passes, central peaks unchanged and buildup of new peaks and broadening of the influenced zone are observed. Also, plastic strain from finishing weld pass at the bottom surface is more evident. After nine weld passes, the extension of the plastically strained zone is continued. Finally, two formed peaks of plastic strain at the bottom surface are the result of clamps resistance, as well.

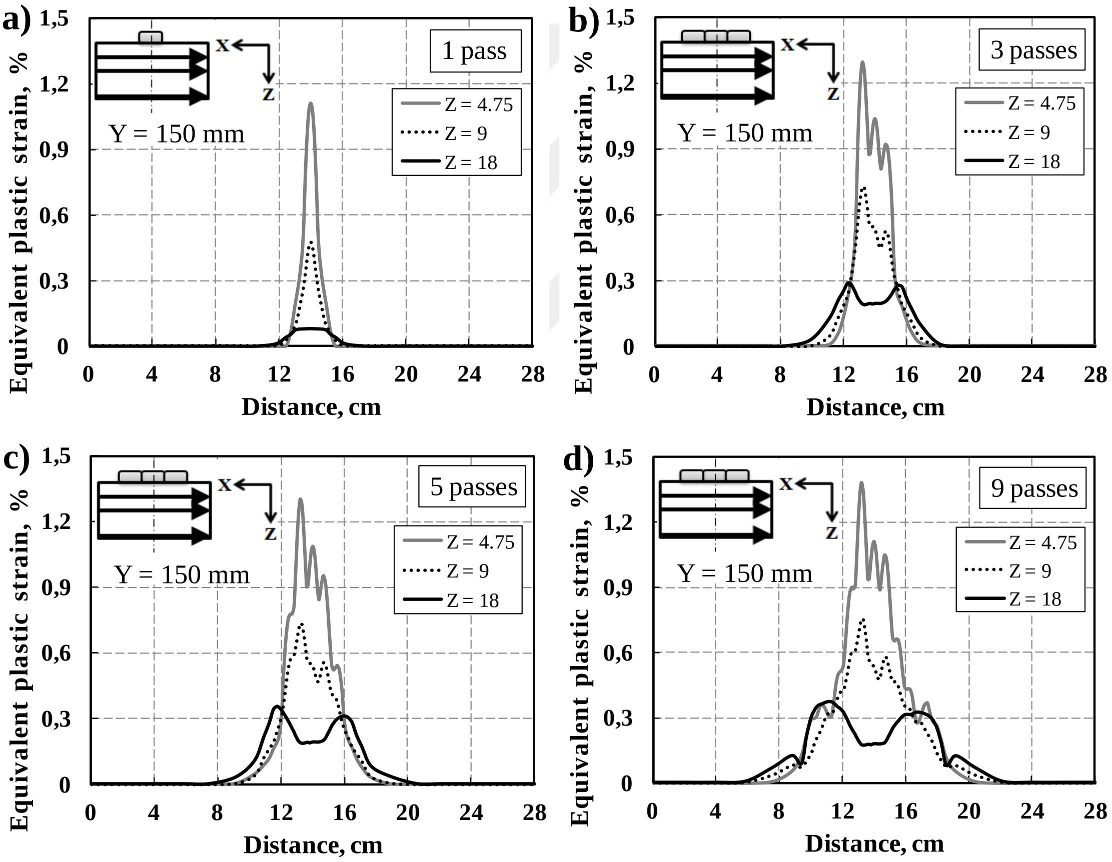

Figure 5.17 Distributions of equivalent plastic strain (Case A)

Distortion profiles in longitudinal and transverse directions are given in Fig.5.18. There is a direct dependence of the distortion on the weld pass quantity − the more the weld seams are on the surface, the greater final deformations of the plate. Need to note the light growing inclination of the profiles in transverse cross-section due to the weld pass deposition fashion.

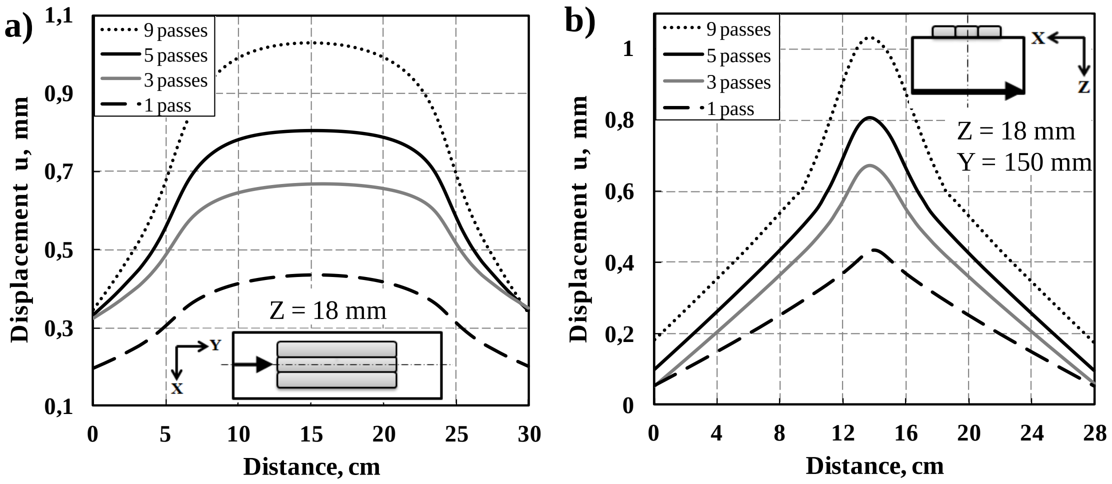

Figure 5.18 Distortion profiles for the bottom surfaces of the plates (Case A)
(a) longitudinal direction, (b) transverse direction

In general, the most critical is the single-bead-on-plate configuration which necessitates the following heat treatment, in multi-pass surfacing welding a partial heat treatment occurs from the consequent weld passes. With growing number of weld passes, transverse stresses may become dominating over the longitudinal at the bottom surface of the plate. Weld pass sequencing in the multi-pass surfacing welding influences on the plastic strain formation character and distortion symmetry.

5.2.3 Effect of interpass temperature

Jiang and Yahiaoui [110] after investigation of interpass temperature effect on weld-induced residual stress distributions in a thick-walled piping branch junction concluded that the interpass temperature greatly affects the magnitudes of the residual stresses, especially those near the weld. Increasing the interpass temperature reduces the thermal gradients, thus helping to reduce residual stresses at a rate between 0.1 and 0.7 MPa/°C at most peak value locations.

The influence of interpass temperature was studied on the model of Case B: 205°C and 80°C. Thermal cycles are presented in Fig.5.19. In order to unload the graph and facilitate its understanding each cycle is displayed partly − a peak before welding is shown to indicate the lowest temperature before melting (205°C or 80°C), and two peaks after solidification are expressed to demonstrate the heat influence from subsequent weld passes. For the case of 205°C, temperatures of the first and the second following peaks reach 647°C and 323°C; for the case of 80°C − 528°C and 206°C, respectively.

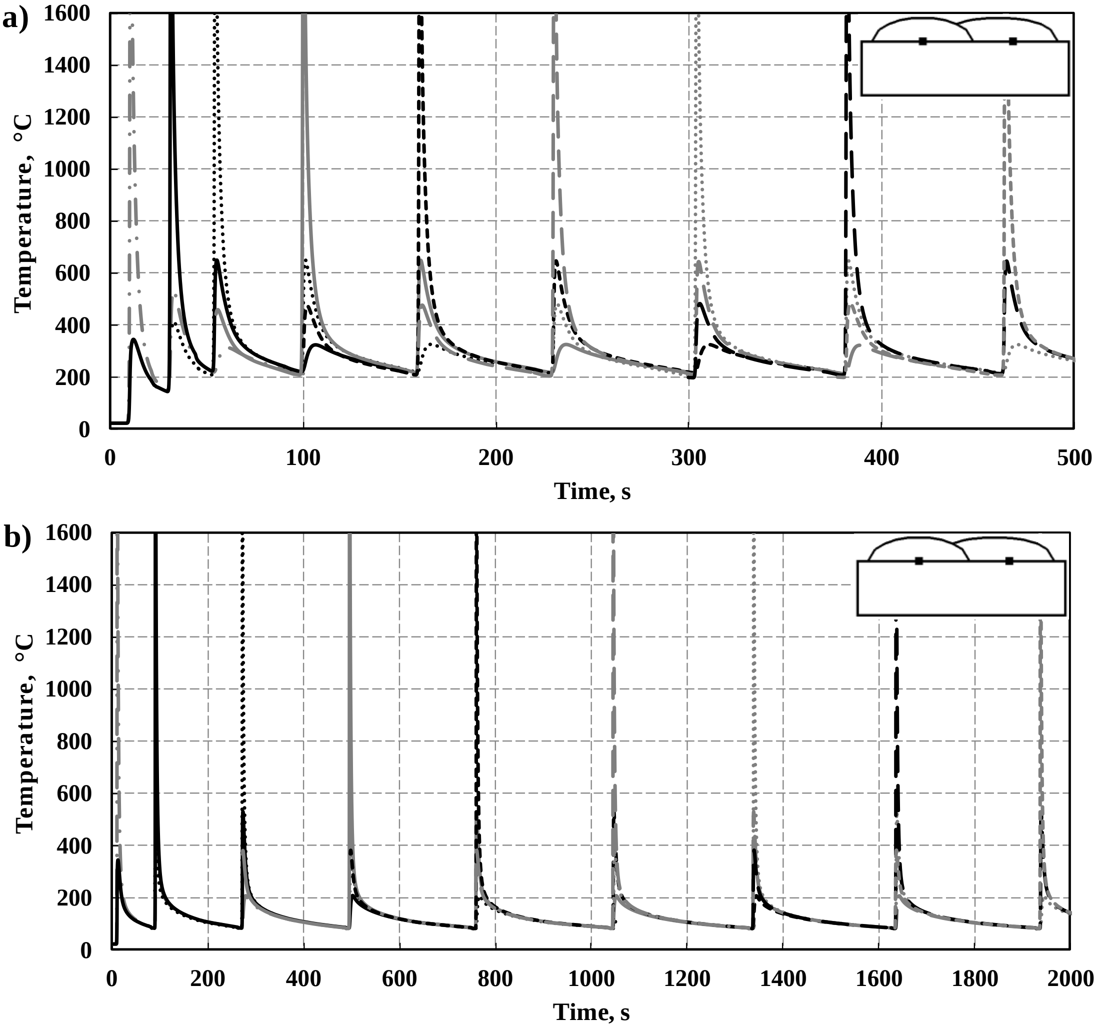

Figure 5.19 Thermal cycles for the weldings
with the interpass temperatures of a) 205°C and b) 80°C

Distribution of residual stress components on the layer under the weld seams at about HAZ (Z = 2.25 mm) and on the bottom surface (Z = 18 mm) of the welded plate are presented in Fig.5.20. At the upper layer, the maximum values of the longitudinal stress σ_{yy} in both cases are of the same range. Peaks are more brightly expressed in case with 80°C. Also, some more asymmetry is obtained on the edges of the component in welding with 205°C. Transverse stress σ_{xx} distribution is almost unchanged from interpass temperature altering. Concerning, the bottom surface of the plate at decreased interpass temperature transverse stresses appear to be more significant than longitudinal. Its distribution implies that it is due to overall welding direction which is performed along the X axis. Longitudinal stress profile also indicates to the effect of overall direction of the surfacing welding. Also, bottom surface edges demonstrates more inequality in welding with 205°C. In all considered cases, longitudinal stresses are tensile in the region of WM and HAZ and compressive far away from HAZ; and transverse stresses are always tensile.

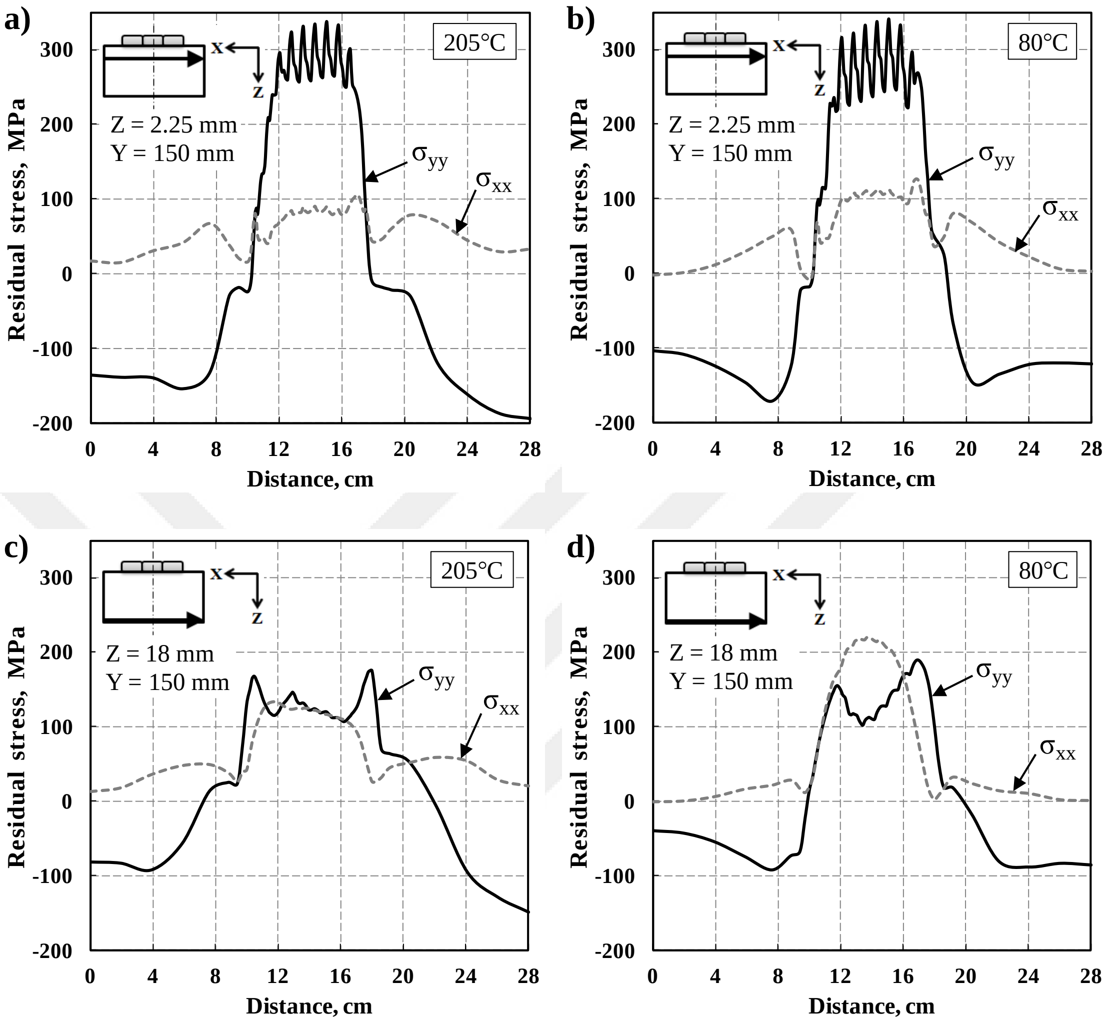

Figure 5.20 Longitudinal and transverse stress distributions in midway section (Case B)

Fig.5.21 displays profiles of displacement of the plate edges at the start and end sides. There is light differences in the values of longitudinal shrinkage u_{yy} and angular distortion, the end side is slightly more effected. Also, comparatively to the welding with 80°C interpass temperature that with 205°C gives more unequal distortion. Means, welding with elevated interpass temperatures is more sensitive to the weld pass sequencing, and in cases of larger squares and scales of surfacing welding this fact should be definitely considered.

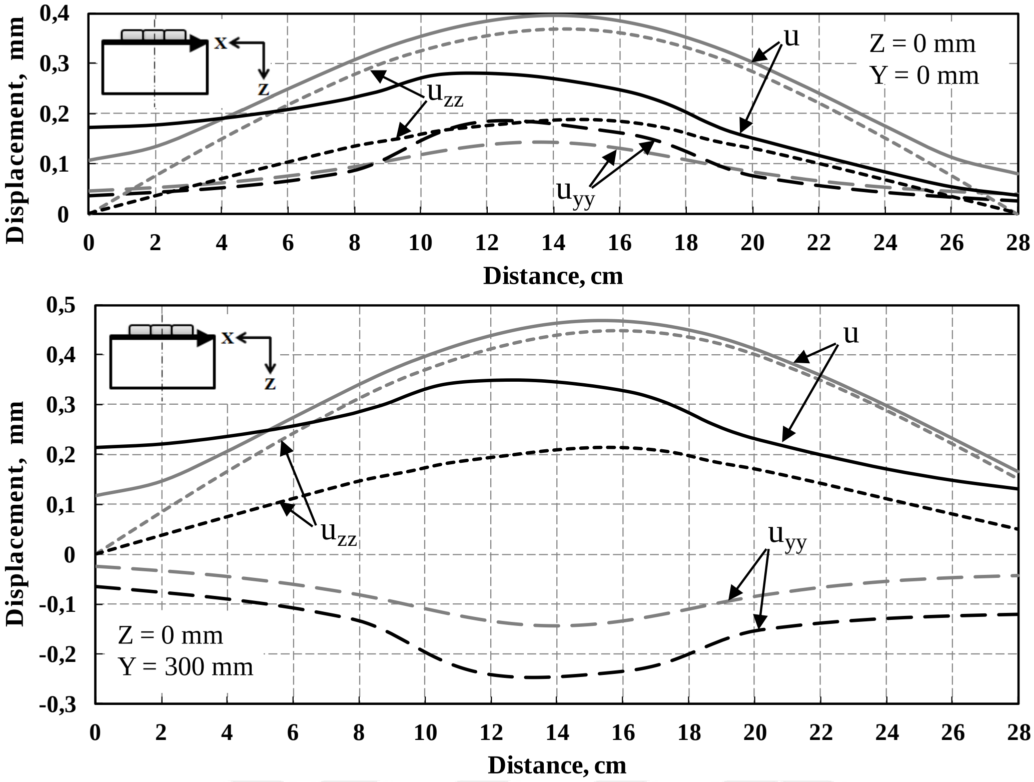

Figure 5.21 Displacement profiles at plate edges from start and end sides for the interpass temperatures of 80°C (grey lines) and 205°C (black lines) (Case B)

Distortion of the bottom surface obtained after cooling down to RT and unclamping is presented in Fig.5.22 below. As in the case with welding on V-groove, after the welding with 205°C interpass temperature, bending is less due to higher longitudinal shrinkage of the weld seam and higher contraction of the region around it. Weld pass deposition sequencing shows its significant influence on the final geometrical configuration of the section.

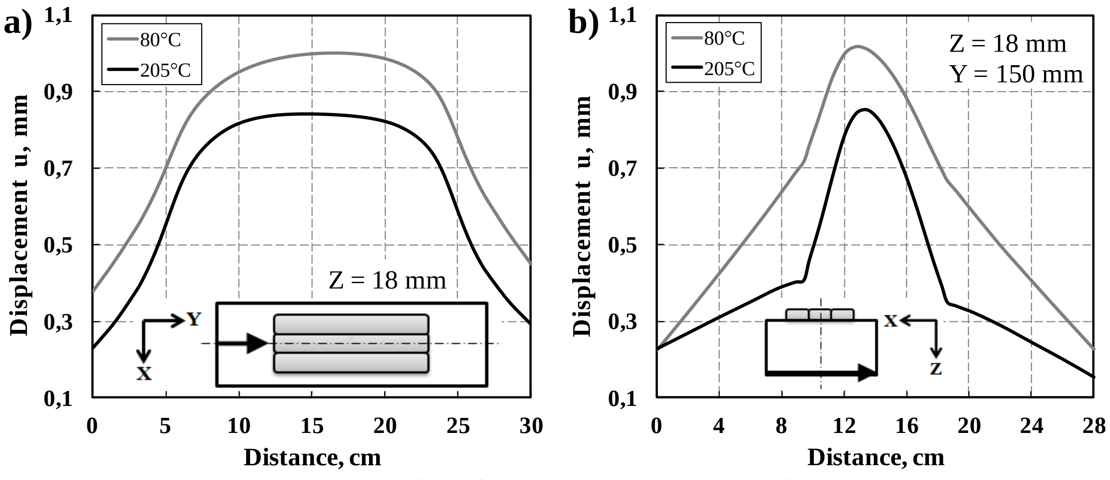

Figure 5.22 Distortion profiles for the bottom surface of the plate (Case B)
(a) longitudinal direction, (b) transverse direction

Fig.5.23 illustrates equivalent plastic strain distributions in the mid-way cross-section in different depths. Profiles of plastic strains for layers through WM and at HAZ are similar and reach respectively 2.8% (Z = 0 mm) and 2.1% (Z = 2.25 mm), therefore only differing profiles are presented in Fig.5.23. Elevated interpass temperatures induce increased plastic strains in the material of the plate. Also, there is a dependence in their formation in accord with overall welding direction and due to the position angle at which the welding torch is inclined in X-Z plane relatively to the previous weld bead.

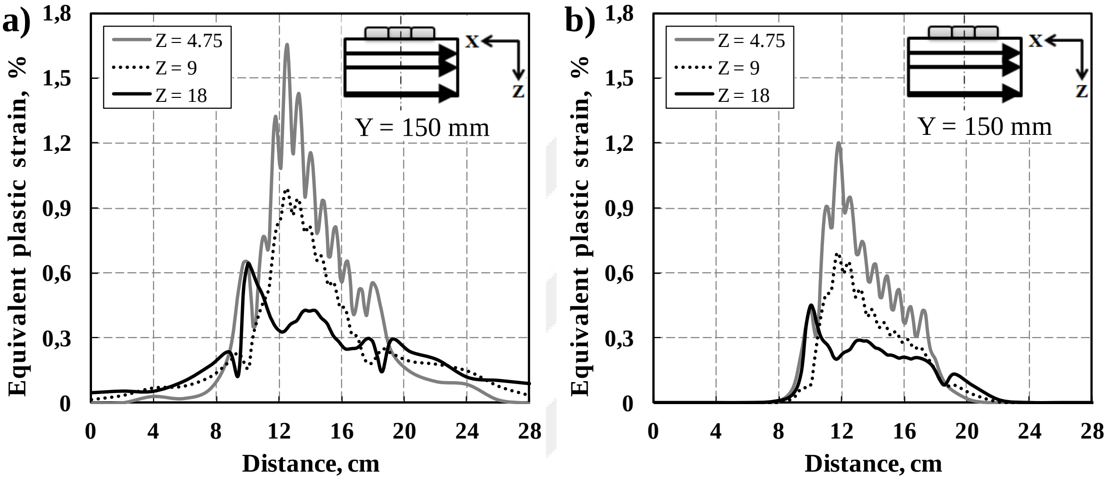

Figure 5.23 Equivalent plastic strain distributions (Case B): a) 205°C and b) 80°C

Fig.5.24a demonstrates that there is almost no difference in weld metal microstructure composition at raised interpass temperature. As higher the interpass temperature, so HAZ extends deeper into the bulk. And depending on welding technology, process parameters and problem scale this extension may play a role. Amount of martensite for bainitic steel is very low, and Fig.5.24b shows just tendency of increasing of martensite amount with higher interpass temperature. For steels with significant content of martensite phase this fact should be taken into account. Interesting, that for welding on V-groove the opposite effect is observed. The most probable explanation here is that due to the location of the weld bead on the surface and accelerated heat losses, the cooling rate is higher for higher interpass temperature than for lower interpass temperature. Higher cooling rates are known to lead to higher amounts of martensite.

Additional discussion of interpass temperature effect on residual stresses state is continued in following Subsection 5.2.4.

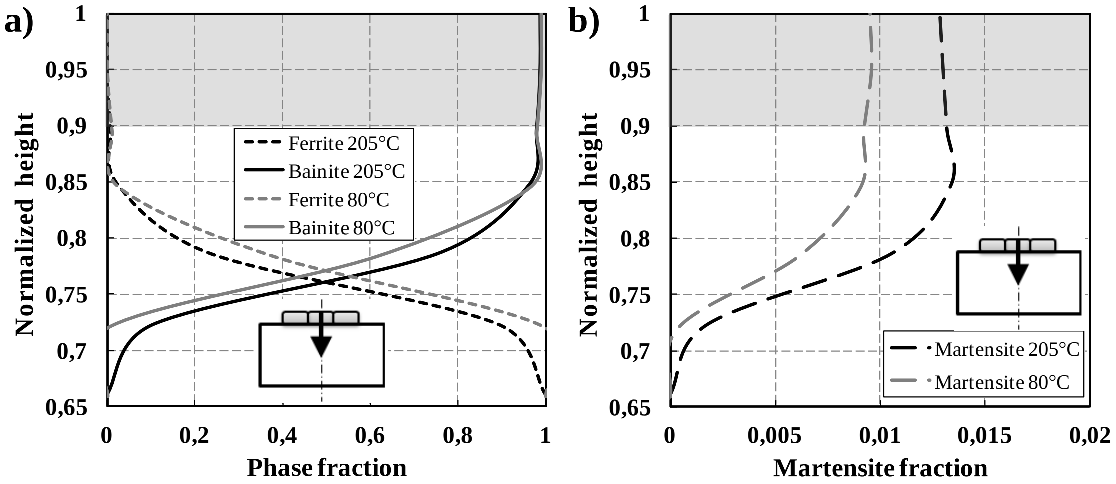

Figure 5.24 Phase fractions for 80°C and 205°C interpass temperatures at midway section of the plate (Case B)

5.2.4 Effect of sequencing of weld passes

Welding sequence is known to be one of the key parameters of the welding process due to great influence on final distortion of the construction. This aspect was studied by many authors as experimentally, so numerically. Sattari-Far and Javadi [77] have numerically investigated the effect of nine different schemes of welding sequences on resulting deformations of pipe geometry after single-pass butt-joint welding, and benefits of welding sequence to substantially decrease the distortions have been revealed. Gannon et al. [85] reported numerical study of the influence of four various welding sequences on residual stresses and distortion of plates with T-joint. Deshpande et al. [91] on the basis of the butt weld joint showed that the sequences starting from the middle of the plates to the ends of the plates predicted less cambering than sequences staring from the edges of the plates.

In the present study, the objective is to investigate the influence of deposition sequence on welding residual stresses distribution and distortion. Three cases with different deposition sequences were computed (Fig.5.13). In addition to cases A and B, case C is considered in this Subsection. Interpass temperature for all cases was kept at 80°C.

Distribution of residual stresses for Case B is presented in Fig.5.20b,d, and it is obviously that even though the deposition sequences of separate weld passes in Case B are different from those in Case C, the final residual stresses profiles in both cases completely matches. The possible reason is that overall surfacing welding direction in two cases is identical and this has the largest contribution to the finishing stress state of the component. Therefore, Fig.5.25 presents comparison of the longitudinal and transverse residual stresses distributions at the middle cross-section along the depicted paths among Case A and Case C only.

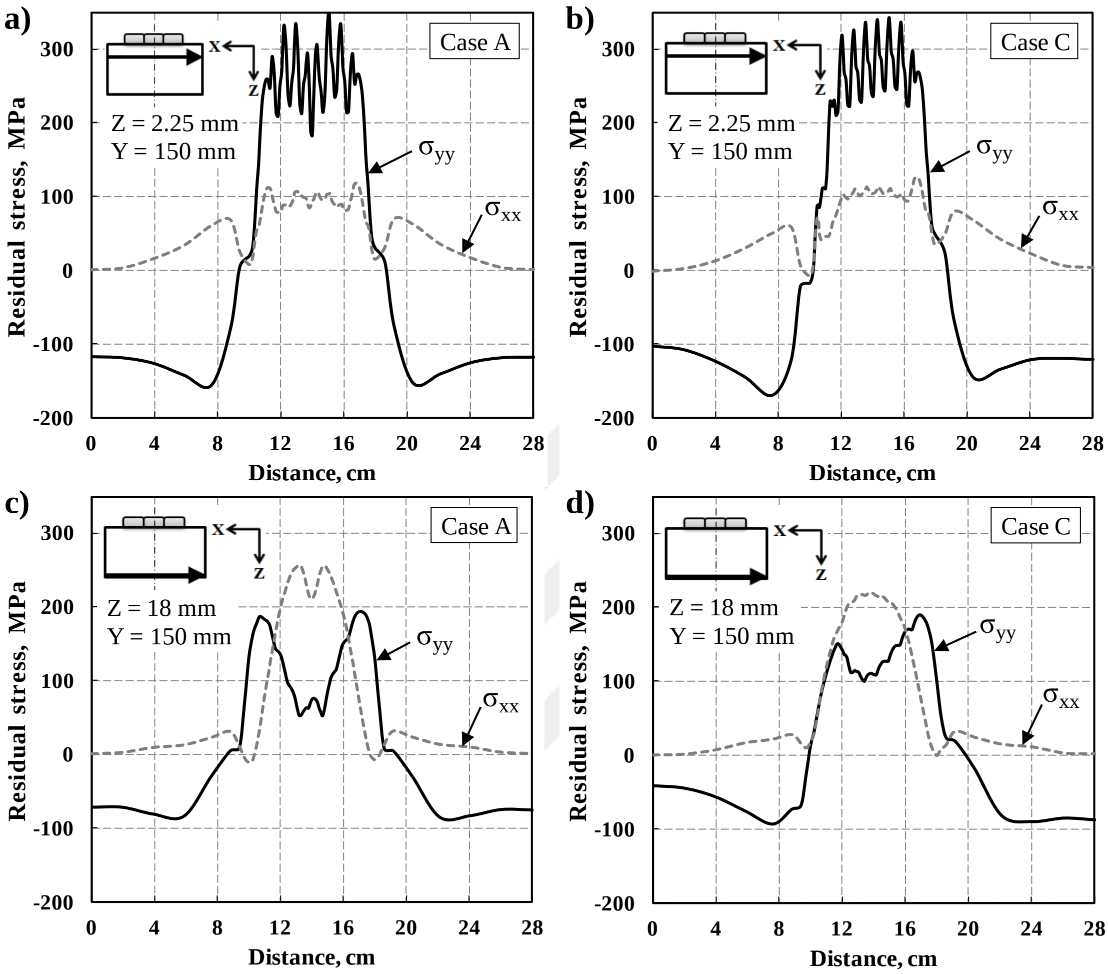

Figure 5.25 Longitudinal and transverse stress distributions in midway section

Carefully comparing Case A and Case C, it is seen that there is little difference at the HAZ level passing under the weld beads (Fig.5.25a,b). Both longitudinal and transverse stress components are respectively of the same value ranges. Peak values are obtained for tensile longitudinal stresses about 340-350 MPa. Distinction is in light asymmetry in Case C due to the difference in general surfacing welding directions. As for bottom surface (Fig.5.25c,d), distinction in residual stresses fields is more evident. Stress values are expectedly lower than that from 2.25 mm level, and tensile transverse stresses now dominate over tensile longitudinal stresses in both cases, but profile asymmetry in Case C is much more pronounced. And the upmost tensile transverse stress magnitude in Case C is 220 MPa and that in Case A is 257 MPa, which is higher at approximately 17%.

Deng [111] noted, in principle, when the subsequent pass is performed it will reheat the prior weld beads, and hence the stress field induced by the prior weld passes will be significantly changed. If the heat input of the subsequent weld pass is large enough, the stresses at and near the prior weld beads will be largely cancelled because the high peak temperature (higher than the mechanical melting point) can adequately soften this region during heating.

The simulation results suggest that the deposition fashion has significant influence on the residual stresses distribution.

To examine welding distortions, middle cross-sections were considered. Fig.5.26 shows the welding induced deformations in longitudinal and transverse directions.

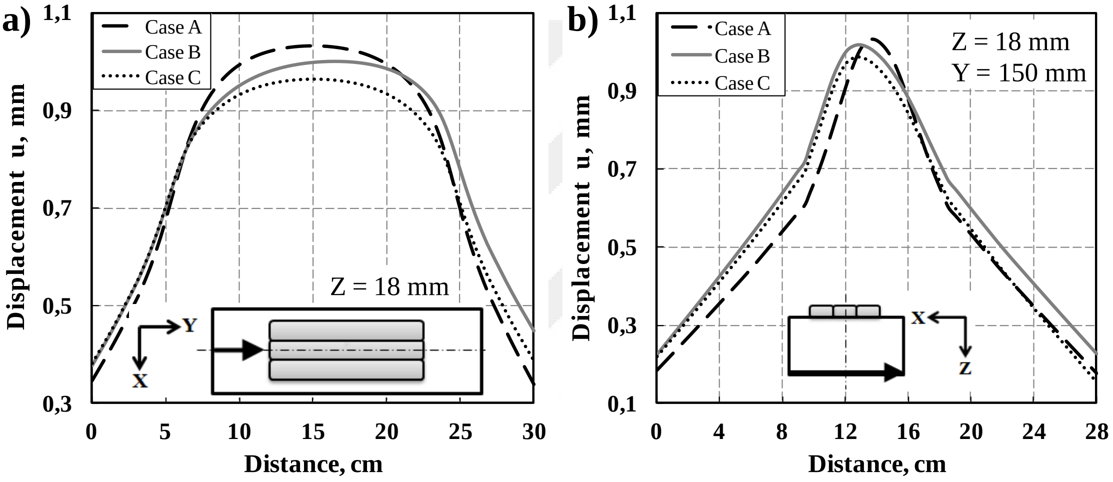

Figure 5.26 Distortion profiles for the bottom surface of the plate
(a) longitudinal direction, (b) transverse direction

In spite of the fact that overall route of surfacing welding in Case C is close to that in Case B (from one side to another side), in longitudinal direction Case C demonstrates symmetric profile (Fig.5.26a). Also, symmetric profile is observed in Case A, when overall surfacing movement is from the center to the sides. In Case A the overall welding direction is uneven, in Case C separate weld pass deposition is uneven, whereas in Case B the deposition is strictly ordered. This suggests that any kind of irregularity of deposition order has positive effect on deformation mode. Particularly, lower final displacement value in Case C than that in Case A indicates that unevenness of individual weld passes looks to be of more priority than variation of general surfacing direction. Though, here it is talked only of a fractions of a millimeter, need to remember of the problem scales, namely, of joint geometry, plate thickness, technology parameters etc. The larger the considered problem, the bigger deformations may be derived.

Fig.5.26b shows the distortion of bottom surface in the middle cross-section among three simulation cases. Only Case A demonstrates symmetric profile, and deformations in Cases B and C are both inclined to the start side of overall surfacing (left side on the graph). Comparing with residual stresses distributions, it is possible to conclude that creep process is involved since first weld passes being constantly stressed are repeatedly subjected to reheating from subsequent weld passes. As a result stress relief and increased deformation is obtained in the zones under first weld seams.

Next, deformation profiles from plate borders are presented in Fig.5.27. For end edge, varying components of displacement are also presented to clarify the distortion modes.

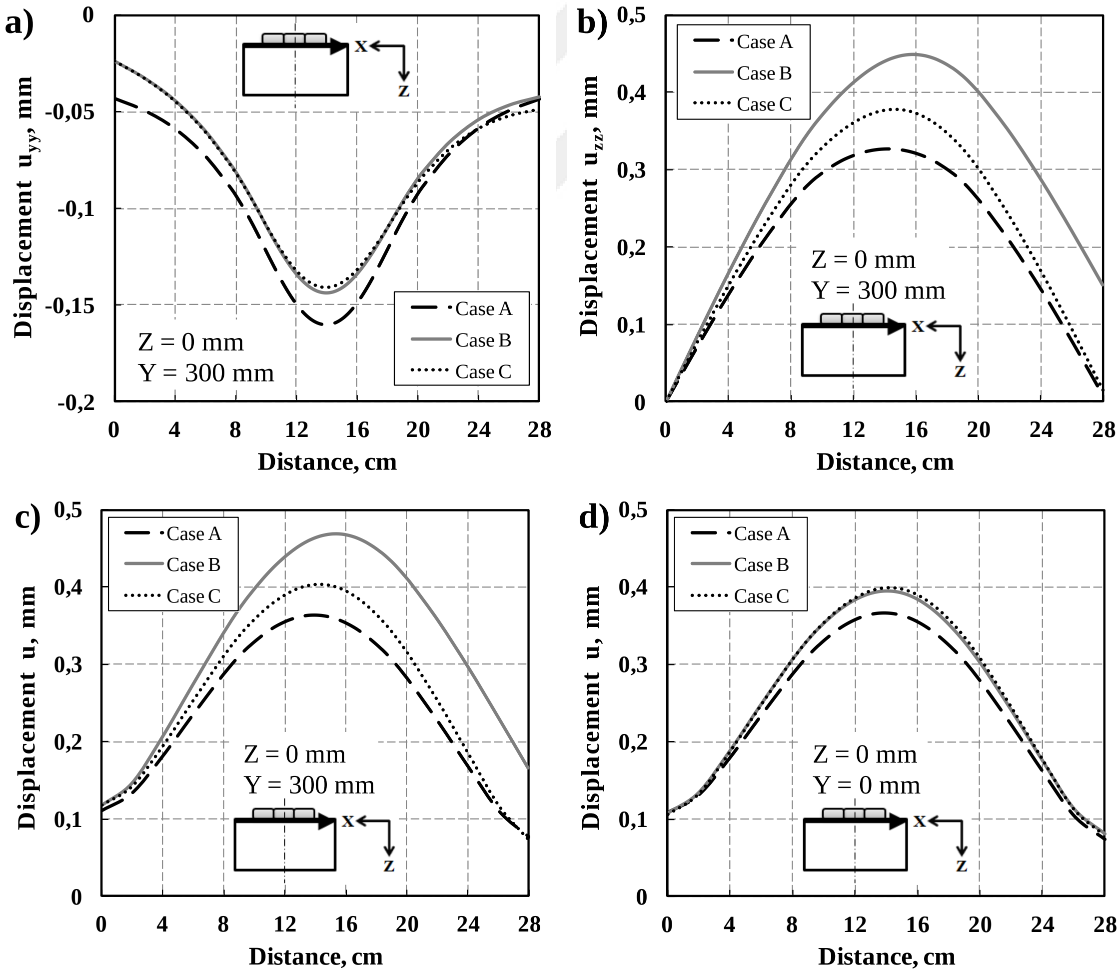

Figure 5.27 Displacement profiles at the plate edges
from (a, b, c) end and (d) start sides

Firstly, distortion profiles at the end edge (Fig.5.27c) are more influenced than at the start side (Fig.5.27d). The worst results are expectedly in Case B. The better situation is in Case C when alternating weld seams are employed. And the Case A looks as advantageous when welding is performed from the center of the plate to the sides. Secondly, concerning the components of the end edge distortion, longitudinal shrinkage u_{yy} in the center of the component (Fig.5.27a) in Case A is maximum among other two cases, at the same time the profile is the most symmetrical. Longitudinal shrinkage u_{yy} in Case B and C coincided. Also, transverse component u_{xx} of distortion (Fir.5.27b) looks to contribute to overall distortion most of all. In all cases, peak values come to the center, just in Case B and C there is a light shift to the last weld passes side, which is more evident in Case B.

Fig.5.28 shows plastic strain distributions measured from three through thickness levels in the transverse direction at middle cross-section of the welded sample. Profiles of Case B completely coincided with that of Case C, and therefore is not presented.

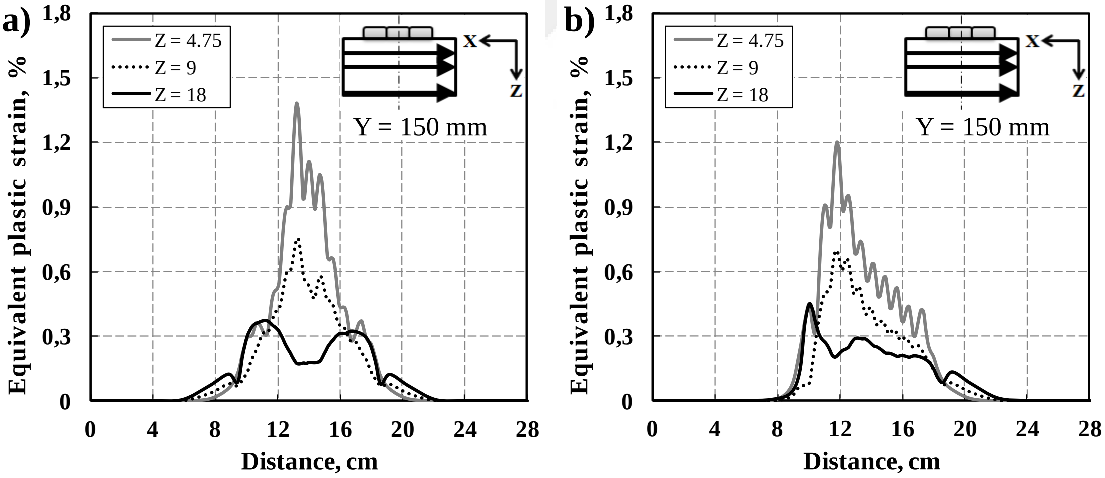

Figure 5.28 Equivalent plastic strain distributions: a) Case A, b) Case C

For the level at 4.75 mm deep from the top surface, peak values of plastic strain reaches 1.38% in Case A and 1.20% in Case C. This comes from the twice as much reheating of first weld pass in Case A from both sides. Away from first passes plastic strain level slowly decreases. Expectedly, in all the levels plastic strain distribution is more symmetrical in Case A than that in Case C.

As it was shown previously for single-bead-on-plate welding, equivalent plastic strains at start and end sides are much less than those in midway section, therefore, it is not presented here. But need to note, that for Case C its pattern appears to be more symmetrical and close to that of Case A as for start, so for end sides.

Fig.5.29 displays fields of final longitudinal residual stresses in middle-way cross-section of the component for all considered cases.

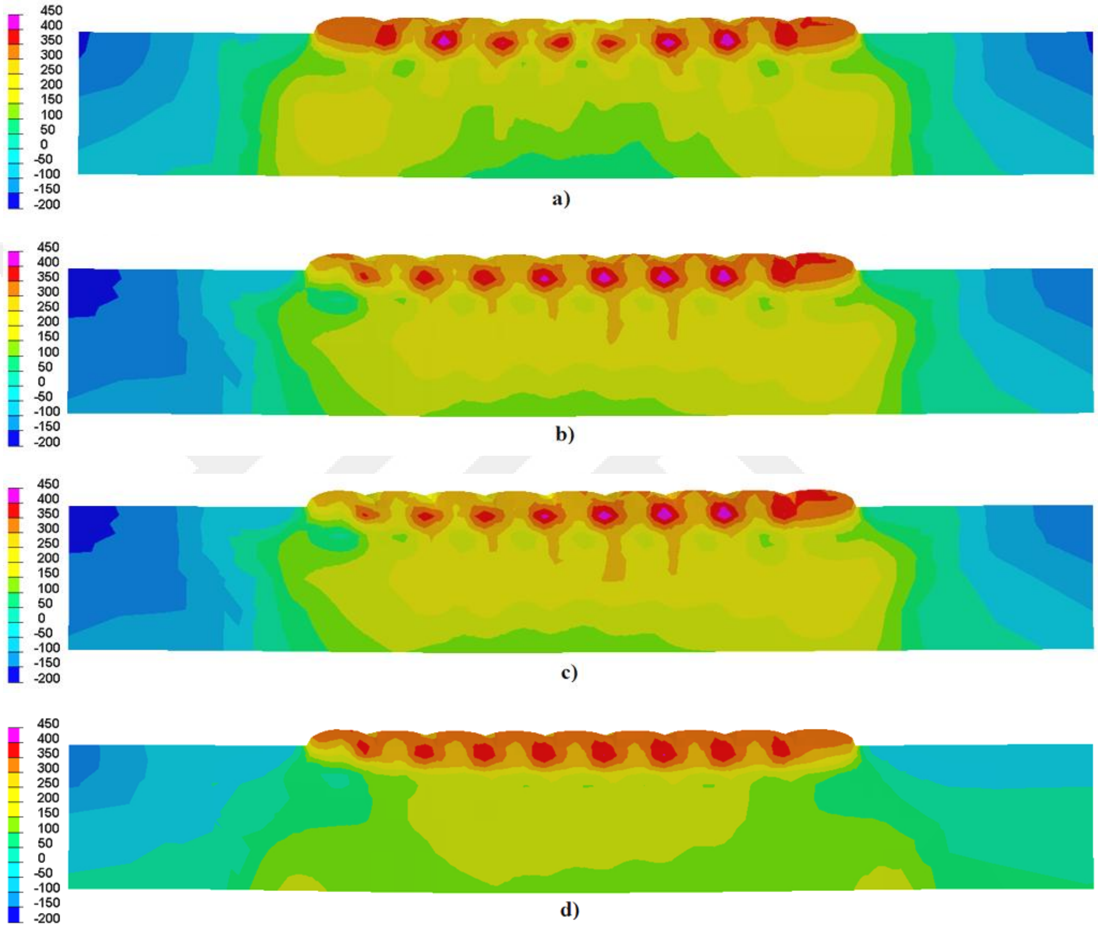

Figure 5.29 Longitudinal residual stresses in the transverse cross-sections:
a) Case A; b) Case B; c) Case C; d) Case B (interpass temperature 205°C)

Symmetric distribution of residual stresses is observed in Case A; in Case B and C due to the weld bead deposition sequence the field is asymmetric as in the weld seams, so in the body of the component. In the mid-way cross-section, stress states in Case B and Case C are quite identical. Also, in Case B and C first weld passes are considerably relieved from the heat of consequent passes. Stress state of the finishing weld passes (from right side) in Case B and C are resembling to last weld passes of Case A from both sides. And, in all cases finishing weld passes are in raised tensile stress state. In Case A, at the lower side of the plate under the surfacing welding, less stressed zone is more extensive than that in Case B and C.

Considering stress state of the "hot" Case B (Fig.5.29d), interpass temperature appears to have good effect on the weld seam metal − longitudinal residual stresses are more uniform and local peak values are decreased. However, the stresses in the body of the component in the whole are increased than in "cold" Case B (Fig.5.29b).

Fig.5.30 illustrates distribution of transverse (left column) and longitudinal (right column) residual stresses at the top surface of the component.

In Case A, the first weld pass is characterized with the highest values of tensile transverse stresses having a decreasing trend in the transverse direction to the side weld seams. This stress is accumulated during series of expansions-compressions caused by thermal cycles of following weld passes acting close from both sides. On the contrary, in Case B, the first weld pass is less stressed and tensile transverse stresses grow in direction to the final weld seams. At the welding start side, tensile stresses are higher than that at the welding end side. This is the influence of the designed energy ramps of the arc power at the beginning and termination of the weld (Table 7), given as 1.25 and 0.75, respectively. In Case C, where the start of the subsequent weld pass is at the end of the prior one, tensile transverse stresses at the both sides are similar. In "hot" Case B, the beneficial influence of the raised interpass temperature on the transverse stresses of the weld seams is confirmed, as well.

In Case A, the first weld pass is characterized with the highest values of tensile transverse stresses having a decreasing trend in the transverse direction to the side weld seams. This stress is accumulated during series of expansions-compressions caused by thermal cycles of following weld passes acting close from both sides. On the contrary, in Case B, the first weld pass is less stressed and tensile transverse stresses grow in direction to the final weld seams. At the welding start side, tensile stresses are higher than that at the welding end side. This is the influence of the designed energy ramps of the arc power at the beginning and termination of the weld (Table 7), given as 1.25 and 0.75, respectively. In Case C, where the start of the subsequent weld pass is at the end of the prior one, tensile transverse stresses at the both sides are similar. In "hot" Case B, the beneficial influence of the raised interpass temperature on the transverse stresses of the weld seams is confirmed, as well.

Case A

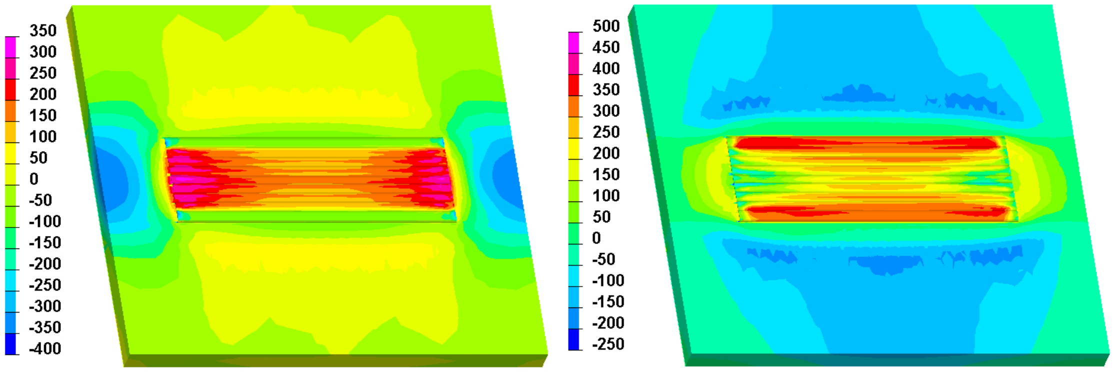

Case B

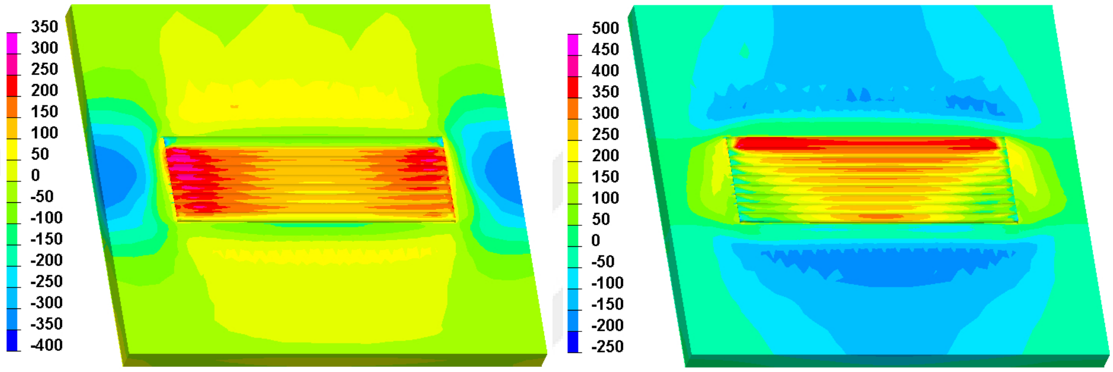

Case C

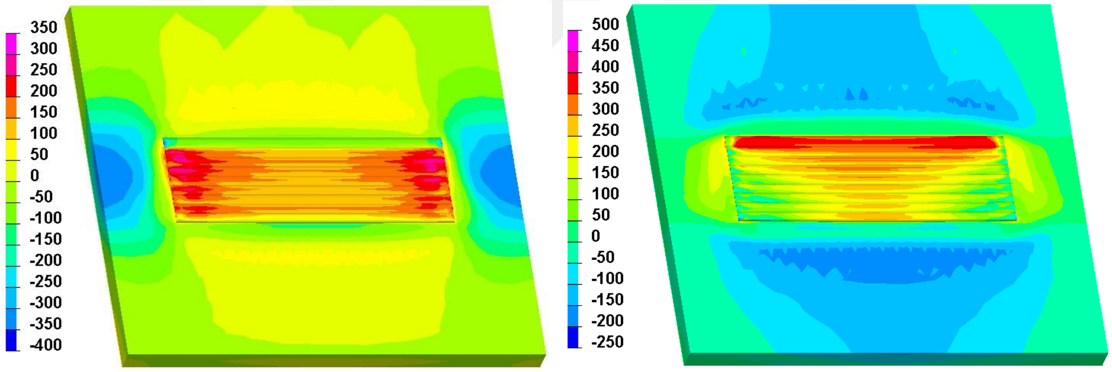

Case B (interpass temperature 205°C)

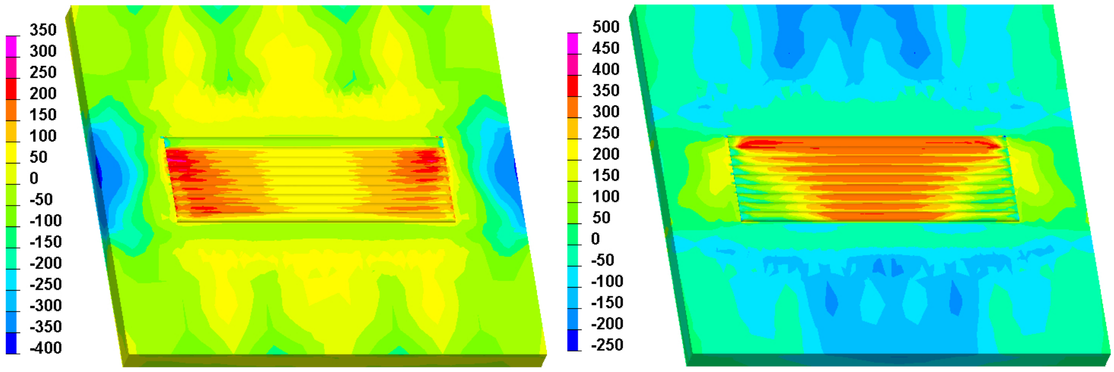

Transverse stresses σ_{xx}, MPa Longitudinal stresses σ_{yy}, MPa

Figure 5.30 Transverse and longitudinal residual stress distributions

Generalizing, last weld passes are free of transverse stresses in all considered cases since they did not endure heavy expansion-contraction cycles at all. Also, the medium regions of all surfacing weldings are defined as relieved zones comparatively to the start and the end sides of the weld beams. This is due to the stress relieving bending and angular deformation of the unrestrained part of the plate under the weld seams. While, the start and the end sides of the beams are surrounded by relatively cold regions of the plate which serve as constraints not allowing relieving deformation to happen. Elevated tensile transverse stresses at the start and the end sides of the weld seams are equilibrated with the compressive stresses at the borders of the plate.

Liang et al. [112] based on numerical and experimental studies on multi-pass welding reported that the transverse stress is very sensitive to deposition pattern.

Longitudinal residual stresses distribution in Case A demonstrates reverse features − the first weld pass is the less stressed now, and at the finishing weld seams the highest tensile longitudinal stresses are positioned. Though, in Case B behavior remained the same, namely, tensile longitudinal stresses grow in transverse direction to the finishing weld beads. Almost a half of first weld passes is in significantly relieved stress state. As Case C shows, alternating of the start and the end of the welding passes does not notably impact on the final longitudinal residual stresses distribution. As of the "hot" Case B, elevated interpass temperature shows increased tensile longitudinal stresses of surfacing welding, though returning to the stress field in the cross-section (Fig.5.29) it becomes clear that it is related mainly to the top layer of the surfacing welding.

Concerning the regions outside of the surfacing welding, alike picture is observed in all considered cases, namely, compressive residual stress field propagates in order to balance the stress state of the component.

Summarizing the study, it is possible to conclude that the deposition sequence of the weld passes during surfacing welding can significantly affect the welding deformation. In distortion point of view, Case A gives more symmetric deformation profile, but not the smallest. The smallest deformation profile is obtained in Case C, but not symmetric. Hence, among these three cases combination of cases A and C seems to be the most reasonable procedure of surfacing welding.

CHAPTER 6

CONCLUSIONS AND FUTURE WORKS

Welding residual stresses affect the safety and service lifetime of the constructions. Formation of residual stresses, distortion and microstructure evolution in multi-pass welding and surfacing welding on pipeline HSLA steels were numerically investigated. A procedure for three-dimensional finite element analysis of temperature field, stress-strain state and phase changes in weldments was developed by using ESI SYSWELD & VISUAL WELD software. Numerical results were verified by comparisons with the results of various tests and measurements, such as molten pool profile calibration, microstructure investigation, hardness measurement, residual stress measurement by XRD. Influences of the subsequent weld passes, the interpass temperature, and the unclamping temperature on the residual stress state were investigated. The following conclusions can be drawn from this study:

1. Clamping is one of the essential technological parameters; and for numerical investigations, all geometrical sizes and positions should be correctly reproduced.

The unclamping temperature which is related to unclamping time in technological process, appear to be influential on final residual stress level and distortions. Unclamping the weldments at temperatures higher than 50°C can entail unreasonable raise of residual stresses. This is especially related to the multi-pass weldings of thick-walled objects when cooling rate slows down after each weld pass and to the works at an accelerated paces in conditions of lack of time for complete cooling down. Although, residual stresses may be mitigated by consequent heat treatment, distortions remain unchanged. Residual stress relaxation process was suggested as a key mechanism of stress reduction in the component at the clamped state.

2. In multi-pass weldings on V-groove, partial heat treatment of earlier weld passes occurs due to subsequent weld runs. Greater quantity of weld passes results in decreasing of longitudinal residual stress level at the backside of the weldment and

approaching it to the magnitudes of the transverse stresses. Strain development demonstrates similar dependence at the backside of the plate − later weld passes reduce effect of initial weld passes. At the upper surface, greater quantity of weld passes gives raise to strain level. With increasing weld pass number, final distortion asymmetry progresses.

3. In the case of multi-pass welding on V-groove, interpass temperature mainly influences on the backside of the welded plate giving rise of longitudinal residual stresses. Interpass temperatures lower than 50°C leads to evidently higher distortions. Also after welding with lower interpass temperature (80°C), the weldment is subjected to higher final longitudinal bending and less longitudinal shrinkage. And welding with higher interpass temperature (205°C) appeared to be more susceptible to heat input cycles and expectedly gave more inequality of overall distortion.

4. In the case of multi-pass surfacing welding, interpass temperature similarly shows its effect mainly on the backside of the plate. For 80°C interpass temperature, in the weldment the transverse stresses prevail over longitudinal ones, final longitudinal bending of the component is higher and longitudinal shrinkage is lower than that for the case with 205°C. Whereas for 205°C interpass temperature, distortion inequality in the transverse direction is greater.

5. With increasing number of passes in surfacing welding, the longitudinal residual stresses level tends to the reduction due to partial heat treatment coming from the heat of last weld passes. But at the backside, with greater number of passes transverse residual stresses may considerably exceed longitudinal residual stresses. Also, distortion of the plate with surfacing welding confirms direct dependence on pass quantity.

6. In the surfacing welding, the sequence of the weld passes significantly affects the distortion of the plate. The most uneven weld deposition mode results in more uniform residual stress field and deformation.

As future work, it is recommended to continue numerical studies by focusing on the industrial applications of multi-pass weldings with different joint shapes, deposition sequences, alteration of technological parameters, clamping configurations and conditions.

REFERENCES

[1] M.M. Gorbunov-Posadov, Extensible programs, Poliptih, Moscow, 1999. In Russian.

[2] T. Zacharia, J.M. Vitek, J.A. Goldak, T.A. Debroy, M. Rappaz, H. Bhadeshia, “Modeling of fundamental phenomena in welds”, Modelling and Simulation in Materials Science and Engineering, Vol.3, pp.265–88,1995.

[3] P.J. Withers, “Residual stress and its role in failure”, Reports on Progress in Physics, Vol.70, pp.2211-2264, 2007.

[4] X. Shan, C.M. Davies, T. Wangsdan, N.P. O’Dowd, K.M. Nikbin, “Thermo-mechanical modelling of a single-bead-on-plate weld using the finite element method”, International Journal of Pressure Vessels and Piping, Vol.86, pp.110-121, 2009.

[5] Practical residual stress measurement methods / edited by Gary S. Schajer, John Wiley & Sons Inc., 2013.

[6] S. Kou, Welding metallurgy, 2nd Ed., John Wiley & Sons Inc., 2003.

[7] Metallurgy and mechanics of welding: processes and industrial applications / edited by Régis Blondeau, John Wiley & Sons Inc., 2008.

[8] Welding in engineering, Volume 1 / edited by N.A. Olshanskiy, Mashinostroenie, 1978. In Russian.

[9] K. Easterling, Introduction to the physical metallurgy of welding, 2nd Ed., Butterworth-Heinemann, 1992.

[10] K. Masubuchi, Analysis of Welded Structures: Residual Stress, Distortion, and their Concequences, Pergamon Press Ltd, 1980.

[11] W. Zinn, B. Scholtes, “Residual stress formation processes during welding and joining”, Handbook of Residual Stress and Deformation of Steel / edited by G. Totten, M. Howes, T. Inoue, ASM International, Materials Park, pp.391-396, 2002.

[12] H. Wohlfahrt, “Consequences of austenite transformation for the formation of welding residual stresses”, Härterei-Technische Mitteilungen, Vol.41, pp.248-257, 1986. In German.

[13] R.H. Leggatt, “Residual stresses in welded structures”, International Journal of Pressure Vessels and Piping, Vol.85, pp.144-151, 2008.

[14] E. Macherauch, H. Wohlfahrt, “Different sources of residual stress as a result of welding”, Residual Stresses in Welded Construction and their Effects, The Welding Institute Publications, London, 1977.

[15] I.A. Birger, Residual stresses, Mashgiz, 1963. In Russian.

[16] L. Chaowen, W. Yong, C. Yuhua, “Influence of peak temperature during in-service welding of API X70 pipeline steels on microstructure and fracture energy of the reheated coarse grain heat-affected zones”, Journal of Materials Science, Vol.46, pp.6424-6431, 2011.

[17] C. Ruud, “Measurement of residual stresses”, Handbook of Residual Stress and Deformation of Steel / edited by G. Totten, M. Howes, T. Inoue, ASM International, Materials Park, pp.99-117, 2002.

[18] N.S. Rossini, M. Dassisti, K.Y. Benyounis, A.G. Olabi, “Methods of measuring residual stresses in components”, Materials and Design,Vol.35, pp.572-588, 2012.

[19] A. De, T. DebRoy, “A perspective on residual stresses in welding”, Science and Technology of Welding and Joining, Vol.16, pp.204-208, 2011.

[20] G. Verhaeghe, Predictive formulae for weld distortion, a critical review, TWI, 1998.

[21] G.A. Nikolaev, S.A. Kurkin, V.A. Vinokurov, Welded structures. Strength of welded joints and deformations of structures, Visshaya shkola, 1982. In Russian.

[22] D. Radaj, Heat Effects of Welding: temperature field, residual stress, distortion, Springer-Verlag, 1992.

[23] R.V. Preston, “Modelling of residual stresses in welded aerospace alloys”, Ph.D. Thesis, University of Cambridge, 2000.

[24] A.M. Akbari Pazooki, “Distortion control during welding”, Ph.D. Thesis, Delft University of Technology, 2014.

[25] J.L. Hansen, “Numerical modelling of welding induced stresses”, Ph.D. Thesis, Technical University of Denmark, 2003.

[26] M. Birk-Sørensen, “Simulation of welding distortions in ship section”, Ph.D. Thesis, Technical University of Denmark, 1999.

[27] Processes and mechanisms of welding residual stress and distortion / edited by Z. Feng, Woodhead Publishing Limited, 2005.

[28] J.B. Leblond, J. Devaux, “A new kinetic model for anisothermal metallurgical transformations in steels including effect of austenite grain size”, Acta Metallurgica, 32(1), pp.137–146, 1984.

[29] D.F. Watt, L. Coon, M.J Bibby, J. Goldak, C. Henwood, “An algorithm for modeling microstructural development in weld heat-affected zones”, Acta Metallurgica, 36 (11), pp.3029-3035, 1988.

[30] C. Henwood, M. Bibby, J. Goldak, D. Watt, “Coupled transient heat transfer – microstructure weld computations, Part B”, Acta Metallurgica, 36 (11), pp.3037-3046, 1988.

[31] L. Karlsson, “Thermal Stresses in Welding”, in R.B. Hetnarski (ed.), Thermal Stresses, Vol.1, pp.300-389, Elsevier, 1986.

[32] J. Goldak, “Computational Weld Mechanics as a Coupled Problem”, Proc. of the 5th Int. Conf. on Modelling of Casting, Welding and Advanced Solidification Processes V, edited by M. Rappaz, M. R. Özgü and K. W. Mahin, The Minerals, Metals & Materials Society, USA, pp.85-96, 1991.

[33] L.-E. Lindgren, “Finite Element Modeling and Simulation of Welding. Part 1-3”, Journal of Thermal Stresses, Vol.24 (2-4), 2001.

[34] K.J. Bathe, Finite element procedures, Prentice Hall, 1996.

[35] A. Hrennikoff, “Solution of problems of elasticity by the framework method”, Journal of applied mechanics, 8.4, pp.169–175, 1941.

[36] O.C. Zienkiewicz, The Finite Element Method, 3rd ed., McGraw-Hill, 1977.

[37] T. Inoue, “Metallo-thermo-mechanics − application to quenching”, Handbook of Residual Stress and Deformation of Steel / edited by G. Totten, M. Howes, T. Inoue, ASM International, Materials Park, pp.296-311, 2002.

[38] L.-E. Lindgren, Computational welding mechanics. Thermomechanical and microstructural simulations, Woodhead Publishing Limited, 2007.

[39] L. Tall, “The strength of welded build-up columns”, Ph.D. Thesis, Lehigh University, 1961.

[40] V.A. Vinokurov, Weld deformations and stresses, Mashinostroenie, 1968. In Russian.

[41] Y. Ueda, T. Yamakawa, “Analysis of thermal elastic-plastic stress and strain during welding by finite element method”, Transactions of the Japan Welding Society, Vol.2(2), pp.90-100, 1971.

[42] T. Iwaki, K. Masubuchi, “Thermo-elastic analysis of orthotropic plate by the finite element method”, Journal of the Society of Naval Architects of Japan, Vol.130, pp.195-204, 1971.

[43] Y. Fujita, Y. Takeshi, M. Kitamura, T. Nomoto, “Welding stresses with special reference to cracking”, IIW Doc X-655-72, 1972.

[44] H.D. Hibbitt, P.V. Marcal, “A numerical thermo-mechanical model for the welding and subsequent loading of a fabricated structure”, Computers & Structures, Vol.3, pp.1145-1174, 1973.

[45] E. Friedman, “Thermomechanical analysis of the welding process using the finite element method”, ASME Journal of Pressure Vessel Technology, Vol.97(3), pp.206-213, 1975.

[46] J. Goldak, A. Oddy, M. Gu, W. Ma, A. Mashaie, E. Hughes, “Coupling heat transfer, microstructure evolution and thermal stress analysis in weld mechanics”, in IUTAM Symposium on the Mechanical Effects of Welding, Springer-Verlag, pp. 1-30, 1992.

[47] R. Radaj, “Finite element analysis of welding residual stresses”, Proceedings of 2nd International Conference on Residual Stresses (ICRS-2), p.510, 1988.

[48] M.O. Näsström, L. Wikander, L. Karlsson, L.E. Lindgren, J. Goldak, “Combined 3D and shell modelling of welding”, Proceedings of IUTAM Symposium on the mechanical effects of welding, pp.197-206, 1992.

[49] M.O. Näsström, “Thermo-mechanical modelling of welding with experimental verification”, Ph.D. Thesis, Luleå University, 1992.

[50] H.K.D.H. Bhadeshia, “Modelling of steel welds”, Materials Science and Technology, Vol.8, pp.123-133, 1992.

[51] SYSWELD 2008 Welding simulation - User's guide.

[52] J.A. Goldak, M. Akhlaghi, Computational welding mechanics, Springer, 2005.

[53] C.H. Gür, J. Pan, Handbook of Thermal Process Modeling of Steels, Taylor and Francis, 2009.

[54] V. Pavlyk, U. Dilthey, “A numerical and experimental study of fluid flow and heat transfer in stationary GTA weld pools”, in H. Cerjak (ed.), Mathematical Modelling of Weld Phenomena 5, The Institute of Materials, 2001.

[55] Y. Ueda, H. Murakawa, N. Ma, Welding deformation and residual stress prevention, Elsevier Inc., 2012.

[56] D. Radaj, H. Porzner, S. Braun, “Numerische Simulation von Eigenspannungen und Verzug bei Schweißverbindungen aus AlMgSi-Legierungen”, Konstruktion, 7/8, 1998.

[57] R.S. Funderburk, “A look at heat input”, Welding Innovation, Vol.XVI, No.1, 1999.

[58] V.I. Spivakov, E.A. Orlov, P.L. Litvinenko, A.V. Nogovitsyn, “Kinetics of Austenite Transformation and Bainite Structure Formation during Strain-Heat Hardening of Low-Perlite Steel X70 (X 65) (API 5L Gr X-60, API 5L Gr X-70) Plates for Gas Pipelines”, Metallurgical and Mining Industry, Vol. 2, No. 1, pp.39-42, 2010.

[59] API Specifications 5L, Specifications for Line Pipe, forty-fourth ed., American Petroleum Institute, p.108, 2007.

[60] J. Lu, “Quantitative microstructural characterization of microalloyed steels”, Ph.D. Thesis, University of Alberta, 2009.

[61] D. Deng, H. Murakawa, “Finite element analysis of temperature field, microstructure and residual stress in multi-pass butt-welded 2.25Cr-1Mo steel pipes”, Computational Materials Science, Vol.43, pp.681-696, 2008.

[62] H.K.D.H. Bhadeshia, “Material factors”, Handbook of Residual Stress and Deformation of Steel / edited by G. Totten, M. Howes, T. Inoue, ASM International, Materials Park, pp.3-10, 2002.

[63] J.J. Xu, P. Gilles, Y.G. Duan, C.Yu, “Temperature and residual stress simulations of the NeT single-bead-on-plate specimen using SYSWELD”, International Journal of Pressure Vessels and Piping, Vol.99-100, pp.51-60, 2012.

[64] O. Muránsky, C.J. Hamelin, M.C. Smith, P.J. Bendeich, L. Edwards, “The effect of plasticity theory on predicted residual stress fields in numerical weld analyses”, Computational Materials Science, Vol.54, pp.125-134, 2012.

[65] T. Schenk, “Modelling welding distortion. Influence of clamping and sequencing”, Ph.D. Thesis, Delft University of Technology, 2011.

[66] M.C. Smith, P.J. Bouchard, M. Turski, L. Edwards, R.J. Dennis, “Accurate prediction of residual stress in stainless steel welds”, Computational Materials Science, Vol.54, pp.312-328, 2012.

[67] S.K. Bate, R. Charles, D. Everett, D. O'Gara, A. Warren, S. Yellowlees, “Sensitivity of predicted residual stresses to modelling assumptions”, 16th European conference on fracture, pp.73-78, 2006.

[68] L. Depradeux, J.F. Jullien, “2D and 3D numerical simulations of TIG welding of a 316L steel sheet”, Revue Européenne des Éléments, Vol.13, pp.269-288, 2004.

[69] K. Satoh, “Transient thermal stresses of weld heat-affected zone by both-ends-fixed bar analogy”, Kovove Materialy, Vol.8, pp.569-587, 1970.

[70] W.K.C. Jones and P.J. Alberry, “Residual Stresses in Welded Constructions”, Welding Institute, Paper 2, 1977.

[71] H.K.D.H. Bhadeshia, “Possible effects of stress on steel weld microstructures”, in H. Cerjak (ed.), Mathematical Modelling of Weld Phenomena 2, The Institute of Materials, pp.71-118, 1995.

[72] M. Wolff, M. Böhm, D. Helm, “Material behavior of steel − Modeling of complex phenomena and thermodynamic consistency”, International Journal of Plasticity, Vol.24, pp.746-774, 2008.

[73] D. Dubois, J. Devaux, J.B. Leblond, “Numerical simulation of welding operation: calculation of residual stresses and hydrogen diffusion”, 5th International Conference on Pressure Vessel Technology, Vol.11, pp.1210-1239, 1984.

[74] J.B. Leblond, J. Devaux, J.C. Devaux, “Mathematical modelling of transformation plasticity in steels I: Case of ideal-plastic phases”, International Journal of Plasticity, Vol.5, pp.551-572, 1989.

[75] A.S. Oddy, “Three-dimensional finite deformation, thermal-elasto-plastic finite element analysis”, Ph.D. Thesis, Carleton University, 1987.

[76] B. Brickstad, B.L. Josefson, “A parametric study of residual stresses in multi-pass butt-welded stainless steel pipes”, International Journal of Pressure Vessels and Piping, Vol.75, pp.11-25, 1998.

[77] I. Sattari-Far, Y. Javadi, “Influence of welding sequence on welding distortions in pipes”, International Journal of Pressure Vessels and Piping, Vol.85, pp.265-274, 2008.

[78] P. Michaleris, X. Sun, “Finite element analysis of thermal tensioning techniques mitigating weld buckling distortion”, Welding Journal, Vol.76, pp.451-457, 1997.

[79] L. Troive, “Deformations and stresses in welded pipes − Numerical and experimental investigation”, Ph.D. Thesis, Luleå University, 1996.

[80] L.E. Lindgren, L. Karlsson, “Deformation and stresses in welding of shell structures”, International Journal for Numerical Methods in Engineering, Vol.25, pp.635-655, 1988.

[81] J. Goldak, A. Oddy, M. McDill, A. Chakravarti, M. Bibby, R. House, “Progress in computing residual stress and strain in welds”, Trends in Welding Research, p.523, 1986.

[82] P. Michaleris, Z. Feng, G. Campbell, “Evaluation of 2D and 3D FEA models for predicting residual stresses and distortion”, Proceedings of ASME Pressure Vessels and Piping Conference, PVP-Vol.347, p.91, 1997.

[83] J. Sakkiettibutra, F. Vollertsen, “Possibilities and limitations of geometric simplifications for calculations of residual stresses and distortions”, Production Engineering. Research and Development, Vol.5, pp.485-495, 2011.

[84] P. Duranton, J. Devaux, V. Robin, P. Gilles, J.M. Bergheau, “3D modelling of multipass welding of a 316L stainless steel pipe”, Journal of Materials Processing Technology, Vol.153-154, pp.457-463, 2004.

[85] L. Gannon, Y. Liu, N. Pegg, M. Smith, “Effect of welding sequence on residual stress and distortion in flat-bar stiffened plates”, Marine Structures, Vol.23, pp.385-404, 2010.

[86] I. Sattari-Far, M.R. Farahani, “Effect of weld groove shape and pass number on residual stresses in butt-welded pipes”, International Journal of Pressure Vessels and Piping, Vol.86, pp.723-731, 2009.

[87] G. Erian, “Non-destructive evaluation of residual stresses in the multi-pass steel weldments”, Master Thesis, Middle East Technical University, 2012.

[88] U. Peil, M. Wichers, “Schweißen unter Betriebsbeanspruchung – Werkstoffkennwerte für einen S355 J2G3 unter Temperaturen bis 1200°C”, Stahlbau, Vol.73, pp.400-416, 2004. In German.

[89] S.J. Lewis, H. Alizadeh, C. Gill, A. Vega, H. Murakawa, W. El-Ahmar, P. Gilles, D.J. Smith, C.E. Truman, “Modelling and measurement of residual stresses in autogenously welded stainless steel plates: Part 1 − fabrication and modelling”, International Journal of Pressure Vessels and Piping, Vol.86, pp.798-806, 2009.

[90] Y. Javadi, "Investigation of clamping effect on the welding residual stress and deformation on Monel plates by using the ultrasonic stress measurement and finite element method", Journal of Pressure Vessel Technology, Vol.137(1), 2015.

[91] A.A. Deshpande, L. Xu, W. Sun, D.G. McCartney, T.H. Hyde, "Finite-element-based parametric study on welding-induced distortion of TIG-welded stainless steel 304 sheets", The Journal of Strain Analysis for Engineering Design, Vol.46, pp.267-279, 2011.

[92] C. Batıgün, "An investigation of the effect of material size on the distortion behavior during welding", 18th International Metallurgy and Materials Congress, Istanbul, Turkey, 2016.

[93] DIN EN ISO 15614-1 Welding procedure test, Part 1: Arc and gas welding of steels and arc welding of nickel and nickel alloys, 2004.

[94] A. Yaghi, T.H. Hyde, A.A. Becker, W. Sun, J.A. Williams, "Residual stress simulation in thin and thick-walled stainless steel pipe welds including pipe diameter effects", International Journal of Pressure Vessels and Piping, Vol.83, pp.864-874, 2006.

[95] I.N. Ponomareva, "Development of the procedure for calculated estimation of residual weld stresses in pipeline welds", Ph.D. Thesis, Bauman Moscow State Technical University, 2013. In Russian.

[96] H. Alipooramirabad, R. Ghomashchi, A. Paradowska, M. Reid, "Residual stress-microstructure-mechanical property interrelationships in multipass HSLA steel welds", Journal of Materials Processing Technology, Vol.231, pp.456-467, 2016.

[97] D. Löhe, O. Vöhringer, "Stability of residual stresses", Handbook of Residual Stress and Deformation of Steel / edited by G. Totten, M. Howes, T. Inoue, ASM International, Materials Park, pp.54-69, 2002.

[98] M.C. Zondi, "Factors that affect welding-induced residual stress and distortions in pressure vessel steels and their mitigation techniques: a review", Journal of Pressure Vessel Technology, Vol.136, pp.1-9, 2014.

[99] H.W. Lee, S.W. Kang, "The relationship between residual stresses and transverse weld cracks in thick steel plate", American Welding Society, Welding Journal, pp.225-230, 2003.

[100] A. Hasui, O. Morigaki, Surfacing and spraying, Mashinostroenie, Moskow, 1985. In Russian, translated from Japanese.

[101] J. Goldak, M. Asadi, J. Zhou, S. Tchernov, D. Downey, “Optimization of a weld overlay on a plate structure”, Journal of Pressure Vessel Technology, Vol.132, pp.9, 2010.

[102] C. Bayley, J. Goldak, “Welding induced distortions and strains of a built-up panel, experiment and numerical validation”, Journal of Pressure Vessel Technology, Vol.134, pp.7, 2012.

[103] J. Katsuyama, M. Udagawa, H. Nishikawa, M. Nakamura, K. Onizawa, “Evaluation of weld residual stress near the cladding and J-weld in reactor pressure vessel head for the assessment of PWSCC behavior”, E-Journal of Advanced Maintenance, Vol.2, pp.50-64, 2010.

[104] M. Udagawa, J. Katsuyama, H. Nishikawa, K. Onizawa, “Evaluation of residual stress near the weld overlay cladding by welding and post-weld heat treatment”, Welding Internaional, Vol.28 (7), pp.521-534, 2014.

[105] A. Pahkamaa, L. Karlsson, J. Pavasson, M. Karlberg, M. Näsström, J. Goldak, “A method to improve efficiency in welding simulations for simulation driven design”, Proceedings of the ASME IDETC/CIE 2010, Vol.3, pp.81-90, Canada.

[106] W. Jiang, Y. Luo, B.Y. Wang, S.T. Tu, J.M. Gong, “Residual stress reduction in the penetration nozzle weld joint by overlay welding”, Materials and Design, Vol.60, pp.443-450, 2014.

[107] J.W.H. Price, A.M. Paradowska, R. Ibrahim, T.R. Finlayson, “Residual stresses evaluation in welds and implications for design for pressure vessel applications”, Journal of Pressure Vessel Technology, Vol.128, pp.638-643, 2006.

[108] A. Paradowska, J.W.H. Price, R. Ibrahim, T.R. Finlayson, “A neutron diffraction study of residual stress due to welding”, Journal of Materials Processing Technology, Vol.164-165, pp.1099-1105, 2005.

[109] A. Paradowska, J.W.H. Price, R. Ibrahim, T.R. Finlayson, R. Blevins, M. Ripley, “Residual stress measurements by neutron diffraction in multi-bead welding”, Physica B, Vol.385-386, pp.890-893, 2006.

[110] W. Jiang, K. Yahiaoui, "Effect of the interpass temperature on the predicted residual stress distributions in a multipass welded piping branch junction", The Journal of Strain Analysis for Engineering Design, Vol.43, pp.109-119, 2008.

[111] D. Deng, "Influence of deposition sequence on welding residual stress and deformation in an austenitic stainless steel J-groove welded joint", Materials and Design, Vol.49, pp.1022-1033, 2013.

[112] W. Liang, H. Murakawa, D. Deng, "Investigation of welding residual stress distribution in a thick-plate joint with an emphasis on the features near weld end-start", Materials and Design, Vol.67, pp.303-312, 2015.

VITA

Nuriya Garipova was born in Ufa, Russian Federation. She received her Engineer degree with Honour from Equipment and Technology of Welding Engineering Department of Ufa State Aviation Technical University. She has worked as a manufacturing engineer in Welding Technologies Department of Ufa Engine-production Industrial Association (JSC «UMPO») that produces turbojet engines for Sukhoi aircrafts. In 2009, she enrolled in the graduate program in Metallurgical and Materials Engineering at Middle East Technical University, also obtained fellowship from the Scientific and Technological Research Council of Turkey (TÜBİTAK-BİDEB) under «2215 - PhD Fellowship Programme for Foreign Citizens» and began to pursue her Ph.D. degree. Her main areas of interest are welding technologies and welding computational mechanics.

Publications:

1. N. Garipova, C. Batıgün, C.H. Gür, "Numerical and experimental determination of the residual stress state in multipass welded API 5L X70 plates", Materials Testing, Vol.56, pp.831-836, 2014 (№10).
2. N. Garipova, C. Batıgün, C.H. Gür, "A study on residual stress distribution determination on multipass welded steel plate", Proceedings of 3rd International Conference on Welding Technologies and Exhibition (ICWET'14), 21-23 May 2014, Manisa, Turkey.
3. N. Garipova, C. Batıgün, C.H. Gür, "Determination of residual stress field on a multipass welded steel butt-joint by finite element modeling", Proceedings of 17th International Metallurgy and Materials Congress (IMMC), 11-13 September 2014, Istanbul, Turkey.